NEXT GENERATION ENGINEERING

SMART SOLUTIONS AND APPLICATIONS

Editors

Sabri KOÇER

Özgür DÜNDAR

ISRES Publishing

NEXT GENERATION ENGINEERING

SMART SOLUTIONS AND APPLICATIONS

Editors
Sabri KOÇER
Özgür DÜNDAR

ISRES Publishing

Next Generation Engineering: Smart Solutions and Applications

Editors

Sabri KOCER

Ozgur DUNDAR

This book was typeset in 10/12 pt. Times New Roman, Italic, Bold and Bold Italic.

Next Generation Engineering: Smart Solutions and Applications

Published by ISRES Publishing, International Society for Research in Education and Science (ISRES). Includes bibliographical references and index.

ISBN
978-625-6959-95-8

Date of Issue
December, 2025

Contact
Aşkan Mah. Akınbey Sok. No: 5/A Meram/Konya/Türkiye
isresoffice@gmail.com
www.isres.org

Next Generation Engineering: Smart Solutions and Applications

Edited by

Sabri KOCER

Professor, Necmettin Erbakan University

Faculty of Engineering

Department of Computer Engineering, Konya, Türkiye

Ozgur DUNDAR

Necmettin Erbakan University,

Faculty of Aviation and Space Sciences,

Department of Aerospace Engineering, Konya, Türkiye

Language Editor

Lecturer Ceren DOĞAN

School of Foreign Languages, Necmettin Erbakan University, Konya, Türkiye

Email : cerendogan@erbakan.edu.tr

Cover Design & Layout

Resul BÜTÜNER

Ministry of National Education,

Directorate General for Innovation and Educational Technologies, Ankara, Türkiye

Email : resul.butuner@eba.gov.tr

Table of Contents

Citation

Kocer, S., & Dundar, O. (Eds.). (2025). *Next Generation Engineering: Smart Solutions and Applications*. ISRES Publishing.

Preface

This work, titled **Next Generation Engineering: Smart Solutions and Applications**, is a periodical scientific publication consisting of carefully selected and invited chapters in its field. This edition brings together 16 different scientific studies focusing on next-generation engineering solutions in the fields of Engineering, Basic Sciences, and Advanced Technology.

All chapters submitted to the book have been rigorously reviewed by at least two international referees to ensure the highest level of scientific quality and originality. The main objective of this book is to provide readers with a scientifically strong, peer-reviewed, and up-to-date publication in the fields of basic sciences, engineering, and advanced technology.

The book **Next Generation Engineering: Smart Solutions and Applications** compile brand new ideas and applications concerning advanced engineering and smart solutions. The work sheds light on the future of engineering disciplines by presenting innovative approaches in Aerospace Engineering, Biomedical and Health Technologies, Embedded Systems and Energy Efficiency studies, artificial intelligence-based optimization, image processing (YOLO), and natural language processing (NLP) applications, and Communication Technologies (data compression, video compression).

In this book, besides modeling real system behaviors with artificial intelligence-based learning algorithms, detailed studies on smart systems developed and implemented using embedded systems for the health, manufacturing, and service sectors are discussed. Furthermore, original scientific studies including the contributions that can be made with artificial intelligence and meta-heuristic optimization techniques to problems that may be encountered in different disciplines are presented to the readers' attention.

We hope that the book will arouse curiosity about science and technology, be useful to new scientists, science readers, and anyone who wants to learn the mystery of science and make a significant contribution to the literature in these fields.

December, 2025

Sabri KOÇER
Professor, Necmettin Erbakan University
Faculty of Engineering
Department of Computer Engineering, Konya, Türkiye
Email: skocer@erbakan.edu.tr

Özgür DÜNDAR
Asistant Professor, Necmettin Erbakan University,
Faculty of Aviation and Space Sciences,
Department of Aerospace Engineering, Konya, Türkiye
Email: ozdundar@erbakan.edu.tr

In This Book

In Chapter 1, This chapter examines the control system required to lock the spacecraft onto a specific target while it is moving at varying speeds and in different directions in orbit. The spacecraft position, velocity and acceleration data are constantly needed to orient the spacecraft to nadir point which is considered the centre of the Earth. Euler angles are used to obtain the transformations between the spacecraft's body reference frame and the Earth-centred inertial frame. Since the spacecraft is constantly in motion, Euler transformations are performed consistently, and a target reference frame are obtained from spacecraft to inertial frame. A dynamic model of a spacecraft with three reaction wheels was developed for system dynamics. The PI control method was applied to enable spacecraft to perform target manoeuvres determined by transformation matrices while moving at varying speeds and accelerations. The differences between the target reference axis and the body reference axis were considered as errors and attempts were made to eliminate these errors using PI control. The results obtained show that the PI controller performs well in tracking the target point in three axes for a spacecraft in an elliptical orbit.

In Chapter 2, This chapter presents a systematic analysis of 3D printing research in Turkey, evaluating 61 doctoral and medical specialization theses retrieved from the Council of Higher Education (YÖK) database. The study aims to map national research trends, revealing a distinct "bipolar" ecosystem. While an initial review of doctoral work indicated a dominance of Science and Engineering (79%), the inclusion of medical and dentistry specialization theses shifts the majority to Health Sciences (54.1%). Engineering research primarily targets material development and innovative manufacturing, whereas the health sector particularly dentistry focuses heavily on the clinical validation of materials and surgical simulation. A critical gap identified is the near-total absence of Artificial Intelligence (AI) integration; only one study utilized AI, despite its necessity for Industry 4.0. The authors conclude that to advance beyond manual parameter testing, Turkey's academic infrastructure must urgently bridge the gap between physical production and cognitive AI systems.

In Chapter 3, Accurate prediction of airfoil self-noise is crucial for the design of quiet Urban Air Mobility (UAM) vehicles, as conventional methods like wind tunnel testing and Computational Fluid Dynamics (CFD) are often high-cost or computationally intensive. This study proposes a reliable and fast hybrid prediction framework for the self-noise estimation of the NACA 0012 airfoil based on experimental data. The proposed methodology utilizes the Adaptive Network Based Fuzzy Inference System (ANFIS), with its membership function parameters optimized using three distinct metaheuristic algorithms: Particle Swarm Optimization (PSO), Genetic Algorithm (GA), and Ant

Colony Optimization (ACO). The models were trained and validated using open-source experimental datasets from NASA. Comparative analysis revealed that the PSO-ANFIS hybrid model demonstrated the most superior performance, achieving a minimal Root Mean Square Error (RMSE) of 2.6684 on the training data and 2.8521 on the independent test data. The close proximity of the training and testing error metrics confirms the model's high accuracy and excellent generalization capability without overfitting. This successful integration of metaheuristics and ANFIS provides a reliable, fast, and low-cost tool for complex aerodynamic noise prediction and can serve as a starting point for the design of low-noise airfoils.

In Chapter 4, This chapter presents the design and development of an artificial intelligence–based autonomous pesticide robot capable of performing targeted spraying in orchard environments. Conventional spraying methods often result in excessive chemical usage, uneven coverage, and operator exposure to hazardous substances. To address these limitations, the proposed system integrates computer vision algorithms and deep learning detection algorithms to detect tree canopies, identify pest-affected zones, and apply pesticides precisely where needed. A deep learning model is employed for real-time foliage and pest-spot recognition. The robot dynamically adjusts spray intensity and angle based on canopy density and target location, significantly reducing chemical waste. Experimental field tests demonstrate that the proposed system achieves high detection accuracy and consistent spray distribution compared to traditional blanket spraying methods. The results highlight the potential of AI-driven robotic systems to improve agricultural sustainability, reduce human risk, and optimize crop protection practices.

In Chapter 5, This chapter presents the design and implementation of a low-cost, wirelessly controlled bionic hand system that utilizes flexible sensor–based motion detection to achieve real-time replication of human finger movements. The proposed system integrates a wearable glove equipped with flex sensors, an Arduino Nano–based data acquisition unit, an nRF24L01 wireless communication module, and a tendon-driven robotic hand controlled by an ESP32 microcontroller. The mechanical structure of the robotic hand is handcrafted from wood and incorporates fishing-line tendon mechanisms alongside a compact 3D-printed servo chamber, offering an accessible and customizable alternative to commercially available prosthetic solutions. Signal acquisition, filtering, and sensor-to-servo mapping are carried out through lightweight control algorithms designed to minimize latency and ensure smooth actuation. Experimental evaluations demonstrate that the system successfully mimics natural flexion–extension patterns with high responsiveness and functional stability. Compared to conventional wired prosthetic systems, the wireless architecture significantly enhances user mobility, comfort, and operational flexibility. Owing to its open-source hardware and software design, the platform provides a versatile foundation for future enhancements, including multi-sensor fusion, machine learning–based gesture recognition, and integration with electromyography signals. Overall, this study contributes an affordable and scalable approach to assistive robotics by combining handcrafted mechanical components with modern embedded technologies to support rehabilitation, research, and educational applications.

In Chapter 6, This study proposes a new hybrid model that aims to eliminate the problem of getting stuck in local minima during the training process of Artificial Neural Networks (ANNs) using derivative-based techniques. To overcome this problem, a new meta-heuristic algorithm called LevySAO is presented, which combines the Snow Ablation Optimizer (SAO) algorithm with the Levy Flight mechanism. The proposed LevySAO algorithm was used to create a YSA-LevySAO hybrid model by optimizing the weights and bias values of the YSA. The classification performance of the model was tested on 15 different datasets commonly known in the literature, and the results obtained were evaluated using basic metrics such as sensitivity, specificity, precision, and F1-score. The success of the YSA-LevySAO hybrid model was compared with hybrid models developed with 12 different meta-heuristic algorithms in the literature. According to comprehensive experimental studies and Friedman test results, the proposed YSA-LevySAO model was found to have the best Average Success Ranking (ASR) in three of the four metrics (specificity, sensitivity, and F1-score). These findings prove that the developed LevySAO algorithm is a highly promising and effective alternative for addressing optimization problems in ANN training.

In Chapter 7, This chapter examines course and exam timetabling problems, which remain among the most extensively studied NP-hard optimization challenges, driven by increasingly complex academic regulations, resource limitations, and the rapid transformation of higher education environments. This review systematically examines metaheuristic-based solution methodologies for university course and exam scheduling published between 2020 and 2026. A structured selection strategy was applied to identify studies exclusively focusing on metaheuristic or hybrid metaheuristic techniques such as Genetic Algorithms, Simulated Annealing, Variable Neighborhood Search, Hyper-heuristics, Artificial Bee Colony, Whale Optimization Algorithm, and Firefly Algorithm and their applications on real-world and benchmark datasets. Recent literature demonstrates three dominant trends: the increasing prevalence of hybrid metaheuristics that combine global exploration with strong local search operators, significant improvements achieved through multi-neighborhood and hyper-heuristic frameworks, and a gradual shift toward multi-objective and integrated models. Despite promising developments, major research gaps remain, particularly the limited number of integrated course and exam timetabling formulations and the underutilization of machine learning–assisted metaheuristics. This review presents a unified synthesis of methodological advancements, highlights emerging trends, and offers a strategic roadmap for future innovations in metaheuristic timetabling research.

In Chapter 8, This study addresses the challenges of modeling and analyzing high-order Linear Time-Invariant (LTI) systems, where classical Model Order Reduction (MOR) techniques often fail to simultaneously achieve optimal transient and steady-state responses. To overcome these limitations, a metaheuristic optimization approach utilizing the Artificial Bee Colony (ABC) algorithm is introduced to derive accurate, low-order representations. The primary novelty lies in the systematic analysis of how different error-based performance indices namely the Integral of Squared Error (ISE), Integral of Absolute Error (IAE), Integral of Time-weighted Absolute Error (ITAE), and Mean Squared Error (MSE) influence the dynamic characteristics of the resulting reduced model. The ABC algorithm was employed to optimize the parameters of a second-order model to match the step response of a ninth-order benchmark system, minimizing a cost function defined by a weighted sum of these indices. The experimental evaluations conclusively demonstrated that the ABC-based reduction method not only achieved rapid convergence and computational efficiency but also produced models with superior fidelity and dynamic flexibility compared to prominent benchmark techniques. Specifically, IAE achieved a critically damped response with minimal overshoot, ITAE resulted in the fastest settling time (approx. 1.5 seconds) and superior error attenuation, and MSE provided a highly balanced dynamic response.These findings establish the ABC algorithm as a reliable, robust, and versatile parameter-tuning tool for real-time control applications, allowing engineers to tailor the reduction process based on specific dynamic requirements such as speed, stability, or overshoot minimization.

In Chapter 9, This chapter introduces a novel approach to reducing the power consumption of battery-constrained sensor applications through the nPZero power-saving chip, manufactured by Nanopower Semiconductor AS. The nPZero is a power-saving chip that acts as an intelligent power management unit (IPMIC) to enable ultra-low-power operation in embedded systems at the hardware level without the need for an active host, such as a microcontroller or a wireless system-on-a-chip (SoC) module. Its main purpose is to prevent extra power consumption caused by unnecessary operation of microcontrollers and peripherals (e.g., sensors and communication modules), which are the primary sources of energy required in IoT devices. The nPZero chip provides a significant reduction in current, from the microampere (μA) to the nanoampere (nA) level, thereby extending battery lifetime from weeks to years. As a consequence, battery lifetime extension helps to reduce the volume of annual production and the generation of electronic waste. In the experimental study, NanoPower's nPZero Evaluation Kit (EVK) was used to verify the validity of an advanced power management in terms of current consumption. The aim is to experimentally evaluate the hardware-based power management approach in terms of current consumption, low-power mode transition performance, and overall power efficiency. The obtained test results show the hardware-based power management approach not only enhances energy efficiency but also improves thermal stability, system reliability, and long-term circuit robustness.

In Chapter 10, This chapter, titled “Advanced Optoelectronic Approaches in SpO_2 Measurement Systems,” provides an in-depth analysis of pulse oximetry technology, extending from biophysical principles to advanced hardware control. It highlights critical limitations in current devices, specifically “occult hypoxemia,” where racial bias in calibration algorithms causes dangerous overestimation of oxygen levels in dark-skinned individuals due to melanin interference. Distinct from simulation-based studies, the authors utilize a “Hardware-in-the-Loop” laboratory testbench featuring a dynamic tissue phantom to replicate real-world optical scattering and circulatory conditions. The research comparatively evaluates classical PID control versus an Artificial Neural Network (ANN) for regulating LED current. Experimental results demonstrate that the ANN controller significantly outperforms the PID method; while the PID controller exhibited varying instability and a high overshoot of 28.51%, the ANN achieved zero overshoot, superior noise rejection, and effective motion artifact suppression. The study concludes that integrating AI-driven control and spectral analysis is essential to ensure equitable clinical accuracy across all skin tones.

In Chapter 11, This chapter aims to measure the size distribution of metal particles of varying dimensions using image processing techniques applied to images obtained from a scanning electron microscope (SEM). Both traditional manual measurement techniques and advanced image-processing-based methods were employed during the analysis. In particular, the You Only Look Once (YOLO) algorithm was utilized as a deep learning–based approach for the detection and classification of metal particles. YOLO performs object detection and localization rapidly and with high accuracy, providing significant advantages in particle size measurement. The accuracy, sensitivity, and processing time of the algorithms used in this study were compared, and their performance was evaluated against conventional methods such as ImageJ. The obtained data were examined through statistical analyses, and the most suitable method was identified. The results demonstrate the advantages of the YOLO algorithm in determining particle size distribution in SEM images and indicate that image-processing-based algorithms can serve as efficient and effective tools for particle size analysis.

In Chapter 12, In this study, the integrated use of data compression and digital modulation techniques was examined to ensure the efficient transmission of image data in a wireless environment. A gray-level image was selected as the image data and compressed using the Huffman coding method. The compressed bit sequence was modulated using the Binary Phase Shift Keying (BPSK) method as the digital modulation technique. The modulated signals were passed through an AWGN (Additive White Gaussian Noise) channel, which is accepted as a noisy channel model. The performance of the system was observed at different SNR (Signal-to-Noise Ratio) values, and a demodulation process was applied post-transmission. On the receiver side, the Huffman decoding process was performed to convert the compressed data back into an image. As a result of the simulations performed, both the data compression success and the Bit Error Rate (BER) of the system were examined. The transmission reliability in the AWGN environment was evaluated alongside the compression ratio obtained through Huffman coding. This study is significant for demonstrating the effectiveness of image transmission, particularly in wireless communication environments with low bandwidth and limited energy resources

In Chapter 13, In this study, natural language processing was performed using a dataset of comments collected from a Turkish movie review website. The data used in the study were commented on and rated by users on the Turkish movie review website. These data were rated on a scale from 0.5 to 5.0. Feature selection metrics are widely used in the field of statistics. After the data was obtained, the contribution of LR to its success was determined by using the discriminative feature of feature selection metrics in comments belonging to various categories with Logistic Regression (LR) to meet the requirements of this research. In the proposed system design, an accuracy rate of 89% was achieved when classifying only positive and negative categories. Based on the findings in the literature review, the proposed system design proves that feature selection metrics can be successfully used in sentiment analysis. It is believed that this proposed new system design will bring a new perspective to the field of sentiment analysis.

In Chapter 14, In this study, an alternative particle size measurement method, which can be used particularly in the production processes of materials like cement, gypsum, and polymer-modified cement used as binders in construction, has been developed. It has been observed that the developed piezo-acoustic size measurement method can mostly measure the sizes of powder particles smaller than 100 microns. In the study, cement, gypsum, and polymer-modified materials were sieved using 3 sieves of 33, 45, and 91 microns, and they were separated into 3 different size classes: 0-33, 33-45, and 45-91 microns. The materials were measured with the developed measurement setup, and the effect of material type and size class difference on the measurements was observed. According to the obtained results, it was seen that the size measurements of different powder particles below 100 microns can be performed with the developed piezo-acoustic technique.

In Chapter 15, This study emphasizes the concept of disease, the prevalence of cancer, and the importance of early diagnosis. According to the Turkish Statistical Institute (TÜİK), circulatory system diseases were the leading cause of death in 2022–2023, followed by tumors. Cancer is a significant disease characterized by the uncontrolled proliferation of cells and their acquisition of the ability to metastasize, affecting the individual's biopsychosocial integrity. Imaging methods such as X-ray, CT, MRI, and mammography play a critical role in early diagnosis. In the analysis of medical images, artificial intelligence–based Convolutional Neural Networks (CNNs) provide high accuracy in detecting, classifying, and recognizing complex anatomical structures and lesions. CNN architecture consists of convolution, activation, pooling, and fully connected layers. Studies in the literature demonstrate that CNNs achieve diagnostic performance comparable to, or even exceeding, that of expert clinicians in diseases such as skin cancer, tuberculosis, breast cancer, and COVID-19.

In Chapter 16, In this study, the video compression performance and visual quality impacts of H.264 (AVC) and H.265 (HEVC) video codecs were comparatively evaluated. The methodology employed in the research was based on quantitative and objective metrics, experimentally validated, and supported with graphical analyses. The analysis was conducted using the Hand Wash Dataset, which contains videos demonstrating the seven-step handwashing procedure recommended by the World Health Organization (WHO) and is publicly available on the Kaggle platform. The videos included in this dataset were selected because they represent realistic human action scenarios, making them suitable for evaluating visual quality and compression performance in practical applications.

In Chapter 17, Wearable medical technologies are transforming healthcare services toward a preventive and personalized model. Clinically validated devices such as smartwatches, ECG belts, continuous glucose monitors, and smart garments enable real-time and remote monitoring of patients' physiological data, including heart rhythm, blood pressure, and oxygen saturation. This continuous monitoring improves the management of chronic diseases, facilitates early diagnosis, and reduces hospital visits and healthcare costs. Advances in sensor technologies, wireless communication, and artificial intelligence–driven data analytics further enhance the capabilities of these devices. However, challenges related to data security, clinical validation, and regulatory standards must be overcome to achieve widespread adoption. Ultimately, wearable technologies constitute a cornerstone of a more proactive, efficient, and patient-centered healthcare system.

Managing Editors

Sabri KOÇER, PhD, He graduated from the Electrical Engineering Department of Selcuk University. He completed his graduate and his doctorate in Gazi University. Currently, Necmettin Erbakan University, Faculty of Engineering, Computer Engineering is working. Electronics, Computer, Artificial Intelligence, Image Processing, Telecommunication, Signal Processing and Biomedical studies in the area.
Email: skocer@erbakan.edu.tr , **ORCID:** 0000-0002-4849-747X

Özgür DÜNDAR, PhD, works at Necmettin Erbakan University, Department of Astronautical Engineering. He graduated from the Electrical and Electronics Engineering Department of Selcuk University. He worked as an Automation Engineer for a while. His master's and doctorate degrees are from Selçuk University, Institute of Science and Technology, Department of Electrical and Electronics Engineering. Special fields of study are Automation, Artificial Intelligence, Robotic, Communication, Electromagnetic and Micro Strip Patch Antenna designs.
Email: ozdundar@erbakan.edu.tr , **ORCID:** 0000-0002-4142-4446

Contributors

Nur Sena KOCAKILIÇ
Necmettin Erbakan University, Faculty of Aviation and Space Sciences, Department of Aerospace Engineering, Konya, Türkiye

Amine EL ARUK
Necmettin Erbakan University, Faculty of Aviation and Space Sciences, Department of Aerospace Engineering, Konya, Türkiye

Seda Nur ÇAKICI
Necmettin Erbakan University, Faculty of Aviation and Space Sciences, Department of Aerospace Engineering, Konya, Türkiye

Muhammet ÖZTÜRK
Necmettin Erbakan University Faculty of Aviation and Space Sciences, Department of Aeronautical Engineering Konya, Türkiye

Murat KARAKOYUN
Necmettin Erbakan University, Faculty of Engineering
Department of Computer Engineering, Konya, Türkiye

Saliha Banu ERTÜRK
Necmettin Erbakan University, Faculty of Engineering (Graduate)
Department of Computer Engineering, Konya, Türkiye

Mehmet DURSUN
Necmettin Erbakan University, Faculty of Aviation and Space Sciences, Department of Aviation Electrics and Electronics, Konya, Türkiye

Hasan ÇINAR
Necmettin Erbakan University, Faculty of Aviation and Space Sciences, Department of Aeronautical Engineering, Konya, Türkiye

Engin Hasan ÇOPUR
Necmettin Erbakan University, Faculty of Aviation and Space Sciences, Department of Aerospace Engineering, Konya, Türkiye

Hasan Huseyin BILGIC
Necmettin Erbakan University, Faculty of Aviation and Space Sciences, Department of Aeronautical Engineering, Konya, Türkiye

Mehmet SAVAN
Necmettin Erbakan University, Faculty of Aviation and Space Sciences, Department of Aeronautical Engineering, Konya, Türkiye

Yunus Emre GÖKTEPE
Necmettin Erbakan University, Faculty of Engineering
Department of Computer Engineering, Konya, Türkiye

Mehmet TORUN
Necmettin Erbakan University, Faculty of Engineering,
Department of Computer Engineering, Konya, Türkiye

Ahmet ÖZKIŞ,
Necmettin Erbakan University, Faculty of Engineering,
Department of Computer Engineering, Konya, Türkiye

Feyza Nur ÖZDEMİR
Necmettin Erbakan University, Faculty of Engineering (Graduate),
Department of Computer Engineering, Konya, Türkiye

Halil İbrahim AYAZ
Necmettin Erbakan University, Faculty of Engineering,
Department of Industrial Engineering, Konya, Türkiye

Sena EMİL
Necmettin Erbakan University, Faculty of Engineering,
Department of Industrial Engineering, Konya, Türkiye

Musa KURUÇAY
Demsay Elektronik A.Ş.,
İstanbul, Türkiye

Onur İlyas YAVUZ
Demsay Elektronik A.Ş.,
İstanbul, Türkiye

Hakkı SOY
Necmettin Erbakan University, Faculty of Engineering,
Department of Electric Electronic Engineering, Konya, Türkiye,

Beyza DÜNDAR
Necmettin Erbakan University, Faculty of Engineering,
Department of Computer Engineering, Konya, Türkiye

Sabri KOCER
Necmettin Erbakan University, Faculty of Engineering,
Department of Computer Engineering, Konya, Türkiye

Özgür DÜNDAR
Necmettin Erbakan University, Faculty of Aviation and Space Sciences,
Department of Aerospace Engineering, Konya, Türkiye

Batuhan KOYUNCU
Necmettin Erbakan University, Faculty of Engineering,
Department of Electric Electronic Engineering, Konya, Türkiye

Nihat ÇANKAYA
Necmettin Erbakan University Konya Organized Industrial Zone Vocational School,
Department of Electronics and Automation Control and Automation Technology
Konya, Türkiye

Uçman ERGÜN
Afyon Kocatepe University, Faculty of Engineering,
Department of Biomedical Engineering, Afyon, Türkiye

Yasin Can BAĞANA
R&D ve Laboratory Unit, Teknopol İstanbul
University of Health Sciences,İstanbul,Türkiye

Celal Onur GÖKÇE
Afyon Kocatepe University, Faculty of Engineering,
Department of Software Engineering, Afyon, Türkiye

Elif AKTEPE
Afyon Kocatepe University, Afyon Vocational School,
Department of Electronics and Automation, Afyon, Türkiye

Muhammed KARAALTUN
Necmettin Erbakan University, Faculty of Engineering
Department of Computer Engineering, Konya, Türkiye

Nonlinear Dynamics based Nadir-point Attitude Control Design for Satellites in Elliptical Orbits

Nur Sena KOCAKILIÇ
Necmettin Erbakan University

Amine EL ARUK
Necmettin Erbakan University

Seda Nur ÇAKICI
Necmettin Erbakan University

Muhammet ÖZTÜRK
Necmettin Erbakan University

To Cite This Chapter:
Kocakilic, N. S., El Aruk, A., Cakici, S. N., & Ozturk, M. (2025). Nonlinear dynamics based nadir-point attitude control design for satellites in elliptical orbits. In S. Kocer & O. Dundar (Eds.), *Next generation engineering: Smart solutions and applications* (pp. 1–12). ISRES Publishing.

Introduction

Spacecraft attitude and orbit control systems are important challenges ensuring mission success in modern space engineering. These systems allow satellites to maintain the desired orientation and position required for communication, ground imaging and Earth observation. The relationship between orbital motion and attitude control has been examined extensively, as accurate coupling of both dynamics guarantees that the satellite continuously maintains its pointing requirements during flight (Curtis, 2005; Wertz, 2012).

In general, the orbital dynamics of a satellite describe its path around Earth, while the dynamics determine its orientation in three-dimensional space. To ensure that observation or communication instruments remain directed toward Earth, the attitude control system must operate synchronously with the orbital motion. For this reason, the Radial–Tangential–Normal (RTN) reference frame is frequently used in orbital-attitude studies to define real-time reference directions that depend on the satellite's instantaneous position and velocity (Sidi, 1997; Vallado, 2013).

Various control methods have been proposed to improve spacecraft stability and pointing precision. Among them, Proportional–Integral–Derivative (PID) controllers are widely applied because of their simplicity and ease of implementation in real-time systems (Wie, 2008; Borase et al., 2021). Nevertheless, spacecraft dynamics are nonlinear, and direct linear control may not always yield accurate results. Consequently, many studies have focused on linearization techniques and adaptive optimization to enhance controller performance under nonlinear conditions (Moldabekov et al., 2023; Zhou, 2019).

Recent work by Çakıcı et al. (2025) proposed a nonlinear spacecraft attitude model controlled by reaction wheels through a PID structure. Their study demonstrated that by linearizing the nonlinear dynamics around a small-angle equilibrium point, analytically tuned PID coefficients can stabilize the system effectively. This approach achieved high pointing accuracy, minimal overshot, and improved steady-state behavior. Integrating a DC motor model into the reaction-wheel system also enhanced the torque response and control efficiency, showing that well-tuned PID controllers remain effective for complex nonlinear spacecraft systems.

Other researchers have emphasized the importance of combining orbital propagation with attitude control for realistic simulation environments. Studies by Abdelrahman et al. (2020), Khan et al. (2022), and Yang et al. (2021) presented different approaches for integrated orbit-attitude control, where the desired orientation is continuously derived from the orbital trajectory. These integrated frameworks provide better understanding of satellite behavior and enable verification of control algorithms before in-orbit operation.

In this chapter, an integrated spacecraft orbit and attitude control simulation is presented. The orbital motion is modeled using classical three-body dynamics, while the attitude control subsystem employs a PID controller with reaction wheels to maintain continuous nadir-pointing orientation. The simulation framework is developed to generate orbital data that is used to attain attitude references and to control the spacecraft to minimize pointing errors over time. This chapter therefore offers both theoretical background and a practical example of the coupling between orbit and attitude control for educational and research purposes.

Orbital Motion and Its Role in Satellite Dynamics

Every integrated space simulation begins with the orbital model, which is responsible for calculating the satellite's motion around the central body. For our baseline analysis, we employ the simplest possible model: the classical Two-Body Problem. This formulation assumes Earth and the satellite are perfect point masses interacting only through gravity. We purposely neglect complex real-world forces, such as atmospheric drag or the effects of the Earth's non-uniform gravity, to ensure a clean model that focuses purely on validating the performance of our attitude control system.

The gravitational attraction between the Earth and the satellite is defined by Newton's Law of Universal Gravitation, which describes the force acting between two masses as:

$$\mathbf{F} = -\frac{GM_E m}{r^2}\boldsymbol{u_r} \tag{1}$$

where G is the gravitational constant, M_E is the mass of the Earth, m is the satellite's mass, r is the distance between them, and $\vec{\boldsymbol{u}}_{\boldsymbol{r}}$ is the unit position vector. Combining this with Newton's Second Law $\mathbf{F} = m\ddot{\mathbf{r}}$ gives the classical two-body orbital equation, expressed as

$$\ddot{\mathbf{r}} = -\frac{\mu}{r^3}\mathbf{r} \tag{2}$$

In this equation, μ = GM_E (the Earth's gravitational parameter) that M_E represents the mass of the Earth and G represents the gravitational constant. The variable $\mathbf{r}$ is the satellite's position vector. When we numerically integrate this equation over time, it provides the precise satellite position (**r**) and velocity (**v**) vectors in non-rotating Earth-Centered inertial frame.

Orbital Reference Frames and Their Role in Attitude Control

The most critical function of the orbital model, within our integrated project, is not just to calculate the orbit, but to provide the dynamic reference guide for the attitude control subsystem. The instantaneous position (**r**) and velocity (**v**) vectors are used to construct the Radial–Tangential–Normal (RTN) reference frame.

Think of the RTN frame as the satellite's local reference frame at any given moment. Its axes are defined as:

- Radial ($\widehat{\boldsymbol{R}}$): Points straight down to the center of Earth.
- Tangential ($\widehat{\boldsymbol{T}}$): Points in the direction of the satellite's motion.
- Normal ($\widehat{\boldsymbol{N}}$): Completes the right-handed system, perpendicular to the orbit plane.

For our required mission objective nadir-pointing (keeping the satellite's camera or antenna et. continuously aimed at Earth below) we need the satellite's body axis to always align with the Radial axis ($\widehat{\boldsymbol{R}}$). The desired Euler angles are automatically computed from the RTN rotation matrix, which provides the attitude controller with a perfect, dynamically linked reference. This process ensures complete orbit-attitude synchronization, making the orbital model the essential foundation for coordinated performance in the overall simulation.

Euler Angles

Orientation of any rigid in 3D space can be represented by Euler Angles. To describe its attitude a set of three Euler angles are used. These angles are denoted as:

Yaw (**ψ**): Rotation about the Z-axis

Pitch (**θ**): Rotation about the Y-axis

Roll **(φ)**: Rotation about the X-axis

Euler angles show us how an object in 3D space is oriented relative to another reference coordinate system. Euler angles also let us see the situation in a quite clear way since it is a compact system consisting of three values as $\phi, \theta \; and \; \psi$. In case of a transformation between the frames such as from the Body to Inertial axis or the opposite, the order of the angles matters regarding the way transformation matrixes are obtained.

There are three different transformation matrixes for each of the axes.

$$R_x(\varphi) = \begin{bmatrix} 1 & 0 & 0 \\ 0 & \cos\varphi & \sin\varphi \\ 0 & -\sin\varphi & \cos\varphi \end{bmatrix} \quad (3)$$

$$R_y(\theta) = \begin{bmatrix} \cos\theta & 0 & -\sin\theta \\ 0 & 1 & 0 \\ \sin\theta & 0 & \cos\theta \end{bmatrix} \quad (4)$$

$$R_z(\psi) = \begin{bmatrix} \cos\psi & \sin\psi & 0 \\ -\sin\psi & \cos\psi & 0 \\ 0 & 0 & 1 \end{bmatrix} \quad (5)$$

Transformation matrixes are calculated by multiplying each matrix that the rotation occurs, respectively. In aerospace area the 3-2-1 rule is generally used due to its alignment with aircraft body axes (Bernstein 2019). Therefore, the multiplication order is z axis and y axis then the outcome of it and the x axis. For transformations from Body to Inertial:

$$R_{bi} = \begin{bmatrix} c\theta c\psi & c\theta s\psi & -s\theta \\ s\varphi s\theta c\psi - c\varphi s\psi & s\varphi s\theta s\psi + c\varphi c\psi & s\varphi c\theta \\ c\varphi s\theta c\psi + s\varphi s\psi & c\varphi s\theta s\psi - s\varphi c\psi & c\varphi c\theta \end{bmatrix} = \begin{bmatrix} R_{11} & R_{12} & R_{13} \\ R_{21} & R_{22} & R_{23} \\ R_{31} & R_{32} & R_{33} \end{bmatrix} \quad (6)$$

$$R_{bi} = R_z(\psi) * R_y(\theta) * R_x(\varphi) \quad (7)$$

where $c_\phi = \cos\phi$, $s_\phi = \sin\phi$, $c_\theta = \cos\theta$, $s_\theta = \sin\theta$, $c_\psi = \cos\psi$, $s_\psi = \sin\psi$.

The R_{bi} matrix is what transforms a vector either from Body frame to Inertial frame or from Inertial frame to Body frame.

$$R_i = R_{bi} * R_b \quad (8)$$

$$R_b = R_{bi}^T * R_i \quad (9)$$

Lastly, to obtain The Euler Angles from this transformation matrix, the inverse trigonometric calculations are required.

$$\theta = -\arcsin(R_{13}) \quad (10)$$

$$\varphi = \arctan 2(R_{23}, R_{33}) \quad (11)$$

$$\psi = \arctan 2(R_{12}, R_{11}) \quad (12)$$

Arctan2 is used instead of arctan to make sure that the angle is in the right quadrant. The only argument of arctan is the ratio of y and x while the arctan2 takes them separately.

Therefore, arctan2 has two arguments and by using their signs the right quadrant can be determined since it covers the full 360 degrees. With arctan it is between +90 and -90 degrees, if the arguments both have the same sign than the information regarding the quadrant cannot be determined.

Spacecraft Dynamics

This study focuses on the attitude stabilization performance of a three-axis controlled communication satellite that is subject to small but continuous external disturbances. To ensure reliable Earth-pointing operations, the spacecraft maintains a fixed orientation using internally generated control torques provided by momentum wheels. These wheels are driven by electric motors that adjust their rotational speeds to counteract disturbance-induced deviations. For full three-axis attitude control capability, at least three reaction wheels are required, each aligned with one of the spacecraft's principal axes (x, y, z).

Satellite attitude control encompasses the techniques and systems employed to preserve or modify the spacecraft's orientation in accordance with mission objectives. Continuously pointing antennas, payload instruments, or sensors toward designated targets is crucial to fulfilling communication and observation requirements. In most modern spacecraft, this functionality is achieved by internal actuation devices, primarily reaction wheels, which can generate precise control torques without requiring propellant consumption. When larger attitude maneuvers or momentum desaturation operations become necessary, external actuators such as thrusters are employed to support the control system.

The motion of a spacecraft in orbit is typically analyzed by decomposing its dynamics into two principal domains: orbital and attitude dynamics. Orbital dynamics describe the translational motion governed predominantly by Earth's gravity and influenced by secondary perturbations such as atmospheric drag, solar radiation pressure, and gravitational irregularities. Conversely, attitude dynamics govern the rotational motion of the spacecraft and determine how it maintains a desired orientation relative to an inertial or orbit-fixed reference frame. Together, these components form the analytical foundation of spacecraft guidance, navigation, and control systems, ensuring satisfaction of both trajectory and pointing requirements.

A reaction wheel consists of a rapidly rotating flywheel whose stored angular momentum is controlled by adjusting its speed by an electric motor. Any acceleration or deceleration of the wheel causes an equal and opposite torque on the satellite body. Thus, the spacecraft's rotational response can be modeled using the principle of angular momentum conservation, which accounts for both rigid-body dynamics and the contribution of multiple spinning wheels.

Spacecraft mass equation can be given as;

$$m = m_0 + \sum_{i=1} m_i \tag{13}$$

where m_0 represents spacecraft body mass, m_i represents mass of momentum wheels and m represents the total mass.

The overall angular momentum of the satellite, denoted as H_G, represents the combined contribution of the spacecraft body and the rotating momentum wheels.

$$H_G = H_G^{body} + \sum_{i=1}^{n} H_i \tag{14}$$

This equation defines angular momentum where H_i represents angular momentum of wheels, H_{body} represents angular momentum of the spacecraft's body.

Spacecraft angular momentum can be given as:

$$H_G^{(bo\,dy)} = I_G^{(bo\,dy)} x\ \omega \tag{15}$$

In this expression, H_G corresponds to the combined spacecraft angular momentum evaluated at its center. The term I_G stands for the spacecraft's inertia tensor at the same point, while ω indicates the angular velocity.

The angular momentum vector can be calculated as;

$$\begin{bmatrix} H_x \\ H_y \\ H_z \end{bmatrix} = \begin{bmatrix} I_x \times \omega_x \\ I_y \times \omega_y \\ I_z \times \omega_z \end{bmatrix} \tag{16}$$

The matrix form can be given as;

$$H = \begin{bmatrix} I_{xx} & I_{xy} & I_{xz} \\ I_{yx} & I_{yy} & I_{yz} \\ I_{zx} & I_{zy} & I_{zz} \end{bmatrix} \begin{bmatrix} \omega_x \\ \omega_y \\ \omega_z \end{bmatrix} \tag{17}$$

The spacecraft's total rotational inertia, cannot change unless an external torque acts upon it

$$\frac{dH_g}{dt} = 0 \tag{18}$$

As a result of these circumstances, a spacecraft that is already rotating will maintain its rotational direction and rate, while a non-rotating spacecraft will remain motionless in the default of external disturbances. This fundamental principle of angular momentum conservation plays a key role in maintaining the passive stability of satellites and other spacecrafts in orbit. Consequently, any intentional change in attitude must be generated internally through actuators such as reaction wheels or gyroscopes, which modify the system's angular momentum to produce the required control torques.

If there is an external torque effect:

$$M = \frac{dH_g}{dt} = 0 \tag{19}$$

$$H_G = H_p \times H_\omega \tag{20}$$

H_G is cross product of H_p and H_ω that the H_ω represents angular momentum of the spacecraft's body, H_p represents angular momentum of reaction wheel and H_G represents the total angular momentum of the system.

At the initial moment, both the spacecraft structure and the reaction wheel are assumed to have no rotational motion, meaning their initial angular velocities are zero.

$$\begin{bmatrix} H_\omega \\ H_p \end{bmatrix} = \begin{bmatrix} I_\omega \, x \, \omega_\omega \\ I_p \, x \, \omega_p \end{bmatrix} \tag{21}$$

Angular velocity of the spacecraft;

$$\omega_P = -\frac{I_\omega}{I_p}\omega_\omega \tag{22}$$

The spacecraft attitude is parameterized using Euler angles, whose time derivatives are kinematically related to the angular velocity vector expressed in the body-fixed reference frame. This relationship establishes a fundamental connection between the spacecraft's rotational dynamics and its attitude kinematics, ensuring that the orientation evolution can be accurately described and predicted. The resulting formulation constitutes the basis for characterizing the spacecraft's attitude behavior and is subsequently employed in the development of the attitude control system. To provide independent control authority along all rotational degrees of freedom, three identical reaction wheels are constrained along the principal axes of the spacecraft body.

$$I_G^{(v)} = \begin{bmatrix} A & 0 & 0 \\ 0 & B & 0 \\ 0 & 0 & C \end{bmatrix} \tag{23}$$

Momentum wheels inertia tensors are given as;

$$\left[I_G^{(1)}\right] = \begin{bmatrix} I & 0 & 0 \\ 0 & 0 & 0 \\ 0 & 0 & 0 \end{bmatrix} \quad \left[I_G^{(2)}\right] = \begin{bmatrix} 0 & 0 & 0 \\ 0 & J & 0 \\ 0 & 0 & 0 \end{bmatrix} \quad \left[I_G^{[3]}\right] = \begin{bmatrix} 0 & 0 & 0 \\ 0 & 0 & 0 \\ 0 & 0 & J \end{bmatrix} \tag{24}$$

The rotational motion is characterized by the body angular velocity components $(\omega_x,\ \omega_y,\ \omega_z)$ while the spin rates of the three momentum wheels are denoted by $\omega^{(1)}, \omega^{(2)}, \omega^{(3)}$. The total angular momentum H_G of the system can then be expressed as:

$$\{H_G\} = \left[I_G^{(v)}\right]\{\omega\} + \sum_{j=1}^{3}\left[I_G^{\{v\}}\right]\left(\{\omega\} + \left\{\omega_{rel}^{(i)}\right\}\right) \tag{25}$$

$$\{H_G\} = \begin{bmatrix} A+I+2J & 0 & 0 \\ 0 & B+I+2J & 0 \\ 0 & 0 & C+I+2J \end{bmatrix}\{\omega\} + \begin{bmatrix} I & 0 & 0 \\ 0 & I & 0 \\ 0 & 0 & I \end{bmatrix} \cdot \begin{bmatrix} \dot\omega^{(1)} \\ \dot\omega^{(2)} \\ \dot\omega^{(3)} \end{bmatrix} \tag{26}$$

By solving the equations, we obtain the angular accelerations of the reaction wheels on three axes. The results are given below.

$$\begin{bmatrix} \dot{\omega}^{(1)} \\ \dot{\omega}^{(2)} \\ \dot{\omega}^{(3)} \end{bmatrix} = \begin{bmatrix} \frac{(\boldsymbol{M_G})_x}{I} + \frac{B-C}{I}\omega_y\omega_z - \left(1+\frac{A+2J}{I}\right)\dot{\omega}_x + \omega^{(2)}\omega_z - \omega^{(3)}\omega_y \\ \frac{(\boldsymbol{M_G})_y}{I} + \frac{C-A}{I}\omega_x\omega_z - \left(1+\frac{B+2J}{I}\right)\dot{\omega}_y + \omega^{(3)}\omega_x - \omega^{(1)}\omega_z \\ \frac{(\boldsymbol{M_G})_z}{I} + \frac{A-B}{I}\omega_x\omega_y - \left(1+\frac{C+2J}{I}\right)\dot{\omega}_z + \omega^{(1)}\omega_y - \omega^{(2)}\omega_x \end{bmatrix} \quad (27)$$

PID Control

This section describes the PID (Proportional-Integral-Derivative) control application. To do this, it is first necessary to understand the effect of each PID parameter on the system. A PID controller consists of three parameters: Proportional, Integral, and Derivative coefficients.

Proportional **(P):** Multiplies the current error by a fixed coefficient.

Integral **(I):** Eliminates steady-state error by accumulating past errors and multiplying them by the error.

Derivative **(D):** Uses the rate of change of error to reduce oscillations. Multiplies the change in error by a fixed coefficient.

The combination of these three terms allows precise and stable control of the spacecraft attitude towards the desired orientation. The desired orientation of the satellite, represented by the Euler angles $\phi_{\text{desired}}, \theta_{\text{desired}}, \psi_{\text{desired}}$, is determined from the Earth-pointing geometry of the satellite. These desired attitude angles serve as the reference setpoints for the PID controller.

Figure 1

Flowchart of the Control System

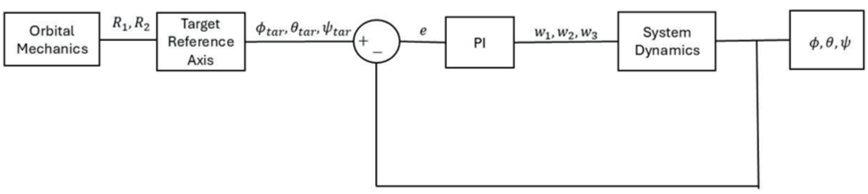

The spacecraft orientation is determined by using Euler angles. So; firstly, the two-body position are calculated by using Orbital Mechanics in 3D space. After determining the Euler angles, a PI position control is implemented to control the reaction wheels angular velocities. So, the orientation of the spacecraft is determined with respect to its own reference axis. The angle values relative to the body reference axis have been recalculated relative to the inertial frame and used as input to the spacecraft attitude system. The general structure is given in Figure 1.

Result

The spacecraft's z-axis is aligned so that it points towards the center of the Earth while the spacecraft is moving in an elliptical orbit. The reason for choosing an elliptical orbit is to ensure that the rate of change of the z-axis is non-zero.

At the initial stage, the spacecraft was launched at a speed of 7058 km on the main x-axis and 6 km/s on the main y-axis. To better analyze the results, no position or velocity was specified on the main z-axis, so the satellite was moved along two axes in orbit. As a result of the angular transformations performed using Euler angles, the x and y axes remain constant while the z-axis is in constant motion.

Figure 2

ϕEuler Angles in Time

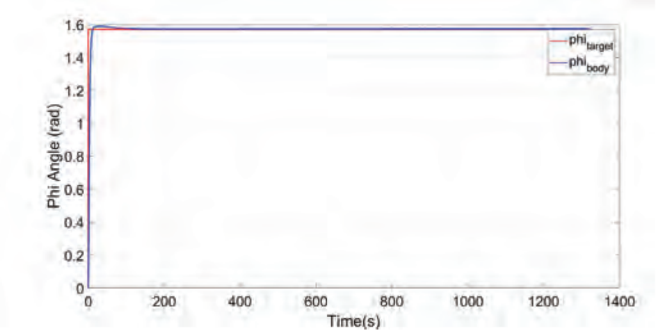

The satellite moves along the main x-axis as shown in Figure 2. It first made a 90-degree angle and attempted to maintain this angle.

As shown in Figure 3, it was not expected to make any angle on the y-axis. Although it made some overshoots in the early stages of the test due to the angles it made on the other axes, it subsequently settled on the target.

Figure 3

θEuler Angles in Time

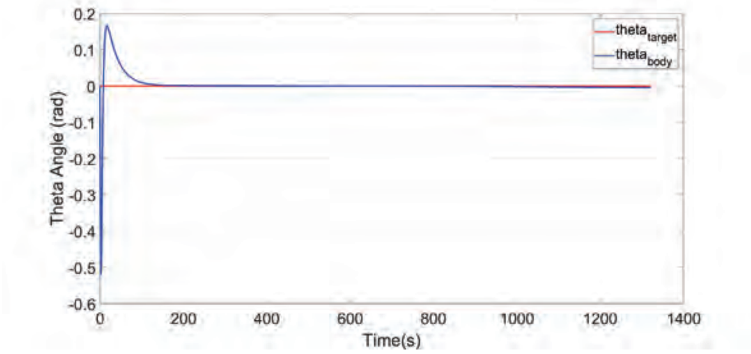

Figure 4

ψEuler Angles in Time

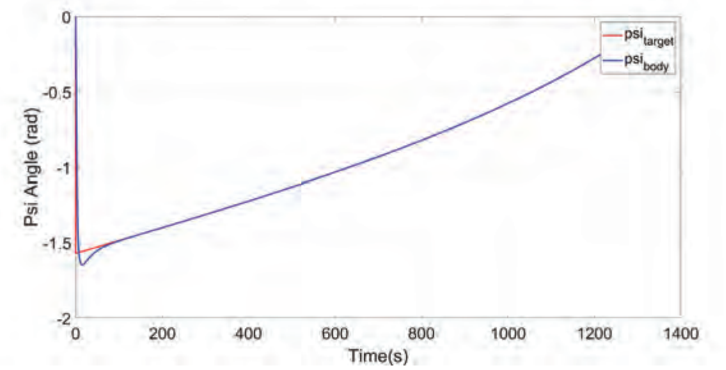

The satellite's main z-axis moved as shown in Figure 4. It exhibited a -90-degree turn at the start of the test. Depending on the satellite's orbital motion, it attempted to remain adjacent to the target z-axis at increasing speeds. The Figure 2-4 results show that the overshoot is low, the systems' reaction is fast and there is no chattering in control signal. This performance is acceptable for nonlinear system control with a linear control approach.

The elliptical orbit around an earth-fixed point starting from the initial altitude is shown in Figure 5 for 30 minutes. As it is seen in Figure 5, the satellite begins its orbit at the apoapsis point at 7058 km on the main x-axis and continues its orbit at a periapsis distance of 3300 km.

Figure 5

The Elliptic Orbit in 3D Plane For 30 Minutes

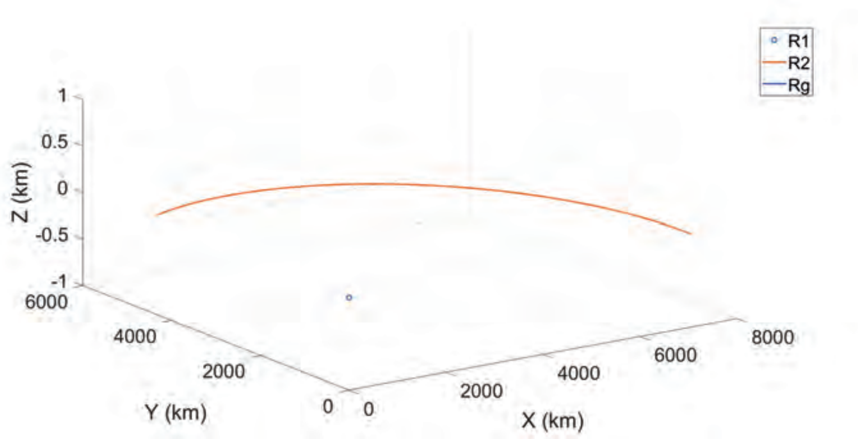

Figure 6

The Control Signals of The Controller

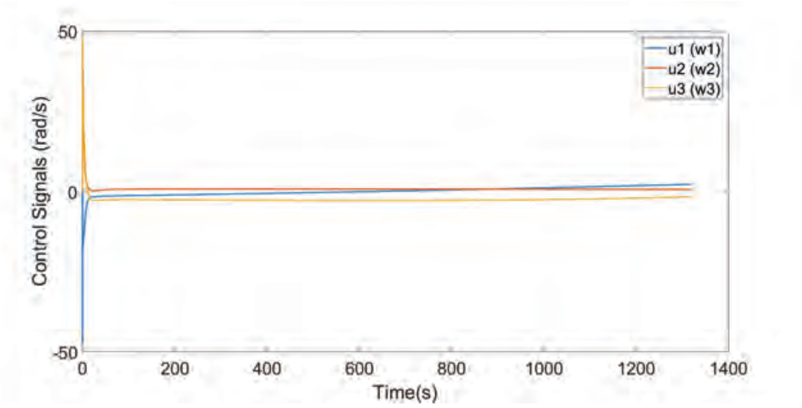

In Figure 6, the control signals are the reaction wheel angular velocities. As seen in Figure 6, the control signal has very fast reactions. The control signals are very smooth and this is very convenient for real time applications. Besides, the control signals have no chattering.

References

Abdelrahman, M., Elshafei, M., & Emara, H. (2020). Attitude control of a satellite using adaptive PID controller. *Journal of Aerospace Engineering, 33*(5), 04020069.

Borase, R. P., Maghade, D. K., Sondkar, S. Y., & Pawar, S. N. (2021). A review of PID control, tuning methods and applications. *International Journal of Dynamics and Control*, *9*(2), 818–827.

Çakıcı, S. N., Kocakılıç, N. S., El Aruk, A., & Öztürk, M. (2025). PID design for nonlinear spacecraft model with reaction wheels. *Aerospace Research Letters (ASREL), 4*(1), 132–146.

Curtis, H. D. (2005). *Orbital mechanics for engineering students* (1st ed.). Oxford: Elsevier Butterworth-Heinemann.

Khan, M. A., Ahmed, M., & Aziz, W. (2022). Nonlinear PID control for satellite attitude stabilization. *Aerospace Science and Technology, 128*, 107042.

Moldabekov, M., Sukhenko, A., Orazaly, Y., & Aden, A. (2023). Dynamics analysis of a nonlinear satellite attitude control system using an exact linear model. *Mathematics, 11*(12), 2614.

Sidi, M. J. (1997). *Spacecraft dynamics and control: A practical engineering approach.* Cambridge: Cambridge University Press.

Vallado, D. A. (2013). *Fundamentals of astrodynamics and applications* (4th ed.). Hawthorne, CA: Microcosm Press.

Wertz, J. R. (2012). *Space mission analysis and design* (3rd ed.). Hawthorne, CA:

Microcosm Press.

Wie, B. (2008). *Space vehicle dynamics and control* (2nd ed.). Reston, VA: AIAA Education Series.

Yang, H., Wang, Y., & Li, Z. (2021). Optimization-based hybrid control for satellite attitude stabilization. *Acta Astronautica, 185*, 153–161.

Zhou, B. (2019). On stability and stabilization of the linearized spacecraft attitude control system with bounded inputs. *Automatica, 105*, 448–452.

Bernstein, D. S. (2019). *Euler angles and aircraft kinematics: The 3-2-1 sequence*. *Journal of Guidance, Control, and Dynamics*, University of Michigan, Department of Aerospace Engineering.

About The Authors

Nur Sena KOCAKILIÇ, is an undergraduate student in Necmettin Erbakan University Her major is Aerospace Engineering and she is currently in her 4th year.
E-mail : 21030031047@erbakan.edu.tr, **ORCID :** 0009-0007-9375-3448

Amine El Aruk, is a fourth-year undergraduate student at Necmettin Erbakan University, majoring in Aerospace Engineering.
E-mail : 22030031801@erbakan.edu.tr, **ORCID :** 0009-0002-1741-8254

Seda Nur Çakıcı, is an undergraduate student in Necmettin Erbakan University. Her major is Aerospace Engineering.
E-mail : 21030031043@erbakan.edu.tr, **ORCID :** 0009-0008-0401-8597

Muhammet ÖZTÜRK, received his B.Sc. degree in astronautical engineering from Istanbul Technical University, Istanbul, Turkey, in 2011. He received his M. Sc. and Ph.D. degrees in Aeronautical and Astronautical Engineering from Istanbul Technical University, Istanbul, Turkey, in 2014 and 2022, respectively. Between 2011 and 2018, he served as a Research Assistant in the Department of Astronautical Engineering at Istanbul Technical University. Between 2018 and 2023, he served as a Research Assistant in the Department of Astronautical Engineering at Necmettin Erbakan University. Since 2023, he has held the position of Assistant Professor in the Department of Aeronautical Engineering at Necmettin Erbakan University, Konya, Turkey. His current research interests are Orbital Mechanics, linear and nonlinear control methods including SMC and Neuro-Fuzzy Control, Fractional Calculus and aeronautical, astronautical research areas.
E-mail : mozturk@erbakan.edu.tr, **ORCID :** 0000-0002-0057-5205

Similarity Index
The similarity index obtained from the plagiarism software for this book chapter is 11%.

A Systematic Analysis of 3D Printing Research in Doctoral and Specialization Theses in Turkey

Elif AKTEPE
Afyon Kocatepe University

Uçman ERGÜN
Afyon Kocatepe University

To Cite This Chapter:
Aktepe, E., & Ergün, U. (2025). A systematic analysis of 3D printing research in doctoral and specialization theses in Turkey. In S. Kocer & O. Dundar (Eds.), *Next generation engineering: Smart solutions and applications* (pp. 13–36). ISRES Publishing.

Introduction

Three-dimensional (3D) printing technologies have evolved beyond prototype production over the last two decades, ushering in an industrial revolution and rapidly developing in Turkey, as well as globally, becoming a research field that is expanding its interdisciplinary reach. Initially viewed solely as rapid modeling tools, these technologies are now fundamentally changing manufacturing paradigms across numerous sectors, including aerospace, biomedical applications, personalized medicine, and sustainable architecture. Advantages such as the easy production of complex geometries, localization of supply chains, and minimizing waste have made 3D printing a cornerstone of the fourth industrial revolution. At the forefront of this transformation is the academic world, particularly doctoral and specialist research.

The most in-depth and original contributions to the scientific, industrial, and societal applications of this technology are generally made through doctoral studies. One of the most critical indicators reflecting a country's technological competence, innovation capacity, and future research priorities is the in-depth and original academic work conducted in that field. Doctoral and specialist dissertations, in particular, offer the most significant contributions to the scientific, industrial, and societal applications of a technology. Therefore, a systematic analysis of these studies provides critical data for understanding the current state of the literature and its evolution. Examining these theses, specifically for Turkey, is of strategic importance for identifying the country's position in this global technology race, its strengths, and underexplored research areas.

In this context, this study aims to systematically examine doctoral theses conducted on 3D printing in Turkey, revealing current research trends, their interdisciplinary distribution, and potential research gaps in the literature. The findings are intended to guide future researchers and provide a valuable perspective for decision-makers shaping science and technology policies. This analysis will provide a comprehensive map of

Turkey's academic knowledge in the field of 3D printing, laying a solid foundation for future steps.

A search of the Council of Higher Education (YÖK) National Thesis Center database analyzed 33 doctoral theses found with the keyword "3D printing" as of November 15, 2025. The findings show that a significant 79% (26 theses) of the research is concentrated in the field of science and engineering. Research in this field focuses particularly on bioengineering, polymer science and technology, and mechanical engineering, with topics such as the development of new materials, optimization of printing parameters, and improvement of mechanical properties being prominent. Although relatively few in number, these theses in the field of health sciences (5 theses; 15%) have shown a significant increase recently, demonstrating their high innovation and application potential. Implant designs, tissue engineering, and prosthetic applications constitute the main research themes of this group. Studies conducted within the framework of social sciences (2 theses; 6%) shed light on the social, legal, and cultural dimensions of technology. Intellectual property rights, restoration of archaeological artifacts, and architectural applications are prominent topics in this field. 3D printing research conducted at the doctoral level in Turkey is most concentrated in the sciences and engineering fields; however, notable examples are also emerging in the health and social sciences. This demonstrates that 3D printing is increasingly being considered not only in the context of manufacturing and material development but also in healthcare and socio-cultural contexts.

At this point, the unique nature of the academic structure in Turkey reveals why a doctoral-focused analysis is methodologically inadequate. In Turkey, a significant portion of applied and clinical research, particularly within the scope of Specialization in Medicine (TUS) and Specialization in Dentistry (DUS) programs, is conducted in the "Specialization Theses" format, rather than in "Ph.D." These theses are classified differently from doctoral theses in the YÖK database and were excluded from the initial search of 33 theses. Therefore, the "engineering-heavy" and "weak in terms of education/clinical practice" picture reflects only a portion of Turkey's total academic knowledge. The primary objective of this study is to transcend these limitations and integrate this critical clinical literature, which falls outside the "doctoral" status of the Council of Higher Education (YÖK) system, into the existing analysis. In this context, the study included 33 doctoral dissertations, 24 Dentistry Specialization Theses, and 4 Medical Specialization Theses. This integration brings the total number of theses to 61, fundamentally redrawing Turkey's 3D printing map. This study aims to create a holistic and integrated map of Turkey's academic knowledge in 3D printing and to reinterpret research trends based on this expanded and corrected dataset.

Methodology

The methodological basis of this study is doctoral dissertations made publicly available by the YÖK National Thesis Center, the most comprehensive and reliable archive of academic research in Turkey. Choosing YÖK as the data source was a strategic decision to ensure the validity of the study and the generalizability of its findings. Because this platform hosts postgraduate theses completed at all universities in Turkey, it provides the ideal and unbiased basis for generating a national overview of a specific research area.

To define the boundaries of the research and ensure the reproducibility of the findings, the fundamental principles of the systematic review approach were adopted for the literature review. Unlike traditional literature reviews, this method relies on a predetermined, transparent, and reproducible protocol. This aims to minimize researcher bias and provide a holistic picture of the existing literature. To this end, a comprehensive database search was conducted to fully identify doctoral and specialist research on 3D printing technologies, using the keyword “3D printing,” the most widely used term in the academic literature in Turkey. Alternative terms, such as “additive manufacturing,” were also considered; however, since “3D printing” yielded the most comprehensive results, the search was limited to this term.

To clarify the study’s scope, inclusion and exclusion criteria were carefully defined. The search was completed as of November 15, 2025, and only doctoral and specialist theses were included in the data set. Other publication types, such as master’s theses, articles, proceedings, and book chapters, were excluded to limit the research focus to the most in-depth and original academic studies. This meticulous search and filtering process yielded a total of 61 doctoral and specialist theses conducted across various disciplines and meeting the research criteria.

In the second stage of the data analysis, a thematic approach was used to categorize the 61 theses obtained. The official disciplinary field specified in the YÖK database for each thesis was accepted as the primary criterion.

Based on this objective criterion, doctoral theses were grouped under three main categories: Science and Engineering Sciences, Health Sciences, and Social Sciences.

Using a similar approach, the objective criterion for the four Medical Specialization theses was the official “Field of Specialization” specified in the YÖK database. Based on this criterion, these theses were classified under four different clinical disciplines: Neurosurgery, Orthopedics and Traumatology, Emergency Medicine, and Plastic and Reconstructive Surgery.

Dentistry Specialization theses are included under a single, homogeneous category in the YÖK system as "Dentistry Specialization." Therefore, the "thematic focus" criterion was applied to separate these 24 theses into meaningful groups. Based on this objective criterion, the theses were classified as follows: They are grouped under three main clinical validation clusters: (1) Mechanical, Optical Properties and Durability, (2) Dimensional Accuracy and Marginal Adaptation, and (3) Surface Properties and Biocompatibility.

This classification, rather than simply providing a list, systematically outlines the scientific areas in which doctoral-level 3D printing research in Turkey is currently focused and identifies areas that still hold potential for development. This methodology enhances the scientific value of the study by ensuring that the results are both reliable and interpretable.

Findings

Analysis of Doctoral Theses

Distribution of Doctoral Theses by Discipline

The 33 doctoral theses obtained as a result of the review were divided into three main categories based on disciplines to provide a clear picture of research trends in Turkey. The most striking finding in this distribution is that Science and Engineering Sciences have a strong advantage with 26 theses. This confirms that 3D printing technology is inherently based on fundamental engineering fields, including materials science, mechanical design, and manufacturing processes. The prominence of fields such as Bioengineering and Biotechnology (6 theses), Mechanical Engineering (4 theses), and Polymer Science and Technology (3 theses) within this category indicates that research is concentrated on medical applications, new materials development, and industrial automation.

In contrast, fields such as Health Sciences (5 theses) and Social Sciences (2 theses) have a narrower scope. In the healthcare field, the focus on direct clinical applications such as Dentistry, Pharmacy, Pharmacology, and Physiology symbolizes the transition of technology from the laboratory to patient care. In the social sciences, the inclusion of topics such as Archaeology and Law demonstrates that the impact of 3D printing on cultural heritage and legal frameworks has also entered the academic agenda. This interdisciplinary distribution summarizes the current state of research in Turkey, and detailed data is presented in Table 1. A graphical representation of the distribution is provided in Figure 1 for a clearer understanding.

Table 1

Distribution of Doctoral Theses on 3D Printing in Turkey by Discipline (n=33)

Main Category	Sub-discipline	Number of Theses (n)	Percentage (%)
Science and Engineering Sciences	Bioengineering and Biotechnology	6	18.2
	Mechanical Engineering	4	12.1
	Polymer Science and Technology	3	9.1
	Physics and Physical Engineering	2	6.1
	Other (15 Different Fields)	11	33.3
	Subtotal	**26**	**78.8**
Health Sciences	Dentistry	3	9.1
	Bioengineering	1	3.0
	Pharmacy and Pharmacology	1	3.0
	Subtotal	**5**	**15.2**
Social Sciences	Archaeology	1	3.0
	Law	1	3.2
	Subtotal	**2**	**6.1**
	TOTAL	**33**	**100.0**

Explanatory note: *The data in the table are calculated based on the numbers in the text. The "Other" category includes fields, each represented by a thesis.*

Figure 1.

Distribution Graph of Doctoral Theses on 3D Printing in Turkey by Discipline

Trends in Academic Interest by Year

The distribution of doctoral theses on 3D printing technologies in Turkey by year strikingly illustrates how academic interest has matured and gained momentum over time. The early period between 2006 and 2020 can be characterized as an “exploratory phase,” with only five theses completed; during these years, the technology received limited attention from leading researchers.

The real turning point occurred in 2022. The significant increase that began that year, reaching a new peak of nine theses in 2025, followed by six theses in 2023, eight in 2024, and nine in 2025, demonstrates that 3D printing is no longer a niche topic but a mainstream research area. The fact that nine theses were completed even in the first ten months of 2025 confirms that this intense interest is not a passing fad, but rather a sustainable upward trend. These data clearly demonstrate that the technology has taken root in the academic ecosystem in Turkey, providing a solid foundation for future research.

Figure 2

Graph of the Increase in the Number of Completed Theses by Year

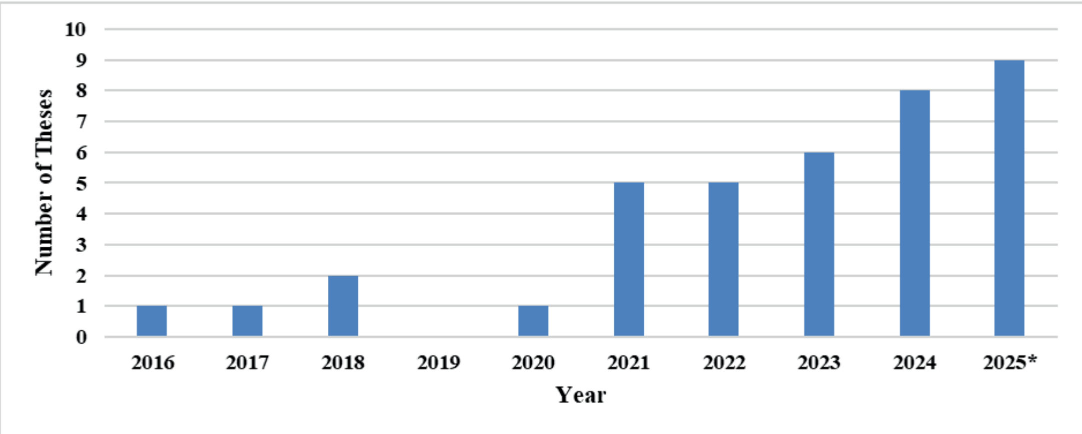

Explanatory note (*): *Data from the first 10 months of 2025 are reflected in the graph.*

Thematic Clusters in Science and Engineering

Analyzing 26 theses in science and engineering can be grouped under three thematic clusters, which represent the principal axes of the research agenda in Turkey. This classification allows studies to be grouped according to common objectives, rather than simply listing them. These themes are: (1) Biomedical Applications and Tissue Engineering, (2) Advanced Materials and Sustainability, and (3) Innovative Manufacturing Processes and System Design. This structure will be examined in detail in the following sections.

Biomedical Applications and Tissue Engineering

Studies in this field focus on developing direct solutions for human health by utilizing the customization and complex geometry capabilities offered by 3D printing technology.

This thematic cluster represents the most potent and most concentrated area of research in Turkey. Studies focus particularly on advanced topics such as regenerative medicine, controlled drug release, and personalized implant design. This thematic cluster (Science and Engineering) also has strong synergy with studies classified under Health Sciences (see Section 3.4) but sharing similar objectives in topics such as 3D bioprinting (e.g., Tekin, 2025) and targeted drug delivery systems (e.g., Ege, 2024).

Bone tissue engineering is at the heart of research in this field. Söğüt (2023) achieved controlled drug release through antibiotic-loaded bone grafts produced with a 3D printer, a critical step toward treating bone infections such as osteomyelitis. Similarly, Delibalta (2024) developed functional biomaterials that both increased durability and facilitated cell attachment by using additional coatings and support layers to accelerate bone repair. Demirtaş (2016), a pioneer in this field, presented a promising approach to bone regeneration by developing vascularized bone models using specialized biomaterials and additives. Innovative device designs for specific organs and tissues are also attracting attention. Bedir (2024) produced microneedle patches containing antibiotics and growth factors for eardrum repair using Digital Light Processing (DLP). Erdoğuş (2022) designed a new vascular stent made of biodegradable materials using Fused Deposition Modeling (FDM) as a powerful alternative to existing metal stents. Numanoğlu (2025) presented options for treating nerve injuries that provide more efficient nutrient and substance transport compared to conventional methods, utilizing guide channels with various porous structures. Finally, some research has focused on the development of basic biomaterials and clinical planning. Yalman (2025) produced highly cellular-compatible structures for tissue engineering using bioink derived from brown algae. Çıklaçandır (2023) aimed to increase surgical efficiency and safety by using 3D-printed patient bone models for preoperative simulations. Altundağ Erdoğan (2025) made a significant contribution to cancer studies by examining triple-negative breast cancer stem cells in 3D bone-like models and investigating the effects of drug treatment on metastasis-related genes.

Advanced Materials and Sustainability

Research in this theme focuses on materials, the most fundamental components of 3D printing technology, aiming to enhance their functionality, durability, and environmental friendliness. Studies in this group focus on developing high-performance composites that integrate sustainability and circular economy principles into the production process.

To achieve this performance improvement goal, Oran (2022) radically altered the properties of 3D printer filaments by adding carbon nanotube additives. This additive has been proven to increase the material’s mechanical strength and heat resistance significantly and, when used at specific ratios, provide effective electrical conductivity. Such conductive composites offer new opportunities for printing integrated sensors or electronic components.

The sustainability axis is the strongest aspect of this theme. Researchers focus on transforming waste materials into valuable resources. Bahçegül (2022) successfully developed biomaterials suitable for 3D printing using agricultural waste, such as corn cobs, without requiring chemical processing, thereby offering an environmentally friendly alternative. Using a similar circular economy approach, İlcan (2024) developed new binder materials for 3D-printed structures using construction and demolition waste. This work aimed to maximize waste utilization while simultaneously improving both the mechanical and environmental performance of the printed structures. In the field of architecture, Ceylan Engin (2025) developed a polycarbonate composite reinforced with natural fibers, such as hemp. The more potent properties of this new material, compared to industry standards such as Polylactic Acid (PLA) and Acrylonitrile Butadiene Styrene (ABS), represent a significant step toward sustainable building materials.

Finally, some studies have combined sustainability with improved functionality. Tezel (2025) produced self-healing tissue scaffolds using photopolymers derived from environmentally friendly sources. These materials demonstrate both high durability and effective healing efficiency, proving that sustainability and functionality can be combined in the biomedical field.

Innovative Manufacturing Processes and System Design

The studies in this cluster aim to fundamentally improve 3D printing technology itself, its processes, or the systems it integrates with. Research focuses on software, automation, system integration, and new application methodologies, rather than materials, pushing the boundaries of the technology's potential.

A group of researchers in this field aims to extend 3D printing beyond the confines of traditional workshops by combining it with automation and robotic systems. One of the most striking examples of this visionary approach is the mobile production system developed by Ghaziani (2023), which can print in flight through the collaboration of multiple drones. This system offers potential, particularly for difficult-to-access construction sites or for rapid post-disaster reconstruction. On the software side of manufacturing automation, Gündüz (2024) developed an innovative algorithm that transfers digital design and material information directly to the robotic manufacturing process. In the medical field, Totuk (2023) designed a flexible and functional soft robotic peristaltic pump suitable for medical applications using 3D printing.

Efforts to transform technology into "smart" systems also stand out in this cluster. Bayram (2018) developed portable sensing devices integrated with smartphone-based optical systems, leveraging the low-cost prototyping advantage of 3D printing. Yazlık

(2025) presented one of the rare AI applications in this review, combining thermochromic (color-changing based on temperature) PLA material with deep learning algorithms and establishing a temperature monitoring system with over 96% accuracy. At the micro level, Waquar (2022) developed micro-sensitive temperature sensors more quickly and cost-effectively using 3D printing compared to traditional methods, offering an alternative to microelectronic systems (MEMS) manufacturing processes.

Some studies have used 3D printing as an innovative tool to improve industrial and medical processes. Delibaş (2022) aimed to reduce mold costs for low-volume production by producing small-scale sheet metal forming molds using low-melting metal alloys. In the field of medical device design, Öztürk (2017) prototyped a complex coil design for magnetic resonance (MRI) devices with a 3D printer, facilitating the development of devices that are difficult to manufacture using traditional methods. Similarly, Biltekin (2018) designed a new applicator used in gynecological cancer treatment that improves patient comfort, highlighting the role of 3D printing in personalized medical device production. Finally, some theses have taken 3D printing to unexpected areas or addressed it at the system level. Diri Kenger (2020) modeled the role of 3D printers in recycling-focused supply chains, examining the logistics and sustainability aspects. Ay Dilsiz (2023) examined mineral precipitation in geothermal fields using artificial crack models produced with 3D printing for the energy sector. Kılıç (2023) opened a new horizon in the field of food science and technology by developing a functional product that can be printed using a 3D food printer from whey. The studies in this cluster demonstrate that 3D printing is not just an “object maker,” but also a key enabler in the development of complex systems and new scientific research tools.

Clinical and Applied Studies in Health Sciences

Theses in the field of health primarily focus on the biomedical and clinical applications of 3D printing, specifically on how the technology can be used to benefit patients directly. Unlike engineering research, studies in this field aim to improve existing clinical practices or develop new treatment methods, rather than focusing on material production. This trend is progressing in two main areas: dentistry and pharmacological applications.

The clearest examples of this trend are seen in dentistry. Research has focused on improving the clinical applicability of 3D-printed prostheses. For instance, Atılgan (2024) examined the surface quality of denture base materials produced with 3D printers by comparing different polishing methods (mechanical, chemical, etc.). This study aimed to directly enhance the clinical applicability of 3D-printed prostheses by determining the most suitable finishing technique for achieving patient comfort and ensuring the mechanical durability of the prosthesis. Taking research in this area a step further, Sözüöz (2025) comprehensively analyzed not only the mechanical and surface properties but also how different 3D printing technologies (DLP and LCD) and fabrication angles affect critical biological responses of these materials, such as the degree of conversion, cytotoxicity, and Candida albicans adherence. Sözüöz's study demonstrated that fabrication parameters (especially the angle increase) have a direct and significant impact not only on physical but also on biocompatibility and candidal adherence, providing essential data for the reliability of 3D-printed prostheses. Similarly, İskurt Mısıroğlu (2024) optimized the mechanical properties and durability of personalized orthodontic brackets produced using 3D printing, employing advanced simulation techniques such as finite element analysis.

Another innovative dimension of clinical applications has emerged in pharmacological treatments. Ege (2024) investigated the therapeutic potential of 3D-printed polymeric patches loaded with Moringa oleifera plant extract and chemotherapeutic agents on colon cancer cells. The study demonstrated that these bright patches triggered cell death (apoptosis) in cancer cells, demonstrating the strong potential of 3D printing for targeted drug delivery systems and innovative cancer treatments.

Similarly, 3D printing technology bridges the gap between pharmacology and regenerative medicine, providing innovative solutions for managing chronic wounds. Tekin (2025) used 3D bioprinting technology to develop a hybrid wound scaffold loaded with topical insulin for the treatment of chronic diabetic wounds. This study achieved the controlled release of insulin in both encapsulated and free forms (7.5 IU total) for 10 days using a bioink based on sodium alginate and silk fibroin. The developed hybrid wound scaffold was proven to be cytotoxic in vitro and significantly increased wound healing rate in diabetic rat models in vivo at the macroscopic, microscopic, and biochemical levels (markers such as MMP-2, TNF-α, etc.). This thesis is significant because it highlights the crucial role that 3D bioprinting plays in developing functional tissue engineering products that not only produce scaffolds but also provide complex, controlled drug delivery.

Cultural and Legal Studies in the Social Sciences

Studies in the social sciences reveal that 3D printing technology is not merely a technical innovation but a force that reshapes social and cultural norms. Doctoral dissertations in this field examine the two areas where this impact is most evident: cultural heritage and law. Ulalian Bishop (2025) reviewed the completion of missing parts of archaeological ceramic artifacts using 3D technologies. This study not only presented a technical restoration process but also raised deep ethical issues, such as "authenticity," "accuracy," and "reversibility." This dissertation highlights the potential of 3D printing to revolutionize cultural heritage conservation and museum display practices. Another groundbreaking impact of the technology is in the field of law. Güven (2024) examined the effect of 3D printing on intellectual property law from a comparative perspective (Turkish, German, EU). With the individualization and digitalization of production, the status of "digital model files" and the "physical objects" printed from them within the context of copyright protection has become complex. This study examines the inadequacy of existing legal frameworks in addressing this new form of production and the urgent need for regulation. These two theses clearly demonstrate how 3D printing is not only focused on engineering and healthcare, but also how it has generated significant and deeply rooted debates in fundamental societal areas, from the definition of cultural heritage to the protection of intellectual property.

Analysis of Medical Specialization Theses

The four theses identified in the TUS field, although small in number, differ significantly thematically from both the doctoral and dental fields. These theses focus directly on surgical practice and educational methodology. The thematic distribution of these four theses shows that half of the research focuses directly on educational practices (Table 2).

Table 2

Thematic Distribution of Medical Specialization Theses (n=4)

Main Category	Thematic Cluster (Sub-discipline)	Number of Theses
Medical Specialization	Surgical Education and Skill Development	2
	Surgical Technique Validation and Planning	1
	Tissue Engineering and Bioprinting	1
	TOTAL	**4**

Tissue Engineering and Bioprinting

A thesis by Büyükdoğan (2019) examined the bioprinting method (using a polycaprolactone scaffold and stem cells) in a rabbit model as a solution to the lack of cartilage tissue in rhinoplasty revision surgeries. This study demonstrates complete synergy with a cluster of Bioengineering doctoral dissertations (e.g., Demirtaş, 2016 - vascularized bone models; Tekin, 2025 - hybrid wound scaffold). This thesis confirms the ultimate goal of applying fundamental science research to clinical surgical practice at the laboratory level.

Surgical Technique Validation and Planning

Gülhan (2025) developed a new "cervicothoracic transpedicular freehand stabilization technique" in the field of neurosurgery and tested its validity and reliability on 3D-printed spine models. This study uses 3D printing not as a final product, but as a validation and testing tool for complex surgical procedures. This approach is a direct counterpart to Çıklaçandır's (2023) thesis (patient bone models for preoperative simulation) in clinical practice.

Surgical Education and Skill Development (Simulation)

This is the most prominent and strategic thematic cluster among medical specialty theses.

Gilik (2022) developed a "low-budget simulation model (phantom)" incorporating vertebral anatomy printed from patient CT images to improve the ultrasound-guided lumbar puncture (LP) skills of emergency medicine residents. He demonstrated that the group receiving practical training on this model scored significantly higher in terms of "LP success" and "confidence level" than the group receiving only didactic training. Similarly, Özer (2025) compared the effectiveness of traditional 2D Computed Tomography (CT) slices, 3D printed models, and Virtual Reality (VR) headsets in teaching orthopedic residents how to diagnose and interpret complex calcaneal fractures (Sanders classification). The results showed that the 3D printing method yielded the most successful results in terms of "interobserver agreement." These two theses (Gilik, 2022; Özer, 2025) are essential for the use of 3D printing technology in medical education.

Analysis of Specialization Theses in Dentistry

The identification of a dense cluster of 24 theses at the DUS level necessitates a reassessment of the actual volume and focus of research in this field. While doctoral theses generally focus on developing "new" materials and methods (e.g., developing algae-based bioink), Dentistry theses concentrate on testing the clinical performance, reliability, and limitations of newly introduced commercial 3D printing resins and digital workflows compared to conventional methods. This highlights the importance of validation during the transition of technology from the laboratory to the clinic. When Dentistry theses are summarized thematically in a format similar to Table 1, it is seen that the vast majority of research focuses on testing material properties (Table 3). The graphical distribution is provided in Figure 2.

Table 3

Distribution of 3D Printing-Related Dentistry Theses by Discipline in Turkey (n=24)

Main Category	Sub-discipline	Number of Theses (n)	Percentage (%)
Dentistry Specialization	Mechanical, Optical Properties, and Durability	14	58.4
	Dimensional Accuracy and Marginal Adaptation	6	25.0
	Surface Properties and Biocompatibility	2	8.3
	Other (Endodontic Applications)	2	8.3
	TOTAL	24	100.0

Figure 2

Distribution Graph of Dentistry Theses on 3D Printing in Turkey by Sub-Discipline

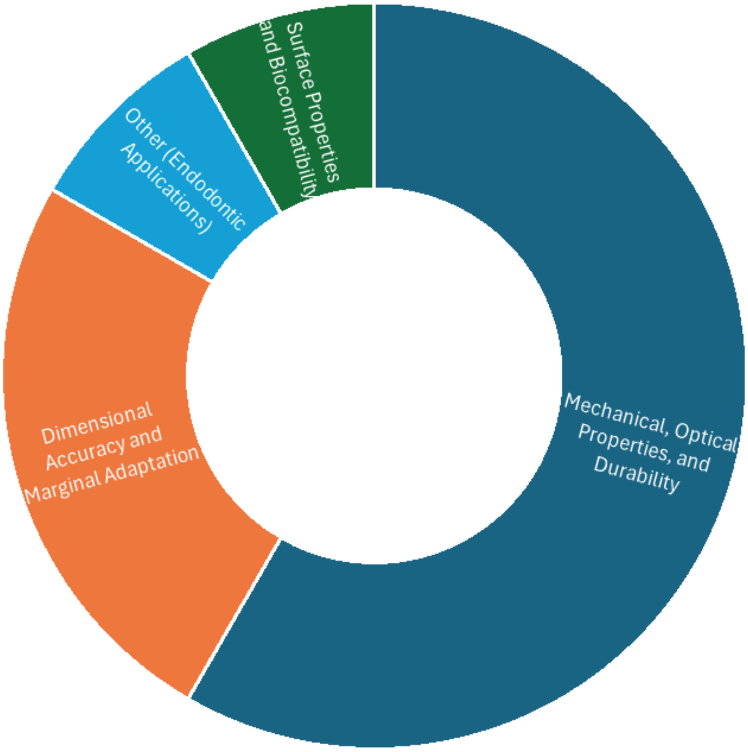

Mechanical, Optical Properties, and Durability

This area is the most dominant research trend in Dentistry Specialization theses. These studies compare the mechanical and aesthetic performance of 3D-printed materials (permanent crown resins, denture bases, and occlusal splints) with that of traditional materials (PMMA and composite resins) in vitro.

Wear, Fracture, and Mechanical Durability: Studies have examined the degree of polymerization and mechanical properties of 3D-printed denture bases (Sönmez Yılmaz, 2025), the mechanical properties of different CAD/CAM denture base materials (Sakarya, 2025), and the wear of occlusal splint materials produced with varying methods of manufacturing (conventional, subtractive, additive) (Kaygı, 2024). Additionally, the mechanical properties of dental restorations made from different resins using 3D printing have been compared (Çebi Gül, 2023).

Color Stability and Optical Properties: Studies have focused on the effects of different surface treatments on color stability in 3D-printed total denture base materials (Doymuş, 2021), the color properties of different 3D-printed permanent restoration resins (Çoban Gündoğan, 2024), the coloration properties of 3D materials and posterior composite resins (Emiroğlu, 2024), and the optical properties of conventional/digital acrylic resins (Güler, 2025).

Aging and Environmental Effects: This group evaluated the performance of materials under harsh conditions simulating the oral environment. Examples include the evaluation of the effect of thermal cycling on conventional and 3D produced base materials (Pektaş Özkanlı, 2022), the comparison of the tooth bond strengths of denture base resins produced with different methods after being kept in gastric acid (Kızılırmak, 2024), the comparison of the water absorption of 3D printing resins and conventional composite resins (Metin, 2025), and the effect of aging on the mechanical properties of occlusal splint materials (Bıkmaz, 2023).

Dimensional Accuracy and Marginal Adaptation

The most critical step in digital dentistry workflows is how faithfully the physical model or restoration produced conforms to the digital design and the patient's anatomy. The theses in this cluster focus on this topic.

Model Accuracy: These studies tested the accuracy of 3D-printed dental models themselves. Çınar (2025) compared the effect of resin viscosity (low vs. high) on model accuracy and precision with plaster models and found that low-viscosity resins yielded more accurate results than plaster. Taş (2022) and Yurdakurban (2023) also examined the accuracy of 3D-printed dental models and the dimensional properties of different model designs, respectively.

Restoration Fit and Marginal Adaptation: These studies examined how well the restoration fits the tooth, ensuring a proper fit and marginal adaptation. Yiğin (2025) investigated the effect of preparation design on the marginal adaptation of 3D-printed onlays; Oğuzhan (2023) evaluated the marginal adaptation of indirect restorations fabricated with a 3D printer; and Güngör (2022) digitally evaluated the fit and accuracy of temporary restorations fabricated with different methods.

Surface Properties and Biocompatibility

This theme encompasses studies examining both the aesthetic (gloss) and biological (bacterial adhesion) effects of the material's surface quality. Yumak (2025) compared the surface gloss of 3D-printed resins after different polishing methods (mechanical vs. chemical) and aging (brushing). Emiroğlu (2024) examined surface roughness and microhardness properties, while Güntekin (2022) analyzed the surface properties of 3D-printed composites after aging in a chewing simulator.

This thematic cluster directly parallels the doctoral dissertations in his analysis. For example, Atılgan's (2024) thesis examined the surface quality of denture base materials and different polishing methods. More importantly, Sözüöz's (2025) thesis analyzed how manufacturing parameters (pressure angle, etc.) affect not only cytotoxicity but also Candida albicans retention (biological response). This demonstrates that surface roughness studies are critical not only for aesthetics but also for preventing infections such as denture stomatitis and promoting patient health.

Integrated Analysis

Bipolar Research Ecosystem

Research on 3D printing in Turkey exhibits a "bipolar" research ecosystem, with a clear thematic and motivational distinction between the doctoral and specialist (TUS/DUS) levels.

1. Development Pole - Doctoral: This pole is overwhelmingly focused on Engineering and Science. The primary goal of research is to develop new materials (e.g., bioink, sustainable composites), new processes (e.g., drone printing, robotic systems), and new basic science applications (e.g., tissue engineering, targeted drug delivery).

2. Validation and Application Pole – Specialization: This pole is entirely clinically focused. The primary goal of research is to validate and apply technologies that have been developed or commercially launched. This pole is further divided into two:

Clinical Validation: The primary objective is to test whether new 3D printing resins and digital workflows are mechanically, aesthetically, and dimensionally adequate or superior for clinical use compared to traditional methods.

Clinical Application: The primary objective is to use the technology as a tool for surgical planning, technical development, and medical education.

Combined Analysis of Doctoral and Specialist Theses

3D printing research in Turkey is intensively conducted not only at the doctoral level but also at the specialist levels in Medicine and Dentistry. At this point, the initial distribution based on the YÖK classification in Table 1 creates a methodological limitation. The five "Health Sciences" doctoral theses in Table 1 (3 in Dentistry, 1 in Pharmacy, and 1 in Physiology) are focused on "clinical" and "health" aspects in terms of content and purpose. These theses serve the same primary purpose (improving healthcare practices) as the 28 theses from the Medical and Dental Specializations examined in Sections 3.2 and 3.3.

Therefore, to obtain the most accurate picture of Turkey's 3D printing research map, a reclassification based on the content of these theses is necessary, moving beyond the YÖK Doctoral classification. In this integrated approach, 24 theses from the Dental Specializations and four from the Medical Specializations were combined under the main category of "Health Sciences."

When this methodological correction is applied, the distribution of the 61 theses dataset by discipline differs dramatically from the "engineering-dominated" picture presented in Table 1. The new distribution reveals that Health Sciences, with 33 theses (54.1%), is the most dominant field in 3D printing research in Turkey, surpassing Science and Engineering Sciences with 26 theses (42.6%) (Table 4). The distribution of all these on 3D printing in Turkey by discipline is shown in Figure 3. The increasing trend of doctoral and specialty theses prepared on 3D printing in Turkey over the years is seen in Figure 4.

Table 4

Integrated Disciplinary Distribution of All Theses (PhD + Specialization) on 3D Printing in Turkey (n=61)

Main Category	Subcategory (Source)	Number of Theses (n)	Number of Theses (n)	Overall Rate (%)
Health Sciences	Dentistry Specialization	Clinical Material Validation	24	39.3
	PhD	Dentistry (Clinical Focus)	3	4.9
	Medical Specialization	Surgical Education and Practice	4	6.6
	PhD	Pharmacy/Physiology (Clinical Focus)	2	3.3
		Subtotal	**33**	**54.1**
Science and Engineering Sciences	PhD	Bioengineering (Basic Science)	6	9.8
	PhD	Mechanical Engineering	4	6.6
	PhD	Polymer Science and Technology	3	4.9
	PhD	Other Engineering/ Science Fields	13	21.3
		Subtotal	**26**	**42.6**
Social Sciences	PhD	Archaeology	1	1.6
	PhD	Law	1	1.6
		Subtotal	**2**	**3.3**
		TOTAL	**61**	**100.0**

Figure 3

Distribution Graph of All Theses on 3D Printing in Turkey by Discipline

Figure 4

Number of All Theses (PhD + Specialization) on 3D Printing in Türkiye

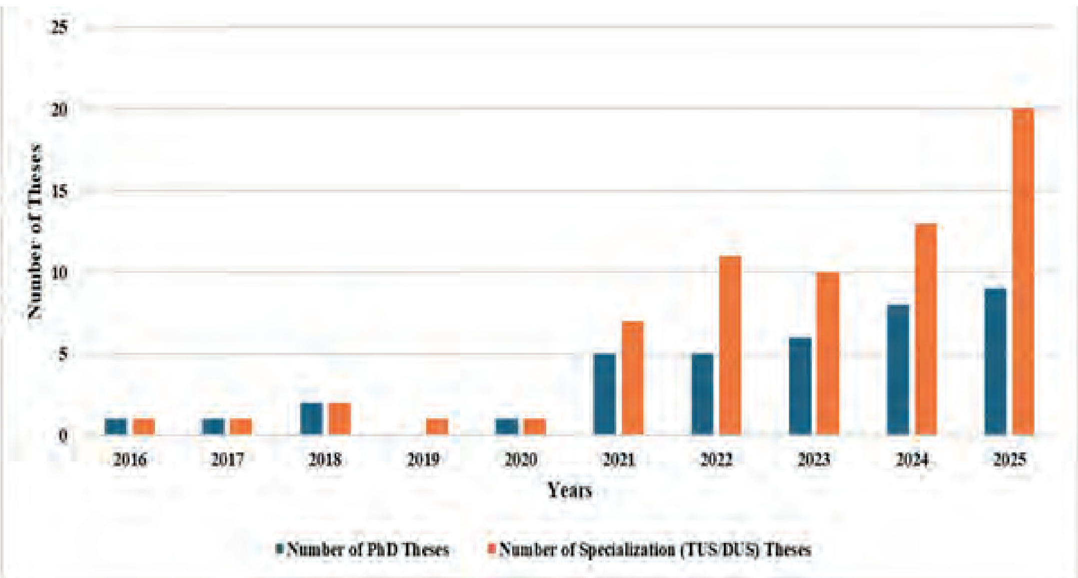

This new classification (Table 5 and Figure 3) clearly illustrates the "bipolar" nature of the research ecosystem in Turkey. While 42.6% of the research is concentrated in the development-focused Science and Engineering field, a larger percentage, 54.1%, is clustered in the application- and validation-focused Health Sciences field. This demonstrates that the technology is not only being developed in the laboratory but is also being intensively transferred to clinical applications and validated.

Artificial Intelligence Integration

One of the primary motivations for this systematic review is to measure the alignment of academic research in Turkey with the global "Industry 4.0" vision. This vision is based on the integration of physical production systems, such as 3D printing, with cognitive systems, including Artificial Intelligence (AI). By offering revolutionary potentials such as real-time optimization of printing parameters, material property prediction, and generative design, AI has the capacity to transform 3D printing processes from manual and trial-and-error processes to smart and predictable ones. This integration is one of the most essential criteria demonstrating the technological maturity of the national research ecosystem. Therefore, a holistic dataset of 61 theses (33 PhD, 24 Dentistry, and 4 Medicine) was meticulously examined for the presence of this critical cognitive integration. The analysis reveals that the lack of AI in doctoral dissertations (only 1 in 33) becomes even more vital and evident with the addition of specialist dissertations. None of the 24 Dentistry Specialization Theses and 4 Medicine Specialization Theses analyzed utilize AI, machine learning, or generative design in their methodologies.

This confirms the need for further research in Turkey to achieve Industry 4.0's vision of combining "cognitive" (AI) and "physical" (3D printing) systems. Intensive "parameter testing" studies, particularly in the field of dentistry (e.g., the effects of resin viscosity (Çınar, 2025), printing angle, or polishing methods (Yumak, 2025) on outcomes), provide an ideal basis for AI optimization and predictive modeling. However, all of these studies rely on traditional statistical methods (e.g., ANOVA, t-test) to analyze their results. Research has focused on trial-and-error-based manual processes rather than intelligent manufacturing processes.

Discussion and Conclusion

An integrated analysis of doctoral and specialist theses on 3D printing in Turkey (61 theses in total) provides a much more nuanced and comprehensive insight into the current state, strengths, and potential future directions of the country's research ecosystem than could be obtained by examining just 33 doctoral theses.

The most striking finding is that the dominance of "Science and Engineering" (79%) in the 33 doctoral theses completely reverses when specialist theses in Medicine and Dentistry are included. The integrated analysis (see Table 4) clearly reveals that Health Sciences (54.1%) is the most dominant field in 3D printing research in Turkey, surpassing Science and Engineering (42.6%). This demonstrates that Turkey's academic strength exhibits a "bipolar" structure: (1) strong Basic Science and Materials Development, driven by Science/Engineering doctoral dissertations, and (2) intensive Clinical Validation and Application, driven by Health Sciences, primarily through 24 Dentistry Specialization theses. This concentration in Health Sciences proves that Dentistry is no longer an "accelerating" field, but rather a "mature clinical validation" center, with its contribution focused on intensive materials testing. However, this holistic systematic analysis confirmed and even deepened several strategic research gaps. The most significant deficiency identified was the almost nonexistent presence of AI-based studies. Of the 61 theses examined, only one dissertation utilized AI methodologies. The fact that none of the 28 clinical specialization theses (24 DUS, 4 TUS) utilized AI or machine learning confirmed and deepened this strategic gap, which is not limited to the doctoral level but encompasses the entire academic ecosystem. Intensive "parameter testing" studies, particularly in the field of dentistry (e.g., the effect of resin viscosity, pressure angle, or polishing methods on results), provide an ideal basis for AI optimization and predictive modeling. However, all 24 theses rely on trial-and-error manual processes and traditional statistical methods (ANOVA, t-test, etc.) to analyze the results, representing a significant missed opportunity for "smart" manufacturing processes.

In conclusion, a total of 61 doctoral and specialist theses on 3D printing in Turkey demonstrate a remarkable interdisciplinary diversity, spanning materials science, healthcare, cultural heritage, and law. These studies indicate that the country possesses both a solid foundation of fundamental science and engineering, as well as extensive clinical validation and application competence (primarily in dentistry) in this technology field. However, the future vision that must be built upon this solid foundation is to extend the burgeoning strengths in medicine, such as AI integration (especially for clinical parameter optimization) and educational applications to other disciplines (e.g., Dentistry, Engineering), which should be a strategic priority.

References

Altundağ Erdoğan, Ö. (2025). Targeting circulating breast cancer stem cells via mTOR and WNT inhibitors after bone metastasis (Doktora tezi). Hacettepe Üniversitesi, Ankara.

Atılgan, B. (2024). 3 boyutlu yazıcılar ile baskılama tekniği ile üretilen protez kaide materyallerine uygulanan cila yöntemlerinin yüzey pürüzlülük ve mikrosertlik değerlerine etkisinin incelenmesi (Doktora tezi). İstanbul Üniversitesi, İstanbul.

Ay Dilsiz, E. (2023). CaCO3 çökelmesinin çatlaklı ortamda akış davranışına etkilerinin incelenmesi (Doktora tezi). İstanbul Teknik Üniversitesi, İstanbul.

Bahçegül, E. G. (2022). Tarımsal atıklardan elde edilen biyopolimerlerin üç boyutlu (3B) baskısı (Doktora tezi). Orta Doğu Teknik Üniversitesi, Ankara.

Bayram, A. (2018). Development of 3D-printed plastic based low-cost sensing systems (Doktora tezi). İzmir Katip Çelebi Üniversitesi, İzmir.

Bedir, T. (2024). Dijital ışık işleme yöntemi ile mikroiğne içeren kulak zarı yaması üretimi (Doktora tezi). Marmara Üniversitesi, İstanbul.

Bıkmaz, M. H. (2023). 3 boyutlu yazıcılar ile üretilen oklüzal splint materyallerinin mekanik ve yüzey özelliklerine yaşlandırmanın etkisinin in-vitro değerlendirilmesi (Diş Hekimliği Uzmanlık). Ankara Üniversitesi, Ankara.

Biltekin, F. (2018). Vajinal kaf brakiterapi uygulamaları için yoğunluk ayarlı aplikatör tasarımı: Dozimetrik fizibilite çalışması (Doktora tezi). Hacettepe Üniversitesi, Ankara.

Büyükdoğan, H. (2019). Tavşan modelinde rinoplasti komplikasyonlarına yeni bir çözüm tekniği: Biyoyazıcı ile doku üretimi (Tıpta Uzmanlık). Ankara Üniversitesi, Ankara

Ceylan Engin, İ. (2025). 3B baskı için kenevir lifiyle güçlendirilmiş polikarbonat kompozit üretimi ve mimari uygulamalarda kullanımı (Doktora tezi). Kocaeli Üniversitesi, Kocaeli.

Çebi Gül, B. (2023). Üç boyutlu yazıcı ile farklı rezinlerden üretilen dental restorasyonların mekanik özelliklerinin incelenmesi (Diş Hekimliği Uzmanlık). İnönü Üniversitesi, Malatya.

Çıklaçandır, S. (2023). Finite element analysis-based pre-operative planning applications of tooth, tibia, and femur bones (Doktora tezi). İzmir Katip Çelebi Üniversitesi, İzmir.

Çınar, G. (2025). Farklı viskoziteye sahip 3B baskı dental modeller ve konvansiyonel alçı modellerde tarama abutmenti ile modelin doğruluk ve hassasiyetinin değerlendirilmesi (Diş Hekimliği Uzmanlık). Selçuk Üniversitesi, Konya.

Çoban Gündoğan, Z. (2024). Üç boyutlu yazıcı ile üretilen farklı daimi restorasyon reçinelerinin renk özelliklerinin ve aşınma dirençlerinin karşılaştırılması (Diş Hekimliği Uzmanlık). Bezm-i Alem Vakıf Üniversitesi, İstanbul.

Delibalta, C. G. (2024). Kemik doku mühendisliği uygulamaları için fonksiyonel polimerik kompozit biyomalzeme üretimi ve karakterizasyonu (Doktora tezi). Muğla Sıtkı Koçman Üniversitesi, Muğla.

Delibaş, H. (2022). Development of a new sheet metal forming technique using low melting alloy 3D printers (Doktora tezi). Çukurova Üniversitesi, Adana.

Demirtaş, T. T. (2016). Kemik hasarları için vaskülarize kemik doku mühendisliği: 3B biyoyazıcı ile hidrojel/hücre/biyosinyal sistemlerin hazırlanması (Doktora tezi). Hacettepe Üniversitesi, Ankara.

Diri Kenger, Z. (2020). Disassembly and distribution planning considering 3D printing technology (Doktora tezi). Gaziantep Üniversitesi, Gaziantep.

Doymuş, Y. Ş. (2021). Üç boyutlu yazıcıyla üretilmiş total protez kaide materyalinde yapılan farklı yüzey işlemlerinin renk stabilitesine etkisi (Diş Hekimliği Uzmanlık). Hacettepe Üniversitesi, Ankara.

Ege, H. (2024). Moringa oleifera yüklü üç boyutlu baskı yamalarının in vitro kolon kanser hücrelerinde etki mekanizmalarının araştırılması (Doktora tezi). İstanbul Üniversitesi-Cerrahpaşa, İstanbul.

Emiroğlu, H. Ç. (2024). 3B materyallerin ve posterior kompozit rezinin yüzey pürüzlülüğü, mikrosertlik ve renklenme özelliklerinin incelenmesi (Diş Hekimliği Uzmanlık). Sağlık Bilimleri Üniversitesi, İstanbul.

Erdoğuş, H. B. (2022). Eriyik yığma modelleme ile üretilen polimerik hibrit stent tasarımı ve mekanik karakterizasyonu (Doktora tezi). Bursa Teknik Üniversitesi, Bursa.

Ghaziani, M. (2023). Fused filament fabrication via multi quadcopter collaboration (Doktora tezi). Orta Doğu Teknik Üniversitesi, Ankara.

Gilik, B. E. (2022). Düşük bütçeli simülasyon modeline dayalı eğitim ile acil tıp asistanlarının ultrason rehberliğinde lomber ponksiyon yapma becerisinin değerlendirilmesi(Tıpta Uzmanlık). Ankara Yıldırım Beyazıt Üniversitesi, Ankara.

Güler, E. (2025). Konvansiyonel ve dijital yöntemle üretilen akrilik rezinlerin optik ve mekanik özelliklerinin araştırılması (Diş Hekimliği Uzmanlık). Uşak Üniversitesi. Uşak.

Gülhan, A. A. (2025). Servikotorasik transpediküler serbest el stabilizasyon tekniği ve 3B baski ile güvenilirlik testi (Tıpta Uzmanlık). Sağlık Bilimleri Üniversitesi, İstanbul.

Gündüz, G. (2024). A tool oriented approach to digital making and control in design (Doktora tezi). İstanbul Teknik Üniversitesi, İstanbul.

Güngör, S. (2022). Farklı yöntemler ile üretilmiş geçici restorasyonlarda: dijital olarak; uyum, doğruluk, kararlılık ve okluzal aşınmanın değerlendirilmesi: İn-vitro çalışma (Diş Hekimliği Uzmanlık). Necmettin Erbakan Üniversitesi, Konya.

Güntekin, N. (2022). Çiğneme simülatöründe yaşlandırma sonrası, 3 boyutlu baskı cihazı kullanılarak üretilen kompozit numunelerin, farklı cad/cam kompozit materyaller ile yüzey özellikleri açısından karşılaştırılması (Diş Hekimliği Uzmanlık). Necmettin Erbakan Üniversitesi, Konya.

Güven, K. (2024). Karşılaştırmalı hukukta fikri haklar bakımından üç boyutlu yazıcılar (Doktora tezi). Ankara Üniversitesi, Ankara.

İlcan, H. (2024). Development of low alkalinity activated construction and demolition waste based geopolymer binder systems for 3D printing application (Doktora tezi). Hacettepe Üniversitesi, Ankara.

İskurt Mısıroğlu, S. (2024). Üç boyutlu yazıcı ile üretilen ortodontik braketlerin mekanik özelliklerinin sonlu elemanlar analizi ile incelenmesi (Doktora tezi). Sağlık Bilimleri Üniversitesi, İstanbul.

Kaygı, Y. D. (2024). Konvansiyonel, eksiltmeli ve tabakalı üretim yöntemleri ile farklı yüksekliklerde üretilen oklüzal splint materyallerinin aşınmasının değerlendirilmesi (Diş Hekimliği Uzmanlık). Bezm-i Alem Vakıf Üniversitesi, İstanbul.

Kılıç, S. (2023). Üç boyutlu baskısı yapılabilir lor bazlı zenginleştirilmiş fonksiyonel ürün üretimi ve karakterizasyonu (Doktora tezi). Ondokuz Mayıs Üniversitesi, Samsun.

Kızılırmak, B. (2024). Farklı yöntemlerle üretilmiş protez kaide rezinlerinin gastrik asitte bekletildikten sonra diş bağlanma dayanımlarının karşılaştırılması (Diş Hekimliği Uzmanlık). Necmettin Erbakan Üniversitesi, Konya.

Metin, Z. I. (2025). 3D baskı reçinelerinin ve geleneksel kompozit rezinlerin su emiliminin karşılaştırılması (Diş Hekimliği Uzmanlık). Ordu Üniversitesi, Ordu.

Numanoğlu, A. (2025). Üçlü periyodik minimal yüzeyler kullanılarak sinir kılavuz kanallarının (NGC) tasarımı ve üretimi (Doktora tezi). Gazi Üniversitesi, Ankara.

Oğuzhan, A. (2023). Üç boyutlu yazıcı ile üretilen indirekt restorasyonların marjinal adaptasyon ve bağlanma dayanımının incelenmesi (Diş Hekimliği Uzmanlık). Ege Üniversitesi, İzmir.

Oran, S. (2022). Üç boyutlu yazıcılar için karbon nanotüp takviyeli nanokompozit filamentlerin üretilmesi (Doktora tezi). Yalova Üniversitesi, Yalova.

Özer, M. (2025). Kalkaneus kırıkları sanders sınıflamasının ortopedi asistanları tarafından öğrenilmesi ve yorumlanması: Bilgisayarlı tomografi görüntüleri, üç boyutlu baskı ve sanal gerçeklik gözlükleri ile yapılan kıyaslamalı bir çalışma (Tıpta Uzmanlık). İstanbul Üniversitesi-Cerrahpaşa, İstanbul.

Öztürk, Y. (2017). Development of a uniform magnetic field generator for magnetic resonance applications (Doktora tezi). Gebze Teknik Üniversitesi, Kocaeli.

Pektaş Özkanlı, S. (2022). Konvansiyonel yöntemle ve üç boyutlu yazıcılarda üretilen kaide materyallerinin bazı mekanik ve fiziksel özelliklerine termal siklusun etkisinin değerlendirilmesi (Diş Hekimliği Uzmanlık). Ankara Üniversitesi, Ankara.

Sakarya, S. (2025). Farklı CAD/CAM protez kaide materyallerinin mekanik özelliklerinin incelenmesi (Diş Hekimliği Uzmanlık). Atatürk Üniversitesi, Erzurum.

Söğüt, O. (2023). Osteomyelit tedavisine yönelik 3B yazdırma yöntemi ile ilaç yüklü kemik greftlerinin geliştirilmesi (Doktora tezi). Süleyman Demirel Üniversitesi, Isparta.

Sönmez Yılmaz, K. N. (2025). 3B baskılama yöntemiyle üretilen protez kaidelerinde polimerizasyon derecesi, boyutsal değişim ve mekanik özelliklerin değerlendirilmesi (Diş Hekimliği Uzmanlık). İstanbul Üniversitesi, Malatya.

Sözüöz, B. (2025). Farklı tipte 3B yazıcılar kullanılarak, farklı yerleştirme açıları ve farklı eğim konfigürasyonları ile üretilen tam protez kaide materyallerinin dönüşüm derecesi, sitotoksisite ve kandida tutulumu yönünden karşılaştırılması (Doktora tezi). Sağlık Bilimleri Üniversitesi, İstanbul

Taş, H. (2022). Üç boyutlu baskı tekniğiyle üretilen dental modellerin doğruluğunun değerlendirilmesi (Diş Hekimliği Uzmanlık). İnönü Üniversitesi, Malatya.

Tekin, T. (2025). Kronik yara tedavisinde topikal insülin: 3B baskı teknolojisiyle hibrit yara iskelesi geliştirilmesi, In Vitro ve In Vivo değerlendirilmesi (Doktora tezi). Gazi Üniversitesi, Ankara.

Tezel, Ö. (2025). 3D-uv biyo-yazıcı tekniği ile hibrit doku iskelelerinin hazırlanması ve uygulama etkinliğinin incelenmesi (Doktora tezi). Marmara Üniversitesi, İstanbul.

Totuk, O. H. (2023). Yumuşak robotik peristaltik pompa tasarımı, analizi ve geliştirilmesi (Doktora tezi). İskenderun Teknik Üniversitesi, Hatay.

Ulalian Bishop, S. (2025). 3D technologies for archaeological ceramic loss compensation (Doktora tezi). Koç Üniversitesi, İstanbul.

Waquar, T. (2022). Design, analysis and production of temperature sensor using microstereolithography technique (Doktora tezi). Marmara Üniversitesi, İstanbul.

Yalman, V. (2025). 3 boyutlu biyobasım tekniğinde kullanılmak üzere uygun polimerik yapıların hazırlanması (Doktora tezi). Yıldız Teknik Üniversitesi, İstanbul.

Yazlık, E. N. (2025). Termokromik PLA ile derin öğrenme tabanlı anlık sıcaklık izleme sistemi ve uygulamaları (Doktora tezi). Erciyes Üniversitesi, Kayseri.

Yiğin, S. (2025). 3B baskı reçine ile yapılmış onleylerin marjinal adaptasyonuna preparasyon tasarımının etkisi (Diş Hekimliği Uzmanlık). Ordu Üniversitesi, Ordu.

Yumak, İ. (2025). 3B baskı olarak üretilen reçinelerin yüzey parlaklıklarının mekanik ve kimyasal yaşlandırmalar sonucundaki değişimlerinin incelenmesi (Diş Hekimliği Uzmanlık). Ege Üniversitesi, İzmir.

Yurdakurban, E. (2023). 3 boyutlu baskı teknolojileri ile üretilen farklı dental model tasarımlarının boyutsal özelliklerinin karşılaştırılması (Diş Hekimliği Uzmanlık). Sağlık Bilimleri Üniversitesi, İstanbul.

About The Authors

Elif AKTEPE received her bachelor's degree from the Department of Biomedical Engineering at Afyon Kocatepe University in Afyon, Turkey, in 2020, and her master's degree from the Department of Biomedical Engineering at the same university in 2022. She is currently pursuing her PhD in Electrical and Electronics Engineering at Afyon Kocatepe University, which she began in 2022. She currently serves as a lecturer in the Electronic Automation Department of Afyon Vocational School in Afyon. Her current research interests include biomedical technologies, 3D printing technologies, and artificial intelligence systems.

E-mail: eaktepe@aku.edu.tr, **ORCID:** 0000-0002-2375-2040

Uçman ERGÜN received his BS in Electrical and Electronics Engineering from Eskişehir Osmangazi University, Eskişehir, in 1996. He completed his MS in Electrical Education from Afyon Kocatepe University, Afyon, in 1999. He received his PhD in Electronics and Computer Education from Gazi University, Afyon, in 2005. He is currently an Associate Professor in the Department of Biomedical Engineering at Afyon Kocatepe University, Afyon. His current research interests include biomedical technologies, image processing, artificial intelligence, natural language processing, and deep learning.

E-mail: uergun@aku.edu.tr, **ORCID:** 0000-0002-9218-2192

Similarity Index:

The similarity index obtained from the plagiarism software for this book chapter is 2%.

Airfoil Self-Noise Prediction of the NACA 0012 Airfoil using ANFIS Optimized by PSO, GA, and ACO

Hasan ÇINAR
Necmettin Erbakan University

Engin Hasan ÇOPUR
Necmettin Erbakan University

Hasan Huseyin BILGIC
Necmettin Erbakan University

To Cite This Chapter:
Çınar, H., Çopur, E. H., & Bilgic, H. H. (2025). Airfoil self-noise prediction of the NACA 0012 airfoil using ANFIS optimized by PSO, GA, and ACO. In S. Kocer & O. Dundar (Eds.), *Next generation engineering: Smart solutions and applications* (pp. 37–49). ISRES Publishing.

Introduction

Urban Air Mobility (UAM) vehicles generate significant noise pollution due to their rotary-wing configurations, which should be carefully addressed during their design process (Kim, 2022). Regulations and requirements concerning UAM noise are comprehensively described in the International Civil Aviation Organization (ICAO) Document 9911 and the European Civil Aviation Conference (ECAC) Document 29 (Rizzi, Letica, Boyd, & Lopes, 2024). The sources of noise pollution in UAM vehicles include airfoil self-noise, blade-vortex interaction, blade-airframe interaction, and fuselage-wake interaction (Rizzi et al., 2020). This study focuses on estimating the self-noise generated by the NACA 0012 airfoil, which represents a major area of interest in noise pollution research. The NACA 0012 aerofoil has been assessed in the context of urban air mobility in a few recent studies(Wild & Jones, n.d.; Wright, n.d.).

The primary source of airframe noise is self-noise, which occurs when an aerofoil interacts with its boundary layer (Rastgoo & Khajavi, 2023). The magnitude and characteristics of airfoil self-noise are influenced by the geometric design parameters of the airfoil (such as trailing edge shape, leading edge configuration, thickness, and camber), the flow conditions (including Reynolds number, angle of attack, and Mach number), as well as the coupling between the flow field and structural dynamics (Nadkarni, Vijay, & Kamath, 2023). Given that UAM vehicles operate in densely populated metropolises for passenger or cargo transportation, noise pollution emerges as a critical issue. Moreover, noise pollution not only affects social acceptance and passenger comfort but also has implications for the vehicle's overall power consumption (Lyu, Seth, & Liem, 2024). Therefore, it should be considered as fundamental design parameter for vehicles design in UAM.

For the design of low-self-noise airfoils, it is essential to consider the flow field around the airfoil during the design phase (Aihara, Goude, & Bernhoff, 2021). This analysis can be performed using either wind tunnel experiments or computational fluid dynamics (CFD) simulations (Casalino & Barbarino, 2011). However, wind tunnel testing is often impractical due to its high cost and time requirements. Although CFD simulations solve the Navier–Stokes equations, they are typically associated with significant computational burden. As an alternative, low-noise airfoil designs can be developed through noise estimation methods based on existing datasets (Martinez, Afonso, & Lau, 2022). In this way, prediction studies can assist to new design studies that will reduce self-noise of an airfoil (example of (Hu, Wan, Ye, Sun, & Lu, 2022)).

In recent years, numerous studies have focused on airfoil noise prediction. Reference (Amirsalari & Rocha, 2023) (Doolan & Moreau, 2022) provide a review of noise computation, prediction, and optimisation methods of the airfoils. Basically, the approaches to model, compute, and predict flow-induced noise are categorised as the mathematical model-based, data-driven, experimental-based, and hybrid approaches. Particularly, data-driven estimation methods are of great interest due to their high accuracy and the fact that they do not rely on any mathematical model. Reference (Redonnet, Bose, Seth, & Li, 2024) implements a deep neural network that is a data-driven method to predict the self-noise of NACA 0012 by remaining within the error limits of 1.5-2.5 dB. For same airfoil, Reference (Radha Krishnan & Uppu, 2023) applied neural network by optimized with an quasi Newton method. Reference (Yang et al., 2024) implements a convolutional neural network to predict the noise of wind turbine airfoil. Reference (Pandey, Pandey, & Gupta, 2024) applied random forests, support vector regression, CatBoost, XgBoost, Gradient Boosting and Decision Trees to predict the noise of the NACA0012 airfoil. Reference (Dündar & Koçer, 2024, Zhang, Wang, Yang, & Zhang, 2024) used a random forest algorithm to predict the overall sound pressure level (OASPL) distribution for the supercritical airfoil RAE2822. Additionally, besides machine learning based techniques, fuzzy logic based studies have been conducted for airfoil noise prediction (example of (Kasnako˘ Glu, Mehmet¨, & Efe, 2008; Nikolić et al., 2016; Shamshirband, Petković, Hashim, & Motamedi, 2014). In summary, many studies have been conducted on data-driven based airfoil self-noise estimation using machine learning algorithms and fuzzy logic.

This study implements the Adaptive Network Based Fuzzy Inference System (ANFIS) method, aided by metaheuristic algorithms, for self-noise estimation of the NACA 0012 profile. The ANFIS membership function parameters are optimised using the PSO, GA, and ACO algorithms to enhance estimation performance. In privious studies ((Guvenc, Bilgic, Cakir, & Mistikoglu, 2022; Uzun, Bilgiç, Çopur, & Çoban, 2024)), the effectiveness of the metaheuristic and ANFIS hybrid estimation method has been verified in applications such as aerodynamic force estimation and decision-making systems. Similarly, this study also implements the hybrid estimation technique combining metaheuristics and ANFIS for self-noise estimation of NACA 0012 airfoil.

Accurate prediction of airfoil-induced noise is crucial for optimizing wing design parameters and improving the overall operational efficiency of aircraft. This study aims to achieve a precise estimation of the intrinsic noise generated by pressure fluctuations around the airfoil surface. In contrast to conventional approaches, an ANFIS optimized through metaheuristic search algorithms was employed as the estimation framework. The model was trained and validated using open-source experimental datasets obtained from NASA. The proposed methodology can facilitate the development and evaluation of novel airfoil geometries and configurations.

The structure of this study is organized as follows. Section 2 presents the methodology adopted in this study, along with a detailed defination of the airfoil dataset. This section also elaborates on the metaheuristic-based approach developed for noise prediction. Section 3 discusses the experimental results and provides a comparative analysis of the findings. Section 4 presents the discussion and outlines potential directions for future research on airfoil noise prediction. Finally, section 5 summarizes the main conclusions drawn from the study.

Methodology

Figure 1 illustrates the airfoil noise estimation methodology proposed in this study giving three main stages. In the first stage, the airfoil dataset was divided into 20% training data and 80% testing data to implement the estimation algorithms. The dataset included five input parameters; frequency, angle of attack, chosen length, free-stream velocity, and suction-side displacement thickness; and one output parameter, the scaled sound pressure level. In the second, ANFIS approach, enhanced with metaheuristic optimization algorithms (Particle Swarm Optimization (PSO), Genetic Algorithm (GA), and Ant Colony Optimization (ACO)), was implemented to estimate the airfoil self-noise. In the final stage, the performance of the applied algorithms was evaluated and compared with similar studies available in the literature considering root mean square error (RMSE) rates.

Figure 1

Graphical Abstract of Proposed Prediction Approach

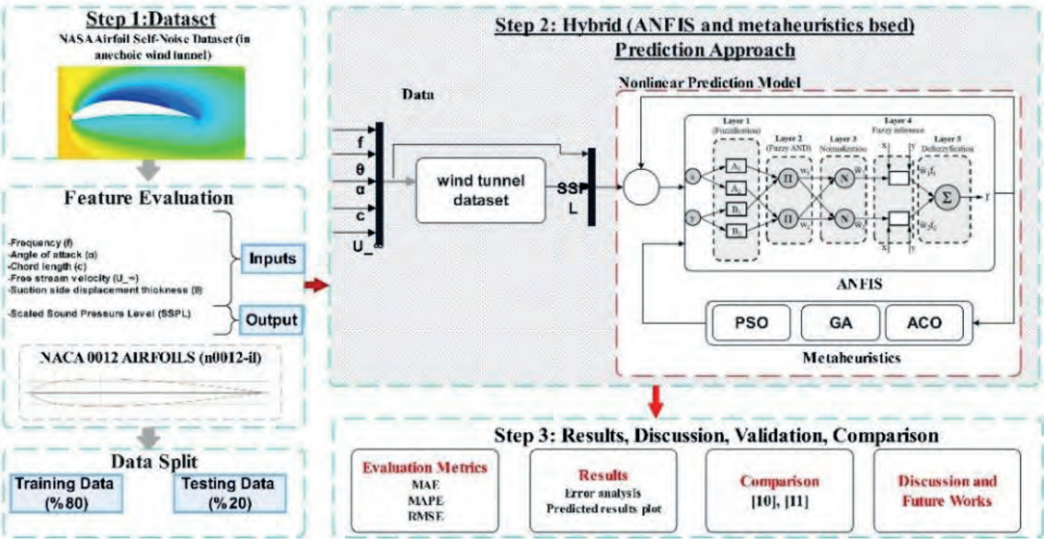

Definition of Dataset

This study utilizes the dataset obtained from wind tunnel measurements reported in the Reference (Brooks, Stuart, & Marcolini, 1989). The dataset includes input variables such as frequency (Hz), angle of attack (°), chord length (m), free-stream velocity (m/s), and suction-side displacement, as well as the output variable, the scaled sound pressure level (dB). In the experiments, wings with a span of 45.72 cm and NACA 0012 airfoil profiles having chord lengths of 2.54, 5.08, 10.16, 15.24, 22.86, and 80.4 cm were tested. The tests were conducted in a rectangular, closed-section wind tunnel with a cross-section of 30.48 × 45.72 cm (Brooks et al., 1989). The models were examined at various angles of attack under a maximum free-stream velocity of 71.3 m/s, corresponding to a Mach number of 0.208 and a Reynolds number of 1.5×10^5. Figure 3 illustrates the variation of the scaled sound pressure level with respect to the suction-side displacement thickness and the free-stream velocity.

Figure 2.

a-) Scaled Sound Pressure Level Versus Suction Side Displacement Thickness

b-) Scaled Sound Pressure Level Versus Free-Stream Velocity

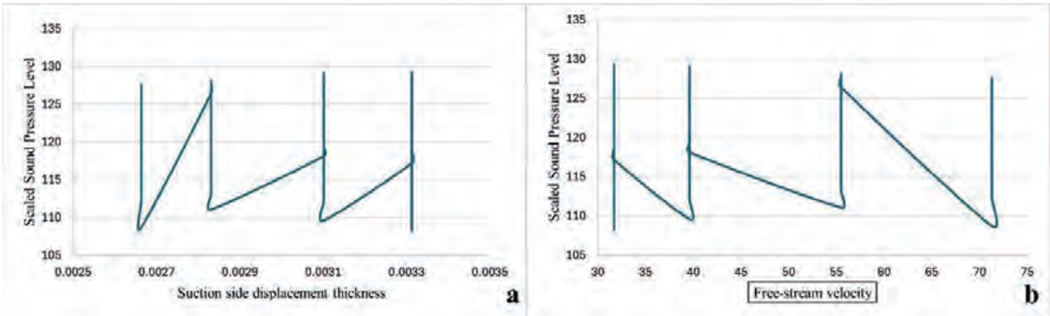

.

Prediction Methods

In this study, the ANFIS method, assisted with the integration of PSO, GA, and ACO, is employed to estimate the self-noise of an airfoil. The comparative performance of these metaheuristic algorithms in improving the ANFIS model is examined. In the proposed coupled estimation framework, metaheuristic algorithms are utilized to optimize the parameters of the ANFIS membership functions, as the accuracy of ANFIS extremely rely on the appropriate design and tuning of these functions. Three metaheuristic algorithms are selected, and their effects on the performance and prediction accuracy of the coupled estimation model are compared. This section provides a brief overview of the structure of the metaheuristic-assisted estimation approach.

Particle swarm optimization aided ANFIS

Figure 3 illustrates the main structure of the proposed hybrid estimation approach that is combined with ANFIS and PSO. For simplicity, the architecture of ANFIS is given in this Figure is for a two-input one-output system. However, the problem proposed in this study has five inputs and one-output variables. Also, Figure 3 shows the flow chart of both the PSO algorithm and ANFIS structure. ANFIS is a modelling technique that combines parallel computing of artificial neural networks and the heuristic computing capabilities of fuzzy logic rules. Modeling data sets containing multiple inputs and outputs can be created using ANFIS (Jang, 1993). The PSO algorithm (Kennedy & Eberhart, 1995), introduced in 1992, is a flock-based search algorithm that follows the rules (Rao, 2019): 1-) an individual in the flock approaches another individual 2-) an individual moves in the average direction of other individuals. 3-) an individual moves in the average direction between other individuals, except for very large gaps in the flock.

Figure 3.

The Main Framework of the Hybrid Prediction Method with PSO Assistance

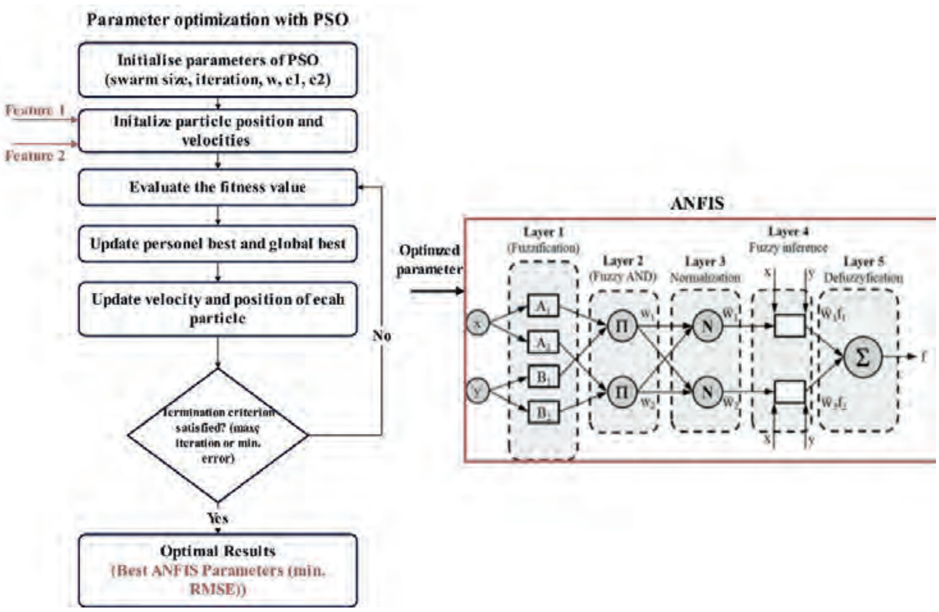

Genetic algorithm aided ANFIS

Figure 4 illustrates the structure of the hybrid estimation method assisted by the GA. GA developed for optimization problems be of mixed continuous discrete variables, and discontinuous and nonconvex design spaces, based on reproduction, crossover and mutation of natural genetics (Goldberg, 1989; Rao, 2019). In the algorithm, each iteration evaluates the suitability of the updated result until the required number of iterations is reached, or the minimum RMSE is achieved. In conclusion, optimized parameters improve the prediction accuracy of ANFIS.

Figure 4.

The main framework of the hybrid prediction method with GA assistance

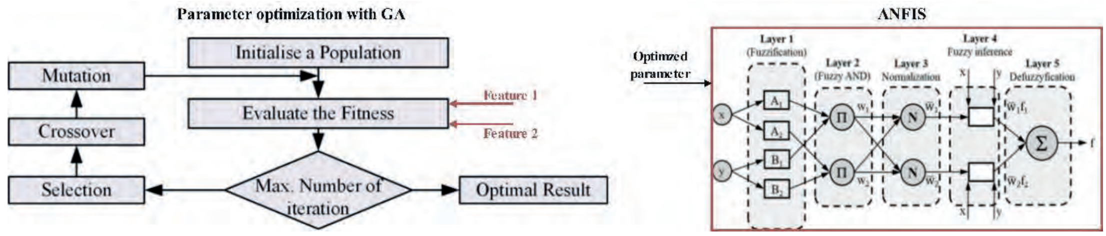

Ant colony optimization aided ANFIS

Figure 5 illustrates the structure of the hybrid estimation approach assisted ACO algorithm. The bee algorithm, developed in the 1990s, is inspired by the cooperative behavior of bees to find the shortest path for foraging (Colorni, Dorigo, & Maniezzo, 1991).

Figure 5

The Main Framework of the Hybrid Prediction Method with ACO Assistance.

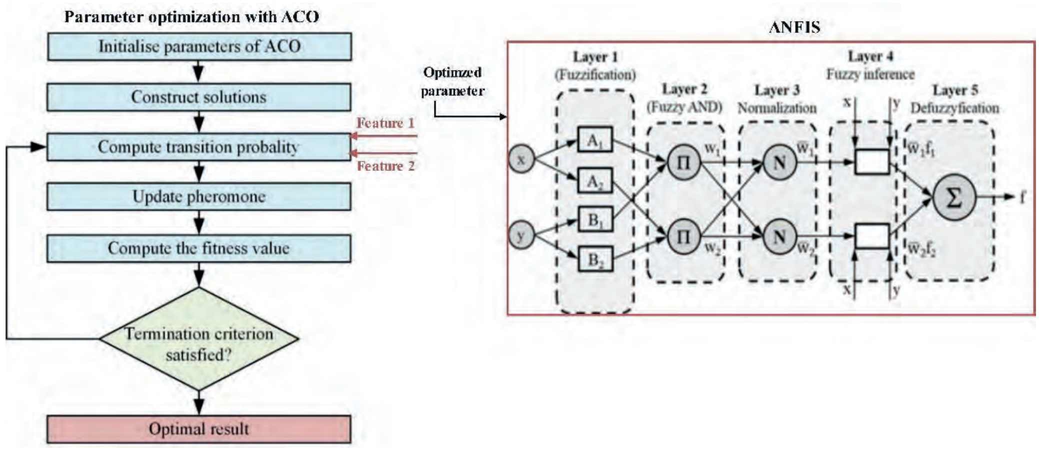

Results

The accuracy and generalizability of predictive models rely heavily on the quality of the data preprocessing stage. Effective data preprocessing directly impacts both the model's learning capacity and the reliability of the results obtained. While models often learn patterns effectively from data in its original order, this can lead to bias if the sample order contains an implicit structure, thereby negatively impacting the model's generalization ability on unseen data.

Therefore, the 1503 samples (data points) used in the study were initially randomly shuffled to maximize the model's generalizability and ensure the statistical reliability of the performance metrics. Random shuffling not only mitigates the risk of overfitting by reducing dependency between sequential samples, but it also increases the consistency of performance measurements by lowering the standard deviation of results.

Following the shuffling process, the data were divided into two main subsets: 1200 samples were allocated to the model development phase (used for training and internal validation), while the remaining 303 samples were reserved as an independent test set. The 1200 samples used in the development phase were further split into subsets (training and validation) to allow for parameter optimization and hyperparameter tuning.

Finally, the 303 samples, which were not used in the model development phase at all, were utilized as the final test set to evaluate the models' true performance. This rigorous division ensured that the models' predictive capability was measured against completely unseen data, objectively demonstrating the generalizability of the developed models.

Figure 6 presents the detailed training and independent testing results for the PSO (Particle Swarm Optimization) supported ANFIS (Adaptive Neuro-Fuzzy Inference System) algorithm developed for SSPL (Sound Pressure Level) estimation. To evaluate the model's performance, key statistical metrics Mean Squared Error (MSE), Root Mean Squared Error (RMSE), and Standard Deviation (STD)were calculated for both the training and testing phases.

The model's performance during the training phase is notably strong. The MSE, RMSE, and STD values were determined to be 7.1206, 2.6684, and 2.669, respectively. These low error values indicate that the ANFIS model, optimized by PSO, successfully learned the complex patterns within the training dataset. The test results on the independent dataset, which was not used during training, provide a measure of the model's true generalization capability: The MSE, RMSE, and STD values were calculated as 8.1342, 2.8521, and 2.8548, respectively.

The fact that all statistical parameter values for the training and testing phases are exceptionally close to each other constitutes the most critical finding of this study. Specifically, the minimal difference between the Training RMSE (2.6684) and the Test RMSE (2.8521) definitively proves that the model did not fall into the trap of overfitting. This proximity clearly demonstrates the high accuracy and applicability of the PSO-ANFIS model to new and previously unseen datasets, thereby establishing the reliability of the developed estimation approach.

Figure 6

Training and Test Results of PSO Aided ANFIS Algorithm for SSPL

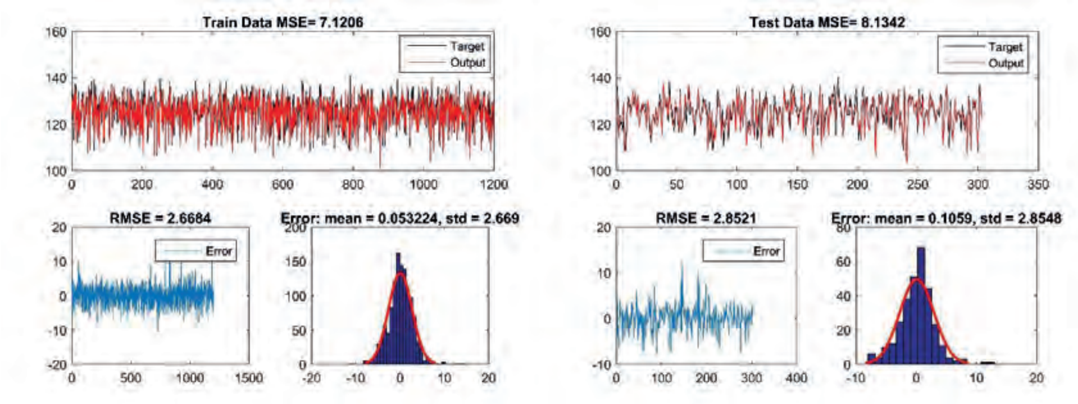

As part of the holistic evaluation of the study, the performance of the other meta-heuristic optimization algorithms developed alongside the PSO-based ANFIS model was also analyzed. Figure 7 presents the training and independent testing results for the GA (Genetic Algorithm) supported ANFIS model for SSPL estimation, while Figure 8 illustrates the training and testing performance of the ACO (Ant Colony Optimization) supported ANFIS model.

The primary observation across all three models is the closeness of the statistical error parameters, such as MSE, RMSE, and STD, between the training and independent testing results. This consistency confirms that both the GA and ACO-based models also demonstrated applicability to new datasets without suffering from the problem of overfitting.

However, upon an in-depth examination of the performance of all models, it was determined that the error metrics (MSE and RMSE) for the GA and ACO-supported ANFIS models were significantly higher compared to the PSO-supported ANFIS model. This finding indicates that the PSO algorithm was substantially more effective in optimizing the membership functions and rule base of the ANFIS model than the other two meta-heuristic approaches. Considering the lowest error metrics achieved and the highest prediction reliability, the PSO-based ANFIS approach clearly stands out as the method exhibiting the most superior performance for SSPL estimation. This comparative analysis reinforces the main conclusion of the study, scientifically demonstrating that the proposed PSO-ANFIS model is the optimum solution for complex aerodynamic noise prediction.

Figure 7

Training and Test Results of GA Aided ANFIS Algorithm for SSPL

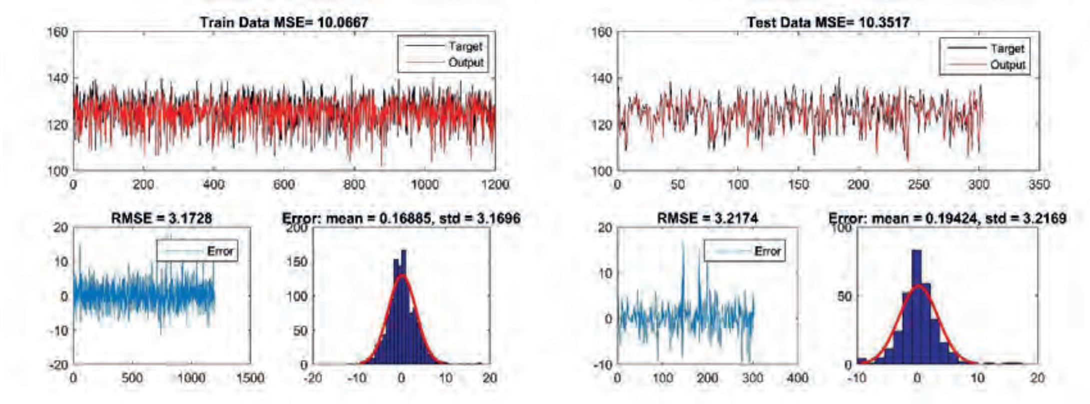

Figure 8

Training and Test Results of ACO Aided ANFIS Algorithm for SSPL

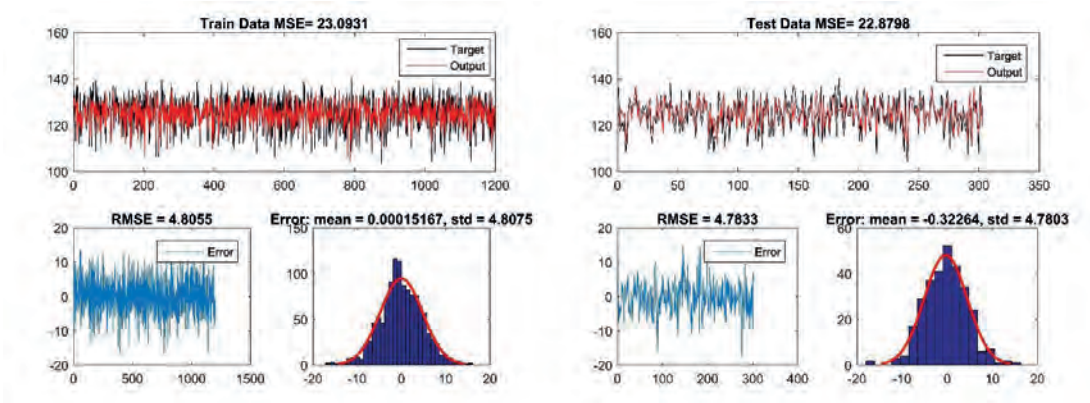

Discussion and Future Works

While this study proves the effectiveness of metaheuristics assisted ANFIS for airfoil self-noise prediction, it may have several improvements. First, the method implemented only for one type of airfoil (NACA 0012), it can be applied on different type airfoil profiles. Future works could consider automated feature engineering to enhance adaptability of proposed method in this study. Second, other alternatives instead of metaheuristics for ANFIS parameter optimization can be tested on this dataset. Third, the study focused on three metaheuristics algorithms (PSO, GA, ACO), while these due to what has been proven in the literature. However, exploring other optimization algorithms or hybrid approaches for parameter optimization of ANFIS could yield further results. This study only focuses on estimating the self-noise of the NACA 0012 airfoil. Noise estimation can be used to design low-noise airfoils. Therefore, this study can be used to validate future CFD studies, and low-noise airfoil design can be achieved using CFD studies. In summary, this study can be a starting point for wing designs with low noise pollution. The acceptable level of noise pollution is one of the barriers to the broad use of urban air mobility, so designers should bear that in mind.

Conclusion

Applied aerodynamic analysis studies, despite providing consistent and reliable results, involve a long preparation period and are high-cost. Moreover, a significant limitation is the low resolution of the data obtained, meaning the flow field can only be examined at a limited number of points. Conversely, numerical simulation studies can provide detailed flow information at a much higher resolution and stand out due to their low cost. However, the accuracy and reliability of numerical models, especially in complex aerodynamic noise prediction, still lag behind experimental applications. In this study, a hybrid parameter estimation approach was proposed, which combines the high consistency of experimental results with the advantages of speed and low cost offered by simulation studies. Within this scope, ANFIS (Adaptive Neuro-Fuzzy Inference System) was implemented for the self-noise prediction of the NACA 0012 airfoil. To maximize prediction success and the model's generalization capability, meta-heuristic search algorithms (ACO, GA, and PSO) were utilized for the fine-tuning of ANFIS parameters. The obtained results clearly indicate that the proposed hybrid approach provides high accuracy and efficiency in aerodynamic noise prediction. This successful integration once again demonstrates the potential of experimental data-driven artificial intelligence models, particularly in modeling complex physical phenomena such as noise. Consequently, the developed method proves that it can be readily used as a reliable and fast prediction tool in similar engineering processes (e.g., aerodynamic performance, structural health monitoring, vibration analysis).

References

Aihara, A., Goude, A., & Bernhoff, H. (2021). Numerical prediction of noise generated from airfoil in stall using LES and acoustic analogy. *Noise and Vibration Worldwide, 52*(10), 295–305. doi:10.1177/09574565211030706

Amirsalari, B., & Rocha, J. (2023, September 1). Recent Advances in Airfoil Self-Noise Passive Reduction. *Aerospace*. Multidisciplinary Digital Publishing Institute (MDPI). doi:10.3390/aerospace10090791

Brooks, T. F., Stuart, D., & Marcolini, M. A. (1989). *NASA Reference Publication 1218 Airfoil Self-Noise and Prediction*.

Casalino, D., & Barbarino, M. (2011). Stochastic method for airfoil self-noise computation in frequency domain. *AIAA Journal, 49*(11), 2453–2469. doi:10.2514/1.J050773

Colorni, A., Dorigo, M., & Maniezzo, V. (1991). Distributed optimization by ant colonies: Proceedings of the First European Conference on Artificial Life. *Paris, 134*, 142.

Doolan, C., & Moreau, D. (2022). Airfoil noise mechanisms and control. In *Flow Noise: Theory* (pp. 139–171). Springer.

Dündar, Ö., & Koçer, S. (2024). Pneumonia Detection from Pediatric Lung X-Ray

Images Using Artificial Neural Networks. Journal of Polytechnic, 27(5).

Goldberg, D. E. (1989). Genetic algorithm in search, optimization and machine learning, addison. *W Esley Publishing Company, R Eading, MA*, *1*(98), 9.

Guvenc, M. A., Bilgic, H. H., Cakir, M., & Mistikoglu, S. (2022). The prediction of surface roughness and tool vibration by using metaheuristic-based ANFIS during dry turning of Al alloy (AA6013). *Journal of the Brazilian Society of Mechanical Sciences and Engineering*, *44*(10), 474.

Hu, Y. Sen, Wan, Z. H., Ye, C. C., Sun, D. J., & Lu, X. Y. (2022). Noise reduction mechanisms for insert-type serrations of the NACA-0012 airfoil. *Journal of Fluid Mechanics*, *941*. doi:10.1017/jfm.2022.337

Jang, J.-S. (1993). ANFIS: adaptive-network-based fuzzy inference system. *IEEE Transactions on Systems, Man, and Cybernetics*, *23*(3), 665–685.

Kasnako˘ Glu, C. C., Mehmet¨, M., & Efe, M. (2008). *Prediction of Dynamical Properties of Flow Over a Three-element Airfoil via Computationally Intelligent Architectures*. *COEX*.

Kennedy, J., & Eberhart, R. (1995). *Particle swarm optimization*. In *Proceedings of ICNN'95-international conference on neural networks* (Vol. 4, pp. 1942–1948). ieee.

Kim, J. H. (2022). Urban Air Mobility Noise: Further Considerations on Indoor Space. *International Journal of Environmental Research and Public Health*, *19*(18). doi:10.3390/ijerph191811298

Lyu, Y., Seth, A., & Liem, R. P. (2024). Fuel consumption and trailing-edge noise tradeoff studies via mission-based airfoil shape optimization. *Aerospace Science and Technology*, *151*. doi:10.1016/j.ast.2024.109331

Martinez, R. V., Afonso, F., & Lau, F. (2022). Aerodynamic Shape Optimisation of a Camber Morphing Airfoil and Noise Estimation. *Aerospace*, *9*(1). doi:10.3390/aerospace9010043

Nadkarni, S. B., Vijay, G. S., & Kamath, R. C. (2023). Comparative Study of Random Forest and Gradient Boosting Algorithms to Predict Airfoil Self-Noise. *Engineering Proceedings*, *59*(1). doi:10.3390/engproc2023059024

Nikolić, V., Petković, D., Por, L. Y., Shamshirband, S., Zamani, M., Ćojbašić, Ž., & Motamedi, S. (2016). Potential of neuro-fuzzy methodology to estimate noise level of wind turbines. *Mechanical Systems and Signal Processing*, *66–67*, 715–722. doi:10.1016/j.ymssp.2015.05.005

Pandey, H., Pandey, P., & Gupta, D. (2024). *Airfoil Self Noise Prediction Using Machine Learning and Explainable AI*. In *RAICS - IEEE Recent Advances in Intelligent*

Computational Systems. Institute of Electrical and Electronics Engineers Inc. doi:10.1109/RAICS61201.2024.10689885

Radha Krishnan, N. S., & Uppu, S. P. (2023). A novel approach for noise prediction using Neural network trained with an efficient optimization technique. *International Journal for Simulation and Multidisciplinary Design Optimization, 14*. doi:10.1051/smdo/2023002

Rao, S. S. (2019). *Engineering optimization: theory and practice*. John Wiley & Sons.

Rastgoo, A., & Khajavi, H. (2023). A novel study on forecasting the airfoil self-noise, using a hybrid model based on the combination of CatBoost and Arithmetic Optimization Algorithm. *Expert Systems with Applications, 229*. doi:10.1016/j.eswa.2023.120576

Redonnet, S., Bose, T., Seth, A., & Li, L. K. B. (2024). Airfoil self-noise prediction using deep neural networks. *Engineering Analysis with Boundary Elements, 159*, 180–191. doi:10.1016/j.enganabound.2023.11.024

Rizzi, S. A., Boyd, D. D., Bent, P., R&t, B., Louis, S., Henderson, B. S., … Cruz, S. (2020). *Urban Air Mobility Noise: Current Practice, Gaps, and Recommendations*. Retrieved from http://www.sti.nasa.gov

Rizzi, S. A., Letica, S. J., Boyd, D. D., & Lopes, L. V. (2024). Prediction of Noise-Power-Distance Data for Urban Air Mobility Vehicles. *Journal of Aircraft, 61*(1), 166–182. doi:10.2514/1.C037435

Shamshirband, S., Petković, D., Hashim, R., & Motamedi, S. (2014, July 30). Adaptive neuro-fuzzy methodology for noise assessment of wind turbine. *PLoS ONE*. Public Library of Science. doi:10.1371/journal.pone.0103414

Uzun, M., Bilgiç, H. H., Çopur, E. H., & Çoban, S. (2024). The aerodynamic force estimation of a swept-wing UAV using ANFIS based on metaheuristic algorithms. *The Aeronautical Journal, 128*(1322), 739–755.

Wild, O. D., & Jones, A. R. (n.d.). *Urban Air Mobility: Effects of increasing three-dimensionality on fixed and rotary wings in unsteady aerodynamic environments*.

Wright, S. J. (n.d.). *Fundamental Aeroelastic Analysis of an Urban Air Mobility Rotor*.

Yang, H., Yuan, W., Zhu, W., Sun, Z., Zhang, Y., & Zhou, Y. (2024). Wind turbine airfoil noise prediction using dedicated airfoil database and deep learning technology. *Applied Energy, 364*. doi:10.1016/j.apenergy.2024.123165

Zhang, Q., Wang, X., Yang, D., & Zhang, W. (2024). Data-driven prediction of aerodynamic noise of transonic buffeting over an airfoil. *Engineering Analysis with Boundary Elements, 163*, 549–561. doi:10.1016/j.enganabound.2024.04.006

About the Authors

Hasan ÇINAR received the B.Sc. (Hons.) and M.Sc. degrees in Mechanical Engineering from Selçuk University, and the PhD. degree in Mechanical Engineering from Gebze Technical University, in Türkiye. He is currently an assistant professor at the Necmettin Erbakan University, Konya, Türkiye. His research interests include machine learning and its applications in aviation, hybrid energy storage, energy management, urban air mobility, propulsion systems, computational fluid dynamics, and unmanned aerial vehicles.

E-mail: hasan.cinar@erbakan.edu.tr, **ORCID:** 0000-0001-8718-3767

Engin Hasan ÇOPUR gradauted as a mechanical engineer in 2007 from Gazi University which is located in Ankara, the capital city of Türkiye. Then started my MSc study in the same university and completed it in 2011. During this period, the author was also working as a research assistant there. After completing MSc study, author was able to obtain a state funding for my PhD study in UK and gained a Phd position in University of Southampton. Then author returned Turkey and started working as a lecturer in 2017 in Necmettin Erbakan University which is located in Konya Türkiye. Since 2017, author held the same position.

E-mail: ehcopur@erbakan.edu.tr, **ORCID:** 0000-0003-0837-1255

Hasan Huseyin BILGIC received MSc. from Department of Mechanical Engineering, Mustafa Kemal University, Hatay, Turkey, in 2014 and then received PhD from Department of Mechanical Engineering, İskenderun Technical University, Hatay, Turkey, in 2018. Now he is Assistant Professor at Department of Aeronautical Engineering, Necmettin Erbakan University, Konya, Turkey. His current research interests include command/ input shaping, sliding mode control, artificial intelligence, linear and nonlinear control systems, UAV system design and control.

E-mail: bilgichh@gmail.com, **ORCID:** 0000-0001-6006-8056

Similarity Index :

The similarity index obtained from the plagiarism software for this book chapter is 12%.

Artificial Intelligence-Based Autonomous Tree Pesticide Robot for Targeted Spraying

Muhammed KARAALTUN
Necmettin Erbakan University

To Cite This Chapter:
Karaaltun, M. (2025). Artificial intelligence–based autonomous tree pesticide robot for targeted spraying. In S. Kocer & O. Dundar (Eds.), *Next generation engineering: Smart solutions and applications* (pp. 50–67). ISRES Publishing.

Introduction

Robotics is an interdisciplinary field that combines computer science and engineering (Birk, 2011). The purpose of robotics is to help people in many jobs by designing intelligent machines. Robotics develops machines that can replace humans and replicate human actions (Moravec, 1988). Robots can be used in many situations and for many purposes, such as the examination of radioactive materials and detecting bombs, as well as in production processes or in areas where humans cannot survive, such as in space, underwater, in high heat, and in hazardous materials (Piantadosi, 2003;Kocer & Butuner, 2021). In recent years, it has emerged that robots are frequently used in the agricultural realm. In fields with large areas, performing many functions by robots provides great advantages in terms of time and finances. Different types of robots are used in various fields. As some examples, we can also show workers, protective, doctors, farmers, and other types of robots (Sparrow & Howard, 2021). Robot usage can ensure that operations are performed more quickly and efficiently. At the same time, robots are used in heavy and large-scale works that require human power, in places where human safety is at risk, and to reduce the amount of defective production (Adesiji et al., 2025). As technology advances, the tasks of robots are also diversified; nowadays, robots are used in many important fields such as medicine, agriculture, manufacturing, and aviation. In general, robots use a specific algorithm tailored to the task at hand to perform their tasks. With the advent of machine learning algorithms, robots have begun to take part in tasks such as decision making, prediction, recognition, and classification. Artificial neural networks, decision trees, and Convolutional Neural Networks (CNN) are types of machine learning algorithms (Pu et al., 2019). Recently, the CNN algorithm has been utilized in many fields. Şahin et al. demonstrate the superiority of the CNN algorithm against the current state-of-the-art classification algorithms by applying a simple CNN for age and sex classification (Şahin & Kölüş, 2024). Ulubaba et al. used models of CNN: ResNet-18, ResNet-50, InceptionV3, and EfficientNet-B0 to analyze 470 left-hand X-ray images. Among the tested models, the ResNet-50 outperformed the ResNet-18, InceptionV3, and EfficientNet-B0 models (Ulubaba, Atik, Çiftçi, Eken, & Aldhahi, 2025). Nanyonga et al. evaluated the performance of BERT, CNN, and Long Short-Term Memory (LSTM) deep learning classification algorithms for classifying incidents based on injury severity levels according to accuracy, F1-score, recall, and precision. As a result, the BERT classification algorithm outperformed both LSTM and CNN across all evaluation metrics (Nanyonga, Joiner, Turhan, & Wild, 2025). Lu et al. conduct a comprehensive study on the use of deep learning and traditional classification algorithms in plant leaf disease classification. Consequently, because deep learning classification algorithms are getting better performance than traditional classification algorithms, deep learning algorithms, specifically models of CNN, are commonly used in plant leaf disease classification (Lu, Tan, & Jiang, 2021). Huu et al. demonstrate the promising potential utilization of machine learning classification algorithms in manufacturing. Artificial intelligence and optimization algorithms have been utilized in many fields (H. I. Ayaz & Kamisli Ozturk, 2021). Therefore, artificial intelligence, optimization algorithms, and deep neural networks have emerged as valuable tools among machine learning classification algorithms (Huu et al., 2024). Levine et al. have demonstrated training convolutional neural networks that map raw image pixels directly to robot joint torques for manipulation tasks, providing an early and influential example of end-to-end visuomotor learning for real robots. This work showed that deep networks can represent complex sensor action mappings and be trained with a mix of supervised and policy-search objectives (Levine, Finn, Darrell, & Abbeel, 2016). Levine et al. have collected hundreds of thousands of real grasp attempts and trained a CNN to predict grasp success from monocular images, demonstrating that large-scale data collection enables robust, generalizable grasping policies that can correct mistakes via closed-loop servoing. This study highlighted the importance of scale in supervised robot learning (Levine, Pastor, Krizhevsky, Ibarz, & Quillen, 2018). Levine and Koltun have introduced guided policy search, which uses trajectory optimization to generate guiding samples and converts them into supervised learning targets for neural-network policies, combining the sample efficiency of trajectory methods with the representational power of deep networks. This algorithm influenced many subsequent hybrid model-based / model-free robotic learning approaches (Levine & Koltun, 2013). A probabilistic, Gaussian-process-based framework for very data-efficient control learning in continuous systems, PILCO showed that explicitly modeling uncertainty in learned dynamics can enable learning complex controllers from very few trials—important for real-world robots where trials are expensive (Deisenroth & Rasmussen, 2011). Framed imitation learning as an adversarial game and produced policies that mimic expert behavior without requiring explicit reward engineering. GAIL and its variants have been widely applied to robot imitation tasks where demonstrations are available (Ho & Ermon, 2016). Peng et al. have combined motion-capture/ demonstration data with deep reinforcement learning to learn robust, dynamic locomotion and acrobatic skills in simulated physics environments, showing how example-guided RL can produce richly varied and recoverable behaviors applicable to legged robots and character controllers (Peng, Abbeel, Levine, & Van de Panne, 2018). Mahler et al. have built massive synthetic datasets (Dex-Net 2.0) and trained a Grasp-Quality CNN (GQ-CNN) to predict grasp success from depth images; the approach emphasized training on procedurally generated synthetic data and analytic grasp metrics to scale grasp learning and speed up inference (Mahler et al., 2017). Tobin et al. have proposed domain randomization: training perception/control networks on heavily randomized simulated images so that the learned policies generalize to real images without exact simulation fidelity. This simple but powerful idea has become a standard tool for transferring policies to physical robots (Tobin et al., 2017). Akkaya et al. have combined large-scale simulation, automatic domain randomization (ADR), and reinforcement learning to train a dexterous hand (Dactyl) capable of manipulating a Rubik's Cube in the real world, an example of scaling RL + sim real techniques for high-dimensional manipulation. The work shows both the promise and the massive computational cost of current sim-to-real dexterity efforts (Akkaya et al., 2019). Qi et al. have introduced a neural architecture that directly consumes point clouds for classification and segmentation while respecting permutation invariance—enabling robots to process raw 3D LiDAR/point-cloud data for tasks such as object recognition, scene understanding, and grasp planning (Qi, Su, Mo, & Guibas, 2017). Zhu et al. have developed siamese actor-critic models for target-driven indoor visual navigation, demonstrating that deep RL can learn goal-conditioned navigation policies from visual inputs and generalize to new targets and environments with appropriate training or fine-tuning, relevant for mobile robots and service robots (Zhu et al., 2017). The use of robotics in precision agriculture has transformed traditional pest management practices, enhancing efficiency and reducing chemical waste. This study introduces a machine learning-based tree pesticide robot designed to autonomously detect and treat pest-infested areas on trees. The robot employs CNN for real-time identification and classification of pests, diseased leaves, and healthy foliage, ensuring precise targeting of pesticide application. Leveraging the CNN algorithm, the system achieves high accuracy in distinguishing effected areas, enabling optimized spraying patterns, reduced chemical usage, and improved tree health. Experimental evaluations demonstrate that the CNN-based approach surpasses conventional image processing and alternative machine learning methods in detection accuracy, operational speed, and adaptability to varying tree types and lighting conditions. This research underscores the potential of deep learning-powered robotic systems in advancing sustainable and intelligent agricultural practices.

Materials and Methods

Tree Image Dataset

A tree image dataset used to train a CNN typically consists of a large collection of labeled images representing various tree conditions, including healthy leaves, pest-infested areas, and disease-affected foliage. The dataset is designed to capture a wide range of visual variations, such as different lighting conditions, angles, backgrounds, species types, and growth stages, to ensure that the CNN learns robust and generalizable features. Each image is annotated with class labels or bounding boxes that indicate the presence of pests or diseased regions, enabling the model to distinguish subtle visual patterns such as discoloration, texture changes, and structural deformities on leaves or branches. By training on such a diverse and carefully curated dataset, the CNN learns hierarchical representations that improve its ability to accurately classify and detect effected areas in real-time applications. This dataset plays a crucial role in enhancing the model's accuracy, adaptability, and operational reliability when deployed on autonomous agricultural robots for precision pesticide spraying and tree health monitoring.

Convolutional Neural Network

Feature extraction and classification are the base components of the CNN algorithm. Fig. 1 shows the basic structure of the CNN (Karaaltun, 2024).

Figure 1

The basic structure of the CNN

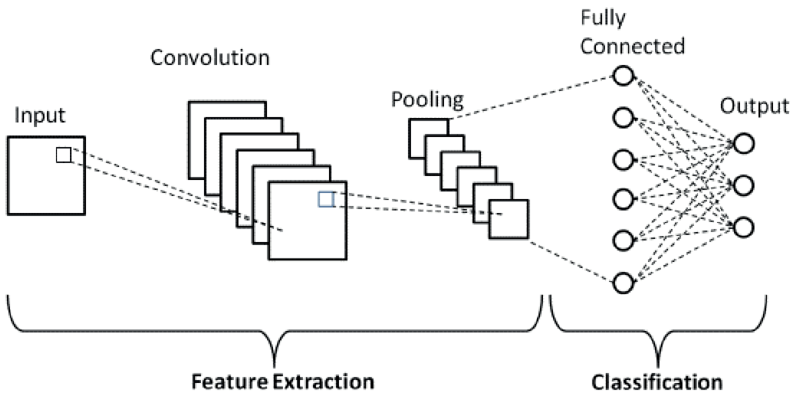

The feature extraction layer consists of input, convolution, and pooling layers. The images found in the input layer, which is the first layer of the CNN, must be given in a certain size. The size of an image given in this layer is of great importance for the final success of the whole system (Erickson et al., 2018). Increasing the size of the incoming image data can increase the accuracy of the model while increasing the duration of the training process. Therefore, it is vital to select an appropriate image size for the input layer of CNN. The convolution is performed by filtering the input image to a certain size. Depending on the size of the images, the filters can be of different sizes, such as 2x2, 3x3, or 5x5. The output of the convolution layer is activated by activation functions: Sigmoid, Tanh, or Rectified Linear Unit (ReLU) (Wang, Li, Song, & Rong, 2020).

The main purpose of the pooling layer, which usually comes after the convolution layer, is to reduce the size of the input matrix for the classification layer. As in the convolution layer, certain filters are defined in the pooling layer. These filters can be moved at a certain step on the image, and the values of the pixels in the image can be calculated in three different ways: maximum pooling, minimum pooling, and average pooling, which are given in **Figure 2** (Zhao & Zhang, 2024). While in maximum pooling, the maximum values of the pixels are taken into account; in minimum pooling, the minimum values of the pixels are taken into account. In average pooling, the average values of the pixels are taken into account (Karaaltun, 2024). The filter size and the step parameters are considered important parameters in the pooling layer (Ahmed, 2020).

Figure 2

Maximum, Minimum, and Average Pooling

The classification layer, which is located after the pooling layer, consists of a fully connected layer consisting of input, hidden, and output layers (Basha, Dubey, Pulabaigari, & Mukherjee, 2020). The learning process of CNN depends on the architecture of this layer. This layer receives its inputs from convolutional and pooling layers, and its outputs are obtained as a result of training (L. Liu, Shen, & van den Hengel, 2016). The number of weights of a fully-connected layer depends on the output size of the previous layers and the number of neurons in the hidden layers. The output of this layer can be calculated using addition, multiplication, and maximization methods (Chen et al., 2020). The addition method is commonly used. To calculate the addition of the classification layer, the values of the inputs to the cell (I) are multiplied by their own weights (w); these weighted inputs are added together to get the net input value, the net input value (addition) formula given in Equation 1.

$$Net\ input\ value\ (addition) = \sum_{i=1}^{m} I_i * W_i \tag{1}$$

To get the final result of the neuron, the activation function, which is known as the transfer function, is applied to the obtained net output value. In the training phase of the CNN classification algorithm, heuristic learning algorithms perform the weight update process by taking the derivative of the activation function. Therefore, choosing easily computable activation functions in the CNN classification layers accelerates the training phase of the CNN classification algorithm. The activation function maps the resulting values to 0 to 1 or -1 to 1, depending on the activation function. Activation functions can be basically divided into two types: linear and non-linear activation functions (Sharma, Sharma, & Athaiya, 2017). The linear activation function may not be effective in our case since it produces the same results in the backpropagation stage. Instead, we would discuss non-linear activation functions such as sigmoid, tangent hyperbolic, and Rectified Linear Unit (ReLU) activation functions, which are extremely efficient in the case of binary classification problems.

Evaluation of Classification Algorithms

Performance evaluation is one of the most important parts of the classification model development process (Kim, 2010). It provides the best classification model that represents our dataset and evaluates how well the chosen model will fit the data. Among different evaluation approaches, the k-fold cross-validation method is the one that may fit our needs (Gorriz, Segovia, Ramirez, Ortiz, & Suckling, 2024). To avoid overfitting, this method uses a test set (examples not seen by the model) to evaluate the performance of the model. It is very important to compare the classification accuracy of the created models with each other, and as a result, the classification model with the best performance accuracy is selected. In the k-fold cross-validation, the training set is divided into k subsets of equal size. At each iteration, the next subset is removed from the training dataset and used as the test set. If k is equal to the sample size, it is called "leave-one-out" (Cawley & Talbot, 2003). K-fold cross-validation splits data coming to the model into random parts, called folds. The model sets aside one fold (sometimes called a "holdout fold") and uses the remaining k-1 pieces for the training. For example, if the value of k is 5, the data will be randomly divided into 5 parts, the model is trained using 4/5 of the data, and the model is tested on the remaining 1/5. Accuracy statistics are evaluated during testing of the model for each part. Which statistical criteria to use depends on the type of model that is evaluated. For example, for classification models, criteria such as classification accuracy, confusion matrix, and error rate are among the most popular techniques. When the evaluation process is completed for all parts, the cross-validation model establishes a performance measure for all data and gives a result as an output. For example, classification accuracy (CA) can be calculated as given in Equation 2.

$$CA_i = \frac{Total\ number\ of\ true\ classifications}{Total\ number\ of\ samples} * 100 \tag{2}$$

where i = 1,2,…,k, during the evaluation phase of classification algorithms, the 10-fold cross-validation method is generally used to prevent overfitting and underfitting problems.

When a classification algorithm is run more than once and the CA of each output is calculated, it is of great importance the consistency of these values. According to Equation 3, it can be calculated using the central distribution standard deviation (σ) method of the data analysis criteria. The standard deviation indicates how similar or close the classification accuracy criteria are obtained from multiple runs (X. Liu, 2012).

$$\sigma = \sqrt[2]{\frac{1}{n-1}\sum_{i=1}^{n}(x_i - \bar{x})^2} \quad (3)$$

Where, x_i is each value in the result set and $\bar{x}$ is the average of the results.

A matrix called the confusion matrix is used to evaluate a trained classification model. Within this matrix, there are numbers that the classification model classifies as correct and incorrect (Sathyanarayanan & Tantri, 2024). The evaluation of trained classification models is the most important task that determines how well the predictive values obtained from the classification models are. The evaluation criteria of a classification model are derived from the confusion matrix given in **Figure 3**.

Figure 3

Confusion Matrix

		Predicted class	
		Positive	Negative
Actual class	Positive	True positive	False negative
	Negative	False positive	True negative

True positives (TP) and true negatives (TN) are samples of positive and negative tests that are correctly predicted by the trained model. False negative (FN) and false positive (FP) test samples are positive and negative test samples that are incorrectly predicted by the trained model. False positive and false negative values occur when the actual class conflicts with the predicted class. The most important goal in trained models is to minimize false negative and false positive values. After obtaining the TP, TN, FP, and FN values in the binary confusion matrix, we can calculate the accuracy, recall, precision, area under the ROC curve, and F1-Score of a trained model (Krstinić, Braović, Šerić, & Božić-Štulić, 2020).

The accuracy, given in Equation 4, is the most intuitive performance measure and is the ratio of correctly predicted sample numbers to total sample numbers (H. İ. Ayaz & Öztürk, 2023). Accuracy can be an important criterion, but when there are symmetrical datasets where false positive and false negative values are nearly the same, it is useful to look at other parameters to evaluate the performance of the trained model (Vujović, 2021).

$$Accuracy\ (AC) = \frac{TP + TN}{TP + FP + FN + TN} \quad (4)$$

Recall, given in Equation 5, is the ratio of the number of correctly predicted positive samples to the total number of samples. The recall value rises at a low rate with a false negative value. Sensitivity is known as the true positive rate (Mijwil & Aljanabi, 2024).

$$Recall\ (REC) = \frac{TP}{TP\ + \text{FN}} \quad (5)$$

Precision, given in Equation 6, is the ratio of the number of correctly predicted negative samples to the total number of predicted negative samples. The false-positive rate is low in classification models with a high precision value. Precision was known as the true negative rate (Patro & Patra, 2014).

$$\text{Precision (PRE)} \ = \frac{TN}{TN + FP}\text{Precision (PRE)} \ = \frac{TN}{TN + FP} \quad (6)$$

F1-score, given in Equation 7, is the weighted average of recall and precision values. Therefore, this value takes into account both false positives and false negatives. The F1-score is often more useful than accuracy, especially if you have an uneven class distribution. Accuracy works best if true positive and false negative values have similar costs. If the cost of false positives and false negatives is different, it is better to look at both recall and precision values (Fourure, Javaid, Posocco, & Tihon, 2021).

$$F1 - \text{Score} = 2 * \frac{\text{Precision} * Recall}{\text{Precision} + Recall} \quad (7)$$

Robots

Robots have become one of the most dynamic and transformative technologies of the modern era, shaping industries, societies, and daily life in unprecedented ways. A robot is generally defined as a programmable machine capable of carrying out tasks autonomously or semi-autonomously, often performing actions that are repetitive, dangerous, or too complex for humans (Rayhan, 2023). From manufacturing floors and surgical rooms to outer space and personal households, robots have evolved from mechanical prototypes to highly intelligent systems powered by advanced electronics, sensors, and artificial intelligence. As robotics continues to expand across disciplines, it plays an increasingly critical role in enhancing productivity, safety, and innovation in countless domains. The concept of robots has existed for centuries, found in myths, early automata, and mechanical inventions designed to mimic human or animal behavior (Stone, 2018). However, the modern field of robotics began to take shape in the mid-20th century, particularly with the development of industrial robots capable of automated manufacturing. One of the earliest commercially successful robots, the Unimate, revolutionized assembly lines in the 1960s by performing precise and repetitive tasks such as welding and material handling (Packianathan, Arumugam, Natarajan, & Malaiarasan, 2024). This marked the beginning of a technological wave that would spread across industries and set the stage for today's highly sophisticated robotic ecosystems. At its core, a robot is composed of several key components: mechanical structure, actuators, sensors, control systems, and software. The mechanical structure defines the robot's physical form, whether it is a robotic arm, humanoid robot, mobile platform, or aerial drone. Actuators provide motion, converting electrical signals into mechanical force through motors, hydraulic systems, or pneumatic systems. Sensors enable robots to perceive their environment, detect obstacles, measure distances, monitor internal states, and interact safely with objects or humans. These sensors may include cameras, LiDAR, ultrasonic sensors, force sensors, temperature sensors, and many others. Control systems process sensor data and determine how a robot should behave, while software and algorithms translate high-level tasks into low-level actions. Robots can be categorized into several major types depending on their structure, function, or application domain. Industrial robots are among the most prevalent, widely used in manufacturing for operations such as welding, painting, assembly, and packaging (Gasparetto & Scalera, 2019). Their precision, speed, and endurance make them essential to mass production and automation. Service robots, on the other hand, are designed to assist humans in daily activities. These include cleaning robots, delivery robots, medical robots, and rescue robots. Mobile robots navigate through physical environments using mapping and localization techniques, while drones operate in the air for tasks such as surveillance, inspection, and photography. Humanoid robots attempt to replicate human form and movement, enabling them to perform tasks designed for people or interact socially. The integration of artificial intelligence has significantly expanded the capabilities of robots. Traditionally, robots relied on fixed programming and predictable environments, limiting their ability to adapt or make decisions. Today's intelligent robots use machine learning, computer vision, and advanced planning algorithms to understand their surroundings, recognize objects, and adjust their behavior dynamically. AI-enabled robots can learn from experience, collaborate with humans, and perform more complex and unstructured tasks (Papadopoulos, Antona, & Stephanidis, 2021). Examples include autonomous vehicles that navigate traffic, surgical robots that assist with precision operations, and warehouse robots that coordinate logistics with minimal human intervention. This shift from mechanical automation to intelligent autonomy marks a major evolution in the field of robotics. Robots play an increasingly vital role in industries where accuracy, safety, and efficiency are critical. In healthcare, surgical robots enable minimally invasive procedures with enhanced precision, reducing recovery time for patients. Assistive robots support elderly individuals, improve mobility, and monitor health conditions. In agriculture, robots help plant, harvest, and monitor crops, improving yields and addressing labor shortages. In construction, robots automate repetitive processes such as bricklaying or site inspection, improving safety in hazardous environments. Space robotics has enabled exploration of planets, moons, and asteroids through rovers and landers capable of operating in extreme conditions far beyond human reach. Despite their advantages, robots also pose challenges that require careful consideration. Safety remains a primary concern, especially when robots share workspaces with humans. Ensuring reliable performance, avoiding accidents, and designing collaborative robots (cobots) that interact safely with people are major research priorities. Ethical and social issues also arise, such as the impact of robotics on employment, privacy concerns related to autonomous systems, and the moral implications of using robots in warfare or surveillance. Establishing regulations and standards is essential to guide the responsible development and deployment of robotic technologies. The future of robotics promises even greater advances as hardware, software, and AI continue to evolve. Developments in soft robotics, inspired by biological systems, aim to create flexible and adaptive robots capable of delicate interactions. Swarm robotics explores the collective behavior of large groups of simple robots working together to achieve complex goals, similar to ants or bees. Human-robot interaction research focuses on enabling robots to understand human emotions, communicate effectively, and collaborate more naturally. Robots are also becoming increasingly accessible, with educational platforms and low-cost components enabling students and hobbyists to explore robotics from an early age. In conclusion, robots have progressed from mechanical curiosities to powerful intelligent tools that influence nearly every aspect of modern life. They enhance efficiency in industries, improve the quality of healthcare, expand the boundaries of exploration, and assist individuals in everyday tasks. As robotics continues to advance, it brings both opportunities and responsibilities, requiring thoughtful design, ethical consideration, and a commitment to using technology for the benefit of society. The ongoing evolution of robotics will undoubtedly shape the future, offering new possibilities for innovation, collaboration, and human progress.

NVIDIA Jetson Nano

The NVIDIA Jetson Nano is a powerful, compact, and energy-efficient edge AI computing platform designed to enable developers, students, and researchers to build intelligent systems (Nano, 2019). First introduced by NVIDIA as part of the Jetson family, the Jetson Nano brings affordable GPU-accelerated computing to embedded applications, supporting real-time artificial intelligence tasks such as image classification, object detection, speech processing, robotics control, and autonomous navigation. Despite its small size, roughly the size of a credit card, the Jetson Nano delivers impressive computational capabilities, making advanced AI development accessible to a wide range of users. At the core of the Jetson Nano is the NVIDIA Maxwell GPU architecture with 128 CUDA cores, paired with a quad-core ARM Cortex-A57 CPU. This combination provides enough processing power to run multiple neural networks simultaneously while managing high-resolution computer vision tasks. The board includes 4 GB of LPDDR4 RAM, enabling smooth performance for modern deep learning frameworks such as TensorFlow, PyTorch, and NVIDIA's own TensorRT. As a result, developers can deploy convolutional neural networks for robotics, smart cameras, and IoT edge devices without requiring large servers or cloud infrastructure. Connectivity and expandability are key strengths of the Jetson Nano. The board supports a variety of interfaces—including USB 3.0, GPIO pins, I2C, SPI, UART, and MIPI CSI camera inputs—allowing integration with sensors, cameras, actuators, and custom electronics. This flexibility makes the platform especially popular in robotics and embedded vision projects where real-time perception and control are essential. The Jetson Nano Developer Kit also includes a 40-pin GPIO header compatible with Raspberry Pi accessories, enabling easy prototyping and educational experimentation. Another major advantage of the Jetson Nano is its software ecosystem. It runs on JetPack, NVIDIA's comprehensive SDK that includes a Linux-based operating system (L4T), GPU-accelerated libraries, and deep learning tools. JetPack provides seamless support for CUDA, cuDNN, TensorRT, OpenCV, ROS (Robot Operating System), and deep learning inference engines (Nano, 2019). This integrated environment simplifies deploying AI models and accelerates the entire development workflow—from training to optimization and inference. With extensive documentation and a large developer community, users can quickly build sophisticated AI applications even with limited experience. The Jetson Nano has become widely adopted in education, research, and industry due to its balance of performance, affordability, and ease of use. It is particularly influential in robotics competitions, autonomous machine development, smart surveillance, and real-time edge AI applications. By enabling high-performance AI at low power, the NVIDIA Jetson Nano represents a major step toward democratizing artificial intelligence and empowering innovators to bring intelligent systems into the real world.

The Proposed CNN Model

The proposed CNN model is a powerful and specialized architecture designed to classify and detect tree images with high accuracy, robustness, and computational efficiency. Its design addresses the challenges commonly found in natural outdoor environments, such as varying illumination, background complexity, leaf occlusion, and inconsistent tree structures, by integrating deep hierarchical feature extraction layers, multi-scale processing, and an optimized detection module. This makes the model suitable for real-world agricultural applications, including tree health monitoring, pest detection, and precision spraying systems. The architecture begins with a deep feature extraction backbone composed of several convolutional blocks, each utilizing small 3×3 kernels, batch normalization, and ReLU activation. These layers extract and refine visual patterns from the input images, starting with low-level details like edges, textures, and color transitions before progressing to high-level structural attributes such as branch formations, leaf density, and pest-induced anomalies. By gradually increasing the number of filters from 32 up to 256, the network gains the capacity to learn highly discriminative and abstract features that are essential for accurate classification and detection of tree conditions. To strengthen its representational power, the proposed CNN model incorporates multi-scale feature extraction by including parallel convolutional paths with different receptive field sizes. This enables the network to analyze tree structures at various spatial levels, capturing both fine-grained details and global patterns. Additionally, residual skip connections are integrated to prevent gradient vanishing and to maintain stable training in deeper layers, thereby enhancing performance without compromising computational efficiency. For detection tasks, the model includes a lightweight region proposal and bounding-box regression module inspired by modern object detection frameworks. This component uses convolutional layers to generate candidate regions of interest and predicts bounding-box coordinates around tree areas or localized symptoms such as pest spots or diseased regions. The detection head works synergistically with the classification layers to ensure that the model not only identifies the presence of a specific tree condition but also precisely localizes it within the image. To reduce overfitting and improve generalization, Dropout layers and Global Average Pooling are utilized in the final stages. Global Average Pooling replaces traditional flattening, significantly lowering the number of trainable parameters while preserving essential global image representations. The model concludes with fully connected layers followed by a Softmax activation for classification and a regression head for detection outputs. Optimizers such as Adam or RMSProp, along with learning-rate schedulers, ensure fast and stable convergence during training. Overall, the proposed CNN model presents a highly capable and powerful structure designed specifically for tree image classification and detection. Its combination of deep feature extraction, multi-scale analysis, robust detection mechanisms, and strong regularization techniques makes it well-suited for deployment in modern agricultural systems, providing reliable, efficient, and real-time decision support for tree monitoring and automated intervention applications. The structure of the proposed CNN model is given in Table 1.

Table 1

The structure of the proposed CNN model

Layer	Out put	# of Parameters
conv2d_1 (Conv2D)	(NO, 84, 84, 32)	896
GlobalAveragePooling2D()	(NO, 42, 42, 32)	0
conv2d_2 (Conv2D)	(NO NO, 42, 42, 64)	18496
GlobalAveragePooling2D()	(NO, 21, 21, 64)	0
conv2d_3 (Conv2D)	(NO, 21, 21, 128)	73856
GlobalAveragePooling2D()	(NO, 11, 11, 128)	0
conv2d_4 (Conv2D)	(NO, 11, 11, 256)	295168
GlobalAveragePooling2D()	(NO, 6, 6, 256)	0
dropout_4 (Dropout)	(NO, 6, 6, 256)	0
flatten_1 (Flatten)	(NO, 9216)	0
dense_1 (Dense)	(NO, 256)	2359552
dropout_5 (Dropout)	(NO, 256)	0
dense_2 (Dense)	(NO, 256)	65792
dropout_6 (Dropout)	(NO, 256)	0
dense_3 (Dense)	(NO, 10)	2570

Experimental Results and Analysis

In this section, the test of the proposed system for the cleaner robot was conducted. In the test phase, Nano Jetson was used as an image processing and object recognition tool. firstly, Ubuntu Linux was installed, and then the image processing and CNN library were installed on the MicroSD card. In this study, several state-of-the-art CNN models were evaluated to identify the most effective architecture for tree pest and disease detection. The experiments were conducted using the tree image dataset, which includes annotated images of healthy, diseased, and pest-effected leaves. All models were trained under identical conditions, using the same training-validation split, data augmentation strategy, learning rate schedule, and batch size to ensure a fair comparison. The CNN models evaluated included the proposed CNN model, AlexNet, VGG16, VGG19, ResNet50, MobileNetV2, and EfficientNet-B0. The tree dataset was applied to evaluate the performance of the proposed CNN structure. The results of the proposed CNN structure and commonly used CNN models are given in **Table 2**.

Table 2

The results of the CNN models

CNN Models	Evaluation Criteria %			
	AC	PRE	REC	F1-Score
Proposed Model	0.96	0.95	0.96	0.95
AlexNet	0.93	0.92	0.93	0.90
VGG16	0.95	0.93	0.95	0.92
VGG19	0.95	0.94	0.95	0.93
ResNet50	0.94	0.93	0.94	0.92
MobileNetV2	0.92	0.90	0.92	0.87
EfficientNet-B0	0.93	0.91	0.93	0.90

According to the results in Table 2, the proposed CNN structure obtained classification accuracy, precision, recall, and F1-Score of 0.96, 0.95, 0.96, and 0.95, respectively. The performance metrics used to compare the models were accuracy, precision, recall, and F1-score. Across all models, the proposed CNN model consistently outperformed competing architectures in both classification accuracy and robustness across varying lighting conditions and tree types. Specifically, the proposed CNN model achieved the highest overall accuracy, surpassing 96%, while models such as AlexNet, MobileNetV2, and EfficientNet-B0 showed significantly lower accuracy due to their shallower network structures and limited feature extraction capabilities. While deeper models like VGG16 and VGG19 demonstrated competitive accuracy levels, they exhibited slightly higher misclassification rates in images containing heavy shadows or overlapping leaves. ResNet50 also performed well but showed a tendency to overfit during training, indicating less generalization capability on the tree dataset. In addition to accuracy, the proposed CNN model offered an optimal balance between precision and recall. Therefore, the proposed

CNN model outperformed AlexNet, VGG16, VGG19, ResNet50, MobileNetV2, and EfficientNet-B0 models according to F1-score. Although architectures like VGG16 and VGG19 achieved better performance in accuracy, their reduced parameter size led to lower detection precision, particularly for small pests and early-stage disease symptoms. The proposed CNN model, with its well-structured convolutional and pooling layers, delivered consistently high recall values, indicating superior sensitivity in detecting even subtle signs of pest infestation. Furthermore, the confusion matrix of the proposed CNN model revealed fewer false positives and false negatives compared to other models, confirming its reliability for real-time deployment on the autonomous pesticide-spraying robot. This reliability is crucial for precision agriculture applications, where incorrect classifications can result in unnecessary chemical usage or missed pest-infested areas. Overall, the results demonstrate that the proposed CNN model is the most effective CNN model for pest and disease recognition in tree images, offering the best trade-off between accuracy, generalization capability, and operational performance for autonomous agricultural systems.

Conclusion

This study demonstrates the effectiveness of a machine learning-based tree pesticide robot that leverages CNN for precise pest detection and targeted pesticide application. The integration of CNN allows the robot to accurately distinguish between healthy and affected foliage, ensuring efficient and minimal use of chemicals. Experimental results confirm that the CNN-based approach outperforms traditional image processing and other machine learning algorithms in terms of detection accuracy, speed, and adaptability to varying environmental conditions. By enabling autonomous operation, reducing human labor, and promoting sustainable pest management, this system highlights the significant potential of deep learning in modern agriculture. Overall, the proposed framework provides a robust and intelligent solution for precision tree pesticide application, paving the way for more efficient, eco-friendly, and cost-effective agricultural practices.

References

Adesiji, A. D., Ibitoye, S. E., Mahamood, R. M., Olayemi, O. A., Omoniyi, P. O., Jen, T. C., & Akinlabi, E. T. (2025). Safety Considerations in Deployment of Robotic Systems–A Systematic Review. *Journal of Field Robotics*.

Ahmed, W. S. (2020). *The impact of filter size and number of filters on classification accuracy in CNN.* Paper presented at the 2020 International conference on computer science and software engineering (CSASE).

Akkaya, I., Andrychowicz, M., Chociej, M., Litwin, M., McGrew, B., Petron, A., . . . Ribas, R. (2019). Solving rubik's cube with a robot hand. *arXiv preprint arXiv:1910.07113*.

Ayaz, H. I., & Kamisli Ozturk, Z. (2021). A mathematical model and a heuristic approach for train seat scheduling to minimize dwell time. *Computers & Industrial Engineering, 160*, 107590.

Ayaz, H. İ., & Öztürk, Z. K. (2023). Shilling attack detection with one class support vector machines. *Necmettin Erbakan Üniversitesi Fen ve Mühendislik Bilimleri Dergisi, 5*(2), 246-256.

Basha, S. S., Dubey, S. R., Pulabaigari, V., & Mukherjee, S. (2020). Impact of fully connected layers on performance of convolutional neural networks for image classification. *Neurocomputing, 378*, 112-119.

Birk, A. (2011). What is robotics? An interdisciplinary field is getting even more diverse. *IEEE robotics & automation magazine, 18*(4), 94-95.

Cawley, G. C., & Talbot, N. L. (2003). Efficient leave-one-out cross-validation of kernel fisher discriminant classifiers. *Pattern recognition, 36*(11), 2585-2592.

Chen, H., Wang, Y., Xu, C., Shi, B., Xu, C., Tian, Q., & Xu, C. (2020). *AdderNet: Do we really need multiplications in deep learning?* Paper presented at the Proceedings of the IEEE/CVF conference on computer vision and pattern recognition.

Deisenroth, M., & Rasmussen, C. E. (2011). *PILCO: A model-based and data-efficient approach to policy search.* Paper presented at the Proceedings of the 28th International Conference on machine learning (ICML-11).

Erickson, B. J., Korfiatis, P., Kline, T. L., Akkus, Z., Philbrick, K., & Weston, A. D. (2018). Deep learning in radiology: does one size fit all? *Journal of the American College of Radiology, 15*(3), 521-526.

Fourure, D., Javaid, M. U., Posocco, N., & Tihon, S. (2021). *Anomaly detection: How to artificially increase your f1-score with a biased evaluation protocol.* Paper presented at the Joint European conference on machine learning and knowledge discovery in databases.

Gasparetto, A., & Scalera, L. (2019). A brief history of industrial robotics in the 20th century. *Advances in Historical Studies, 8*, 24-35.

Gorriz, J. M., Segovia, F., Ramirez, J., Ortiz, A., & Suckling, J. (2024). Is K-fold cross validation the best model selection method for Machine Learning? *arXiv preprint arXiv:2401.16407*.

Ho, J., & Ermon, S. (2016). Generative adversarial imitation learning. *Advances in neural information processing systems, 29*.

Huu, P. N., Van, D. P., Xuan, T. H., Ilani, M. A., Trong, L. N., Thanh, H. H., & Chi, T. N. (2024). enhancing Additive Digital Manufacturing with supervised classification machine learning algorithms. *The International Journal of*

Advanced Manufacturing Technology, 133(3), 1027-1043.

Karaaltun, M. (2024). Whole image average pooling-based convolution neural network approach for brain tumour classification. *Neural Computing and Applications, 36*(3), 1351-1367.

Kim, Y. S. (2010). Performance evaluation for classification methods: A comparative simulation study. *Expert Systems with Applications, 37*(3), 2292-2306.

Krstinić, D., Braović, M., Šerić, L., & Božić-Štulić, D. (2020). Multi-label classifier performance evaluation with confusion matrix. *Computer Science & Information Technology, 1*(2020), 1-14.

Kocer, S. & Butuner, R. (2021). Pic Microcontroller. In S. Kocer, O. Dundar & R. Butuner (Eds .), *Programmable Smart Microcontroller Cards* (pp. 126 –148). ISRES Publishing.

Levine, S., Finn, C., Darrell, T., & Abbeel, P. (2016). End-to-end training of deep visuomotor policies. *Journal of Machine Learning Research, 17*(39), 1-40.

Levine, S., & Koltun, V. (2013). *Guided policy search.* Paper presented at the International conference on machine learning.

Levine, S., Pastor, P., Krizhevsky, A., Ibarz, J., & Quillen, D. (2018). Learning hand-eye coordination for robotic grasping with deep learning and large-scale data collection. *The International journal of robotics research, 37*(4-5), 421-436.

Liu, L., Shen, C., & van den Hengel, A. (2016). Cross-convolutional-layer pooling for image recognition. *IEEE transactions on pattern analysis and machine intelligence, 39*(11), 2305-2313.

Liu, X. (2012). Classification accuracy and cut point selection. *Statistics in medicine, 31*(23), 2676-2686.

Lu, J., Tan, L., & Jiang, H. (2021). Review on convolutional neural network (CNN) applied to plant leaf disease classification. *Agriculture, 11*(8), 707.

Mahler, J., Liang, J., Niyaz, S., Laskey, M., Doan, R., Liu, X., . . . Goldberg, K. (2017). Dex-net 2.0: Deep learning to plan robust grasps with synthetic point clouds and analytic grasp metrics. *arXiv preprint arXiv:1703.09312*.

Mijwil, M. M., & Aljanabi, M. (2024). A comparative analysis of machine learning algorithms for classification of diabetes utilizing confusion matrix analysis. *Baghdad Science Journal, 21*(5), 24.

Moravec, H. (1988). *Mind children: The future of robot and human intelligence*: Harvard University Press.

Nano, N. J. (2019). NVIDIA Jetson Nano. In.

Nanyonga, A., Joiner, K. F., Turhan, U., & Wild, G. (2025). Deep Learning Approaches for Classifying Aviation Safety Incidents: Evidence from Australian Data. *AI, 6*(10), 251.

Packianathan, R., Arumugam, G., Natarajan, S. K., & Malaiarasan, A. (2024). Machine Vision and Industrial Robotics in Manufacturing. In *Machine Vision and Industrial Robotics in Manufacturing* (pp. 299-313): CRC Press.

Papadopoulos, G. T., Antona, M., & Stephanidis, C. (2021). Towards open and expandable cognitive AI architectures for large-scale multi-agent human-robot collaborative learning. *Ieee Access, 9*, 73890-73909.

Patro, V. M., & Patra, M. R. (2014). Augmenting weighted average with confusion matrix to enhance classification accuracy. *Transactions on Machine Learning and Artificial Intelligence, 2*(4), 77-91.

Peng, X. B., Abbeel, P., Levine, S., & Van de Panne, M. (2018). Deepmimic: Example-guided deep reinforcement learning of physics-based character skills. *ACM Transactions On Graphics (TOG), 37*(4), 1-14.

Piantadosi, C. A. (2003). *The biology of human survival: life and death in extreme environments*: Oxford University Press.

Pu, Q., Li, Y., Zhang, H., Yao, H., Zhang, B., Hou, B., . . . Zhao, L. (2019). Screen efficiency comparisons of decision tree and neural network algorithms in machine learning assisted drug design. *Science China Chemistry, 62*(4), 506-514.

Qi, C. R., Su, H., Mo, K., & Guibas, L. J. (2017). *Pointnet: Deep learning on point sets for 3d classification and segmentation.* Paper presented at the Proceedings of the IEEE conference on computer vision and pattern recognition.

Rayhan, A. (2023). Artificial intelligence in robotics: From automation to autonomous systems. *IEEE Transactions on Robotics, 39*(7), 2241-2253.

Sathyanarayanan, S., & Tantri, B. R. (2024). Confusion matrix-based performance evaluation metrics. *African Journal of Biomedical Research, 27*(4S), 4023-4031.

Sharma, S., Sharma, S., & Athaiya, A. (2017). Activation functions in neural networks. *Towards Data Sci, 6*(12), 310-316.

Sparrow, R., & Howard, M. (2021). Robots in agriculture: prospects, impacts, ethics, and policy. *precision agriculture, 22*(3), 818-833.

Stone, W. L. (2018). The history of robotics. In *Robotics and automation handbook* (pp. 8-19): CRC Press.

Şahin, T. N., & Kölüş, T. (2024). Age and sex estimation in children and young adults using panoramic radiographs with convolutional neural networks. *Applied Sciences, 14*(16), 7014.

Tobin, J., Fong, R., Ray, A., Schneider, J., Zaremba, W., & Abbeel, P. (2017). *Domain randomization for transferring deep neural networks from simulation to the real world*. Paper presented at the 2017 IEEE/RSJ international conference on intelligent robots and systems (IROS).

Ulubaba, H. E., Atik, İ., Çiftçi, R., Eken, Ö., & Aldhahi, M. I. (2025). Deep learning for gender estimation using hand radiographs: a comparative evaluation of CNN models. *BMC Medical Imaging, 25*(1), 1-9.

Vujović, Ž. (2021). Classification model evaluation metrics. *International Journal of Advanced Computer Science and Applications, 12*(6), 599-606.

Wang, Y., Li, Y., Song, Y., & Rong, X. (2020). The influence of the activation function in a convolution neural network model of facial expression recognition. *Applied Sciences, 10*(5), 1897.

Zhao, L., & Zhang, Z. (2024). A improved pooling method for convolutional neural networks. *Scientific Reports, 14*(1), 1589.

Zhu, Y., Mottaghi, R., Kolve, E., Lim, J. J., Gupta, A., Fei-Fei, L., & Farhadi, A. (2017). *Target-driven visual navigation in indoor scenes using deep reinforcement learning*. Paper presented at the 2017 IEEE international conference on robotics and automation (ICRA).

About The Author

Muhammed KARAALTUN received a B.S. degree in Software Engineering from Northern Technique University, Kirkuk, Iraq. He received M.S. and Ph.D. degrees in computer engineering from Selcuk University, Konya, Turkey. His research aims to develop and apply methods for data mining and machine learning and to utilize these methods in robots, embedded systems, and control systems. He has published many research papers in reputed international journals indexed in SCI, SCOPUS, and Web of Science.

E-mail : muhammed.karaaltun@erbana.edu.tr, **ORCID :** 0000-0002-6093-6105

Similarity Index:

The similarity index obtained from the plagiarism software for this book chapter is 18%.

Wireless Motion Detection for Bionic Hands: A Flexible Sensor–Based Real-Time Control Application

Yunus Emre GÖKTEPE
Necmettin Erbakan University

Mehmet TORUN
Necmettin Erbakan University

To Cite This Chapter:
Göktepe, Y. E., & Torun, M. (2025). Wireless motion detection for bionic hands: A flexible sensor–based real-time control application. In S. Kocer & O. Dundar (Eds.), *Next generation engineering: Smart solutions and applications* (pp. 68–77). ISRES Publishing.

Introduction

Advances in human–machine interaction and wearable sensing technologies have significantly transformed the field of prosthetic and robotic hand systems (Mu et al., 2025; R. Yin et al., 2021). Contemporary bionic hand designs aim not only to restore lost physical functions but also to enhance user comfort, mobility, and accessibility (Aszmann et al., 2015). Despite these developments, many existing prosthetic hand solutions remain costly, mechanically complex, and limited by wired communication interfaces. These limitations reduce usability in daily life, restrict movement, and hinder widespread adoption, particularly in low-resource settings. Consequently, there is a growing research need for low-cost, wirelessly controlled, portable, and customizable bionic hand systems capable of replicating human hand movements in real time (Guo et al., 2024).

In this context, the present study introduces a novel wireless motion detection–based bionic hand system that leverages flexible sensors and microcontroller-based wireless communication to enable real-time gesture-controlled actuation. The system consists of a wearable glove equipped with flex sensors, an Arduino Nano–based data acquisition unit, a wireless transmission module, and a tendon-driven robotic hand controlled by an ESP32 microcontroller. The robotic hand features a wooden handcrafted structure, fishing-line tendon mechanisms, and servo motors strategically positioned in a compact 3D-printed housing. This hybrid design ensures low production cost, mechanical robustness, and high adaptability for research, education, and rehabilitation settings.

Real-time wireless communication between the user and the robotic platform minimizes latency, enhances natural movement flow, and improves the overall user experience (Won & Iwase, 2024). As a result, the system represents a promising alternative to traditional tethered prosthetic hands, offering improved mobility, user autonomy, and ease of customization. The open-source software and hardware architecture further broaden its potential for future enhancements, such as machine learning–based gesture recognition, multi-sensor fusion, or electromyography (EMG) integration.

Purpose of the Research

The primary purpose of this research is to develop and evaluate an affordable, portable, and wirelessly controlled bionic hand that can accurately replicate human finger movements in real time using flex sensor–based motion detection. By merging handcrafted mechanical components with modern microcontroller technology, the study aims to:

- Demonstrate a low-cost yet effective alternative to commercially available bionic hands.
- Provide a wireless real-time control mechanism that increases user freedom and system usability.
- Design a tendon-driven robotic hand structure that simplifies mechanical complexity while maintaining functional reliability.
- Offer an open-source, extendable platform for future academic research, clinical rehabilitation studies, and educational robotics projects.

Overall, the research seeks to contribute to the development of accessible bionic technologies that support individuals with limb impairments and promote innovative applications within the field of assistive robotics.

Research Problem

Existing prosthetic and robotic hand systems often face challenges such as high costs, wired communication constraints, complex mechanical architectures, and limited customization options. These limitations hinder their effective use in rehabilitation, daily life activities, and research environments (Batista et al., 2025; Guo et al., 2024). The core research problem of this study is therefore defined as follows:

How can a low-cost, tendon-driven, wirelessly controlled bionic hand be designed and implemented to mimic human hand movements accurately and in real time using flexible sensor–based motion detection?

Bionic Hands and Motion-Detection Technologies

Research on bionic hands has increasingly focused on capturing fine-grained human motion and replicating it through robotic mechanisms (Gu et al., 2022). Systems employing flex sensors, myoelectric sensors, or inertial measurement units are widely used for detecting finger joint angles. Flex-sensor–based methods are particularly appealing due to their low cost, ease of mounting, and reliable analog signal profiles (Tumkur, 2018).

Flex sensors operate based on variable resistance values produced during bending. They are commonly integrated into wearable gloves and provide stable readings suitable for real-time robotic control. Literature strongly emphasizes the importance of signal filtering, calibration, and sensor–motor mapping to achieve smooth and accurate robotic finger movements (Atishay. M et al., 2020).

Arduino, ESP32, and similar microcontrollers play a central role in modern prosthetic systems due to their open-source ecosystem, low cost, and flexible connectivity options (Mick et al., 2024). Wireless modules such as nRF24L01 and ESP32's integrated communication protocols enable high-range, low-delay data transmission, which enhances user mobility and system usability.

Robotic hands frequently employ tendon-driven architectures inspired by the biomechanics of the human hand (Li et al., 2025; Zhou et al., 2024). Fishing-line mechanisms have gained increasing attention due to their high durability, lightweight nature, and ability to mimic natural flexion–extension patterns. Recent studies report successful implementation of such mechanisms in low-cost prosthetic prototypes (Llop-Harillo et al., 2020; Sakthirajan, 2024).

Robotic hands are widely used in therapeutic contexts to support motor recovery, hand-coordination training, and neuromuscular rehabilitation. Wireless systems enhance user engagement by increasing mobility and offering more intuitive control, which has been shown to positively affect therapy efficiency (Toro-Ossaba et al., 2023).

System Architecture and Design

Overall System Structure

The bionic hand system consists of two primary components:

1. **Motion Detection Glove:** Equipped with flex sensors measuring finger-bending motions.
2. **Robotic Hand Unit:** Controlled wirelessly through ESP32 microcontroller and servo motors.

Analog sensor signals are captured by Arduino Nano and transmitted wirelessly to the robotic unit. This architecture ensures minimal latency and provides smooth, real-time response to user gestures.

Mechanical Design: Wood-Based Structure and Tendon Mechanism

The robotic hand is crafted manually from wooden plates shaped to resemble human fingers and palm geometry. An image of the robotic hand at the time of design is given in

Figure 1. Small passage holes and metal anchors—adapted from fishing hook structures—are embedded at joint positions to guide fishing-line tendons. The tendons are attached to servo horns and routed through joint channels to finger tips, enabling naturalistic flexion when the motors rotate. This approach reduces mechanical complexity compared to gear-based systems while preserving robustness and manufacturability.

Figure 1

An image from the design process of the robotic hand.

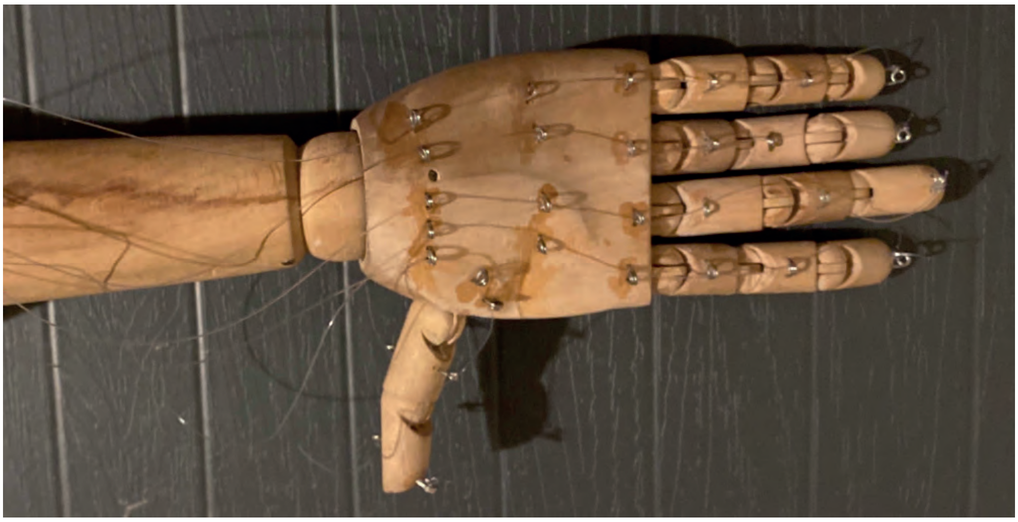

Servo Motor Chamber: Limited 3D Printing Integration

Servo motors (MG996R) are housed in a PLA-based 3D-printed compartment located on the dorsal side of the hand. The printed structure provides proper alignment, vibration resistance, and compact placement for the actuators. Except for this compartment, the entire mechanical assembly is produced through handcrafting, enhancing accessibility and reducing production cost.

Electronic Hardware and Wireless Communication

- The system incorporates:
- Arduino Nano for analog data acquisition (Figure 2.a),
- nRF24L01 module for wireless data transmission (Figure 2.b),
- ESP32 microcontroller for servo control (Figure 2.c),
- MG996R servo motors for finger actuation (Figure 2.d).

Figure 2

Basic electronic elements used in the project; (a) Arduino Nano, (b) nRF24L01 module, (c) ESP32 microcontroller, (d) MG996R servo motor..

a b c d

Wireless communication operates in the 2.4 GHz band and supports high data rates with low latency. The architecture is optimized for delay-free real-time control.

The circuit diagrams of the system to be used on the receiver and transmitter sides of our bionic hand project are shown in Figure 3 and Figure 4.

Figure 3

Receiver side circuit diagram showing the connections of the ESP32 microcontroller, NRF24L01 chip, 5V converter and servo motors.

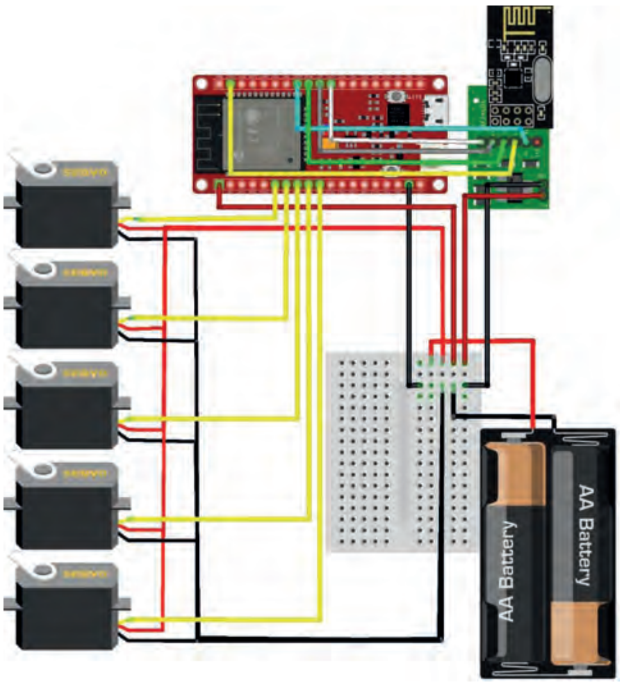

Figure 4

Transmitter side circuit diagram showing the connection of Arduino Nano, Flex sensors, NRF24L01 and 5V converter elements.

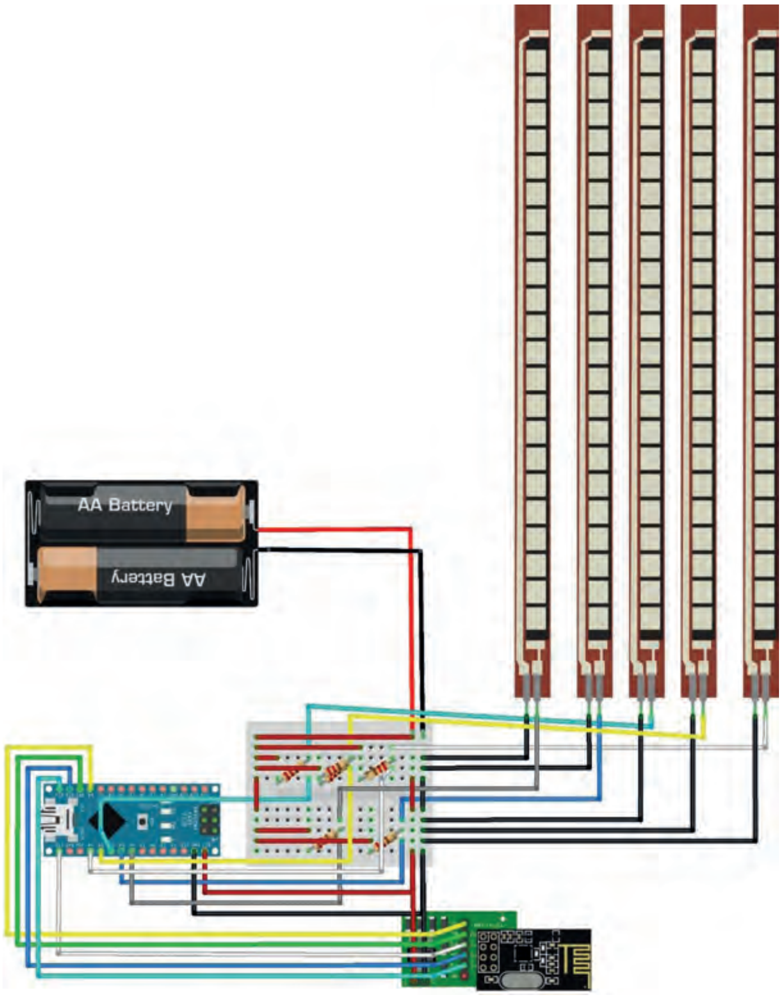

Software Architecture and Control Algorithms

Software was implemented via Arduino IDE. Sensor readings are normalized, minimally filtered, and mapped to servo angles via proportional control logic. To ensure smooth transitions, moving-average filtering is applied, reducing signal noise and enabling natural motion. The ESP32 generates PWM signals in millisecond intervals, maintaining real-time servo responsiveness.

Results and Discussion

The developed system successfully replicates human finger motions through a wireless, low-cost robotic platform. The combination of flex sensors, Arduino-controlled wireless transmission, and servo-driven tendon mechanics provides a coherent and efficient prosthetic architecture. Mechanical experiments confirm that fishing-line tendons provide robust motion with minimal backlash, while wooden structures offer adequate durability and low production cost.

Comparative evaluation with existing systems reveals significant advantages:

- Lower cost due to handcrafted wood and tendon mechanisms,
- Greater portability via wireless control,
- Open-source hardware and software enabling future expansions.

Potential limitations include restricted degrees of freedom compared to advanced commercial prostheses and limited battery capacity in fully mobile configurations. Nevertheless, the system provides a solid foundation for future developments in affordable prosthetic robotics.

Future Integration of Sensor Fusion and Intelligent Control Algorithms

The modular and open-source nature of the presented system provides a suitable foundation for integrating more advanced sensing and control approaches. Sensor fusion techniques combining flex sensors with inertial measurement units (IMUs) or surface electromyography (sEMG) could offer richer motion data and enable more precise gesture classification (Zhang et al., 2026). Such combinations would allow the system to distinguish between subtle motor intentions, partial finger movements, or simultaneous multi-finger gestures—capabilities that are crucial for advanced prosthetic functionality (Krasoulis et al., 2017; Z. Yin et al., 2025).

Machine learning–based gesture recognition is another promising direction (Shahzad et al., 2019). Lightweight neural networks, decision tree–based models, or time-series classifiers running directly on microcontrollers such as the ESP32 could map user motion patterns to predefined hand gestures. This would allow the robotic hand to perform complex actions, including composite grips or adaptive grasp responses, with minimal effort from the user. Real-time adaptation algorithms could further personalize the system by learning from the user's unique movement patterns over time.

Additionally, closing the loop through haptic feedback remains a significant opportunity. Vibrational, pressure-based, or tendon-tension feedback mechanisms would provide users with a sense of touch or grip strength awareness, making the prosthetic system more intuitive and functional. Implementing these features in future research could elevate the system from a low-cost demonstrative platform to a more sophisticated prosthetic prototype with enhanced user engagement.

Conclusion

This chapter introduced a wireless motion detection–based bionic hand system designed to offer an accessible, low-cost, and scalable solution for prosthetic and robotic applications. By integrating flex sensors, wireless communication modules, servo motors, and a tendon-driven wooden hand structure, the system achieves real-time, smooth, and accurate replication of human hand motions.

The proposed design stands out due to its manufacturability, portability, and open-source structure, making it suitable for research laboratories, educational environments, and rehabilitation contexts. Future studies may incorporate advanced machine learning algorithms, adaptive grip control, additional degrees of freedom, and electromyography-based inputs to further enhance functionality and user experience.

Acknowledgement

This book chapter was supported by Necmettin Erbakan University Scientific Research Projects Coordination Unit under Project No. 25LÖKAP31001, titled "Wireless Motion Detection–Based Bionic Hand: Flexible Sensor–Supported Real-Time Control Mechanism."

References

Aszmann, O. C., Roche, A. D., Salminger, S., Paternostro-Sluga, T., Herceg, M., Sturma, A., Hofer, C., & Farina, D. (2015). Bionic reconstruction to restore hand function after brachial plexus injury: A case series of three patients. *The Lancet*, *385*(9983), 2183–2189. https://doi.org/10.1016/S0140-6736(14)61776-1

Atishay. M, D. Mahesh Kumar, Nikhitha. P. Rao, Jyothi. S, Afifa Parveen, & JSS Academy of Technical Education. (2020). Development and Implementation of Real-Time Flex Sensor based Prosthetic Hand. *International Journal of Engineering Research And*, *V9*(04), IJERTV9IS040705. https://doi.org/10.17577/IJERTV9IS040705

Batista, P. G., Vieira, A. C., & Gaspar, P. D. (2025). Robotic Prostheses and Neuromuscular Interfaces: A Review of Design and Technological Trends. *Machines*, *13*(9), 804. https://doi.org/10.3390/machines13090804

Gu, Y., Xu, Y., Shen, Y., Huang, H., Liu, T., Jin, L., Ren, H., & Wang, J. (2022). A Review of Hand Function Rehabilitation Systems Based on Hand Motion Recognition Devices and Artificial Intelligence. *Brain Sciences*, *12*(8), 1079. https://doi.org/10.3390/brainsci12081079

Guo, K., Lu, J., Wu, Y., Hu, X., & Yang, H. (2024). The Latest Research Progress on Bionic Artificial Hands: A Systematic Review. *Micromachines*, *15*(7), 891. https://doi.org/10.3390/mi15070891

Krasoulis, A., Kyranou, I., Erden, M. S., Nazarpour, K., & Vijayakumar, S. (2017). Improved prosthetic hand control with concurrent use of myoelectric and inertial measurements. *Journal of NeuroEngineering and Rehabilitation*, *14*(1), 71. https://doi.org/10.1186/s12984-017-0284-4

Li, H., Ford, C. J., Lu, C., Lin, Y., Bianchi, M., Catalano, M. G., Psomopoulou, E., & Lepora, N. F. (2025). Tactile SoftHand-A: 3D-printed, tactile, highly underactuated, anthropomorphic robot hand with an antagonistic tendon mechanism. *The International Journal of Robotics Research*, 02783649251379516. https://doi.org/10.1177/02783649251379516

Llop-Harillo, I., Pérez-González, A., & Andrés-Esperanza, J. (2020). Grasping Ability and Motion Synergies in Affordable Tendon-Driven Prosthetic Hands Controlled by Able-Bodied Subjects. *Frontiers in Neurorobotics*, *14*, 57. https://doi.org/10.3389/fnbot.2020.00057

Mick, S., Marchand, C., De Montalivet, É., Richer, F., Legrand, M., Peudpièce, A., Fabre, L., Huchet, C., & Jarrassé, N. (2024). Smart ArM: A customizable and versatile robotic arm prosthesis platform for Cybathlon and research. *Journal of NeuroEngineering and Rehabilitation*, *21*(1), 136. https://doi.org/10.1186/s12984-024-01423-9

Mu, G., Zhang, Y., Yan, Z., Yu, Q., & Wang, Q. (2025). Recent advancements in wearable sensors: Integration with machine learning for human–machine interaction. *RSC Advances*, *15*(10), 7844–7854. https://doi.org/10.1039/D5RA00167F

Sakthirajan, N. (2024). *Novel Implementation of Grip Manipulation and Haptic Feedback Into a Prosthetic Arm * SSRN. https://doi.org/10.2139/ssrn.4965605

Shahzad, W., Ayaz, Y., Khan, M. J., Naseer, N., & Khan, M. (2019). Enhanced Performance for Multi-Forearm Movement Decoding Using Hybrid IMU–sEMG Interface. *Frontiers in Neurorobotics*, *13*, 43. https://doi.org/10.3389/fnbot.2019.00043

Toro-Ossaba, A., Tejada, J. C., Rúa, S., & López-González, A. (2023). A Proposal of Bioinspired Soft Active Hand Prosthesis. *Biomimetics*, *8*(1), 29. https://doi.org/10.3390/biomimetics8010029

Tumkur, S. (2018). A Low Cost Prosthetic Hand using Flex Sensors and Servo Motors. *International Journal of Engineering Research*, *6*(13).

Won, J., & Iwase, M. (2024). Highly Responsive Robotic Prosthetic Hand Control Considering Electrodynamic Delay. *Sensors*, *25*(1), 113. https://doi.org/10.3390/s25010113

Yin, R., Wang, D., Zhao, S., Lou, Z., & Shen, G. (2021). Wearable Sensors-Enabled Human–Machine Interaction Systems: From Design to Application. *Advanced Functional Materials*, *31*(11), 2008936. https://doi.org/10.1002/adfm.202008936

Yin, Z., Meng, J., Shi, S., Guo, W., Yang, X., Ding, H., & Liu, H. (2025). A Wearable Multisensor Fusion System for Neuroprosthetic Hand. *IEEE Sensors Journal*, *25*(8), 12547–12558. https://doi.org/10.1109/JSEN.2025.3546214

Zhang, H., Sid'El Moctar, S. M., Boudaoud, S., & Rida, I. (2026). A comprehensive review of sEMG-IMU sensor fusion for upper limb movements pattern recognition. *Information Fusion*, *125*, 103422. https://doi.org/10.1016/j.inffus.2025.103422

Zhou, X., Fu, H., Shentu, B., Wang, W., Cai, S., & Bao, G. (2024). Design and Control of a Tendon-Driven Robotic Finger Based on Grasping Task Analysis. *Biomimetics*, *9*(6), 370. https://doi.org/10.3390/biomimetics9060370

About The Authors

Yunus Emre GÖKTEPE, PhD, is an Assistant Professor at Necmettin Erbakan University. The author's areas of expertise are bioinformatics, artificial intelligence and machine learning. He is still serving as a faculty member of the Department of Computer Engineering, Seydisehir Ahmet Cengiz Engineering Faculty at Necmettin Erbakan University in Konya, Turkey.

E-mail: ygoktepe@erbakan.edu.tr, **ORCID:** 0000-0002-8252-2616

Mehmet TORUN, is an undergraduate student at Seydişehir Ahmet Cengiz Engineering Faculty of Necmettin Erbakan University. His academic interests include bioinformatics, artificial intelligence, and electronic circuit design. He continues his studies in the Department of Computer Engineering at Seydişehir Ahmet Cengiz Engineering Faculty, Necmettin Erbakan University, Konya, Turkey.

E-mail: mehmettorun922@gmail.com, **ORCID:** 0009-0000-0924-6814

Similarity Index:

The similarity index obtained from the plagiarism software for this book chapter is 3%.

A Hybrid Artificial Neural Network Model with Snow Ablation Optimizer Algorithm

Ahmet ÖZKIŞ
Necmettin Erbakan University

Feyza Nur ÖZDEMİR
Doğuş University

To Cite This Chapter:
Özkış, A., & Özdemir, F. N. (2025). A hybrid artificial neural network model with snow ablation optimizer algorithm. In S. Kocer & O. Dundar (Eds.), *Next generation engineering: Smart solutions and applications* (pp. 78-119). ISRES Publishing.

Introduction

Metaheuristic algorithms are problem-solving methods developed by scientists inspired by physical events in nature and the food-seeking and survival behaviors of living things. Thanks to their flexible structure, metaheuristic algorithms can be successfully applied to solve many real-world problems such as numerical optimization (Deng & Liu, 2023; Karaboga & Akay, 2009; Uymaz, Tezel, & Yel, 2015), uncapacitated facility location problems (Cinar & Kiran, 2018; Özkış & Karakoyun), wind turbine placement (Aslan, Gunduz, & Kiran, 2023; Çelik, Yıldız, & Şekkeli, 2018), knapsack (Kong, Tian, & Kao, 2008), assessment of higher education (Towfek, Khodadadi, Abualigah, & Rizk, 2024) and training of artificial neural networks (ANN) (Irmak, Karakoyun, & Gülcü, 2023; Karaboga & Akay, 2007; Mirjalili, 2015). Although many metaheuristic algorithms have been developed to date, new algorithms are still being proposed based on the idea in the No Free Lunch (NFL) (Wolpert & Macready, 1997) theorem that no algorithm can guarantee to reach the most successful result in all problem types. The snow ablation optimizer (SAO) algorithm is one of the current algorithms in this field proposed by Deng and Liu (2023) in 2023, inspired by the physical events that occur during snow melting.

ANN is an algorithm that can learn to perform actions that the human brain can do and produce similar outputs. It has the characteristics of biological neural networks, such as the ability to learn, derive new rules from the information it learns, and explore (Öztemel, 2003). When the literature is examined, it is seen that ANN is used to solve many real world problems (Bui, Nguyen, Ngo, & Nguyen-Xuan, 2020; Chen et al., 2021; Darshan et al., 2021; Kandel et al., 2023; Öztemel, 2003; Sada, 2021). ANN is composed of structures called neurons. In the mathematical modeling of ANN, each neuron is multiplied by a numerical value called weight and goes to the summation function. Then, the result is obtained by going to the activation function. This process performed by the

ANN is called forward propagation. The process of updating weight values with new values is called backpropagation. Derivative-based techniques are generally used in the updating of weights during backpropagation. However, these techniques can sometimes get stuck in local minimum points. To overcome this problem, researchers benefit from metaheuristic algorithms (Mirjalili, 2015).

This study proposed a new LevySAO algorithm using the SAO and the Levy flight mechanism. The proposed LevySAO algorithm was used to update the weight values of the ANN to eliminate the problem of ANN getting stuck in local minima. The developed ANN-LevySAO hybrid model was used in training 15 different classification data sets – aggregation, aniso, balance, ecoli, glass, iris, iris2D, liver, mouse, pathbased, seeds, smiley, varied, vertebral3 ve wine – which are well known in the literature. The success of the model was calculated based on sensitivity, specificity, precision and f1-score metrics. The results of the proposed model were compared with hybrid ANN models developed with 12 different metaheuristic algorithms – AAA, AVOA, CS, DEA, GWO, HBA, MGO, MPA, Puma, RSA, SAO, SCA – that are well known in the literature. The success of the models was ranked according to the obtained metric values and the average success rank (ASR) in all data sets was calculated according to the Friedman test.

According to the ASR values, it is seen that the ANN-LevySAO hybrid model achieved the best ASR value in three of the four metrics (specificity, sensitivity and f1- score). In addition, in one-to-one performance comparisons, the proposed ANN-LevySAO model is the winner in 143 of 180 comparisons for the sensitivity metric, in 146 of 180 comparisons for the specificity metric, in 137 of 180 comparisons for the precision metric, and in 143 of 180 comparisons for the f1-score metric. Hence, one-to-one comparisons showed that the proposed model was much more successful than other models. In addition, the Wilcoxon's signed-rank test results at a 95% confidence interval showed that the proposed model produces statistically significant results in most cases. In summary, it is seen that the proposed model is superior to the compared models in many aspects.

The remainder of the work is organized as follows: Section 1.1 includes a literature summary of studies in which metaheuristic algorithms and ANN are used together. In Section 2, the history and working principle of ANN are explained. Section 3 includes information about the SAO algorithm. In Section 4, the Levy Flight method and the proposed LevySAO algorithm are explained. While the experimental studies are presented in Section 5, the results and recommendations are included in Section 6.

Literature Review on Usage of Metaheuristic Algorithms on Artificial Intelligence Problems

It can be seen in the literature that there are many studies in which ANN and metaheuristic algorithms are used hybridly. Karaboga and Akay (2007) compared the performances of artificial bee colony (ABC), differential evolution (DE) and particle swarm optimization (PSO) algorithms by using them in ANN training. Qiao, Khishe, and Ravakhah (2021) developed the whale optimization algorithm (WOA) and used it to train ANN. Gülcü (2022), developed the DA-MLP model by training the ANN with the dragonfly algorithm (DA) to prevent it from getting stuck at local optimum points. Turkoglu and Kaya (2020) ,trained the ANN with the artificial algae algorithm (AAA) and analyzed its performance on 10 different data sets in the UCI data set. (Maleki, Ghazvini, Ahmadi, Maddah, & Shamshirband, 2019), used ANN and genetic algorithm (GA) to predict moisture in dryers. Aljarah, Faris, and Mirjalili (2018) used WOA in optimizing the connection weights of ANN. Özden and İşeri (2023), developed a hybrid model using the COOT optimization algorithm to prevent the problem of derivative-based techniques getting stuck in local optimum during the ANN training phase. Bairathi and Gopalani (2021) developed the salp swarm algorithm (SSA) and used it in training feedforward neural networks. Kaya (2022), made a comprehensive performance comparison by training ANN with 16 different metaheuristic algorithms such as ABC, cuckoo search (CS) algorithm, PSO, JAYA, sine cosine algorithm (SCA) and WOA. Song, Meng, and Jiang (2022), used the MLP model (EGWO-MLP), which they developed with the elastic gray wolf optimization algorithm, to predict the success of students. J. Li, Soradi-Zeid, Yousefpour, and Pan (2024), used neural networks and differential evolution (DE) algorithm together for emotion recognition in music.Thankachan, Fida, and Pillai (2024) monitored the health of steel structures using a CS-based ANN model. Narayanan, Kasiselvanathan, Gurumoorthy, and Kiruthika (2023) developed the ANN-PSO hybrid model to address the vulnerability of wireless sensor networks, attack detection and prevention. Ansari, Ahmad, Bakar, and Yaakub (2020), trained ANN with magnetic optimization and PSO algorithms to predict the probability of bankruptcy of companies and achieved successful results.

ANN and metaheuristic algorithms are also widely used in solving civil engineering problems. Kazemi, Golafshani, and Behnood (2023) used the ACO+ANN and PSO+ANN models they developed to predict the compressive strength of concrete containing waste foundry sand. Wu, Mei, and Zhao (2023), used an ANN model based on improved whale optimization algorithm (IWOA) to detect damages in pipelines. Tran-Ngoc, Khatir, De Roeck, Bui-Tien, and Wahab (2019), used an ANN model whose training parameters were determined by the CS algorithm to detect damages in bridges and beams. Bui, Nguyen, Chou, Nguyen-Xuan, and Ngo (2018) utilized a modified firefly algorithm (MFA)-based ANN model to predict the compressive and tensile strength of high-performance concrete.

Similar studies have been conducted on the estimation of energy consumption. Chen et al. (2021) developed an ANN and GWO-based model to obtain the optimum operational variables of solid oxide fuel cells and demonstrated that this model reduces the production cost. Bui et al. (2020), developed an ANN model based on electromagnetism-based firefly algorithm (EFA) to predict energy consumption costs in buildings. Talaat, Farahat, Mansour, and Hatata (2020), developed a feed-forward ANN model with the grasshopper optimization algorithm (GOA) to aid in energy production and electricity purchasing planning.

ANN and metaheuristic algorithms are also used in the field of health. Thamaraimanalan and Ramalingam (2024), developed an ANN-grasshopper optimization algorithm (ANN-GOA) model to find abnormal data due to frequent malfunctions of body-worn sensors and the accuracy of the data obtained cannot be understood. Si, Bagchi, and Miranda (2022), used the equilibrium optimizer (EO) algorithm in ANN training for use in medical data classification problems. Zamani and Nadimi-Shahraki (2024), developed an ANN model optimized with the evolutionary crow search algorithm (ECSA) to be used in the diagnosis of chronic diseases. Gong, Gao, and Abza (2020), developed an ANN model using a chaos-based improved WOA to accurately detect the brain tumor site. El-kenawy et al. (2024) proposed a greylag goose optimization (GGO) algorithm and performance analysis of the GGO was conducted on 19 datasets from the UCI repository. Abdollahzadeh et al. (2024) suggested a puma optimizer (PO) algorithm and applied the PO on benchmark and clustering problems.

Literature Review on the SAO Algorithm

Jia et al. (2023), improved the original SAO algorithm by using heat transfer and condensation strategy, considering that with the increase in temperature, water molecules will turn into water vapor and may disrupt the balance between exploration and exploitation. They demonstrated the success of the algorithm they developed by testing it on various benchmarks and engineering problems. Ismaeel et al. (2024), benefited from the SAO algorithm for the optimal placement of generator units. In the study where 6 situations were discussed, it was aimed to minimize the optimum power mismatch values using the SAO algorithm by using 6 generators in 2 loads of 700-1000 MW, 10 generators in 2 loads of 1000-2000 MW and 20 generators in 2 loads of 2000-3000 MW. The study revealed that the SAO reduces fuel cost compared to other algorithms. Since the SAO is a recently proposed algorithm, studies in the literature are limited.

Main Motivation of the Study

In this study, a new metaheuristic algorithm, SAO, is used to optimize the weight and bias values in the artificial neural network. There are different studies in the literature suggesting solutions to the problem of optimizing the weight and bias values in ANN. However, these solutions has some advantages and disadvantages. For this reason, researchers continue to suggest new approaches to solve this problem. SAO is a recently proposed metaheuristic algorithm and has achieved successful results on mathematical benchmark problems. According to our research, there is no comprehensive study using the SAO algorithm in optimizing the weight and bias values in ANN. The main motivation of this study is to eliminate this deficiency in the literature. In this study, a hybrid model (ANN-SAO) was developed to optimize the weight and bias values by using the SAO algorithm together with ANN. In addition, a new modification (LevySAO) that strengthens the local search capability of SAO with Levy flight mechanism was suggested and the LevySAO-ANN hybrid model was developed. The LevySAO-ANN model was run on 15 different classification datasets and performance comparisons were made with 12 different models. Thus, a comprehensive result set was produced for future studies.

Artificial Neural Networks (ANN)

The term Artificial Neural Networks (ANN) has been researched since the early 1900s. In a study conducted by McCulloch and Pitts (1943), they talked about the nervous system and, accordingly, neural networks in neurophysiological terms. Thus, a mathematical model of neural networks was created for the first time. They made a great impact with the work they published. Although Anderson and McNeill (1992), say that ANN cannot do everything and that it is misunderstood by some authors, it is possible to do many things with ANN with today’s technology.

Artificial Neural Networks are systems very similar to biological neural networks. The smallest unit of ANN is called artificial nerve cell. The attributes of the problem that the artificial intelligence system wants to learn are given as input to the artificial nerve cell. These inputs are multiplied by other numerical values called weights and go to the summation function, where the net input is calculated. Once the net input is calculated, it goes to the activation function, then the result is obtained. In Figure 1, an artificial neuron; input, output, summation function, activation function, weight and bias values are shown (Öztemel, 2003).

Figure 1

Basic Components of an Artificial Neural Network

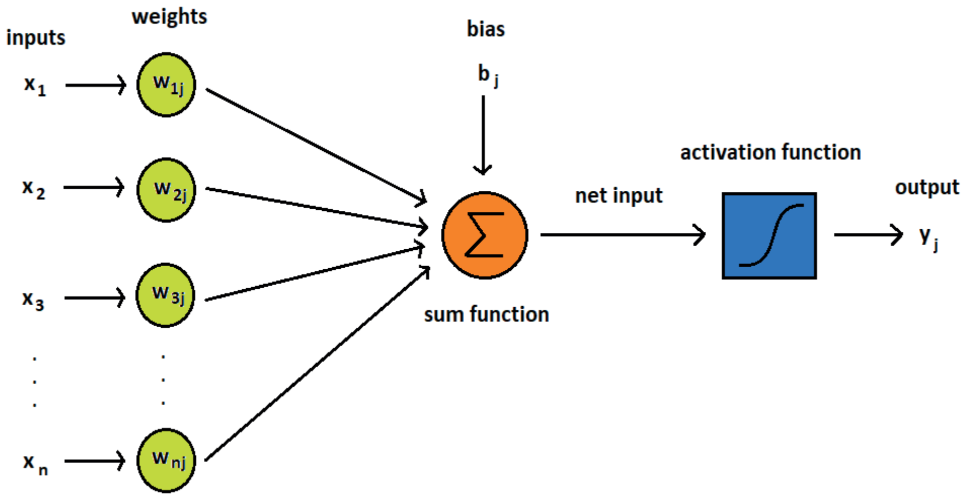

ANN architecture is divided into two: Single Layer Perceptron (SLP) and Multi-Layer Perceptron (MLP). The image in Figure 1, explains the structure of a nerve cell and SLP architecture in its simplest form.

Figure 2

Multi-Layer Perceptron Architecture

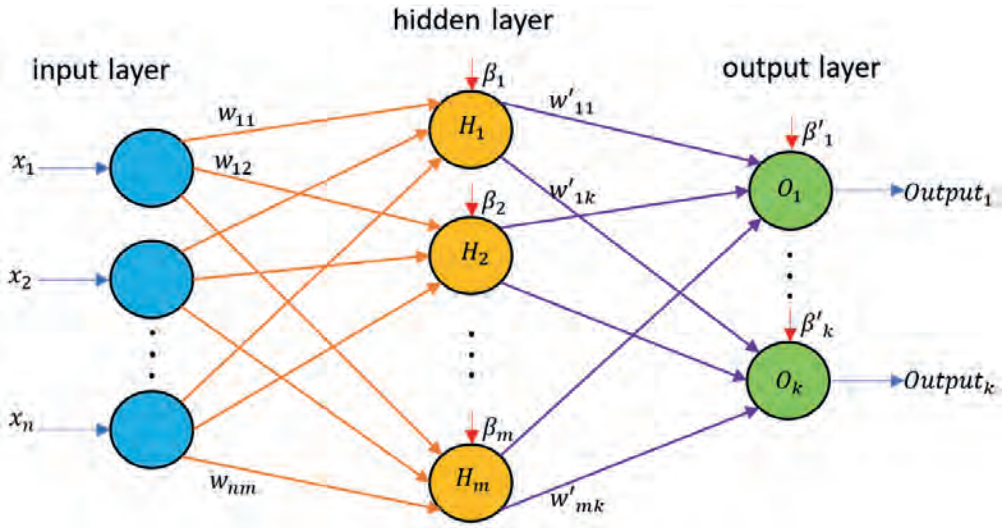

The image in Figure 2 is an example of an MLP architecture. The MLP architecture consists of input, hidden and output layers. There is no exact information about the number of neurons in the intermediate layer and how many intermediate layers should be. In this study, the number of neurons in the intermediate layer was calculated by the method in Equation 1 used by Turkoglu and Kaya (2020) and Mirjalili (2015).

$$NumberOfNeuronsInHiddenLayer = 2 * NumberOfAttributes + 1 \quad (1)$$

ANNs are self-learning mechanisms without the need for human power (Anderson & McNeill, 1992). Although it is not fully known what exactly affects its performance, many studies have revealed that various factors such as the training algorithm, data set pre-processing, and correct setting of parameters can affect its performance (Ataseven, 2013). The first studies about ANN were on SLP architecture. However, when it was realized that SLPs could only learn linear problems, the MLP architecture, which can also learn non-linear problems, was born. Nowadays, many studies are carried out with MLP architecture (Gupta & Deep, 2020) (P. Li, Zhang, Gu, & Duan, 2024) (Raziani, Ahmadian, Jalali, & Chalechale, 2022). MLP architecture was used in this study.

$$Net\ Input = Net(previous) + \sum_{i} (G_i A_i) \tag{2}$$

$$f(Net) = \frac{1}{1 + e^{-Net}} \tag{3}$$

There are many addition and activation functions in the literature. In this study, the summation function given in Eq. 2 was preferred as the accumulation function, and the sigmoid function given in Eq. 3 was preferred as the activation function. After this movement, known as the forward propagation, if the data cannot be classified correctly, the weights are updated with the help of some processes. The process of updating the weights is called backpropagation.

After forward propagation in the training phase, the ANN architecture checks the real class labels in the data set and predicted class labels. Accordingly, it calculates an error value for each sample. In this study, the mean squared error (MSE) method given in Eq. 4 was used to calculate the error.

$$MSE = \frac{1}{r}\sum_{i=1}^{r} \sum_{j=1}^{k} (y_j - \hat{y}_j)^2 \tag{4}$$

Here r is the number of samples in the training set, k is the number of class labels, y is the expected value for the jth output, and $\hat{y}$ is the value predicted by ANN for the jth output. The number of neurons in the layers was set as follows:

- Input Layer: It is determined by the number of attributes in the data set.
- Hidden Layer: It is calculated according to Eq. 1.
- Output Layer: It is determined by the number of classes in the data set.

Hybrid Use of Artificial Neural Networks and Metaheuristic Algorithms

In ANN, gradient-based techniques are generally used to update the weights during backpropagation. As the difficulty level of the problems increases, gradient-based techniques may encounter the problem of getting stuck in local minima and produce unsuccessful results. To overcome this problem, researchers (Gülcü, 2022; Mirjalili, 2015; Özkış, 2024) update the weight values by using metaheuristic algorithms.

The vector of weight values of ANN constitutes the decision variables of metaheuristic algorithms. This situation is shown in Figure 3.

Figure 3

Modeling of Weights as Vectors

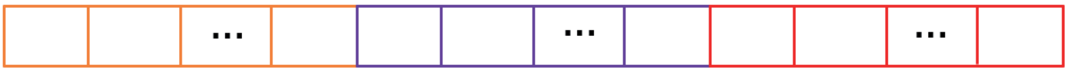

In hybrid models developed by using metaheuristic algorithms, the MSE value given in Eq. 4 is used as the objective function. In this study, a new model is proposed by using the recently proposed SAO algorithm as a hybrid with ANN.

Snow Ablation Optimizer (SAO) Algorithm

Snow Ablation Optimizer (SAO) algorithm is a new metaheuristic algorithm proposed in 2023 (Deng & Liu, 2023). SAO is a nature-inspired algorithm mimicking snow turning into water, water turning into steam, and snow turning into steam through direct sublimation. Sublimation means that solid substances melt with heat and turn into a gas without turning into a liquid.

Figure 4

States of Snow in Nature (Deng & Liu, 2023)

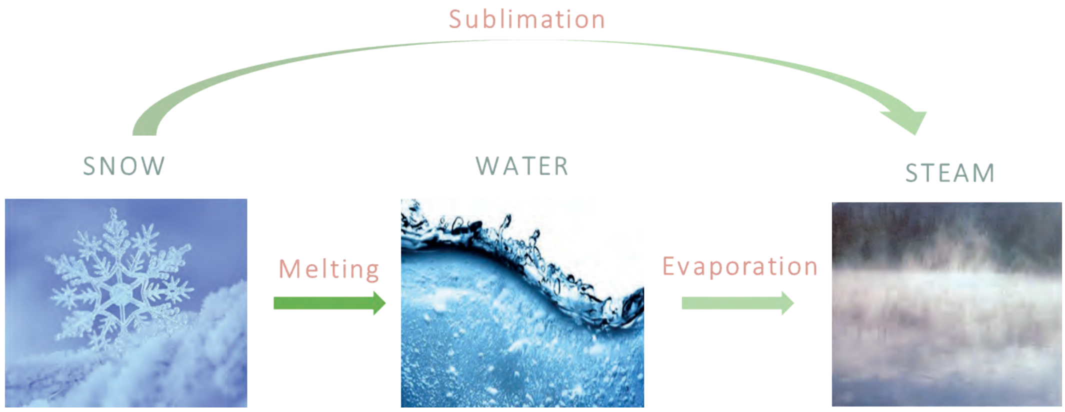

One of the biggest shortcomings in metaheuristic algorithms is the imbalance between exploration and exploitation. SAO is an algorithm created to balance these two situations (Deng & Liu, 2023). The SAO algorithm has four main phases: i) initiation phase, ii) exploration phase, iii) exploitation phase and iv) dual population creation phase.

Initialization Phase: The population is initialized randomly within the boundaries of the search space by Eq. 5.

$$Z = L + \theta \times (U - L) = \begin{bmatrix} z_{1,1} & z_{1,2} & \cdots & z_{1,Dim-1} & z_{1,Dim} \\ z_{2,1} & z_{2,2} & \cdots & z_{2,Dim-1} & z_{2,Dim} \\ \vdots & \vdots & \vdots & \vdots & \vdots \\ z_{N-1,1} & z_{N-1,2} & \cdots & z_{N-1,Dim-1} & z_{N-1,Dim} \\ z_{N,1} & z_{N,2} & \cdots & z_{N,Dim-1} & z_{N,Dim} \end{bmatrix}_{N \times Dim} \quad (5)$$

Here *Z* is a matrix representing the population. *N* is the number of agents in the population, *Dim* is the problem dimension, *L* is the lower bound value of the search space, *U* is the upper bound value of the search space, and θ is an *NxDim* dimensional matrix consisting of random numbers in the range [0, 1].

Exploration Phase: When snow or water evaporates it begins to disperse unevenly. The Brownian motion given in Eq. 6 simulates this irregular distribution.

$$f_{BM}(x;0,1) = \frac{1}{\sqrt{2\pi}} \times exp(-\frac{x^2}{2}) \quad (6)$$

The Brownian motion shown in Figure 5 is a type of random motion. It is an unpredictable process that occurs as a result of the constant collision of particles, especially in liquids and gases, with surrounding molecules.

Figure 5

Brownian Motion

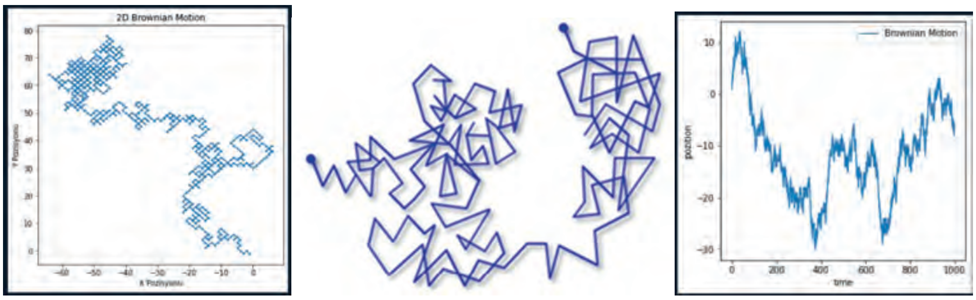

The positions of search agents in the population are updated using Brownian motion as in Eq. 7.

$$Z_i(t+1) = Elite(t) + BM_i(t) \otimes (\theta_1 \times (G(t) - Z_i(t)) + (1-\theta_1) \times (\underline{Z}(t) - Z_i(t))) \quad (7)$$

Here, $i = 1, 2, \ldots, N$ represents the index of the updated agent, *t* represents the current iteration, $BM_i(t)$ represents the Brownian motion, $\otimes$ represents the product of the inputs θ_1 represents a randomly generated number in the range [0,1]. *G(t)* represents the best solution obtained so far, and *Z(t)* represents the vector containing the average of the column-based weights of the population. The average of the positions of the three best-fit individuals and the *N*/2 best-fit individuals is kept in a matrix called the *ElitePool*. *Elite(t)* refers to a randomly selected solution from the *ElitePool*. In this way, elite individuals also play an active role in determining the position.

Exploitation Phase: Imitates the behavior of snow turning into water. At this stage, instead of spreading in the search space, the aim is to perform a local search with the help of the best available solutions. In the exploitation phase, the population is updated with Eq. 8.

$$Z_i(t+1) = M \times G(t) + BM_i(t) \otimes (\theta_2 \times (G(t) - Z_i(t)) + (1-\theta_2) \times (\underline{Z}(t) - Z_i(t))) \quad (8)$$

Here, M represents the snow melt rate and θ_2 represents a random number in the range [-1, 1]. The snow melt rate is expressed by Eq. 9.

$$M = (0.35 + 0.25 \times \frac{e^{\frac{t}{t_{max}}} - 1}{e - 1}) \times T(t), T(t) = e^{\frac{-t}{t_{max}}} \quad (9)$$

Here, t_{max} represents the termination criterion, *e* represents the Euler number, and *T* represents the daily average temperature.

Dual Population Creation Phase: This phase aims to create a balance between exploration and exploitation. Some of the snow that turns into water may evaporate during the search and lose its centrality. To ensure this balance, a dual population structure was created. At the beginning of the search process, the population is randomly divided into two subpopulations consisting of equal numbers of search agents. The first of the subpopulations ($index_a$) is responsible for exploration, and the second ($index_b$) is responsible for exploitation. In each iteration, the number of agents of the second subpopulation is reduced by one, while the number of agents in the other is increased by one.

The location update equations in the exploration and exploitation phases are shown together in Eq. 10.

$$Z_i(t+1) = \{Elite(t) + BM_i(t) \otimes (\theta_1 \times (G(t) - Z_i(t)) + (1-\theta_1) \times (\underline{Z}(t) - Z_i(t))), i \in index_a \; M \times G(t) + BM_i(t) \otimes (\theta_2 \times (G(t) - Z_i(t)) + (1-\theta_2) \times (\underline{Z}(t) - Z_i(t))), i \in index_b \quad (10)$$

The pseudo code of the SAO algorithm is presented in Figure 6.

Figure 6

Pseudo Code of the SAO Algorithm (Deng & Liu, 2023)

To start, the number of individuals in the herd, weight, and tolerance value are determined: $Z_i \; (i = 1,2,\dots,N), t = 0, t_{max}, N_a = N_b = \frac{N}{2}$

Fitness function evaluation is performed.

The best individual available is recorded.

While (t <t_{max})

Snow melt rate is calculated with Eq. 9.

The entire population is randomly split into two subpopulations named N_a and N_b.

Foreach (Individual)

The position of each individual is updated with Eq. 10.

End Foreach

Fitness function evaluation is performed.

The best individual is updated.

End While

Proposed LevySAO Algorithm

In the original SAO algorithm, the population is divided into two at the beginning of the search process, and the first subpopulation (N_a) is responsible for exploration while the second subpopulation (N_b) is responsible for exploitation. At the eazrnd of each iteration, the subpopulation responsible for exploitation decreases by one individual, while the population responsible for exploration increases by one individual. After a while, the number of individuals in the subpopulation containing individuals responsible for exploitation is reset to zero, and the number of individuals in the subpopulation containing individuals responsible for exploration is equal to the total population number. From this stage, the algorithm updates the positions of the particles using only the exploration model. In the SAO algorithm, exploration refers to the searching process around a group of solutions called the elite pool, under the guidance of the general best solution and a central solution that is the average of all solutions (Deng & Liu, 2023). Detailed research conducted for this study shows that at the beginning of the search process, the searches conducted under the guidance of the general best and central solution contribute to the discovery of new solutions, as the iterations progress all solutions become similar to each other and the discovery process becomes stagnant. Since the SAO algorithm does not have a mechanism to eliminate this stagnation, it gets stuck in a local minimum and cannot maintain its success until the last iterations (Jia et al., 2023).

Levy flight is a type of random walk developed in 1937 by a French mathematician Paul Levy. There are many random walk movements in mathematics and modeling. Unlike these movements, Levy Flight determines the step length according to a power law. Levy flight is used to model so-called anomalous propagations (Brown, Liebovitch, & Glendon, 2007). The step length of the Levy flight is determined according to the Levy distribution in Eq. 11.

$$L(s,\gamma,\mu) = \begin{cases} \sqrt{\frac{\gamma}{2\pi}}\, exp\left(-\frac{\gamma}{2(s-\mu)}\right)\frac{1}{(s-\mu)^{\frac{3}{2}}} & 0 < \mu < \infty \\ 0, & otherwise \end{cases} \quad (11)$$

where μ and s are the transmission parameters and samples, respectively. The step length of the Levy flight is calculated with $s = \frac{u}{|v|^{\frac{1}{\beta}}}$. Here, the variables u and v are follow a normal distribution, and β is a fixed parameter (Y. Gao, Zhang, Duan, & Zhang, 2023).

Many animal species use Levy Flight in their foraging strategy. Levy Flight has also been used to improve the performance of many metaheuristic algorithms (Bhullar, Kaur, & Sondhi, 2022; J. Gao, Gao, Ma, Huang, & Yang, 2021; Jamal et al., 2023; Mohseni, Brent, Burmester, & Browne, 2021; Saji & Barkatou, 2021). In the proposed algorithm, a new position update mechanism has been used to overcome stucking into local minima problem of the original SAO. This mechanism is given in Eq. 12.

$$Z_i(t+1) = Elite(t) + 0.01 * LF(1, Dim, 1) \quad (12)$$

Here, LF represents the Levy flight and *Dim* represents the number of dimensions of the problem.

The proposed LevySAO algorithm continues to utilize the Levy flight-enhanced position update mechanism given in Eq. 12 as well as the position update mechanism of the original SAO given in Eq. 7. Which mechanism will be used on the $N_a N_a$ subpopulation is determined by the LevyProb parameter. For each particle, a random number in the range [0, 1] is generated. If the generated number is greater than the LevyProb parameter, the position update mechanism in the original SAO algorithm in Eq. 7 is used, otherwise, the position update mechanism utilizing the Levy flight in Eq. 12 is used. For the LevySAO algorithm to be successful, the LevyProb parameter must take an appropriate value. For this purpose, as a result of the parameter tuning study conducted in Section 5.3, the LevyProb value was determined as 0.9. In the $N_b N_b$ subpopulation, the position update mechanism of the original SAO algorithm given in Eq. 8 is used. The pseudo-code of the proposed algorithm is shown in detail in Figure 7. The flowchart is presented in Figure 8.

Figure 7

Pseudo Code of the LevySAO Algorithm

```
To start, the number of individuals in the herd, weight, and tolerance value are determined:
Z_i (i = 1,2,...,N), t = 0, t_max, N_a = N_b = N/2, levyProb = 0.9
Fitness function evaluation is performed.
The best individual available is recorded.
While (t < t_max)
    Snow melt rate is calculated with Eq. 9.
    The entire population is randomly split into two subpopulations named N_a and N_b.
    Foreach (individual)
            Random number is selected between [0,1].
            If random number > levyProb
                The position of the individuals in the N_a group is updated according to Eq. 7. //Position update
            mechanism of the original SAO algorithm
            Else
                The position of the individuals in the N_a group is updated according to Eq. 12. //Position update
            mechanism utilizing Levy flight
          End If
          The position of the individuals in the N_b group is updated according to Eq. 8.
    End Foreach
    Fitness function evaluation is performed.
    The best individual is updated.
End While
```

Figure 8

Flowchart of the LevySAO Algorithm

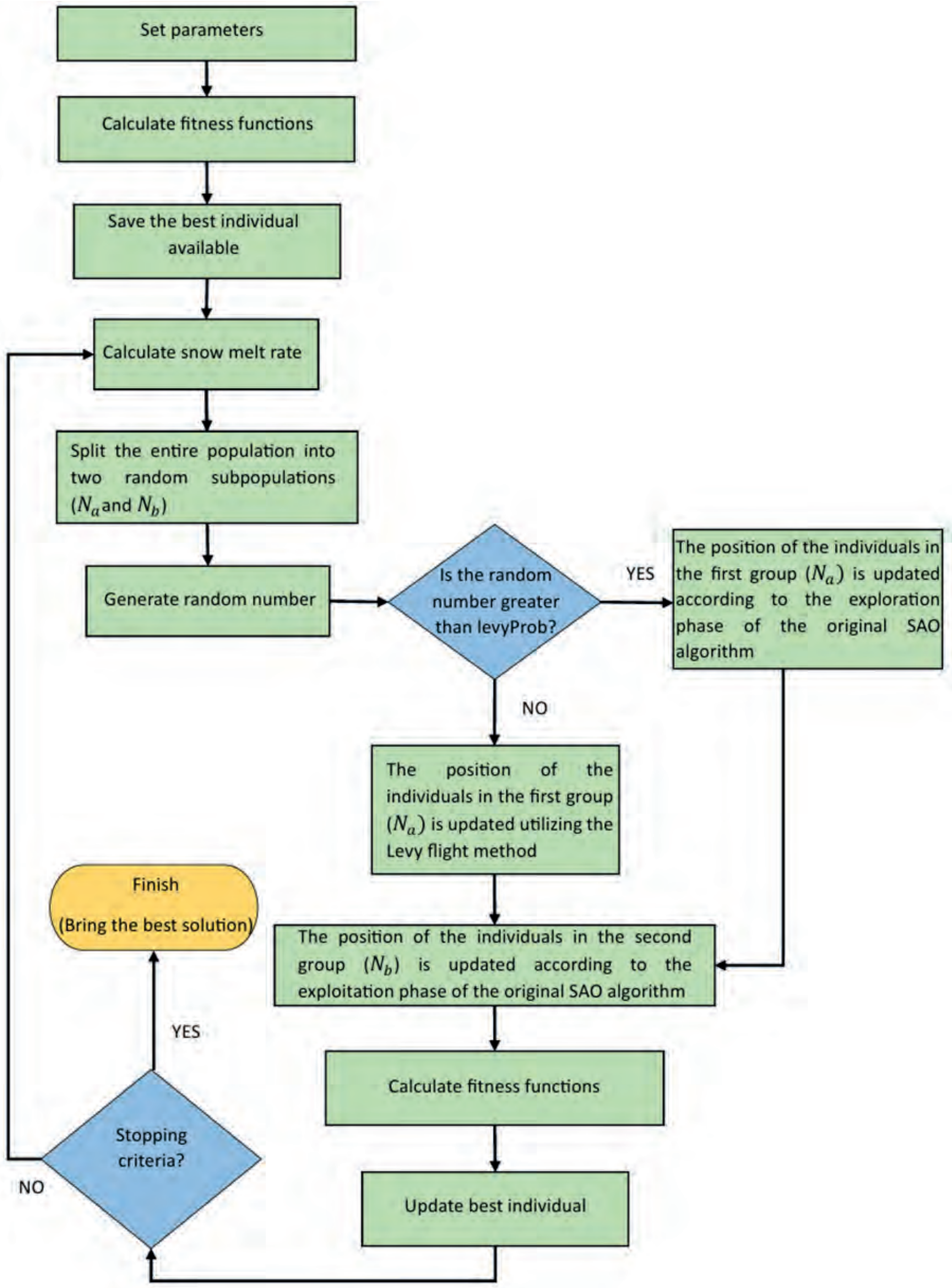

In this study, all experiments were run using the criteria in Table 1 and the performances of the models were scored through sensitivity, specificity, precision and F1-score metrics. Obtained metric values were evaluated according to average success rank and one-to-one performance comparison. The Wilcoxon signed-rank test was applied to evaluate whether the results obtained by the proposed model were statistically significant. In the study, the MSE function given in Eq. 4 was used as the objective function.

Table 1

Running Criteria

population size	50
lower bound - upper bound	[-10,10]
maximum fitness evolution	20,000
iteration number	400
runtime	30

Detailed information and results about the experimental studies are presented below.

Datasets

In the study, 15 different classification datasets named aggregation, aniso, balance, ecoli, glass, iris, iris2D, liver, mouse, pathbased, seeds, smiley, varied, vertebral3 and wine from the UCI Machine Learning Repository (Markelle Kelly) and the literature (Qaddoura, Faris, Aljarah, & Castillo, 2021) were used. Datasets are divided into 75% training and 25% testing. If the number of samples was less than 150, the entire dataset was used in both the training and testing process. Detailed information about the datasets is presented in Table 2.

Table 2

Datasets Used in This Study

Dataset No	Dataset Name	Sample Size	Train Data	Test Data	Attribute No	Class No
1	aggregation	788	594	194	2	7
2	aniso	1500	1125	375	2	3
3	balance	625	469	156	4	3
4	ecoli	336	252	84	7	7
5	glass	214	162	52	9	6
6	iris	150	150	0	4	3
7	iris2D	150	150	0	2	3
8	liver	345	259	86	6	3
9	mouse	490	368	122	2	3
10	pathbased	400	226	74	2	3
11	seeds	400	226	74	2	3
12	smiley	500	375	125	2	4
13	varied	1500	1125	375	2	3
14	vertebral3	310	233	77	6	3
15	wine	178	133	45	13	3

Performance Metrics

Confusion matrix is a performance measurement method that is used frequently in the literature to measure the accuracy of the model and the classification success of datasets. In the confusion matrix, various calculations are made based on the predicted class label and the actual class label, according to the situations given in Figure 9.

Figure 9

Confusion Matrix

		Predicted: Negative	Predicted: Positive
Actual	Negative	True Negative (TN)	False Positive (FP)
	Positive	False Negative (FN)	True Positive (TP)

If the predicted class is positive and the real class is positive, it is called True Positive (TP), and if the predicted class is negative and the real class is negative, it is called True Negative (True Negative, TN). If the estimated class is positive and the real class is negative, it is called False Positive (False Positive FP), and if the estimated class is negative and the real class is positive, it is called False Negative (False Negative, FN). One of these four situations occurs for each sample in the dataset. According to the number of occurrences of these situations, sensitivity, specificity, precision and f1-score metrics are calculated as in Eq. 13-16.

$$\text{Sensitivity} = \frac{TP}{TP+FN} \tag{13}$$

$$\text{Specificity} = \frac{TN}{TN+FP} \tag{14}$$

$$\text{Precision} = \frac{TP}{TP+FP} \tag{15}$$

$$\text{F1-score} = 2 * \frac{Sensitivity * Precision}{Sensitivity + Precision} \tag{16}$$

- Sensitivity is obtained by dividing the true positive values by the total true positive values. It provides information about the proportion of correct predictions among the values belonging to the positive class.
- Specificity is obtained by dividing the true negative values by the total true negative values. It shows how much of the true negative values the model correctly predicts.
- Precision is obtained by dividing the true positive values by the total predicted positive values. This metric provides information about the rate of correct predictions.

- F1-score is the harmonic mean of the sensitivity and precision metrics. It is an important metric in that it prevents creating incorrect models for unevenly distributed datasets.

Metrics take values between [0,1], and as they approach 1, the success of the metrics increases.

Parameter Tuning in the LevySAO Algorithm

In this section, parameter tuning of the proposed algorithm was carried out to determine the most appropriate value of the "LevyProb". LevyProb value was set as 0.1, 0.2, …, 0.9, 1.0 and a total of 10 different LevySAO variants were created. ANN and these LevySAO variants are combined and 10 different hybrid models are developed. All models were run according to the criteria given in Table 1 and the metric results obtained are presented in Tables 3-6. The "mean" column in the tables shows the average metric value obtained as a result of 30 runs, the "std" column shows the standard deviation of 30 runs, and the "rank" column is the Friedman test result as success rank of the model according to the mean value. The bottom row of the tables gives the average success ranking (ASR) of each model according to the Friedman test.

When the results obtained for the sensitivity metric are examined in Table 3, it is seen that the LevySAO09 ranks first in the liver and wine datasets and in terms of ASR takes 1st place with a value of 4.133. In terms of ASR, the LevySAO01 ranked 2nd with a value of 4.6, the LevySAO02 ranked 3rd with a value of 4.933, the LevySAO07 ranked 4th with a value of 5.2, the LevySAO04 ranked 5th with a value of 5.267, the LevySAO1 ranked 6th with a value of 5.4, and the LevySAO08 ranked 7th with a value of 5.867, LevySAO05 and LevySAO06 ranked 8th with a value of 6.2, the original SAO ranked 9th with a value of 6.533, and the LevySAO03 ranked 10th with a value of 6.667.

When the results obtained for the specificity metric are examined in Table 4, it is seen that the LevySAO09 ranks first in the liver, vertebral3 and wine datasets and in terms of ASR takes 1st place with a value of 3.8. In terms of ASR, LevySAO07 ranked 2nd with a value of 4.4, LevySAO01 and LevySAO04 ranked 3rd with a value of 5.067, LevySAO02 ranked 4th with a value of 5.133, LevySAO08 ranked 5th with a value of 5.4, LevySAO1 ranked 6th with a value of 5.933, LevySAO06 ranked 7th with a value of 6, LevySAO05 ranked 8th with a value of 6.067, the Original SAO ranked 9th with a value of 6.33, and the LevySAO03 ranked 10th with a value of 6.733.

When the results obtained for the precision metric are examined in Table 5, it is seen that the LevySAO09 ranks first in the wine dataset and in terms of ASR takes 1st place with a value of 4.933. In terms of ASR, LevySAO1 ranked 2nd with a value of 5, LevySAO04 ranked 3rd with a value of 5.067, LevySAO08 ranked 4th with a value of 5.133, LevySAO02 and LevySAO07 ranked 5th with a value of 5.267, LevySAO01 ranked 6th with a value of

5.8, LevySAO06 ranked 7th with a value of 5.867, LevySAO05 ranked 8th with a value of 6.2, original SAO ranked 9th with a value of 6.533 and LevySAO03 ranked 10th with a value of 7.

When the results obtained for the f1-score metric are examined in Table 6, it is seen that the LevySAO09 ranks first in the liver and wine dataset and in terms of ASR takes 1st place with a value of 4.6. In terms of ASR, LevySAO07 ranked 2nd with a value of 4.733, LevySAO01 ranked 3rd with a value of 4.933, LevySAO1 ranked 4th with a value of 5.133, LevySAO02 ranked 5th with a value of 5.267, LevySAO04 ranked 6th with a value of 5.333, LevySAO08 ranked 7th with a value of 5.467, LevySAO06 ranked 8th with a value of 6.2, LevySAO05 ranked 9th with a value of 6.333, original SAO ranked 10th with a value of 6.867, LevySAO03 ranked 11th with a value of 7.2.

Table 3

Mean, Standard Deviation and Rank of Success Values Obtained by Levysao Variants for The Sensitivity Metric

	SAO			LevySAO01			LevySAO02			LevySAO03			LevySAO04			LevySAO05		
Datasets	mean	std	rank	mean	std	rank	mean	std	rank	mean	std	rank	mean	std	rank	mean	std	rank
aggregation	0.355	0.122	11	0.521	0.145	7	0.53	0.132	5	0.473	0.155	10	0.549	0.134	3	0.49	0.149	9
aniso	1	0	1	1	0	1	1	0	1	1	0	1	1	0	1	1	0	1
balance	0.684	0.084	5	0.684	0.077	4	0.69	0.085	2	0.663	0.053	11	0.666	0.074	10	0.691	0.066	1
ecoli	0.339	0.067	11	0.425	0.084	10	0.442	0.087	9	0.45	0.105	8	0.468	0.081	7	0.493	0.097	4
glass	0.231	0.074	11	0.354	0.08	10	0.399	0.065	8	0.412	0.082	4	0.411	0.09	5	0.41	0.055	6
iris	0.989	0.006	3	0.99	0.005	1	0.98	0.059	4	0.968	0.082	11	0.98	0.059	5	0.979	0.059	7
iris2D	0.97	0.009	1	0.967	0.008	3	0.967	0.008	2	0.946	0.076	10	0.964	0.007	4	0.942	0.075	11
liver	0.396	0.033	11	0.41	0.026	4	0.41	0.025	3	0.412	0.034	2	0.408	0.032	8	0.406	0.027	9
mouse	0.989	0.061	8	0.989	0.061	7	1	0.001	3	0.989	0.061	6	1	0.001	2	0.999	0.003	4
pathbased	0.6	0.076	2	0.602	0.06	1	0.585	0.092	6	0.598	0.032	3	0.58	0.049	8	0.591	0.051	4
seeds	0.728	0.07	10	0.762	0.054	4	0.772	0.076	3	0.748	0.059	9	0.752	0.085	7	0.749	0.078	8
smiley	0.43	0.085	1	0.389	0.094	4	0.352	0.097	10	0.411	0.075	2	0.39	0.088	3	0.379	0.107	7
varied	0.982	0.003	1	0.982	0.002	3	0.982	0.002	4	0.971	0.058	9	0.982	0.002	2	0.982	0.003	2
vertebral3	0.7	0.065	11	0.741	0.066	1	0.72	0.062	6	0.718	0.062	8	0.715	0.075	9	0.713	0.064	10
wine	0.683	0.077	11	0.833	0.144	9	0.834	0.143	8	0.838	0.134	6	0.86	0.134	5	0.805	0.147	10
Avg.			6.533 (9)			4.6 (2)			4.933 (3)			6.667 (10)			5.267 (5)			6.2 (8)

	LevySAO06			LevySAO07			LevySAO08			LevySAO09			LevySAO1		
Datasets	mean	std	rank	mean	std	rank	mean	std	rank	mean	std	rank	mean	std	rank
aggregation	0.555	0.153	2	0.498	0.145	8	0.564	0.141	1	0.535	0.148	4	0.528	0.111	6
aniso	1	0	1	1	0	1	1	0	1	0.989	0.061	2	1	0	1
balance	0.678	0.079	8	0.683	0.057	6	0.679	0.077	7	0.669	0.057	9	0.687	0.076	3
ecoli	0.482	0.085	5	0.482	0.077	6	0.513	0.081	2	0.512	0.079	3	0.524	0.072	1
glass	0.392	0.091	9	0.417	0.098	3	0.407	0.091	7	0.423	0.063	2	0.431	0.072	1
iris	0.979	0.059	8	0.979	0.06	6	0.978	0.059	9	0.989	0.005	2	0.977	0.059	10
iris2D	0.953	0.054	9	0.962	0.016	6	0.962	0.006	5	0.959	0.008	8	0.961	0.004	7
liver	0.405	0.029	10	0.408	0.03	7	0.409	0.028	6	0.413	0.027	1	0.41	0.023	5
mouse	0.966	0.102	10	1	0	1	0.989	0.061	6	0.999	0.003	5	0.988	0.061	9
pathbased	0.589	0.047	5	0.579	0.101	9	0.569	0.04	11	0.582	0.083	7	0.576	0.041	10
seeds	0.753	0.086	6	0.782	0.039	1	0.717	0.103	11	0.774	0.073	2	0.756	0.082	5
smiley	0.373	0.112	8	0.383	0.09	6	0.364	0.096	9	0.348	0.093	11	0.385	0.091	5
varied	0.981	0.002	5	0.98	0.003	8	0.981	0.002	6	0.982	0.002	3	0.981	0.003	7
vertebral3	0.725	0.071	5	0.731	0.053	3	0.729	0.065	4	0.733	0.061	2	0.719	0.093	7
wine	0.881	0.137	2	0.838	0.168	7	0.874	0.14	3	0.908	0.099	1	0.867	0.123	4
Avg.			6.2 (8)			5.2 (4)			5.867 (7)			4.133 (1)			5.4 (6)

Table 4

Mean, Standard Deviation and Rank of Success Values Obtained by Levysao Variants for The Specificity Metric

	SAO			LevySAO01			LevySAO02			LevySAO03			LevySAO04			LevySAO05		
Datasets	mean	std	rank	mean	std	rank	mean	std	rank	mean	std	rank	mean	std	rank	mean	std	rank
aggregation	0.911	0.026	11	0.937	0.026	9	0.944	0.025	6	0.936	0.031	10	0.952	0.023	1	0.937	0.031	8
aniso	1	0	1	1	0	1	1	0	1	1	0	1	1	0	1	1	0	1
balance	0.919	0.017	10	0.921	0.019	9	0.922	0.019	7	0.917	0.015	11	0.921	0.021	8	0.93	0.019	2
ecoli	0.945	0.013	11	0.955	0.01	10	0.955	0.013	9	0.96	0.011	8	0.963	0.01	6	0.961	0.012	7
glass	0.849	0.015	11	0.885	0.024	10	0.898	0.019	7	0.9	0.022	6	0.898	0.023	8	0.901	0.019	3
iris	0.995	0.003	2	0.995	0.003	1	0.99	0.03	3	0.984	0.041	9	0.99	0.03	4	0.989	0.03	6
iris2D	0.985	0.004	1	0.983	0.004	3	0.983	0.004	2	0.973	0.038	10	0.982	0.004	4	0.971	0.038	11
liver	0.729	0.033	11	0.743	0.026	4	0.743	0.025	3	0.746	0.034	2	0.741	0.032	8	0.739	0.027	9
mouse	0.994	0.03	7	0.994	0.03	8	1	0.001	3	0.994	0.03	6	1	0.001	2	1	0.002	4
pathbased	0.796	0.04	1	0.795	0.032	2	0.787	0.048	6	0.792	0.015	3	0.784	0.024	8	0.79	0.026	4
seeds	0.864	0.035	10	0.881	0.027	4	0.886	0.038	3	0.874	0.029	9	0.876	0.043	7	0.875	0.039	8
smiley	0.845	0.044	1	0.824	0.053	3	0.807	0.056	9	0.834	0.044	2	0.823	0.05	4	0.817	0.056	6
varied	0.991	0.001	1	0.991	0.001	2	0.991	0.001	4	0.985	0.029	9	0.991	0.001	2	0.991	0.001	1
vertebral3	0.901	0.015	6	0.905	0.022	2	0.901	0.018	5	0.9	0.019	8	0.899	0.028	9	0.897	0.023	11
wine	0.855	0.031	11	0.922	0.063	8	0.922	0.065	9	0.923	0.06	7	0.935	0.058	4	0.908	0.066	10
Avg.			6.33 (9)			5.067 (3)			5.133 (4)			6.733 (10)			5.067 (3)			6.067 (8)

	LevySAO06			LevySAO07			LevySAO08			LevySAO09			LevySAO1		
Datasets	mean	std	rank	mean	std	rank	mean	std	rank	mean	std	rank	mean	std	rank
aggregation	0.949	0.023	2	0.94	0.026	7	0.947	0.024	4	0.949	0.023	3	0.946	0.02	5
aniso	1	0	1	1	0	1	1	0	1	0.994	0.03	2	1	0	1
balance	0.924	0.021	6	0.928	0.016	3	0.93	0.019	1	0.925	0.013	5	0.926	0.019	4
ecoli	0.963	0.007	5	0.964	0.007	3	0.966	0.008	2	0.963	0.012	4	0.967	0.007	1
glass	0.896	0.027	9	0.902	0.024	1	0.901	0.024	4	0.901	0.02	2	0.9	0.018	5
iris	0.989	0.03	5	0.989	0.03	5	0.989	0.03	7	0.995	0.002	2	0.989	0.029	8
iris2D	0.976	0.027	9	0.981	0.008	6	0.981	0.003	5	0.979	0.004	8	0.981	0.002	7
liver	0.738	0.029	10	0.742	0.03	7	0.742	0.028	6	0.746	0.027	1	0.743	0.023	5
mouse	0.983	0.051	10	1	0	1	0.994	0.03	6	0.999	0.002	5	0.994	0.03	9
pathbased	0.788	0.024	5	0.783	0.051	9	0.778	0.019	11	0.784	0.042	7	0.781	0.02	10
seeds	0.876	0.043	6	0.891	0.019	1	0.858	0.051	11	0.887	0.036	2	0.878	0.041	5
smiley	0.812	0.055	8	0.821	0.051	5	0.806	0.054	10	0.804	0.053	11	0.814	0.051	7
varied	0.991	0.001	5	0.99	0.001	8	0.991	0.001	6	0.991	0.001	3	0.99	0.001	7
vertebral3	0.9	0.023	7	0.903	0.018	3	0.902	0.019	4	0.905	0.019	1	0.899	0.048	10
wine	0.944	0.061	2	0.924	0.078	6	0.941	0.062	3	0.955	0.045	1	0.934	0.059	5
Avg.			6 (7)			4.4 (2)			5.4 (5)			3.8 (1)			5.933 (6)

Table 5

Mean, Standard Deviation and Rank of Success Values Obtained by Levysao Variants For The Precision Metric

	SAO			LevySAO01			LevySAO02			LevySAO03			LevySAO04			LevySAO05		
Datasets	mean	std	rank	mean	std	rank	mean	std	rank	mean	std	rank	mean	std	rank	mean	std	rank
aggregation	0.302	0.111	11	0.463	0.155	7	0.48	0.138	4	0.431	0.173	9	0.501	0.149	3	0.43	0.146	10
aniso	1	0	1	1	0	1	1	0	1	1	0	1	1	0	1	1	0	1
balance	0.67	0.1	8	0.663	0.091	9	0.676	0.101	6	0.656	0.084	11	0.657	0.093	10	0.703	0.105	1
ecoli	0.286	0.082	11	0.386	0.096	10	0.395	0.12	9	0.427	0.119	8	0.464	0.107	7	0.47	0.123	6
glass	0.145	0.098	11	0.302	0.11	10	0.354	0.088	9	0.363	0.091	8	0.384	0.126	2	0.373	0.08	5
iris	0.989	0.006	2	0.99	0.005	1	0.975	0.09	4	0.957	0.124	11	0.973	0.099	6	0.971	0.1	9
iris2D	0.97	0.009	1	0.967	0.008	2	0.967	0.008	3	0.933	0.126	10	0.964	0.007	4	0.931	0.118	11
liver	0.432	0.038	10	0.435	0.028	9	0.441	0.027	3	0.439	0.046	5	0.436	0.034	8	0.437	0.03	7
mouse	0.985	0.076	8	0.985	0.076	7	0.999	0.003	3	0.986	0.076	6	1	0.002	2	0.999	0.004	4
pathbased	0.647	0.116	1	0.567	0.109	6	0.589	0.169	5	0.605	0.136	2	0.596	0.126	4	0.599	0.128	3
seeds	0.745	0.134	10	0.801	0.076	4	0.802	0.11	2	0.785	0.092	6	0.778	0.127	8	0.778	0.127	7
smiley	0.345	0.065	1	0.312	0.081	6	0.285	0.089	10	0.336	0.067	2	0.317	0.077	3	0.306	0.094	7
varied	0.982	0.003	1	0.982	0.002	2	0.982	0.002	6	0.965	0.089	11	0.982	0.002	4	0.982	0.003	5
vertebral3	0.656	0.124	11	0.718	0.123	4	0.711	0.095	6	0.708	0.099	8	0.708	0.14	9	0.711	0.086	7
wine	0.591	0.136	11	0.785	0.202	9	0.795	0.205	8	0.8	0.198	7	0.833	0.189	5	0.757	0.209	10
Avg.			6.533 (9)			5.8 (6)			5.267 (5)			7 (10)			5.067 (3)			6.2 (8)

	LevySAO06			LevySAO07			LevySAO08			LevySAO09			LevySAO1		
Datasets	mean	std	rank	mean	std	rank	mean	std	rank	mean	std	rank	mean	std	rank
aggregation	0.52	0.173	2	0.46	0.154	8	0.526	0.169	1	0.476	0.167	5	0.469	0.129	6
aniso	1	0	1	1	0	1	1	0	1	0.983	0.091	2	1	0	1
balance	0.681	0.094	2	0.671	0.073	7	0.68	0.113	3	0.68	0.109	5	0.68	0.096	4
ecoli	0.482	0.101	5	0.486	0.079	4	0.513	0.098	2	0.49	0.115	3	0.534	0.064	1
glass	0.366	0.099	7	0.375	0.105	4	0.386	0.128	1	0.367	0.075	6	0.382	0.093	3
iris	0.972	0.094	7	0.973	0.091	5	0.972	0.097	8	0.989	0.005	3	0.97	0.096	10
iris2D	0.946	0.089	9	0.962	0.015	6	0.962	0.006	5	0.959	0.007	8	0.961	0.004	7
liver	0.441	0.039	2	0.429	0.05	11	0.438	0.028	6	0.44	0.032	4	0.443	0.021	1
mouse	0.957	0.128	10	1	0	1	0.986	0.076	6	0.999	0.004	5	0.984	0.076	9
pathbased	0.566	0.127	7	0.558	0.173	9	0.528	0.109	11	0.552	0.166	10	0.56	0.111	8
seeds	0.776	0.129	9	0.823	0.026	1	0.727	0.175	11	0.801	0.113	3	0.791	0.114	5
smiley	0.299	0.092	8	0.313	0.081	5	0.292	0.085	9	0.284	0.088	11	0.313	0.083	4
varied	0.982	0.002	7	0.98	0.003	10	0.982	0.002	8	0.982	0.002	3	0.981	0.003	9
vertebral3	0.706	0.126	10	0.726	0.094	1	0.724	0.098	2	0.718	0.108	5	0.723	0.136	3
wine	0.863	0.178	2	0.813	0.225	6	0.847	0.188	3	0.91	0.115	1	0.837	0.179	4
Avg.			5.867 (7)			5.267 (5)			5.133 (4)			4.933 (1)			5 (2)

Table 6

Mean, Standard Deviation and Rank of Success Values Obtained by Levysao Variants for The F1-Score Metric

	SAO			LevySAO01			LevySAO02			LevySAO03			LevySAO04			LevySAO05		
Datasets	mean	std	rank	mean	std	rank	mean	std	rank	mean	std	rank	mean	std	rank	mean	std	rank
aggregation	0.294	0.12	11	0.461	0.153	7	0.475	0.137	6	0.422	0.162	10	0.498	0.147	3	0.429	0.154	9
aniso	1	0	1	1	0	1	1	0	1	1	0	1	1	0	1	1	0	1
balance	0.663	0.083	7	0.654	0.068	8	0.666	0.08	6	0.648	0.064	11	0.651	0.078	10	0.68	0.074	1
ecoli	0.302	0.072	11	0.396	0.085	10	0.407	0.105	9	0.431	0.108	8	0.457	0.091	7	0.47	0.109	6
glass	0.158	0.077	11	0.297	0.093	10	0.359	0.072	8	0.365	0.088	7	0.371	0.1	5	0.37	0.065	6
iris	0.989	0.006	3	0.99	0.005	1	0.977	0.08	4	0.961	0.11	11	0.976	0.083	5	0.974	0.083	8
iris2D	0.97	0.009	1	0.967	0.008	3	0.967	0.008	2	0.938	0.107	10	0.964	0.007	4	0.935	0.104	11
liver	0.378	0.049	11	0.404	0.034	2	0.402	0.034	3	0.401	0.05	4	0.398	0.045	8	0.396	0.039	9
mouse	0.987	0.07	8	0.987	0.07	7	0.999	0.002	3	0.987	0.07	6	1	0.002	2	0.999	0.004	4
pathbased	0.525	0.104	1	0.525	0.082	2	0.503	0.108	4	0.5	0.033	6	0.491	0.038	9	0.503	0.066	5
seeds	0.715	0.105	10	0.763	0.066	4	0.77	0.096	3	0.747	0.08	7	0.747	0.113	6	0.742	0.105	9
smiley	0.378	0.069	1	0.343	0.084	4	0.314	0.092	10	0.367	0.069	2	0.348	0.08	3	0.336	0.098	7
varied	0.981	0.003	5	0.982	0.002	3	0.981	0.002	6	0.967	0.079	11	0.982	0.002	2	0.982	0.003	1
vertebral3	0.657	0.087	11	0.709	0.098	3	0.697	0.077	6	0.697	0.077	7	0.689	0.101	10	0.693	0.077	8
wine	0.614	0.097	11	0.799	0.179	9	0.801	0.181	8	0.805	0.172	7	0.835	0.168	5	0.763	0.184	10
Avg.			6.867 (10)			4.933 (3)			5.267 (5)			7.2 (11)			5.333 (6)			6.333 (9)

	LevySAO06			LevySAO07			LevySAO08			LevySAO09			LevySAO1		
Datasets	mean	std	rank	mean	std	rank	mean	std	rank	mean	std	rank	mean	std	rank
aggregation	0.51	0.164	1	0.453	0.151	8	0.509	0.153	2	0.485	0.155	4	0.475	0.119	5
aniso	1	0	1	1	0	1	1	0	1	0.985	0.081	2	1	0	1
balance	0.666	0.08	5	0.666	0.06	4	0.668	0.085	3	0.653	0.056	9	0.67	0.081	2
ecoli	0.476	0.091	4	0.475	0.075	5	0.504	0.087	2	0.488	0.097	3	0.518	0.064	1
glass	0.355	0.099	9	0.38	0.099	2	0.372	0.104	4	0.376	0.072	3	0.386	0.075	1
iris	0.975	0.081	7	0.975	0.081	6	0.974	0.082	9	0.989	0.005	2	0.973	0.082	10
iris2D	0.949	0.076	9	0.962	0.016	6	0.962	0.006	5	0.959	0.009	8	0.961	0.004	7
liver	0.392	0.042	10	0.399	0.045	7	0.4	0.041	6	0.406	0.033	1	0.401	0.032	5
mouse	0.961	0.116	10	1	0	1	0.987	0.07	6	0.999	0.003	5	0.986	0.07	9
pathbased	0.507	0.061	3	0.495	0.116	7	0.479	0.036	11	0.489	0.089	10	0.493	0.037	8
seeds	0.744	0.115	8	0.787	0.038	1	0.699	0.14	11	0.771	0.094	2	0.753	0.101	5
smiley	0.329	0.097	8	0.342	0.084	6	0.322	0.088	9	0.311	0.09	11	0.343	0.085	5
varied	0.981	0.002	7	0.98	0.003	10	0.981	0.002	8	0.982	0.002	4	0.981	0.003	9
vertebral3	0.691	0.093	9	0.71	0.07	1	0.709	0.08	2	0.707	0.081	4	0.705	0.116	5
wine	0.859	0.167	2	0.808	0.208	6	0.852	0.171	3	0.898	0.116	1	0.839	0.159	4
Avg.			6.2 (8)			4.733 (2)			5.467 (7)			4.6 (1)			5.133 (4)

When the results in Tables 3-6 are evaluated together, it is seen that the LevySAO09 variant has a superior performance than the other variants by obtaining the best ASR values in all 4 metrics. For this reason, the LevySAO09 variant, with the LevyProb parameter set to 0.9, was determined as the proposed algorithm in the study. In the remainder of the study, the LevySAO09 algorithm will be referred to as LevySAO.

Performance Comparison of LevySAO and Other Algorithms

The comparison algorithms used in this study and their specific parameter values are given in Table 7.

Table 7. *Parameters of The Comparison Algorithms*

Algorithm	Year	Parameters
Proposed LevySAO		levyprob=0.9
Cuckoo Search (CS) (Yang & Suash, 2009)	2009	pa = 0.25
Differential Evolution Algorithm (DEA) (Storn & Price, 1997)	1997	cr=0.9, f=0.5
Grey Wolf Optimizer (GWO) (Mirjalili, Mirjalili, & Lewis, 2014)	2014	no parameter
Honey Badger Algorithm (HBA) (Hashim et al., 2022)	2022	beta=6, c=2, vec_flag=[-1, 1]
Artificial Algae Algorithm (AAA) (Uymaz et al., 2015)	2015	k=2, le=0.3, ap=0.5
Marine Predators Algorithm (MPA) (Faramarzi, Heidarinejad, Mirjalili, & Gandomi, 2020)	2020	p=0.5, fads=0.2
Reptile Search Algorithm (RSA) (Abualigah, Abd Elaziz, Sumari, Geem, & Gandomi, 2022)	2022	alpha=0.1, beta=0.005
Snow Ablation Optimizer(SAO) (Deng & Liu, 2023)	2023	no parameter
Sine Cosine Algorithm (SCA) (Mirjalili, 2016)	2016	a=2

Puma Optimizer (PO)	2024	f3_explore = 0;
		f3_exploit = 0;
		mega_explor = 0.99;
		mega_exploit = 0.99;
		pf = [0.5 0.5 0.3];

African Vultures Optimization Algorithm (AVOA) (Abdollahzadeh, Gharehchopogh, & Mirjalili, 2021)	2021	p1=0.6; p2=0.4; p3=0.6; alpha=0.8,betha=0.2, gamma=2.5
Mountain Gazelle Optimizer (MGO)	2024	no parameter

When the sensitivity metric results are examined in Table 8, it is seen that the LevySAO and MGO algorithms ranked first in 6 of 15 datasets – aggregation, ecoli, glass, iris, liver and wine – and achieved the most successful result in terms of ASR with a value of 3.067. In terms of ASR, AAA ranked 2^{nd} with a value of 3.867, while the original SAO algorithm ranked 3rd with a value of 4.067. Other algorithms have not shown remarkable success for this metric.

When the specificity metric results are examined in Table 9, it is seen that the LevySAO algorithm ranked first in 8 of 15 datasets – aggregation, balance, ecoli, glass, iris, liver, vertebral3 and wine – and achieved the most successful result in terms of ASR with a value of 2.8. In terms of ASR, MGO ranked 2nd with a value of 3.2, AAA ranked 3rd with a value of 3.667, and the original SAO algorithm ranked 4th with a value of 4.533. Other algorithms have not shown remarkable success for this metric.

When the precision metric results are examined in Table 10, it is seen that the MGO algorithm achieved the most successful result with a value of 2.6 in terms of ASR. The LevySAO algorithm ranked first in 3 of the 15 datasets – aggregation, ecoli and wine – and ranked 2nd in terms of ASR with a value of 3.4, AAA ranked 3rd with a value of 3.8, and the original SAO algorithm ranked 4th with a value of 4.467. Other algorithms have not shown remarkable success for this metric.

When the f1-score metric results are examined in Table 11, it is seen that the LevySAO algorithm ranked first in 7 of 15 datasets – aggregation, ecoli, glass, iris, liver, varied and wine – and achieved the most successful result in terms of ASR with a value of 3. In terms of ASR, MGO ranked 2nd with a value of 3.133, AAA ranked 3rd with a value of 3.667, and the original SAO algorithm ranked 4th with a value of 4.4. Other algorithms have not shown remarkable success for this metric.

When the results in Tables 8-11 are evaluated together, it is seen that the LevySAO algorithm ranks first in many datasets. Additionally, it achieved the best ASR value in two of the 4 ASR metrics. It shared the first place in one metric. As a result, it was observed that the proposed LevySAO algorithm has a superior performance than the other algorithms in terms of average success.

Table 8

Mean, Standard Deviation and Rank of Success Values Obtained by Levysao and Other Algorithms for The Sensitivity Metric

	LevySAO			AVOA			CS			DEA			GWO			HBA			AAA		
Datasets	mean	std	rank	mean	std	rank	mean	std	rank	mean	std	rank	mean	std	rank	mean	std	rank	mean	std	rank
aggregation	0.535	0.148	1	0.354	0.125	7	0.294	0.050	11	0.355	0.105	6	0.340	0.121	8	0.329	0.117	9	0.388	0.076	4
aniso	0.989	0.061	4	1.000	0.000	1	1.000	0.001	2	1.000	0.000	1	0.999	0.002	3	0.989	0.061	5	1.000	0.000	1
balance	0.669	0.057	5	0.617	0.029	9	0.604	0.037	11	0.682	0.080	3	0.605	0.017	10	0.626	0.040	7	0.658	0.097	6
ecoli	0.512	0.079	1	0.393	0.067	3	0.261	0.038	11	0.289	0.054	10	0.341	0.069	5	0.299	0.071	9	0.385	0.058	4
glass	0.423	0.063	1	0.346	0.075	3	0.243	0.067	8	0.185	0.042	13	0.269	0.080	7	0.227	0.086	10	0.338	0.044	5
iris	0.989	0.005	1	0.941	0.102	11	0.966	0.014	8	0.982	0.011	6	0.953	0.078	10	0.970	0.083	7	0.984	0.006	5
iris2D	0.959	0.008	7	0.942	0.075	10	0.946	0.013	9	0.965	0.007	4	0.960	0.003	6	0.871	0.140	11	0.965	0.006	3
liver	0.413	0.027	1	0.376	0.032	10	0.377	0.031	8	0.389	0.037	6	0.377	0.034	9	0.387	0.029	7	0.399	0.030	3
mouse	0.999	0.003	2	0.931	0.135	10	0.974	0.021	9	0.998	0.004	4	0.977	0.061	8	0.880	0.182	11	0.996	0.005	5
pathbased	0.582	0.083	5	0.556	0.115	9	0.554	0.065	10	0.560	0.050	7	0.540	0.053	11	0.566	0.082	6	0.583	0.078	4
seeds	0.774	0.073	4	0.744	0.086	8	0.752	0.074	6	0.712	0.105	11	0.724	0.084	10	0.750	0.083	7	0.776	0.037	3
smiley	0.348	0.093	9	0.331	0.102	10	0.306	0.087	11	0.405	0.080	5	0.354	0.099	8	0.371	0.095	7	0.417	0.068	4
varied	0.982	0.002	2	0.980	0.003	7	0.970	0.010	11	0.981	0.002	5	0.979	0.003	9	0.981	0.002	4	0.980	0.004	6
vertebral3	0.733	0.061	2	0.653	0.042	9	0.638	0.047	11	0.649	0.045	10	0.695	0.051	5	0.660	0.056	7	0.748	0.053	1
wine	0.908	0.099	1	0.756	0.146	5	0.663	0.057	10	0.635	0.049	12	0.701	0.119	7	0.703	0.111	6	0.766	0.110	4
Avg.			3.067 (1)			7.467 (7)			9.067 (10)			6.867 (6)			7.733 (9)			7.533 (8)			3.867 (2)

	MGO			MPA			Puma			RSA			SAO			SCA		
Datasets	mean	std	Rank	mean	std	rank	mean	std	rank	mean	std	rank	mean	std	rank	mean	std	rank
aggregation	0.485	0.141	2	0.310	0.068	10	0.406	0.106	3	0.220	0.058	13	0.355	0.122	5	0.257	0.031	12
aniso	1.000	0.000	1	1.000	0.000	1	1.000	0.000	1	0.912	0.094	7	1.000	0.000	1	0.981	0.016	6
balance	0.696	0.082	1	0.674	0.092	4	0.624	0.044	8	0.542	0.083	13	0.684	0.084	2	0.565	0.073	12
ecoli	0.457	0.093	2	0.314	0.068	8	0.331	0.049	7	0.146	0.036	13	0.339	0.067	6	0.221	0.061	12
glass	0.414	0.068	2	0.303	0.056	6	0.344	0.068	4	0.204	0.051	11	0.231	0.074	9	0.196	0.055	12
iris	0.988	0.005	3	0.988	0.007	4	0.962	0.057	9	0.769	0.124	13	0.989	0.006	2	0.881	0.084	12
iris2D	0.968	0.008	2	0.960	0.002	5	0.950	0.054	8	0.693	0.067	13	0.970	0.009	1	0.858	0.096	12
liver	0.373	0.025	11	0.391	0.024	5	0.407	0.022	2	0.355	0.037	13	0.396	0.033	4	0.359	0.032	12
mouse	0.999	0.003	1	0.998	0.003	3	0.985	0.060	7	0.546	0.137	13	0.989	0.061	6	0.768	0.122	12
pathbased	0.644	0.081	1	0.559	0.064	8	0.584	0.078	3	0.384	0.160	13	0.600	0.076	2	0.458	0.155	12
seeds	0.767	0.047	5	0.784	0.054	2	0.786	0.072	1	0.577	0.082	13	0.728	0.070	9	0.614	0.076	12
smiley	0.422	0.070	3	0.422	0.061	2	0.373	0.090	6	0.250	0.000	13	0.430	0.085	1	0.263	0.048	12
varied	0.981	0.003	3	0.980	0.003	8	0.978	0.014	10	0.893	0.052	13	0.982	0.003	1	0.949	0.023	12
vertebral3	0.688	0.063	6	0.658	0.046	8	0.714	0.058	3	0.619	0.054	13	0.700	0.065	4	0.631	0.026	12
wine	0.772	0.130	3	0.681	0.080	9	0.846	0.137	2	0.594	0.145	13	0.683	0.077	8	0.638	0.059	11
Avg.			3.067 (1)			5.533 (5)			4.933 (4)			12.467 (12)			4.067 (3)			11.533 (11)

Table 9

Mean, Standard Deviation and Rank of Success Values Obtained by Levysao And Other Algorithms For The Specificity Metric

	LevySAO			AVOA			CS			DEA			GWO			HBA			AAA		
Datasets	mean	std	rank	mean	std	rank	mean	std	rank	mean	std	rank	mean	std	rank	mean	std	rank	mean	std	rank
aggregation	0.949	0.023	1	0.912	0.028	6	0.903	0.009	11	0.912	0.021	5	0.910	0.027	8	0.909	0.028	9	0.915	0.016	4
aniso	0.994	0.030	5	1.000	0.000	1	1.000	0.001	2	1.000	0.000	1	1.000	0.001	3	0.994	0.030	4	1.000	0.000	1
balance	0.925	0.013	1	0.904	0.013	8	0.895	0.027	11	0.925	0.017	2	0.900	0.014	10	0.908	0.013	6	0.904	0.029	7
ecoli	0.963	0.012	1	0.955	0.009	3	0.932	0.010	11	0.939	0.013	9	0.949	0.011	5	0.935	0.017	10	0.954	0.007	4
glass	0.901	0.020	1	0.877	0.020	4	0.854	0.016	8	0.839	0.011	13	0.863	0.019	7	0.852	0.026	9	0.871	0.009	5
iris	0.995	0.002	1	0.971	0.051	10	0.983	0.007	7	0.991	0.006	5	0.977	0.039	9	0.985	0.042	6	0.992	0.003	4
iris2D	0.979	0.004	7	0.971	0.037	10	0.973	0.007	9	0.982	0.003	4	0.980	0.002	6	0.936	0.070	11	0.983	0.003	3
liver	0.746	0.027	1	0.709	0.032	10	0.711	0.031	8	0.723	0.036	6	0.710	0.034	9	0.720	0.029	7	0.733	0.030	3
mouse	0.999	0.002	2	0.966	0.065	10	0.985	0.012	9	0.999	0.002	4	0.988	0.028	8	0.942	0.088	11	0.998	0.003	5
pathbased	0.784	0.042	5	0.773	0.059	10	0.773	0.032	9	0.775	0.025	8	0.765	0.026	11	0.777	0.042	6	0.787	0.040	3
seeds	0.887	0.036	4	0.872	0.043	8	0.876	0.037	6	0.856	0.052	11	0.862	0.042	10	0.875	0.042	7	0.888	0.019	3
smiley	0.804	0.053	9	0.791	0.054	10	0.783	0.052	11	0.840	0.047	5	0.810	0.058	8	0.817	0.054	7	0.847	0.040	1
varied	0.991	0.001	2	0.990	0.002	7	0.985	0.005	11	0.990	0.001	5	0.989	0.002	9	0.990	0.001	4	0.990	0.002	6
vertebral3	0.905	0.019	1	0.882	0.018	9	0.878	0.017	11	0.882	0.013	10	0.902	0.009	3	0.885	0.022	8	0.904	0.015	2
wine	0.955	0.045	1	0.888	0.065	5	0.846	0.025	10	0.831	0.026	12	0.863	0.052	7	0.864	0.049	6	0.891	0.047	4
Avg.			2.8 (1)			7.4 (8)			8.933 (10)			6.667 (7)			7.533 (9)			7.4 (8)			3.667 (3)

	MGO			MPA			Puma			RSA			SAO			SCA		
Datasets	mean	std	rank	mean	std	rank	mean	std	rank	mean	std	rank	mean	std	rank	mean	std	rank
aggregation	0.930	0.025	2	0.907	0.018	10	0.923	0.022	3	0.884	0.021	13	0.911	0.026	7	0.895	0.012	12
aniso	1.000	0.000	1	1.000	0.000	1	1.000	0.000	1	0.956	0.047	7	1.000	0.000	1	0.991	0.008	6
balance	0.921	0.020	3	0.917	0.025	5	0.903	0.015	9	0.846	0.071	13	0.919	0.017	4	0.865	0.063	12
ecoli	0.959	0.008	2	0.941	0.012	8	0.945	0.011	7	0.890	0.018	13	0.945	0.013	6	0.914	0.020	12
glass	0.887	0.016	2	0.866	0.013	6	0.879	0.022	3	0.843	0.013	11	0.849	0.015	10	0.841	0.013	12
iris	0.994	0.003	2	0.994	0.004	3	0.981	0.029	8	0.885	0.062	12	0.995	0.003	1	0.940	0.042	11
iris2D	0.984	0.004	2	0.980	0.001	5	0.975	0.027	8	0.846	0.034	13	0.985	0.004	1	0.929	0.048	12
liver	0.707	0.025	11	0.725	0.024	5	0.740	0.022	2	0.689	0.037	13	0.729	0.033	4	0.694	0.031	12
mouse	1.000	0.001	1	0.999	0.002	3	0.992	0.030	7	0.774	0.071	13	0.994	0.030	6	0.887	0.056	12
pathbased	0.819	0.043	1	0.775	0.032	7	0.787	0.040	4	0.686	0.083	13	0.796	0.040	2	0.723	0.079	12
seeds	0.884	0.023	5	0.892	0.027	2	0.893	0.036	1	0.789	0.041	13	0.864	0.035	9	0.807	0.038	12
smiley	0.841	0.044	4	0.847	0.037	2	0.820	0.053	6	0.750	0.000	13	0.845	0.044	3	0.757	0.028	12
varied	0.991	0.001	3	0.990	0.001	8	0.989	0.007	10	0.947	0.026	13	0.991	0.001	1	0.974	0.012	12
vertebral3	0.896	0.017	6	0.889	0.015	7	0.902	0.017	4	0.865	0.040	13	0.901	0.015	5	0.876	0.011	12
wine	0.894	0.056	3	0.855	0.034	9	0.929	0.060	2	0.800	0.077	13	0.855	0.031	8	0.833	0.031	11
Avg.			3.2 (2)			5.4 (6)			5 (5)			12.4 (12)			4.533 (4)			11.467 (11)

Table 10

Mean, Standard Deviation and Rank of Success Values Obtained by Levysao and Other Algorithms for The Precision Metric

	LevySAO			AVOA			CS			DEA			GWO			HBA			AAA		
Datasets	mean	std	rank	mean	std	rank	mean	std	rank	mean	std	rank	mean	std	rank	mean	std	rank	mean	std	rank
aggregation	0.476	0.167	1	0.303	0.121	5	0.233	0.048	11	0.291	0.092	8	0.297	0.110	7	0.268	0.125	9	0.353	0.073	3
aniso	0.983	0.091	4	1.000	0.000	1	1.000	0.001	2	1.000	0.000	1	0.999	0.002	3	0.983	0.091	4	1.000	0.000	1
balance	0.680	0.109	2	0.613	0.093	8	0.599	0.091	10	0.671	0.084	3	0.579	0.009	11	0.613	0.082	9	0.646	0.098	6
ecoli	0.490	0.115	1	0.380	0.100	3	0.233	0.054	11	0.239	0.062	9	0.294	0.091	5	0.234	0.086	10	0.373	0.077	4
glass	0.367	0.075	2	0.290	0.102	3	0.156	0.072	8	0.098	0.066	13	0.196	0.083	7	0.138	0.092	10	0.278	0.069	4
iris	0.989	0.005	2	0.926	0.154	11	0.967	0.014	7	0.982	0.011	6	0.941	0.128	10	0.958	0.129	8	0.985	0.006	5
iris2D	0.959	0.007	7	0.929	0.122	10	0.946	0.013	8	0.965	0.007	4	0.960	0.004	6	0.818	0.224	12	0.965	0.006	3
liver	0.440	0.032	2	0.426	0.059	6	0.408	0.066	10	0.420	0.088	8	0.379	0.099	11	0.411	0.066	9	0.430	0.034	5
mouse	0.999	0.004	2	0.909	0.175	10	0.974	0.026	8	0.998	0.004	3	0.972	0.083	9	0.851	0.231	11	0.995	0.007	5
pathbased	0.552	0.166	9	0.565	0.181	8	0.624	0.095	3	0.567	0.097	7	0.528	0.132	10	0.514	0.142	11	0.597	0.118	4
seeds	0.801	0.113	5	0.751	0.147	8	0.795	0.071	6	0.740	0.133	11	0.749	0.136	9	0.754	0.152	7	0.817	0.032	4
smiley	0.284	0.088	9	0.259	0.085	10	0.242	0.079	11	0.331	0.071	5	0.285	0.089	8	0.302	0.087	7	0.343	0.061	3
varied	0.982	0.002	2	0.981	0.003	7	0.971	0.009	11	0.981	0.002	5	0.979	0.003	9	0.981	0.002	4	0.981	0.004	6
vertebral3	0.718	0.108	2	0.582	0.120	8	0.559	0.091	11	0.577	0.116	9	0.650	0.126	6	0.574	0.121	10	0.748	0.068	1
wine	0.910	0.115	1	0.694	0.200	5	0.567	0.115	10	0.532	0.083	11	0.607	0.172	8	0.620	0.164	6	0.736	0.171	3
Avg.			3.4 (2)			6.867 (7)			8.467 (9)			6.867 (7)			7.933 (8)			8.467 (9)			3.8 (3)

	MGO			MPA			Puma			RSA			SAO			SCA		
Datasets	mean	std	rank	mean	std	rank	mean	std	rank	mean	std	rank	mean	std	rank	mean	std	rank
aggregation	0.459	0.146	2	0.255	0.056	10	0.346	0.098	4	0.155	0.060	13	0.302	0.111	6	0.198	0.029	12
aniso	1.000	0.000	1	1.000	0.000	1	1.000	0.000	1	0.926	0.096	6	1.000	0.000	1	0.982	0.014	5
balance	0.706	0.095	1	0.648	0.090	5	0.616	0.071	7	0.544	0.033	13	0.670	0.100	4	0.559	0.031	12
ecoli	0.442	0.106	2	0.268	0.089	8	0.282	0.076	7	0.091	0.047	13	0.286	0.082	6	0.158	0.050	12
glass	0.411	0.109	1	0.232	0.102	6	0.271	0.090	5	0.138	0.100	11	0.145	0.098	9	0.114	0.076	12
iris	0.989	0.005	3	0.988	0.007	4	0.957	0.087	9	0.728	0.201	13	0.989	0.006	1	0.885	0.117	12
iris2D	0.968	0.008	2	0.961	0.002	5	0.945	0.084	9	0.641	0.180	13	0.970	0.009	1	0.858	0.137	11
liver	0.423	0.064	7	0.436	0.034	3	0.444	0.020	1	0.287	0.118	13	0.432	0.038	4	0.347	0.104	12
mouse	0.999	0.002	1	0.997	0.005	4	0.979	0.076	7	0.523	0.187	13	0.985	0.076	6	0.768	0.191	12
pathbased	0.675	0.105	1	0.579	0.116	6	0.589	0.128	5	0.334	0.203	13	0.647	0.116	2	0.474	0.228	12
seeds	0.817	0.033	3	0.827	0.046	1	0.822	0.087	2	0.511	0.145	13	0.745	0.134	10	0.549	0.167	12
smiley	0.339	0.061	4	0.348	0.054	1	0.308	0.084	6	0.192	0.008	13	0.345	0.065	2	0.204	0.045	12
varied	0.982	0.003	3	0.980	0.003	8	0.978	0.012	10	0.915	0.033	13	0.982	0.003	1	0.952	0.021	12
vertebral3	0.675	0.135	4	0.585	0.115	7	0.715	0.094	3	0.523	0.060	13	0.656	0.124	5	0.546	0.083	12
wine	0.709	0.192	4	0.607	0.146	7	0.811	0.194	2	0.513	0.213	13	0.591	0.136	9	0.528	0.084	12
Avg.			2.6 (1)			5.067 (5)			5.2 (6)			12.4 (11)			4.467 (4)			11.467 (10)

Table 11

Mean, Standard Deviation and Rank of Success Values Obtained by Levysao and Other Algorithms for The F1-Score Metric

	LevySAO			AVOA			CS			DEA			GWO			HBA			AAA		
Datasets	mean	std	rank	mean	std	rank	mean	std	rank	mean	std	rank	mean	std	rank	mean	std	rank	mean	std	rank
aggregation	0.485	0.155	1	0.300	0.127	5	0.238	0.042	11	0.294	0.096	7	0.289	0.116	8	0.275	0.126	9	0.330	0.073	4
aniso	0.985	0.081	4	1.000	0.000	1	1.000	0.001	2	1.000	0.000	1	0.999	0.002	3	0.985	0.081	4	1.000	0.000	1
balance	0.653	0.056	4	0.595	0.027	9	0.583	0.042	10	0.669	0.078	2	0.583	0.017	11	0.604	0.041	8	0.632	0.086	6
ecoli	0.488	0.097	1	0.375	0.074	3	0.238	0.045	11	0.256	0.056	9	0.310	0.076	5	0.253	0.076	10	0.367	0.058	4
glass	0.376	0.072	1	0.292	0.085	3	0.175	0.064	8	0.113	0.046	13	0.212	0.079	7	0.160	0.092	9	0.277	0.043	5
iris	0.989	0.005	1	0.929	0.137	11	0.966	0.014	7	0.982	0.011	6	0.945	0.109	10	0.962	0.113	8	0.984	0.006	5
iris2D	0.959	0.009	7	0.934	0.105	10	0.946	0.013	9	0.965	0.007	4	0.960	0.003	6	0.837	0.193	12	0.965	0.006	3
liver	0.406	0.033	1	0.346	0.057	9	0.351	0.055	8	0.362	0.065	7	0.342	0.064	10	0.365	0.051	6	0.386	0.045	3
mouse	0.999	0.003	2	0.919	0.158	10	0.972	0.023	9	0.998	0.004	3	0.974	0.073	8	0.861	0.210	11	0.996	0.006	5
pathbased	0.489	0.089	5	0.480	0.122	8	0.467	0.077	10	0.480	0.061	7	0.457	0.046	11	0.487	0.096	6	0.515	0.102	3
seeds	0.771	0.094	5	0.728	0.116	8	0.751	0.075	6	0.698	0.126	11	0.714	0.111	10	0.733	0.120	7	0.780	0.037	3
smiley	0.311	0.090	9	0.289	0.089	10	0.268	0.080	11	0.361	0.073	5	0.313	0.092	8	0.331	0.088	7	0.374	0.063	3
varied	0.982	0.002	1	0.980	0.003	7	0.969	0.010	11	0.981	0.002	5	0.979	0.003	9	0.981	0.002	4	0.980	0.004	6
vertebral3	0.707	0.081	2	0.588	0.062	10	0.583	0.063	11	0.593	0.066	9	0.649	0.077	5	0.598	0.081	8	0.730	0.056	1
wine	0.898	0.116	1	0.706	0.179	5	0.587	0.072	10	0.555	0.060	12	0.634	0.148	7	0.643	0.140	6	0.728	0.140	3
Avg.			3 (1)			7.267 (8)			8.933 (11)			6.733 (7)			7.867 (10)			7.667 (9)			3.667 (3)

	MGO			MPA			Puma			RSA			SAO			SCA		
Datasets	mean	std	rank	mean	std	rank	mean	std	rank	mean	std	rank	mean	std	rank	mean	std	rank
aggregation	0.436	0.147	2	0.252	0.055	10	0.347	0.101	3	0.154	0.058	13	0.294	0.120	6	0.201	0.029	12
aniso	1.000	0.000	1	1.000	0.000	1	1.000	0.000	1	0.902	0.117	6	1.000	0.000	1	0.981	0.016	5
balance	0.683	0.080	1	0.652	0.090	5	0.607	0.052	7	0.509	0.100	13	0.663	0.083	3	0.537	0.081	12
ecoli	0.440	0.094	2	0.279	0.074	8	0.294	0.055	7	0.104	0.039	13	0.302	0.072	6	0.173	0.050	12
glass	0.376	0.077	2	0.239	0.068	6	0.288	0.078	4	0.142	0.069	11	0.158	0.077	10	0.124	0.057	12
iris	0.988	0.005	3	0.988	0.007	4	0.959	0.077	9	0.719	0.169	13	0.989	0.006	2	0.869	0.109	12
iris2D	0.968	0.008	2	0.960	0.002	5	0.947	0.074	8	0.607	0.098	13	0.970	0.009	1	0.843	0.126	11
liver	0.340	0.044	11	0.374	0.035	5	0.397	0.031	2	0.291	0.073	13	0.378	0.049	4	0.318	0.063	12
mouse	0.999	0.002	1	0.998	0.004	4	0.982	0.069	7	0.501	0.152	13	0.987	0.070	6	0.741	0.150	12
pathbased	0.582	0.121	1	0.476	0.081	9	0.508	0.097	4	0.305	0.136	13	0.525	0.104	2	0.373	0.133	12
seeds	0.772	0.045	4	0.787	0.053	1	0.784	0.084	2	0.499	0.101	13	0.715	0.105	9	0.541	0.110	12
smiley	0.372	0.063	4	0.378	0.055	2	0.335	0.086	6	0.217	0.008	13	0.378	0.069	1	0.229	0.046	12
varied	0.981	0.003	3	0.980	0.003	8	0.977	0.015	10	0.887	0.058	13	0.981	0.003	2	0.948	0.024	12
vertebral3	0.648	0.080	6	0.605	0.071	7	0.693	0.079	3	0.546	0.060	13	0.657	0.087	4	0.571	0.040	12
wine	0.725	0.163	4	0.616	0.100	8	0.820	0.171	2	0.514	0.176	13	0.614	0.097	9	0.561	0.070	11
Avg.			3.133 (2)			5.533 (6)			5 (5)			12.4 (13)			4.4 (4)			11.4 (12)

One-to-One Performance Comparisons of LevySAO and Other Algorithms

One-to-one comparison results of the values obtained by the proposed LevySAO algorithm and other algorithms for sensitivity, specificity, precision and f1-score metrics are presented in Tables 12-15. Comparison results are indicated with the letters 'w/l/d' under the "1 to 1" column. The meanings of these letters are as follows:

- win (w) : LevySAO algorithm achieved more successful results than the compared algorithm.
- lost (l) : The compared algorithm achieved more successful results than the LevySAO algorithm.
- draw (d) : LevySAO and the compared algorithm achieved the same result and tied.

Total w/l/d numbers for 15 data sets are given in the bottom row of the relevant column.

- When the sensitivity one-to-one comparison results in Table 12 are examined, it is seen that the LevySAO algorithm is superior to AAA, MGO and SAO in 9 datasets, MPA in 10 datasets, DEA and Puma in 11 datasets, GWO in 12 datasets, AVOA, CS and HBA in 14 datasets, RSA and SCA in 15 datasets. In total, the proposed algorithm was the winner in 143 of the 180 comparisons made for the sensitivity metric.
- When the specificity head-to-head comparison results in Table 13 are examined, it is seen that the LevySAO algorithm is superior to SAO in 9 datasets, AAA and MGO in 10 datasets, MPA and Puma in 11 datasets, DEA and GWO in 12 datasets, HBA in 13 datasets, AVOA, CS in 14 datasets, and RSA and SCA in 15 datasets. In total, the proposed algorithm was the winner in 146 of the 180 comparisons made for the specificity metric.
- When the precision head-to-head comparison results in Table 14 are examined, it is seen that the LevySAO algorithm is superior to MGO in 7 datasets, AAA and SAO in 9 datasets, MPA and Puma in 10 datasets, DEA in 11 datasets, GWO in 12 datasets, AVOA, CS and HBA in 13 datasets, and RSA and SCA in 15 datasets. In total, the proposed algorithm was the winner in 137 of the 180 comparisons made for the precision metric.
- When the f1-score head-to-head comparison results in Table 15 are examined, it is seen that the LevySAO algorithm is superior to MGO in 8 datasets, AAA in 9 datasets, SAO in 10 datasets, MPA and DEA and Puma in 11 datasets, GWO in 12 datasets, HBA in 13 datasets, AVOA, CS in 14 datasets, and RSA and SCA in 15 datasets. In total, the proposed algorithm was the winner in 143 of the 180 comparisons made for the f1-score metric.

When the one-to-one comparison results in Tables 12-15 are evaluated together, it is seen that the proposed LevySAO algorithm is clearly more successful than the other algorithms.

However, it should also be analyzed whether the successful results obtained by the proposed LevySAO algorithm occurred by chance. For this purpose, the Wilcoxon signed-rank test (Wilcoxon, Katti, & Wilcox, 1970) was applied at a 95% confidence interval between the metric values of the proposed algorithm and other algorithms, and the results obtained are presented in the p-value columns in Tables 12-15. The fact that the p-value in the tables is less than 0.05 indicates that the result obtained by the LevySAO algorithm is statistically significant and does not occur by chance. To indicate this situation, a "+" sign has been placed in the sign column of the tables. Otherwise, there is a possibility that the results may occur by chance and a "-" sign is placed in the sign column to indicate this situation. In the bottom row of the relevant column, the total +/- numbers for 15 data sets are given.

- Looking at the results obtained for the sensitivity metric in Table 12:
  in 7 datasets for MGO,
  in 8 datasets for AAA, MPA and Puma and SAO,
  in 9 datasets for AVOA and HBA,
  in 10 datasets for DEA,
  in 12 datasets for CS and GWO,
  in 15 datasets for RSA and SCA
  it is seen that statistically significant results were obtained.

As a result, it was observed that statistically significant results were produced in 121 out of 180 cases for the sensitivity metric. Therefore, a significance rate of 67% was observed for the sensitivity metric.

- Looking at the results obtained for the specificity metric in Table 13:
  in 7 datasets for MGO,
  in 8 datasets for MPA , Puma and SAO,
  in 9 datasets for AAA, AVOA, HBA,
  in 10 datasets for DEA,
  in 11 datasets for CS and GWO,
  in 15 datasets for RSA and SCA
  it is seen that statistically significant results were obtained.

As a result, it was observed that statistically significant results were produced in 120 out of 180 cases for the specificity metric. Therefore, a significance rate of 67% was observed for the specificity metric.

- Looking at the results obtained for the precision metric in Table 14:
  in 4 datasets for MGO,
  in 7 datasets for MPA and Puma,
  in 8 datasets for AAA, AVOA, DEA and SAO,
  in 9 datasets for HBA,
  in 10 datasets for GWO,

in 11 datasets for CS,
in 14 datasets for SCA,
in 15 datasets for RSA
it is seen that statistically significant results were obtained.

As a result, it was observed that statistically significant results were produced in 109 out of 180 cases for the precision metric. Therefore, a significance rate of 61% was observed for the precision metric.

- Looking at the results obtained for the f1-score metric in Table 15:
  in 6 datasets for MGO,
  in 8 datasets for MPA and Puma,
  in 9 datasets for AAA, AVOA, HBA and SAO,
  in 10 datasets for DEA,
  in 11 datasets for CS,
  in 12 datasets for GWO,
  in 15 datasets for RSA and SCA
  it is seen that statistically significant results were obtained.

As a result, it was observed that statistically significant results were produced in 121 out of 180 cases for the f1-score metric. Therefore, a significance rate of 67% was observed for the f1-score metric.

When the Wilcoxon signed-rank results in Table 12-15 are evaluated together, it is seen that the proposed LevySAO algorithm produces statistically significant results in most cases. Therefore, the general significance rate was observed to be 65%.

Table 12

One-to-one Comparison and Wilcoxon Signed-Rank Significance Test Results for The Sensitivity Metric of Levysao and Other Algorithms

	AAA			AVOA			CS			DEA			GWO			HBA		
Datasets	1 to 1	p-value	sign	1 to 1	p-value	sign	1 to 1	p-value	sign	1 to 1	p-value	sign	1 to 1	p-value	sign	1 to 1	p-value	sign
aggregation	w	6.892E-05	+	w	8.919E-05	+	w	1.024E-05	+	w	4.175E-05	+	w	2.597E-05	+	w	2.925E-04	+
aniso	l	1	-	l	1	-	l	5.625E-01	-	l	1	-	l	1	-	w	1	-
balance	w	1.835E-01	-	w	9.034E-05	+	w	3.772E-05	+	l	6.212E-01	-	w	2.987E-06	+	w	8.618E-04	+
ecoli	w	6.984E-06	+	w	3.560E-05	+	w	1.733E-06	+	w	1.919E-06	+	w	3.515E-06	+	w	1.734E-06	+
glass	w	4.860E-05	+	w	2.052E-04	+	w	2.563E-06	+	w	1.920E-06	+	w	5.748E-06	+	w	4.727E-06	+
iris	w	3.144E-03	+	w	6.168E-05	+	w	3.279E-06	+	w	5.011E-03	+	w	3.288E-06	+	w	4.655E-01	-
iris2D	l	2.695E-03	+	w	9.236E-01	-	w	7.484E-05	+	l	8.545E-04	+	l	8.352E-01	-	w	1.502E-02	+
liver	w	6.141E-02	-	w	4.360E-04	+	w	1.715E-05	+	w	2.365E-02	+	w	2.611E-04	+	w	4.674E-03	+
mouse	w	3.906E-03	+	w	3.174E-03	+	w	5.434E-06	+	w	2.891E-01	-	w	1.636E-04	+	w	1.818E-03	+
pathbased	l	9.828E-01	-	w	3.157E-01	-	w	3.784E-02	+	w	5.835E-02	-	w	2.740E-03	+	w	1.404E-01	-
seeds	l	9.904E-01	-	w	1.321E-01	-	w	1.374E-01	-	w	2.354E-02	+	w	2.610E-02	+	w	2.739E-01	-
smiley	l	2.207E-03	+	w	9.029E-01	-	w	7.034E-02	-	l	8.210E-03	+	l	4.734E-01	-	l	2.405E-01	-
varied	w	2.037E-01	-	w	1.572E-01	-	w	4.378E-06	+	w	1.452E-01	-	w	3.069E-04	+	w	2.075E-01	-
vertebral3	l	3.806E-01	-	w	2.588E-05	+	w	1.125E-05	+	w	5.020E-05	+	w	2.996E-02	+	w	2.409E-04	+
wine	w	1.011E-04	+	w	9.201E-04	+	w	3.504E-06	+	w	2.848E-06	+	w	9.718E-06	+	w	3.170E-06	+
	9/6/0		8/7	14/1/0		9/6	14/1/0		12/3	11/4/0		10/5	12/3/0		12/3	14/1/0		9/6

	MGO			MPA			Puma			RSA			SAO			SCA		
Datasets	1 to 1	p-value	sign	1 to 1	p-value	sign	1 to 1	p-value	sign	1 to 1	p-value	sign	1 to 1	p-value	sign	1 to 1	p-value	sign
aggregation	w	2.059E-01	-	w	5.217E-06	+	w	7.712E-04	+	w	2.351E-06	+	w	1.605E-04	+	w	2.603E-06	+
aniso	l	1	-	l	1	-	l	1	-	w	2.597E-05	+	l	1	-	w	6.657E-05	+
balance	l	2.288E-01	-	l	9.914E-01	-	w	1.106E-03	+	w	3.150E-06	+	l	7.241E-01	-	w	6.286E-06	+
ecoli	w	2.849E-02	+	w	1.734E-06	+	w	1.734E-06	+	w	1.730E-06	+	w	3.182E-06	+	w	1.734E-06	+
glass	w	4.284E-01	-	w	4.801E-06	+	w	1.477E-04	+	w	1.734E-06	+	w	2.125E-06	+	w	1.921E-06	+
iris	w	7.150E-01	-	w	2.583E-01	-	w	1.215E-05	+	w	1.715E-06	+	w	8.756E-01	-	w	1.717E-06	+
iris2D	l	8.675E-05	+	l	5.781E-01	-	w	8.112E-01	-	w	1.595E-06	+	l	9.940E-05	+	w	2.826E-06	+
liver	w	9.764E-06	+	w	7.331E-03	+	w	5.593E-01	-	w	2.478E-05	+	w	3.500E-02	+	w	8.452E-06	+
mouse	l	7.813E-01	-	w	4.629E-01	-	w	1.150E-03	+	w	1.709E-06	+	w	1	-	w	1.707E-06	+
pathbased	l	2.728E-02	+	w	1.092E-01	-	l	5.252E-01	-	w	2.594E-05	+	l	4.049E-01	-	w	9.686E-05	+
seeds	w	4.751E-01	-	l	6.558E-01	-	l	7.265E-01	-	w	1.708E-06	+	w	3.511E-02	+	w	3.075E-06	+
smiley	l	6.968E-04	+	l	9.866E-04	+	l	3.215E-01	-	w	4.075E-04	+	l	1.300E-03	+	w	6.139E-04	+
varied	w	6.341E-01	-	w	6.009E-03	+	w	3.206E-02	+	w	1.726E-06	+	l	9.730E-01	-	w	1.706E-06	+
vertebral3	w	1.012E-02	+	w	1.085E-04	+	w	2.094E-01	-	w	3.172E-06	+	w	6.708E-02	-	w	2.555E-06	+
wine	w	2.449E-04	+	w	5.849E-06	+	w	4.383E-02	+	w	2.599E-06	+	w	4.310E-06	+	w	2.804E-06	+
	9/6/0		7/8	10/5/0		8/7	11/4/0		8/7	15/0/0		15/0	9/6/0		8/7	15/0/0		15/0

Table 13

One-to-one Comparison and Wilcoxon Signed-Rank Significance Test Results for The Specificity Metric of Levysao and Other Algorithms

	AAA			AVOA			CS			DEA			GWO			HBA		
Datasets	1 to 1	p-value	sign	1 to 1	p-value	sign	1 to 1	p-value	sign	1 to 1	p-value	sign	1 to 1	p-value	sign	1 to 1	p-value	sign
aggregation	w	3.182E-06	+	w	1.973E-05	+	w	7.691E-06	+	w	5.307E-05	+	w	1.127E-05	+	w	3.065E-04	+
aniso	l	1	-	l	1	-	l	5.625E-01	-	l	1	-	l	1	-	l	1	-
balance	w	1.916E-03	+	w	2.998E-05	+	w	3.401E-05	+	w	8.855E-01	-	w	3.501E-06	+	w	7.738E-05	+
ecoli	w	3.609E-03	+	w	6.424E-03	+	w	1.921E-06	+	w	1.238E-05	+	w	4.196E-04	+	w	1.921E-06	+
glass	w	1.025E-05	+	w	1.360E-04	+	w	1.921E-06	+	w	1.921E-06	+	w	1.238E-05	+	w	2.370E-05	+
iris	w	3.144E-03	+	w	6.168E-05	+	w	3.279E-06	+	w	5.011E-03	+	w	3.288E-06	+	w	4.655E-01	-
iris2D	l	2.695E-03	+	w	9.236E-01	-	w	7.484E-05	+	l	8.545E-04	+	l	8.352E-01	-	w	1.502E-02	+
liver	w	6.141E-02	-	w	4.360E-04	+	w	1.715E-05	+	w	2.923E-02	+	w	2.611E-04	+	w	4.674E-03	+
mouse	w	4.395E-03	+	w	3.174E-03	+	w	5.434E-06	+	w	3.691E-01	-	w	1.636E-04	+	w	1.853E-03	+
pathbased	l	9.569E-01	-	w	3.930E-01	-	w	5.317E-02	-	w	8.401E-02	-	w	3.609E-03	+	w	1.095E-01	-
seeds	l	9.904E-01	-	w	1.321E-01	-	w	1.374E-01	-	w	2.354E-02	+	w	2.610E-02	+	w	2.739E-01	-
smiley	l	1.647E-03	+	w	9.757E-01	-	w	1.216E-01	-	l	5.177E-03	+	l	4.559E-01	-	l	3.027E-01	-
varied	w	2.037E-01	-	w	1.572E-01	-	w	4.378E-06	+	w	1.452E-01	-	w	3.069E-04	+	w	2.075E-01	-
vertebral3	w	8.612E-01	-	w	1.360E-04	+	w	4.860E-05	+	w	3.558E-05	+	w	3.933E-01	-	w	4.196E-04	+
wine	w	7.507E-05	+	w	8.479E-04	+	w	3.499E-06	+	w	2.592E-06	+	w	9.276E-06	+	w	3.501E-06	+
	10/5/0		9/6	14/1/0		9/6	14/1/0		11/4	12/3/0		10/5	12/3/0		11/4	13/2/0		9/6

	MGO			MPA			Puma			RSA			SAO			SCA		
Datasets	1 to 1	p-value	sign	1 to 1	p-value	sign	1 to 1	p-value	sign	1 to 1	p-value	sign	1 to 1	p-value	sign	1 to 1	p-value	sign
aggregation	w	8.217E-03	+	w	9.316E-06	+	w	2.052E-04	+	w	2.127E-06	+	w	6.892E-05	+	w	2.879E-06	+
aniso	l	1	-	l	1	-	l	1	-	w	2.597E-05	+	l	1	-	w	6.657E-05	+
balance	w	4.284E-01	-	w	2.451E-01	-	w	1.714E-05	+	w	4.271E-06	+	w	1.619E-01	-	w	1.476E-04	+
ecoli	w	8.221E-02	-	w	5.217E-06	+	w	1.973E-05	+	w	1.734E-06	+	w	2.370E-05	+	w	1.734E-06	+
glass	w	3.379E-03	+	w	2.353E-06	+	w	1.536E-03	+	w	1.734E-06	+	w	2.127E-06	+	w	1.921E-06	+
iris	w	7.150E-01	-	w	2.583E-01	-	w	1.215E-05	+	w	1.715E-06	+	d	8.756E-01	-	w	1.717E-06	+
iris2D	l	8.675E-05	+	l	5.781E-01	-	w	8.112E-01	-	w	1.595E-06	+	l	9.940E-05	+	w	2.826E-06	+
liver	w	9.764E-06	+	w	7.331E-03	+	w	5.593E-01	-	w	2.478E-05	+	w	3.500E-02	+	w	1.236E-05	+
mouse	l	7.813E-01	-	w	4.629E-01	-	w	1.150E-03	+	w	1.717E-06	+	w	1	-	w	1.720E-06	+
pathbased	l	1.895E-02	+	w	1.535E-01	-	l	6.223E-01	-	w	2.843E-05	+	l	2.622E-01	-	w	9.699E-05	+
seeds	w	4.751E-01	-	l	6.558E-01	-	l	7.265E-01	-	w	1.708E-06	+	w	3.511E-02	+	w	3.075E-06	+
smiley	l	4.898E-03	+	l	1.591E-03	+	l	2.744E-01	-	w	4.075E-04	+	l	6.153E-03	+	w	6.139E-04	+
varied	w	6.341E-01	-	w	6.009E-03	+	w	3.206E-02	+	w	1.726E-06	+	l	9.730E-01	-	w	1.706E-06	+
vertebral3	w	6.268E-02	-	w	3.162E-03	+	w	4.405E-01	-	w	1.127E-05	+	w	3.185E-01	-	w	9.306E-06	+
wine	w	2.238E-04	+	w	6.517E-06	+	w	4.756E-02	+	w	2.595E-06	+	w	4.315E-06	+	w	2.809E-06	+
	10/5/0		7/8	11/4/0		8/7	11/4/0		8/7	15/0/0		15/0	9/5/1		8/7	15/0/0		15/0

Table 14

One-to-one Comparison and Wilcoxon Signed-Rank Significance Test Results for The Precision Metric of Levysao and Other Algorithms

	AAA			AVOA			CS			DEA			GWO			HBA		
Datasets	1 to 1	p-value	sign	1 to 1	p-value	sign	1 to 1	p-value	sign	1 to 1	p-value	sign	1 to 1	p-value	sign	1 to 1	p-value	sign
aggregation	w	1.484E-03	+	w	1.605E-04	+	w	5.752E-06	+	w	5.307E-05	+	w	2.831E-04	+	w	7.143E-04	+
aniso	l	1	-	l	1	-	l	5.625E-01	-	l	1	-	l	1	-	d	1	-
balance	w	3.086E-01	-	w	2.255E-03	+	w	1.036E-03	+	w	6.288E-01	-	w	2.353E-06	+	w	1.226E-03	+
ecoli	w	7.157E-04	+	w	3.854E-03	+	w	2.127E-06	+	w	4.286E-06	+	w	2.163E-05	+	w	3.515E-06	+
glass	w	4.196E-04	+	w	1.833E-03	+	w	2.353E-06	+	w	2.353E-06	+	w	7.691E-06	+	w	4.286E-06	+
iris	w	9.076E-03	+	w	1.246E-04	+	w	2.345E-06	+	w	1.057E-02	+	w	2.824E-06	+	w	4.343E-01	-
iris2D	l	7.075E-04	+	w	5.178E-01	-	w	6.096E-05	+	l	2.441E-04	+	l	5.248E-01	-	w	1.930E-02	+
liver	w	2.301E-01	-	w	3.389E-01	-	w	7.731E-03	+	w	6.583E-01	-	w	8.217E-03	+	w	1.752E-02	+
mouse	w	2.100E-02	+	w	8.545E-04	+	w	5.494E-06	+	w	5.703E-01	-	w	1.905E-04	+	w	1.372E-03	+
pathbased	l	2.301E-01	-	l	6.114E-01	-	l	5.984E-02	-	l	8.130E-01	-	w	4.405E-01	-	w	3.043E-01	-
seeds	l	9.590E-01	-	w	9.777E-02	-	w	1.915E-01	-	w	2.849E-02	+	w	8.590E-02	-	w	1.846E-01	-
smiley	l	2.973E-02	+	w	5.420E-01	-	w	5.784E-02	-	l	6.360E-02	-	l	8.409E-01	-	l	2.293E-01	-
varied	w	2.946E-01	-	w	1.303E-01	-	w	3.505E-06	+	w	2.201E-01	-	w	6.868E-04	+	w	3.126E-01	-
vertebral3	l	2.989E-01	-	w	4.196E-04	+	w	1.639E-05	+	w	1.890E-04	+	w	3.683E-02	+	w	2.052E-04	+
wine	w	4.858E-05	+	w	3.815E-04	+	w	3.159E-06	+	w	2.595E-06	+	w	7.995E-06	+	w	2.471E-06	+
	9/6/0		8/7	13/2/0		8/7	13/2/0		11/4	11/4/0		8/7	12/3/0		10/5	13/1/1		9/6

	MGO			MPA			Puma			RSA			SAO			SCA		
Datasets	1 to 1	p-value	sign	1 to 1	p-value	sign	1 to 1	p-value	sign	1 to 1	p-value	sign	1 to 1	p-value	sign	1 to 1	p-value	sign
aggregation	w	7.813E-01	-	w	7.691E-06	+	w	1.484E-03	+	w	2.127E-06	+	w	1.891E-04	+	w	1.734E-06	+
aniso	l	1	-	l	1	-	l	1	-	w	4.170E-05	+	l	1	-	w	6.686E-05	+
balance	l	3.930E-01	-	w	3.086E-01	-	w	5.667E-03	+	w	3.182E-06	+	w	9.590E-01	-	w	2.603E-06	+
ecoli	w	1.109E-01	-	w	3.882E-06	+	w	4.286E-06	+	w	1.734E-06	+	w	3.882E-06	+	w	1.734E-06	+
glass	l	6.564E-02	-	w	4.860E-05	+	w	4.792E-04	+	w	2.879E-06	+	w	2.353E-06	+	w	1.921E-06	+
iris	w	9.650E-01	-	w	5.509E-01	-	w	1.584E-05	+	w	1.728E-06	+	l	7.534E-01	-	w	1.734E-06	+
iris2D	l	8.171E-05	+	l	1.350E-01	-	w	8.715E-01	-	w	1.674E-06	+	l	6.244E-05	+	w	1.921E-06	+
liver	w	4.048E-01	-	w	7.375E-01	-	l	4.427E-01	-	w	1.149E-04	+	w	3.044E-01	-	w	1.360E-04	+
mouse	l	5.000E-01	-	w	2.344E-01	-	w	2.165E-03	+	w	1.720E-06	+	w	1	-	w	1.721E-06	+
pathbased	l	4.771E-03	+	l	5.236E-01	-	l	3.055E-01	-	w	2.831E-04	+	l	6.830E-03	+	w	8.221E-02	-
seeds	l	9.918E-01	-	l	5.857E-01	-	l	4.165E-01	-	w	5.752E-06	+	w	2.924E-02	+	w	1.238E-05	+
smiley	l	9.737E-03	+	l	1.033E-02	+	l	4.307E-01	-	w	4.075E-04	+	l	1.094E-02	+	w	6.139E-04	+
varied	w	9.702E-01	-	w	1.122E-02	+	w	8.627E-02	-	w	1.734E-06	+	l	7.408E-01	-	w	1.734E-06	+
vertebral3	w	1.846E-01	-	w	3.317E-04	+	w	5.577E-01	-	w	1.494E-05	+	w	5.984E-02	-	w	7.687E-06	+
wine	w	1.183E-04	+	w	6.517E-06	+	w	2.417E-02	+	w	4.283E-06	+	w	5.882E-06	+	w	3.144E-06	+
	7/8/0		4/11	10/5/0		7/8	10/5/0		7/8	15/0/0		15/0	9/6/0		8/7	15/0/0		14/1

Table 15

One-to-one Comparison and Wilcoxon Signed-Rank Significance Test Results for The F1-Score Metric of Levysao and Other Algorithms

	AAA			AVOA			CS			DEA			GWO			HBA		
Datasets	1 to 1	p-value	sign	1 to 1	p-value	sign	1 to 1	p-value	sign	1 to 1	p-value	sign	1 to 1	p-value	sign	1 to 1	p-value	sign
aggregation	w	1.057E-04	+	w	6.320E-05	+	w	9.316E-06	+	w	3.724E-05	+	w	4.449E-05	+	w	3.751E-04	+
aniso	l	1	-	l	1	-	l	5.625E-01	-	l	1	-	l	1	-	d	1	-
balance	w	1.254E-01	-	w	1.127E-05	+	w	4.072E-05	+	l	2.895E-01	-	w	2.353E-06	+	w	5.194E-04	+
ecoli	w	2.597E-05	+	w	3.881E-04	+	w	1.734E-06	+	w	2.879E-06	+	w	1.025E-05	+	w	2.353E-06	+
glass	w	4.072E-05	+	w	4.534E-04	+	w	1.921E-06	+	w	1.921E-06	+	w	6.339E-06	+	w	6.984E-06	+
iris	w	9.674E-04	+	w	3.445E-05	+	w	1.728E-06	+	w	3.837E-03	+	w	2.541E-06	+	w	3.756E-01	-
iris2D	l	9.008E-03	+	w	7.772E-01	-	w	9.813E-05	+	l	2.075E-03	+	l	6.855E-02	-	w	1.238E-02	+
liver	w	4.548E-02	+	w	1.150E-04	+	w	1.238E-05	+	w	1.245E-02	+	w	8.188E-05	+	w	3.378E-03	+
mouse	w	4.395E-03	+	w	3.174E-03	+	w	5.511E-06	+	w	3.691E-01	-	w	1.638E-04	+	w	1.853E-03	+
pathbased	l	4.300E-01	-	w	4.958E-01	-	w	1.109E-01	-	w	3.600E-01	-	w	5.320E-03	+	w	2.301E-01	-
seeds	l	9.754E-01	-	w	1.204E-01	-	w	9.368E-02	-	w	1.566E-02	+	w	3.327E-02	+	w	2.059E-01	-
smiley	l	2.551E-03	+	w	9.757E-01	-	w	5.784E-02	-	l	8.864E-03	+	l	5.281E-01	-	l	2.768E-01	-
varied	w	1.108E-01	-	w	1.121E-01	-	w	2.870E-06	+	w	1.348E-01	-	w	2.669E-04	+	w	1.915E-01	-
vertebral3	l	1.470E-01	-	w	2.370E-05	+	w	1.494E-05	+	w	7.510E-05	+	w	2.183E-02	+	w	1.742E-04	+
wine	w	6.889E-05	+	w	7.509E-04	+	w	2.845E-06	+	w	2.600E-06	+	w	8.843E-06	+	w	2.471E-06	+
	9/6/0		9/6	14/1/0		9/6	14/1/0		11/4	11/4/0		10/5	12/3/0		12/3	13/1/1		9/6

	MGO			MPA			Puma			RSA			SAO			SCA		
Datasets	1 to 1	p-value	sign	1 to 1	p-value	sign	1 to 1	p-value	sign	1 to 1	p-value	sign	1 to 1	p-value	sign	1 to 1	p-value	sign
aggregation	w	2.134E-01	-	w	4.729E-06	+	w	7.157E-04	+	w	1.921E-06	+	w	1.360E-04	+	w	1.921E-06	+
aniso	l	1	-	l	1	-	l	1	-	w	3.459E-05	+	l	1	-	w	6.697E-05	+
balance	l	1.529E-01	-	w	8.130E-01	-	w	1.382E-03	+	w	3.182E-06	+	l	6.733E-01	-	w	3.515E-06	+
ecoli	w	6.871E-02	-	w	2.127E-06	+	w	2.603E-06	+	w	1.734E-06	+	w	2.353E-06	+	w	1.734E-06	+
glass	w	7.813E-01	-	w	6.984E-06	+	w	4.072E-04	+	w	1.734E-06	+	w	1.921E-06	+	w	1.921E-06	+
iris	w	4.380E-01	-	w	1.712E-01	-	w	7.888E-06	+	w	1.731E-06	+	w	8.890E-01	-	w	1.734E-06	+
iris2D	l	8.171E-05	+	l	5.850E-01	-	w	4.919E-01	-	w	1.697E-06	+	l	1.708E-04	+	w	2.353E-06	+
liver	w	2.879E-06	+	w	2.558E-03	+	w	4.427E-01	-	w	1.493E-05	+	w	1.790E-02	+	w	2.370E-05	+
mouse	l	7.813E-01	-	w	4.629E-01	-	w	1.150E-03	+	w	1.720E-06	+	w	1	-	w	1.724E-06	+
pathbased	l	4.318E-02	+	w	2.386E-01	-	l	9.455E-01	-	w	1.238E-05	+	l	2.210E-01	-	w	8.188E-05	+
seeds	l	5.999E-01	-	l	6.884E-01	-	l	8.612E-01	-	w	2.353E-06	+	w	4.383E-02	+	w	3.182E-06	+
smiley	l	5.899E-03	+	l	2.720E-03	+	l	2.857E-01	-	w	4.075E-04	+	l	7.485E-03	+	w	6.139E-04	+
varied	w	4.320E-01	-	w	7.361E-03	+	w	1.008E-02	+	w	1.734E-06	+	w	9.290E-01	-	w	1.734E-06	+
vertebral3	w	3.854E-03	+	w	1.251E-04	+	w	4.284E-01	-	w	3.882E-06	+	w	4.277E-02	+	w	5.214E-06	+
wine	w	1.749E-04	+	w	4.801E-06	+	w	4.270E-02	+	w	2.602E-06	+	w	4.789E-06	+	w	3.144E-06	+
	8/7/0		6/9	11/4/0		8/7	11/4/0		8/7	15/0/0		15/0	10/5/0		9/6	15/0/0		15/0

Conclusion

This article presents a new hybrid model named ANN-LevySAO to optimize weights and bias values of artificial neural networks. The snow ablation optimizer is a metaheuristic algorithm inspired by the physical events that occur during snow melting.

The main contribution of this study can be summarized as follows:

- Local search capability of the SAO algorithm has been improved by using the Levy flight mechanism and the LevySAO algorithm is presented.
- Parameter tuning of the proposed LevySAO algorithm has been done.
- By using the proposed LevySAO algorithm with together the ANN, an ANN-LevySAO hybrid model has been developed.
- ANN-LevySAO hybrid model is run on 15 different classification datasets - aggregation, aniso, balance, ecoli, glass, iris, iris2D, liver, mouse, pathbased, seeds, smiley, varied, vertebral3, wine.
- The ANN-LevySAO hybrid model is compared with 12 different models in terms of sensitivity, specificity, precision and F1-score metric results.
- The obtained metric results were compared using the Friedman test and head-to-head performance comparison methods.
- Comparisons show that the proposed ANN-LevySAO model has significantly superior performance than other models in many cases.
- In addition, the results of the Wilcoxon signed rank test at the 95% confidence interval showed that the proposed model achieved statistically significant results in most cases.
- The ANN-LevySAO model outperforms the ANN-SAO model in almost all cases, which confirms that the proposed LevySAO algorithm improves the performance of the original SAO.

In future studies, the ANN-LevySAO model can be applied to different real-world problems including large datasets. Further research regarding the architecture of the ANN and the role of the activation function would be worthwhile. Besides, the ANN-LevySAO can be hybridized with another metaheuristic algorithm to increase its success.

References

Abdollahzadeh, B., Gharehchopogh, F. S., & Mirjalili, S. (2021). African vultures optimization algorithm: A new nature-inspired metaheuristic algorithm for global optimization problems. *Computers & Industrial Engineering, 158*, 107408. doi:https://doi.org/10.1016/j.cie.2021.107408

Abdollahzadeh, B., Khodadadi, N., Barshandeh, S., Trojovský, P., Gharehchopogh, F. S., El-kenawy, E.-S. M., . . . Mirjalili, S. (2024). Puma optimizer (PO): a novel metaheuristic optimization algorithm and its application in machine learning. *Cluster Computing, 27*(4), 5235-5283. doi:10.1007/s10586-023-04221-5

Abualigah, L., Abd Elaziz, M., Sumari, P., Geem, Z. W., & Gandomi, A. H. J. E. S. w. A. (2022). Reptile Search Algorithm (RSA): A nature-inspired meta-heuristic optimizer. *191*, 116158.

Aljarah, I., Faris, H., & Mirjalili, S. (2018). Optimizing connection weights in neural networks using the whale optimization algorithm. *Soft Computing, 22*, 1-15.

Anderson, D., & McNeill, G. (1992). Artificial neural networks technology. *Kaman Sciences Corporation, 258*(6), 1-83.

Ansari, A., Ahmad, I. S., Bakar, A. A., & Yaakub, M. R. (2020). A hybrid metaheuristic method in training artificial neural network for bankruptcy prediction. *IEEE access, 8*, 176640-176650.

Aslan, M., Gunduz, M., & Kiran, M. S. (2023). A Jaya-based approach to wind turbine placement problem. *Energy Sources, Part A: Recovery, Utilization, and Environmental Effects, 45*(2), 3318-3337. doi:10.1080/15567036.2020.1805528

Ataseven, B. (2013). Yapay sinir ağlari ile öngörü modellemesi. *Öneri Dergisi, 10*(39), 101-115.

Bairathi, D., & Gopalani, D. (2021). Numerical optimization and feed-forward neural networks training using an improved optimization algorithm: multiple leader salp swarm algorithm. *Evolutionary Intelligence, 14*(3), 1233-1249.

Bhullar, A. K., Kaur, R., & Sondhi, S. (2022). Optimization of fractional order controllers for AVR system using distance and levy-flight based crow search algorithm. *IETE Journal of Research, 68*(5), 3900-3917.

Brown, C. T., Liebovitch, L. S., & Glendon, R. (2007). Lévy flights in Dobe Ju/'hoansi foraging patterns. *Human Ecology, 35*, 129-138.

Bui, D.-K., Nguyen, T., Chou, J.-S., Nguyen-Xuan, H., & Ngo, T. D. (2018). A modified firefly algorithm-artificial neural network expert system for predicting compressive and tensile strength of high-performance concrete. *Construction and Building Materials, 180*, 320-333.

Bui, D.-K., Nguyen, T. N., Ngo, T. D., & Nguyen-Xuan, H. (2020). An artificial neural network (ANN) expert system enhanced with the electromagnetism-based firefly algorithm (EFA) for predicting the energy consumption in buildings. *Energy, 190*, 116370.

Chen, X., Yi, Z., Zhou, Y., Guo, P., Farkoush, S. G., & Niroumandi, H. (2021). Artificial neural network modeling and optimization of the Solid Oxide Fuel Cell parameters using grey wolf optimizer. *Energy Reports, 7*, 3449-3459.

Cinar, A. C., & Kiran, M. S. (2018). Similarity and logic gate-based tree-seed algorithms for binary optimization. *Computers Industrial Engineering, 115*, 631-646.

Çelik, İ., Yıldız, C., & Şekkeli, M. (2018). Rüzgâr Enerji Santrali kurulumunda rüzgâr türbinlerinin mikro yerleşimi için bir optimizasyon modeli. *Gazi University Journal of Science Part C: Design Technology, 6*(4), 898-908.

Darshan, R., Pavan, H., Pratheesh, R., Raj, M. S., Suresh, K., & Prathap, C. (2021). *An IoT Enabled Water Management System with Water Usage Prediction using ANN*. Paper presented at the 2021 2nd Global Conference for Advancement in Technology (GCAT).

Deng, L., & Liu, S. (2023). Snow ablation optimizer: A novel metaheuristic technique for numerical optimization and engineering design. *Expert Systems with Applications, 225*, 120069.

El-kenawy, E.-S. M., Khodadadi, N., Mirjalili, S., Abdelhamid, A. A., Eid, M. M., & Ibrahim, A. (2024). Greylag Goose Optimization: Nature-inspired optimization algorithm. *Expert Systems with Applications, 238*, 122147. doi:https://doi.org/10.1016/j.eswa.2023.122147

Faramarzi, A., Heidarinejad, M., Mirjalili, S., & Gandomi, A. H. (2020). Marine Predators Algorithm: A nature-inspired metaheuristic. *Expert Systems with Applications, 152*, 113377.

Gao, J., Gao, F., Ma, Z., Huang, N., & Yang, Y. (2021). Multi-objective optimization of smart community integrated energy considering the utility of decision makers based on the Lévy flight improved chicken swarm algorithm. *Sustainable Cities and Society, 72*, 103075.

Gao, Y., Zhang, H., Duan, Y., & Zhang, H. (2023). A novel hybrid PSO based on levy flight and wavelet mutation for global optimization. *Plos one, 18*(1), e0279572.

Gong, S., Gao, W., & Abza, F. (2020). Brain tumor diagnosis based on artificial neural network and a chaos whale optimization algorithm. *Computational Intelligence, 36*(1), 259-275.

Gupta, S., & Deep, K. (2020). A novel hybrid sine cosine algorithm for global optimization and its application to train multilayer perceptrons. *Applied Intelligence, 50*(4), 993-1026.

Gülcü, Ş. (2022). Training of the feed forward artificial neural networks using dragonfly algorithm. *Applied soft computing, 124*, 109023.

Hashim, F. A., Houssein, E. H., Hussain, K., Mabrouk, M. S., Al-Atabany, W. J. M., & Simulation, C. i. (2022). Honey Badger Algorithm: New metaheuristic algorithm for solving optimization problems. *192*, 84-110.

Irmak, B., Karakoyun, M., & Gülcü, Ş. (2023). An improved butterfly optimization algorithm for training the feed-forward artificial neural networks. *Soft Computing, 27*(7), 3887-3905. doi:10.1007/s00500-022-07592-w

Ismaeel, A. A., Houssein, E. H., Khafaga, D. S., Aldakheel, E. A., AbdElrazek, A. S., & Said, M. (2024). Performance of Snow Ablation Optimization for Solving Optimum Allocation of Generator Units. *IEEE access*.

Jamal, R., Zhang, J., Men, B., Khan, N. H., Youssef, A.-R., Ebeed, M., & Kamel, S. (2023). Optimal scheduling of short-term hydrothermal with integration of renewable energy resources using Lévy spiral flight artificial hummingbird algorithm. *Energy Reports, 10*, 2756-2777.

Jia, H., You, F., Wu, D., Rao, H., Wu, H., & Abualigah, L. (2023). Improved snow ablation optimizer with heat transfer and condensation strategy for global optimization problem. *Journal of Computational Design Engineering Structures, 10*(6), 2177-2199.

Kandel, M. A., Rizk, F. H., Hongou, L., Zaki, A. M., Khan, H., & El-Kenawy, E.-S. M. J. F. L. A. (2023). Evaluating the Efficacy of Deep Learning Architectures in Predicting Traffic Patterns for Smart City Development. *6*(2), 26-26-35.

Karaboga, D., & Akay, B. (2007). *Artificial bee colony (ABC) algorithm on training artificial neural networks.* Paper presented at the 2007 IEEE 15th Signal Processing and Communications Applications.

Karaboga, D., & Akay, B. (2009). A comparative study of artificial bee colony algorithm. *Applied mathematics and computation, 214*(1), 108-132.

Kaya, E. (2022). A comprehensive comparison of the performance of metaheuristic algorithms in neural network training for nonlinear system identification. *Mathematics, 10*(9), 1611.

Kazemi, R., Golafshani, E. M., & Behnood, A. (2023). Compressive strength prediction of sustainable concrete containing waste foundry sand using metaheuristic optimization-based hybrid artificial neural network. *Structural Concrete*.

Kong, M., Tian, P., & Kao, Y. (2008). A new ant colony optimization algorithm for the multidimensional knapsack problem. *Computers Operations Research, 35*(8), 2672-2683.

Li, J., Soradi-Zeid, S., Yousefpour, A., & Pan, D. (2024). Improved differential evolution algorithm based convolutional neural network for emotional analysis of music data. *Applied soft computing, 153*, 111262.

Li, P., Zhang, Y., Gu, J., & Duan, S. (2024). Prediction of compressive strength of concrete based on improved artificial bee colony-multilayer perceptron algorithm. *Scientific Reports, 14*(1), 6414.

Maleki, B., Ghazvini, M., Ahmadi, M. H., Maddah, H., & Shamshirband, S. (2019). Moisture estimation in cabinet dryers with thin-layer relationships using a genetic algorithm and neural network. *Mathematics, 7*(11), 1042.

Markelle Kelly, R. L., Kolby Nottingham. The UCI Machine Learning Repository. Retrieved from https://archive.ics.uci.edu

McCulloch, W. S., & Pitts, W. (1943). A logical calculus of the ideas immanent in nervous activity. *The bulletin of mathematical biophysics, 5*, 115-133.

Mirjalili, S. (2015). How effective is the Grey Wolf optimizer in training multi-layer perceptrons. *Applied Intelligence, 43*, 150-161.

Mirjalili, S. (2016). SCA: a sine cosine algorithm for solving optimization problems. *Knowledge-based systems, 96*, 120-133.

Mirjalili, S., Mirjalili, S. M., & Lewis, A. (2014). Grey wolf optimizer. *Advances in engineering software, 69*, 46-61.

Mohseni, S., Brent, A. C., Burmester, D., & Browne, W. N. (2021). Lévy-flight moth-flame optimisation algorithm-based micro-grid equipment sizing: An integrated investment and operational planning approach. *Energy and AI, 3*, 100047.

Narayanan, S. L., Kasiselvanathan, M., Gurumoorthy, K., & Kiruthika, V. (2023). Particle swarm optimization based artificial neural network (PSO-ANN) model for effective k-barrier count intrusion detection system in WSN. *Measurement: Sensors, 29*, 100875.

Özden, A., & İşeri, İ. (2023). COOT optimization algorithm on training artificial neural networks. *Knowledge and Information Systems, 65*(8), 3353-3383.

Özkış, A. (2024). A multi-population-based marine predators algorithm to train artificial neural network. *Soft Computing, 28*(17), 9547-9574.

Özkış, A., & Karakoyun, M. Kapasitesiz tesis yerleşim problemleri için geliştirilmiş ikili güve alevi optimizasyon algoritması A binary enhanced moth flame optimization algorithm for uncapacitated facility location problems.

Öztemel, E. (2003). *Yapay sinir ağlari*. Istanbul: PapatyaYayincilik.

Qaddoura, R., Faris, H., Aljarah, I., & Castillo, P. A. (2021). Evocluster: an open-source nature-inspired optimization clustering framework. *SN Computer Science, 2*, 1-12.

Qiao, W., Khishe, M., & Ravakhah, S. (2021). Underwater targets classification using local wavelet acoustic pattern and Multi-Layer Perceptron neural network optimized by modified Whale Optimization Algorithm. *Ocean Engineering, 219*, 108415.

Raziani, S., Ahmadian, S., Jalali, S. M. J., & Chalechale, A. (2022). An efficient hybrid model based on modified whale optimization algorithm and multilayer perceptron neural network for medical classification problems. *Journal of Bionic Engineering, 19*(5), 1504-1521.

Sada, S. O. (2021). Improving the predictive accuracy of artificial neural network (ANN) approach in a mild steel turning operation. *The International Journal of Advanced Manufacturing Technology, 112*(9), 2389-2398.

Saji, Y., & Barkatou, M. (2021). A discrete bat algorithm based on Lévy flights for Euclidean traveling salesman problem. *Expert Systems with Applications, 172*, 114639.

Si, T., Bagchi, J., & Miranda, P. B. (2022). Artificial neural network training using metaheuristics for medical data classification: an experimental study. *Expert Systems with Applications, 193*, 116423.

Song, Y., Meng, X., & Jiang, J. (2022). Multi-layer perception model with elastic grey wolf optimization to predict student achievement. *Plos one, 17*(12), e0276943.

Storn, R., & Price, K. (1997). Differential evolution–a simple and efficient heuristic for global optimization over continuous spaces. *Journal of global optimization, 11*, 341-359.

Talaat, M., Farahat, M., Mansour, N., & Hatata, A. (2020). Load forecasting based on grasshopper optimization and a multilayer feed-forward neural network using regressive approach. *Energy, 196*, 117087.

Thamaraimanalan, T., & Ramalingam, S. (2024). Hybrid Artificial Neural Network-based Grasshopper Optimization Algorithm for Anomaly Detection in Wireless Body Area Networks. *IETE Journal of Research*, 1-15.

Thankachan, P., Fida, A., & Pillai, T. M. (2024). *Health monitoring of steel structures using Cuckoo Search algorithm-based ANN.* Paper presented at the Structures.

Towfek, S., Khodadadi, N., Abualigah, L., & Rizk, F. H. (2024). AI in Higher Education: Insights from Student Surveys and Predictive Analytics using PSO-Guided

WOA and Linear Regression. *Journal of Artificial Intelligence in Engineering Practice, 1*(1), 1-17.

Tran-Ngoc, H., Khatir, S., De Roeck, G., Bui-Tien, T., & Wahab, M. A. (2019). An efficient artificial neural network for damage detection in bridges and beam-like structures by improving training parameters using cuckoo search algorithm. *Engineering Structures, 199*, 109637.

Turkoglu, B., & Kaya, E. (2020). Training multi-layer perceptron with artificial algae algorithm. *Engineering Science Technology, an International Journal, 23*(6), 1342-1350.

Uymaz, S. A., Tezel, G., & Yel, E. (2015). Artificial algae algorithm (AAA) for nonlinear global optimization. *Applied soft computing, 31*, 153-171.

Wilcoxon, F., Katti, S., & Wilcox, R. A. (1970). Critical values and probability levels for the Wilcoxon rank sum test and the Wilcoxon signed rank test. *Selected tables in mathematical statistics, 1*, 171-259.

Wolpert, D. H., & Macready, W. G. (1997). No free lunch theorems for optimization. *IEEE transactions on evolutionary computation, 1*(1), 67-82.

Wu, L., Mei, J., & Zhao, S. (2023). Pipeline damage identification based on an optimized back-propagation neural network improved by whale optimization algorithm. *Applied Intelligence, 53*(10), 12937-12954.

Yang, X. S., & Suash, D. (2009, 9-11 Dec. 2009). *Cuckoo Search via Lévy flights.* Paper presented at the 2009 World Congress on Nature & Biologically Inspired Computing (NaBIC).

Zamani, H., & Nadimi-Shahraki, M. H. (2024). An evolutionary crow search algorithm equipped with interactive memory mechanism to optimize artificial neural network for disease diagnosis. *Biomedical Signal Processing Control, 90,* 105879.

About The Authors

Ahmet ÖZKIŞ, received his bachelor's, master's and doctorate degrees from the Department of Computer Engineering of Selçuk University. His areas of expertise are metaheuristic algorithms, artificial intelligence and machine learning. He is still serving as an associate professor of the Department of Computer Engineering at Necmettin Erbakan University in Konya, Türkiye.

E-mail : aozkis@erbakan.edu.tr, **ORCID :** 0000-0002-1899-5494

About The Authors

Feyza Nur ÖZDEMİR is a lecturer in the Artificial Intelligence Operator Program at Doğuş University Vocational School. She has a master's degree in Computer Engineering from Necmettin Erbakan University. Her primary interests are artificial intelligence, metaheuristic algorithms, optimization, and machine learning. She worked in roles such as project manager and researcher in TUBITAK 2209-A projects. She has published five articles in national and international journals.

E-mail : fozdemir@dogus.edu.tr, **ORCID :** 0000-0001-7803-7725

Similarity Index:

The similarity index obtained from the plagiarism software for this book chapter is 23%.

Recent Studies on Metaheuristic Optimization for University Course and Exam Scheduling

Halil İbrahim AYAZ
Necmettin Erbakan University

Sena EMİL
Necmettin Erbakan University

To Cite This Chapter:
Ayaz, H. İ., & Emil, S. (2025). Recent studies on metaheuristic optimization for university course and exam scheduling. In S. Kocer & O. Dundar (Eds.), *Next generation engineering: Smart solutions and applications* (pp. 120–140). ISRES Publishing.

Introduction

University course and examination timetabling problems (UCTP and UETP) have long been recognized as emblematic NP-hard optimization challenges at the intersection of operations research, artificial intelligence, and educational management (Siew et al., 2024; Tan et al., 2021). Modern universities must allocate thousands of students, courses, instructors, and rooms into limited time slots while simultaneously satisfying institutional regulations, pedagogical requirements, and fairness considerations. This complexity has been amplified by massification of higher education, modular curricula, diversified assessment strategies (e.g., online, hybrid, and continuous assessment), and the need to respond rapidly to disruptions such as pandemics or campus closures (Kamisli Ozturk et al., 2024; Modirkhorasani & Hoseinpour, 2024). As a result, timetabling is no longer a purely technical scheduling exercise; it is a core strategic function that shapes student experience, staff workload, and institutional efficiency.

Traditionally, a variety of exact optimization and constraint programming models were proposed to capture the combinatorial structure of UCTP and UETP. While these techniques provide valuable theoretical insights and optimality guarantees on small and medium instances (Dimitsas et al., 2025; Xiang et al., 2024), their applicability rapidly diminishes as problem size, constraint density, and heterogeneity increase (Hacibeyoglu & Ibrahim, 2018). In contrast, metaheuristic approaches such as Genetic Algorithms, Simulated Annealing, Variable Neighborhood Search, swarm intelligence, hyper-heuristics, and hybrid frameworks have proved highly effective in handling realistic, large-scale timetabling instances (Leite et al., 2018; Leite et al., 2019; Bellio et al., 2021; Abayomi-Alli et al., 2019). They offer the flexibility to encode complex constraints, the scalability to cope with thousands of entities, and the robustness to adapt to institutional specifics without redesigning the model from scratch (Doğan & Yurtsal, 2021; Haddad et al., 2022).

Despite the large body of research on timetabling, several developments in the last decade justify a focused re-examination of metaheuristic methodologies (Ibrahim, 2021). First, there has been a clear evolution from single, stand-alone metaheuristics toward hybrid and multi-neighborhood algorithms that combine global exploration with powerful local search operators (Abayomi-Alli et al., 2020; Bellio et al., 2021; Alamri et al., 2020). Second, hyper-heuristics and learning-based controllers have emerged, aiming to automate heuristic selection and improve generalization across instances and institutions (Dewi et al., 2021; Zhu et al., 2026; Muklason et al., 2024). Third, pandemic-aware, decentralized, and mobility-sensitive models have extended the scope of timetabling beyond classical time–room assignment to encompass health risks, travel distances, and multi-campus structures (Kamisli Ozturk et al., 2024; Modirkhorasani & Hoseinpour, 2024; Diri et al., 2025). Finally, the integration of AI, uncertainty modeling, and even quantum-inspired optimization has begun to reshape how timetabling is conceptualized and solved (Thuy & Benoit, 2024; Zhou et al., 2025; Ghaffar et al., 2025).

This chapter is motivated by these rapid methodological and contextual changes. Rather than providing yet another broad overview of all timetabling research, it concentrates specifically on metaheuristic and hybrid metaheuristic solution methodologies for university course and exam timetabling in the recent period (approximately 2019–2026). By focusing on this subset, the chapter aims to: (i) capture the most recent algorithmic innovations (e.g., preference-based Firefly methods, Beluga Whale Optimization, multi-neighborhood SA), (ii) map how metaheuristic design has evolved from single operators to sophisticated hybrid and hyper-heuristic frameworks (Zhu et al., 2026; Al-Betar, 2021), and (iii) identify which types of problem extensions such as pandemic constraints, decentralized centers, and exam content design—have already been addressed and which remain underexplored.

At the same time, this review deliberately acknowledges several limitations in its scope. First, it concentrates on university-level course and examination timetabling, and does not systematically cover primary or secondary school timetabling, workforce rostering, or related scheduling problems, except where they offer direct methodological insight (Tan et al., 2021). Second, the chapter places emphasis on metaheuristic and hybrid metaheuristic approaches; purely exact optimization or constraint-programming-based methods are discussed mainly insofar as they serve as baselines, structural anchors, or components of hybrid frameworks (Xiang et al., 2024; Battistutta et al., 2020). Third, the review is restricted to peer-reviewed journal and conference publications available in English within the specified time window, which means that some relevant technical reports, theses, or non-English contributions may not be captured. Finally, although the chapter includes AI-driven and quantum-inspired work where it directly targets timetabling, it does not attempt an exhaustive survey of general AI or machine learning literature.

Within these boundaries, the chapter makes three main contributions. First, it provides a structured synthesis of 34 peer-reviewed studies, classifying them by solution paradigm (exact and CP-based, metaheuristic, hyper-heuristic and hybrid, pandemic-aware and decentralized, AI-driven and quantum-inspired) and by problem type (course timetabling, exam timetabling, or extended exam content design). Second, it offers a methodological analysis of how specific algorithmic features—such as multi-neighborhood Simulated Annealing (Bellio et al., 2021), GA–Tabu hybrids (Abayomi-Alli et al., 2020), PSO–local search combinations (Abayomi-Alli et al., 2019), Steepest-Ascent Hill Climbing hyper-heuristics (Muklason et al., 2024), and Beluga Whale Optimization for exam generation (Diri et al., 2025)—contribute to improved solution quality, computational efficiency, and adaptability. Third, it distills survey-based insights and research gaps, emphasizing the need for reinforcement-learning-based heuristic selection (Siew et al., 2024; Ghaffar et al., 2025), multi-stakeholder fairness modeling, robust and uncertainty-aware optimization, explainable and trustworthy AI, real-time adaptive scheduling, and integrated course–exam formulations.

The remainder of this article is organized into four main sections. Section 2 presents a comprehensive literature review, structured around five methodological domains that reflect the evolution of timetabling research—from exact and constraint programming approaches to metaheuristics, hyper-heuristics, hybrid systems, and emerging AI-driven or quantum-inspired techniques. Section 3 introduces a methodological taxonomy and classification framework that synthesizes these developments into a unified conceptual structure, enabling clearer comparisons across algorithmic families and application contexts. Section 4 discusses the key findings, research gaps, and implications arising from recent studies, emphasizing methodological trends, unresolved challenges, and opportunities for innovation. Finally, Section 5 offers conclusions and outlines future research directions, highlighting the potential of adaptive, learning-enhanced, and scalable timetabling systems to shape the next generation of educational scheduling.

Literature Review

University course and examination timetabling problems (UCTP and UETP) remain central topics within operations research, artificial intelligence, and educational scheduling systems. As NP-hard combinatorial optimization problems, they require balancing large numbers of hard constraints—such as avoiding student conflicts, respecting room capacities, and ensuring feasibility—with soft constraints involving fairness, workload distribution, travel distance, and user satisfaction. Over the last two decades, a rich ecosystem of solution methodologies has emerged, ranging from exact optimization and constraint programming to metaheuristics, hyper-heuristics, hybrid models, and most recently, AI-driven and pandemic-responsive approaches. This section synthesizes the state of the art by grouping the literature into five domains: exact and constraint programming (CP) techniques, metaheuristic approaches, hyper-heuristic and hybrid strategies, decentralized and pandemic-aware timetabling, and future trends including AI, uncertainty modeling, and quantum optimization.

Exact Optimization and Constraint Programming Approaches

Exact methods constitute the mathematical foundation of timetabling research. Although they often cannot scale to large instances, they provide optimality guarantees, benchmark baselines, and structural insights that inform heuristic frameworks. One of the most significant contributions in recent years is the work by Dimitsas et al. (2025), who provide the first proven optimal result for a classical uncapacitated exam timetabling benchmark. Using a strengthened mixed-integer programming (MIP) formulation enriched with tailored cutting planes and feasibility-preserving transformations, the authors resolve a long-standing open question about the optimal objective value of a benchmark previously treated as too difficult for exact methods. Their findings recalibrate how researchers measure algorithmic performance and highlight the importance of provably optimal reference points.

Similarly, Xiang et al. (2024) develop an extensive MILP formulation for the university course scheduling problem (UCSP), incorporating instructor preferences, balanced weekly distribution, course block structures, and room-type suitability. The authors observe that while exact solvers like CPLEX can handle small problem sizes, real-world datasets with hundreds of courses and thousands of students exceed tractable limits. To overcome this, the study integrates exact modeling with heuristic search through a two-phase strategy in which a genetic algorithm clusters related scheduling components and tabu search refines assignments. The hybrid exact–metaheuristic structure significantly improves solution quality while retaining the interpretability and constraint transparency provided by MILP.

Constraint programming has been leveraged for initial feasibility construction in real-world contexts. In Local Search and Constraint Programming for a Real-World Examination Timetabling Problem (2020), CP generates an initial conflict-free timetable, respecting hard constraints such as exam collisions, invigilation limits, and room capacities. Subsequent local search using swap and Kempe-chain operators optimizes soft objectives, yielding schedules with drastically reduced manual adjustment time. CP’s strength lies in its expressive constraint modeling and backtracking mechanisms, making it an ideal partner for heuristic refinements.

Other constructive approaches, such as graph-coloring-based exam assignment (Rahani et al., 2021), reinforce the role of exact and rule-based logic in building base timetables.

Together, these exact and CP-based methods serve as structural anchors, ensuring robust feasibility and furnishing high-quality baselines for heuristic and hybrid algorithms.

Metaheuristic Approaches

Metaheuristics remain the dominant family of algorithms in timetabling research due to their robustness, scalability, and adaptability to institution-specific parameters. A wide variety of metaheuristics—Simulated Annealing (SA), Genetic Algorithms (GA), Particle Swarm Optimization (PSO), Bees Algorithm, Firefly Algorithm, Harmony Search, and Whale Optimization—have been applied successfully to UETP and UCSP.

Simulated Annealing (SA) and its Variants

SA continues to be a foundational method due to its simplicity and strong performance on diverse datasets. Leite et al. (2018) propose a cellular memetic SA hybrid in which individuals interact through a 2D grid structure, promoting exploration while maintaining solution diversity. The incorporation of threshold-acceptance local search improves fine-grained refinement, resulting in several best-known solutions on Toronto and ITC-2007 benchmarks.

To improve computational efficiency, Leite et al. (2019) introduce Fast Simulated Annealing (FastSA). By dividing the temperature schedule into bins and evaluating only moves associated with recently modified exams, computational costs decrease dramatically, in some cases by more than 40%, without degradation in solution quality.

Building on these advancements, Bellio et al. (2021) develop a two-stage multi-neighborhood SA. Stage one focuses on establishing feasibility using simple neighborhoods (MoveExam, SwapExam), while stage two refines quality using more sophisticated operators (KickExam, Kempe-Chains, SwapPeriods). The approach achieves nine new best-known results on the Carter dataset, highlighting the importance of tailored neighborhood structures.

Genetic Algorithms and Evolutionary Methods

GA-based approaches appear prominently in several studies. Tung et al. (2021) apply a multi-objective GA framework, incorporating constraints such as workload balancing and minimizing consecutive exams. In practice-oriented work, Doğan & Yurtsal (2021) design a GA-based decision support system (DSS) for handling large exam datasets, demonstrating substantial reductions in constraint violations.

Swarm Intelligence and Nature-Inspired Methods

Swarm intelligence approaches have diversified extensively:

- Bees Algorithm (Haddad et al., 2022) optimizes multi-exam composition by balancing exploration (scout bees) and exploitation (worker bees).

- Firefly Algorithm, extended with preference-based stepping mechanisms, accelerates convergence by using student preference profiles as directional cues.
- Particle Swarm Optimization with local search components (Abayomi-Alli et al., 2019) effectively handles the discrete, multi-constraint structure of UETP.
- Harmony Search improvements (Alamri et al., 2020) introduce adaptive pitch adjustment for handling exam–room matching.
- Predator–prey metaheuristics (Tilahun, 2019) offer an innovative competition-driven search model.
- B-Hill Climbing Optimizer (Al-Betar, 2021) integrates greedy hill-climbing with randomization, performing strongly on conflict-intensive cases.

Finally, Lulu et al. (2024) compare GA and SA in a case-study from the University of Sharjah, demonstrating context specificity: GA converges faster computationally, while SA often yields structurally superior schedules.

Metaheuristic studies collectively demonstrate that the key determinants of performance are neighborhood richness, problem-specific operators, and informed move evaluation, rather than the high-level algorithm class.

Hyper-Heuristics and Hybrid Models

Hyper-heuristics (HHs) aim to generalize across problem domains by selecting or generating low-level heuristics dynamically during the search process. Their emphasis on decision rules rather than problem-specific operators allows them to achieve scalability and adaptability, making them particularly attractive for deployment in institutional timetabling environments. Within this context, Dewi et al. (2021) evaluate several HH configurations that combine a Largest Degree construction heuristic with hill-climbing and tabu search improvement mechanisms. Their findings indicate that tabu-search-based HH variants outperform simpler heuristics by up to 58%, demonstrating that the ability to learn and select the most appropriate heuristic at each stage of the search is as critical as the design of the heuristics themselves.

Building on the concept of adaptive heuristic selection, Zhu et al. (2026) introduce the Genetic and Greedy Strategy Hyper-Heuristic (GA_RG_HH). In their framework, a genetic algorithm determines sequences of low-level heuristics—ranging from random to greedy to hybrid operators—whose composition evolves according to the structure of the search landscape. This adaptive sequencing enables the algorithm to outperform traditional approaches such as tabu search, particle swarm optimization, and simulated annealing across multiple datasets, highlighting the benefits of integrating heuristic learning with evolutionary control mechanisms.

At the systems level, Muklason et al. (2024) develop a generic university examination timetabling system built on Steepest-Ascent Hill Climbing hyper-heuristics. Their platform significantly reduces penalty scores compared to standard hill-climbing and illustrates how hyper-heuristic approaches can be embedded within fully automated, institution-ready software systems. By emphasizing modularity and generality, their work showcases the practical value of HHs as robust, reusable scheduling engines.

Hybrid models further extend these advancements by combining algorithmic paradigms to leverage complementary strengths. Examples in the literature include the integration of Genetic Algorithms with Tabu Search, the combination of Particle Swarm Optimization with Local Search, enhancements of Harmony Search using adaptive heuristic mechanisms, GA–SA hybrid structures for decentralized scheduling, metaheuristic–MILP frameworks for handling exact substructures, and quantum annealing paired with classical local search refinements. As noted by Ghaffar et al. (2025), such hybridization strategies consistently yield improvements over single-method approaches, though the systematic evaluation and theoretical grounding of hybrid design choices remain limited. These observations collectively underscore the growing importance of hybrid and hyper-heuristic methods as high-performing, flexible, and generalizable solutions for modern timetabling challenges.

Pandemic-Aware, Mobility-Aware, and Decentralized Timetabling

The COVID-19 pandemic triggered a paradigm shift emphasizing safety, capacity limitations, physical distancing, and decentralized scheduling.

Pandemic-Aware Scheduling

Kamisli Ozturk et al. (2024) propose a decision support system that integrates social distancing, reduced room occupancy, and student-interaction minimization into a multi-objective GA-based scheduler. Their tool handles large data volumes and produces physically distanced, conflict-free timetables across eight departments, showing how epidemiological constraints can be built directly into scheduling.

Decentralized Exam Centers

A more radical structural adaptation appears in Modirkhorasani & Hoseinpour (2024), who introduce decentralized exam scheduling over multiple centers. Their nonlinear model jointly optimizes center selection, travel distances, time-slot assignment, and student–center allocation. The hybrid GA–SA solver significantly outperforms standalone metaheuristics, demonstrating the benefit of hybridization under spatial constraints. Complementary research using Discrete Whale Optimization (D-WOA) further reduces travel distances and improves fairness.

AI-Driven Exam Content Planning

Beyond timetable construction, Diri et al. (2025) propose a Beluga Whale Optimization–based exam suggestion system that constructs balanced exam papers from a 12,000-item question bank. This expands exam optimization into the domain of assessment design, focusing on fairness, difficulty calibration, and item-distribution balance.

These studies collectively reveal that timetabling is evolving from a static scheduling problem into a broader risk-sensitive, mobility-aware, and pedagogically informed decision-making domain.

AI-Driven, Explainable, and Quantum-Inspired Directions

The newest frontier involves AI, learning-based heuristic selection, uncertainty quantification, and quantum optimization.

AI and Explainability

Thuy & Benoit (2024) propose an uncertainty-aware neural decision framework that models epistemic and aleatoric uncertainty while offering interpretable insights. Although not originally applied to timetabling, the methodology is directly relevant to making AI-driven scheduling decisions transparent, especially in sensitive contexts like pandemic scheduling or fairness enforcement.

Quantum Optimization

A novel line of work, (Zhou et al., 2025), maps timetabling into a QUBO structure and uses quantum annealers for initialization before applying classical local search refinements. While experimental, these methods point toward future scalability for very large institutions.

Table 1 provides a structured synthesis of 34 peer-reviewed studies published between 2019 and 2026, covering the full methodological landscape of university course and examination timetabling research. The table categorizes each study according to its primary solution technique, publication details, problem type, and core contributions, enabling a comparative understanding of how different metaheuristic and hybrid approaches address the complexities of timetabling. As shown in the table, a wide spectrum of algorithms—including Genetic Algorithms, Simulated Annealing variants, Firefly and Bee-based swarm intelligence techniques, multi-neighborhood and hyper-heuristic frameworks, as well as emerging quantum-inspired and machine-learning-assisted models—have been applied across both benchmark and real-world datasets.

A prominent pattern observable in the table is the shift from single metaheuristics toward hybrid architectures, such as GA combined with Tabu Search, PSO enhanced with Local Search, and decentralized scheduling models solved via GA–SA hybrids. These studies consistently report improvements in solution quality, convergence speed, or robustness compared to their standalone counterparts. Additionally, multi-neighborhood Simulated Annealing and hyper-heuristic approaches illustrate a second dominant trend, emphasizing adaptability and fine-grained search diversification. The table also highlights methodological expansions beyond classical scheduling tasks, such as exam-content optimization via Beluga Whale Optimization and pandemic-aware models incorporating social distancing and mobility constraints. Finally, the inclusion of exact, graph-coloring, and quantum annealing–based methods underscores the methodological heterogeneity of the field and points to increasing interest in integrating metaheuristics with exact or AI-driven frameworks.

Overall, Table 1 illustrates not only the breadth of solution methodologies applied to timetabling problems but also the evolution of the field toward more hybrid, adaptive, multi-objective, and context-aware optimization strategies. This consolidated view enables researchers to identify dominant methodological directions, gaps in the literature, and promising avenues for future exploration.

Table 1

Summary of Articles

No	Method / Algorithm	APA Reference	Year	Problem Type	Key Contribution
1	GA + Tabu (GATS-CS)	Abayomi-Alli et al.	2020	Exam	Combined GA with TS memory; reduces clashes and improves placement quality.
2	PSO + Local Search	Abayomi-Alli et al.	2019	Exam	Hybrid PSO framework with LS improving exploitation on real datasets.
3	Harmony Search	Alamri et al.	2020	Exam	HS improved with pitch adjustment; better room–exam allocation.
4	B-Hill Climbing	Al-Betar	2021	Exam	Novel discrete hill-climbing variant for high-density conflict graphs.
5	Multi-Neighborhood SA	Bellio et al.	2021	Exam	Two-stage SA producing 9 new best-known results in Carter dataset.
6	Hyper-heuristic	Dewi et al.	2021	Exam	Adaptive HH combining LD, hill-climbing, TS; 18–58% improvement.
7	Optimal MIP	Dimitsas et al.	2025	Exam	First proven optimal benchmark solution for UETP.
8	Beluga Whale Optimization	Diri et al.	2025	Exam Content	AI-based question-set generator; maintains difficulty distribution.
9	GA-based DSS	Doğan & Yurtsal	2021	Exam	Decision support system for large faculties; reduces manual effort.
10	Exact + Metaheuristic	*Carlsson et al.*	2023	Exam	Hybrid exact–heuristic strategy improving feasibility.
11	Systematic Review	Ghaffar et al.	2025	Exam/Course	Identifies gaps in hybridization, ML-assisted timetabling.
12	Bees Algorithm	Haddad et al.	2022	Exam	Multi-exam composition with adaptive neighborhood exploration.

No	Method / Algorithm	APA Reference	Year	Problem Type	Key Contribution
13	Quantum Annealing Hybrid	Zhou et al.	2025	Exam	QUBO-based formulation solved with quantum + classical LS.
14	Pandemic GA Scheduler	Kamisli Ozturk et al.	2024	Exam	COVID-aware model: distancing, capacity, interaction minimization.
15	ABC Review	Karaboga & Basturk	2022	Survey	Comprehensive review of ABC applications in optimization.
16	Memetic Algorithm	Leite et al.	2018	Exam	Cellular memetic structure improving diversity & exploitation.
17	Fast SA	Leite et al.	2019	Exam	Efficient SA using temperature bins; 40% fewer evaluations.
18	CP + Local Search	*Local Search & CP…*	2020	Exam	CP ensures feasibility; LS minimizes soft penalties.
19	GA vs SA	Lulu et al.	2024	Exam	Empirical comparison: GA faster, SA produces higher-quality schedules.
20	Graph Heuristic + LS	Mandal	2020	Exam	Interactive tool combining graph coloring with local refinement.
21	Course Timetabling Metaheuristics	Abdipoor et al.	2023	Course	Comparative analysis: GA, SA, TS, PSO, hybrids.
22	Decentralized Exam Scheduling	Modirkhorasani & Hoseinpour	2024	Exam	Multi-center scheduling minimizing travel distance; GA–SA hybrid best.
23	SAHC Hyper-Heuristic	Muklason et al.	2024	Exam	General-purpose system using steepest-ascent HH.
24	Preference-Based Firefly	Nand et al.	2024	Exam	Forward-looking FA with preference-based weighting.
25	Graph Coloring	Rahani et al.	2021	Exam	Constructive graph-coloring model for undergraduate programs.
26	Survey Methodologies	Siew et al.	2024	Exam	Comprehensive review of exam timetabling methods.
27	School Timetabling Survey	Tan et al.	2021	School/Exam	Reviews optimization strategies in school/education scheduling.
28	Uncertainty + Explainable AI	Thuy & Benoit	2024	AI/General	Framework for epistemic/aleatoric uncertainty; applicable to ML–timetabling.
29	Prey–Predator Algorithm	Tilahun	2019	Exam	Nature-inspired competitive search for discrete constraints.
30	Multi-Objective GA	Tung et al.	2021	Exam	GA minimizing conflicts + workload balance simultaneously.
31	MILP + GA/TS Hybrid	Xiang et al.	2024	Course	Exact–heuristic hybrid model improving quality & scalability.
32	GA–Greedy Hyper-Heuristic	Zhu et al.	2026	Course	GA selects heuristic sequences; strong performance across datasets.
33	Online Exam Scheduling (Bees)	Haddad et al.	2022	Exam	Handles multi-exam scheduling in online platforms.
34	Web-Based Course Timetabling System	Romaguera et al.	2024	Course	Full-stack course timetabling system with automated solver.

Survey Insights and Research Gaps

Comprehensive survey studies by Siew et al. (2024) and Ghaffar et al. (2025) highlight several emerging research directions and expose important methodological gaps that shape the future landscape of university course and examination timetabling.

First, surveys emphasize the increasing relevance of reinforcement learning–based heuristic selection, where learning policies dynamically choose low-level operators or neighborhood structures based on real-time performance feedback. This trend reflects a wider movement toward self-adaptive optimization frameworks that reduce reliance on manually tuned parameters.

Second, both surveys underscore the need for multi-stakeholder fairness modeling, noting that existing formulations predominantly focus on student-centric constraints while overlooking instructor preferences, administrative workload, accessibility considerations, or equity implications across different academic groups. The integration of fairness metrics into multi-objective optimization models remains an open and impactful research avenue.

Third, the literature identifies a growing interest in robust and uncertainty-aware optimization, especially in response to disruptions such as fluctuating enrollments, room unavailability, or sudden shifts in institutional policies. Robust optimization, stochastic modeling, and scenario-based planning are highlighted as under explored methodologies capable of enhancing real-world applicability.

Another gap involves the integration of explainability and trust metrics, particularly as AI-driven timetabling systems gain traction. Stakeholders increasingly demand interpretable decisions, transparent constraint handling, and confidence indicators—requirements that classical metaheuristics do not inherently satisfy.

Furthermore, the surveys point to the rising need for real-time adaptive scheduling, where systems can update timetables instantaneously in response to late enrollment changes, instructor absences, or emergency constraints. Such dynamic re-optimization requires algorithms capable of generating high-quality solutions under strict time limits.

Finally, both works identify the momentum behind hybrid AI–metaheuristic approaches, combining machine learning, hyper-heuristics, reinforcement learning, and classical optimization to achieve superior performance, scalability, and generalization. These hybrid systems offer a promising pathway toward unified, flexible, and context-aware scheduling engines.

Taken together, these insights suggest that the future of timetabling research is likely to converge toward intelligent, adaptive, learning-enhanced, and potentially quantum-assisted scheduling ecosystems. Such systems will extend far beyond the capabilities of traditional optimization approaches by leveraging data-driven intelligence, uncertainty modeling, real-time flexibility, and transparent decision-making frameworks.

Methodological Taxonomy and Classification

Advances in university course and examination timetabling research have created a diverse methodological ecosystem spanning exact optimization, metaheuristics, hyper-heuristics, hybrid models, and emerging AI-driven or quantum-inspired techniques. Understanding how these approaches relate to one another is essential for identifying suitable solution strategies for different institutional contexts. To provide a structured perspective, this section introduces a methodological taxonomy that classifies the 34 studies reviewed into four major categories: (1) Exact and Constraint Programming approaches, (2) Metaheuristic algorithms, (3) Hyper-heuristic and Hybrid frameworks, and (4) AI-driven, Learning-based, and Quantum-inspired methods.

This taxonomy reflects how algorithms differ not only by their labels but also by their underlying search behavior. While population-based metaheuristics such as Genetic Algorithms (GA) and Particle Swarm Optimization (PSO) emphasize distributed exploration, single-solution methods such as Simulated Annealing (SA) focus on controlled neighborhood-based improvement. Hyper-heuristics operate at a higher abstraction level by learning which heuristics to apply under different search conditions. Finally, AI-driven and quantum-inspired approaches point toward future directions where algorithms adapt autonomously, reason under uncertainty, or leverage new forms of computation. Together, these methodological layers illustrate an evolution from direct solution manipulation toward adaptive, learning-enhanced search systems.

Interpretation of the Taxonomy

The taxonomy reveals that timetabling research has moved through several layers of methodological sophistication. Exact and CP methods remain essential for high-fidelity constraint modeling and serve as baselines for evaluating heuristic approaches. Metaheuristics dominate practical applications because of their balance between scalability and flexibility. Hyper-heuristics elevate the search to a higher level by automating heuristic choice, enabling algorithms to generalize across datasets without manual tuning. The emergence of AI-driven and quantum-inspired approaches marks a significant conceptual shift: optimization systems are becoming more autonomous, adaptive, and capable of providing transparent decision support. The classification shows a clear trajectory from classical combinatorial search toward intelligent scheduling ecosystems.

Importance of Methodological Classification

This taxonomy is valuable for several reasons. First, it clarifies methodological boundaries, helping researchers distinguish between search strategies, heuristic operators, and learning mechanisms. Second, the classification highlights the evolution of the field, demonstrating how hybridization and hyper-heuristic design have become integral to achieving high-quality solutions on large-scale instances. Third, by mapping the landscape of existing work, the taxonomy identifies underrepresented areas such as reinforcement-learning-based timetabling, uncertainty-aware optimization, fairness modeling, and quantum-assisted scheduling. Finally, this structured overview supports the development of new frameworks by providing insight into which method classes align best with particular institutional needs, constraints, and computational capacities.

Key Findings, Research Gaps, and Implications

Key Findings from Recent Studies

A synthesis of the 34 reviewed studies reveals several dominant patterns in contemporary timetabling research. One of the most consistent findings is the clear advantage of metaheuristic and hybrid metaheuristic algorithms over purely exact optimization methods. Studies applying multi-neighborhood Simulated Annealing (Bellio et al., 2021), cellular and fast SA variants (Leite et al., 2018, 2019), and evolutionary approaches such as Genetic Algorithms (Tung et al., 2021; Doğan & Yurtsal, 2021) repeatedly demonstrate strong performance in large-scale and highly constrained environments. These approaches outperform exact models not because of the inherent superiority of any single metaheuristic but due to their ability to incorporate rich neighborhood structures, adaptive parameter adjustment, and domain-specific move operators. The literature also shows that hybridization—especially GA–Tabu combinations (Abayomi-Alli et al., 2020), PSO–local search hybrids (Abayomi-Alli et al., 2019), and enhanced multi-stage SA methods—provides further improvements by leveraging the complementary strengths of global and local search mechanisms.

Hyper-heuristics represent another significant development, offering a generalized, higher-level search paradigm capable of selecting or generating heuristics dynamically. Research by Dewi et al. (2021), Zhu et al. (2026), and Muklason et al. (2024) demonstrates that hyper-heuristic controllers improve generalization across datasets while reducing the need for manual parameter tuning. Meanwhile, the emergence of pandemic-aware, mobility-sensitive, and decentralized models has expanded the scope of timetabling research toward more realistic operational constraints. Studies incorporating distancing rules, center allocation, and exam logistics (Kamisli Ozturk et al., 2024; Modirkhorasani & Hoseinpour, 2024) show that timetabling algorithms can be adapted to institutional resilience and risk-sensitive decision-making. Furthermore, the inclusion of AI-driven approaches such as uncertainty-aware neural decision systems (Thuy & Benoit, 2024) and quantum-inspired optimization models (Zhou et al., 2025) illustrates the early stages of a transition toward intelligent, self-adaptive scheduling systems capable of reasoning under uncertainty.

Research Gaps and Unresolved Challenges

Despite notable methodological progress, several substantial gaps remain in the literature. One persistent challenge is the absence of integrated course–exam formulations, even though most universities must coordinate both schedules simultaneously. Existing studies largely treat these problems separately, which limits coherence across curricula and creates operational inefficiencies. Another major gap concerns the limited adoption of reinforcement learning and other adaptive AI methods within timetabling. Although survey studies (Siew et al., 2024; Ghaffar et al., 2025) highlight the potential of RL-guided heuristic selection, no reviewed study offers a mature RL-driven hyper-heuristic capable of long-term adaptation or learning-based parameter control.

Fairness and multi-stakeholder considerations also remain insufficiently addressed. The majority of optimization models prioritize minimizing student conflicts or penalty functions but rarely incorporate instructor workload fairness, accessibility constraints, or equitable room distributions, despite their growing institutional importance. Similarly, the limited use of robust and uncertainty-aware optimization methods means that existing models often assume static input data. Real timetabling environments, however, experience disruptions due to late registrations, instructor absences, or room unavailability, conditions that require stochastic or scenario-based modeling. Another unresolved challenge relates to benchmarking: widely used datasets such as the Carter and ITC sets capture only a narrow subset of real-world complexity. No public dataset currently integrates pandemic-related constraints, geographic mobility, decentralized centers, or fairness considerations, restricting the ability to evaluate next-generation algorithms.

Methodological Trends Identified

The reviewed literature reveals clear methodological trends that characterize the current state of university timetabling research. A prominent trend is the rising popularity of hybrid metaheuristics, where global exploration and local refinement are combined to exploit problem structure more effectively. Examples include multi-phase Simulated Annealing frameworks (Bellio et al., 2021), GA–TS hybrids (Abayomi-Alli et al., 2020), and PSO–local search models (Abayomi-Alli et al., 2019). These algorithms consistently outperform their single-method counterparts, suggesting that hybridization has become a core design principle rather than a supplementary technique.

Another key trend is the increasing emphasis on multi-neighborhood and problem-specific operators, reflecting a shift away from generic search behavior toward highly customized local improvement mechanisms. Concurrently, the adoption of hyper-heuristics shows the growing interest in algorithmic generalization and automation, where high-level controllers select or construct heuristics dynamically based on feedback from the search landscape. Studies by Dewi et al. (2021), Muklason et al. (2024), and Zhu et al. (2026) demonstrate that such frameworks reduce manual intervention and enhance portability across different datasets. Emerging trends further include the integration of AI-driven reasoning, such as uncertainty modeling (Thuy & Benoit, 2024) and hybrid quantum–classical optimization pipelines (2025), signaling an evolution toward intelligent decision-support systems that transcend classical optimization boundaries.

Implications for Research and Practice

The methodological developments and research gaps outlined above have important implications for both academic researchers and institutional practitioners. From a research perspective, the findings indicate that progress will depend less on incremental enhancements to traditional metaheuristics and more on the integration of learning mechanisms, robust modeling, and hybrid computational paradigms. Timetabling is becoming a fertile domain for exploring intersections between optimization, AI, and decision analytics, with potential applications extending into workforce scheduling, transportation planning, and large-scale resource allocation.

For practitioners and universities, the reviewed studies demonstrate that advanced timetabling systems can significantly reduce administrative burden, improve student and instructor satisfaction, and enhance institutional resilience. Hybrid and hyper-heuristic systems—particularly those validated on real-world datasets (e.g., Doğan & Yurtsal, 2021; Kamisli Ozturk et al., 2024)—illustrate how automated scheduling tools can support day-to-day operations without requiring specialized algorithmic expertise. Moreover, the introduction of decentralized and pandemic-aware models highlights the need for timetabling solutions that remain stable under stress, adaptable to policy shifts, and responsive to contextual uncertainties.

Finally, the implications extend to system design and policy. Institutions seeking to implement or modernize scheduling platforms should prioritize algorithms capable of multi-objective trade-offs, real-time adjustment, and transparent decision justification, particularly as regulatory, ethical, and pedagogical demands continue to evolve.

Opportunities for Innovation

Although the current literature demonstrates impressive methodological diversity, it also points toward numerous opportunities for transformative innovation. One promising direction involves developing reinforcement-learning-driven hyper-heuristics capable of autonomously learning heuristic policies that evolve across semesters or datasets. Another opportunity lies in constructing fully integrated course–exam timetabling models, which could improve curriculum alignment, reduce conflicts, and optimize resource usage holistically. Additionally, quantum-inspired optimization methods, while nascent, offer potential pathways for scaling timetabling algorithms to extremely large or complex institutional contexts.

There is also considerable room for the advancement of fairness-aware and explainable timetabling, where optimization models explicitly balance equity among students and staff while providing transparent justification of scheduling decisions. Equally important is the development of real-time adaptive scheduling systems that can dynamically update solutions in response to late changes, disruptions, or evolving operational constraints. Finally, progress in the field depends heavily on the creation of next-generation open benchmark datasets that incorporate mobility, uncertainty, pandemic constraints, and multi-stakeholder fairness metrics, enabling more realistic and rigorous algorithmic evaluation.

Conclusions and Future Directions

This review has examined 34 peer-reviewed studies on university course and examination timetabling published between 2019 and 2026, offering a comprehensive synthesis of methodological advancements and emerging research trajectories. The analysis reveals that timetabling has evolved from a classical combinatorial optimization problem into a multifaceted decision-making domain shaped by pedagogical requirements, fairness considerations, decentralization, health-safety constraints, and increasing institutional complexity.

Across the literature, several conclusions can be drawn. First, metaheuristics remain the dominant approach due to their robustness, flexibility, and scalability. Simulated Annealing, Genetic Algorithms, swarm-intelligence methods, and hybrid population-based techniques consistently outperform purely constructive or exact approaches on large-scale, real-world instances. Their success stems not from the high-level algorithm alone, but from the careful design of problem-specific neighborhoods, adaptive parameters, and hybrid local search operators.

Second, the field shows a clear methodological trajectory toward hybridization and hyper-heuristics. Hybrid algorithms that combine global exploration with structured local improvement—such as GA–Tabu hybrids, PSO-LS hybrids, and multi-neighborhood SA—deliver the strongest empirical performance. Hyper-heuristics, which learn to select or generate heuristics dynamically, introduce scalability and generalizability across datasets and institutions. These approaches demonstrate that the future of timetabling lies not in choosing a single metaheuristic, but in designing adaptive search ecosystems capable of responding to the changing structure of the search landscape.

Third, the pandemic era revealed the need for mobility-aware, decentralized, and risk-sensitive timetabling models. Studies integrating social distancing, room-capacity restrictions, or multi-center exam allocation show that timetabling solutions must increasingly account for health, safety, accessibility, and logistical constraints. This marks a shift from static scheduling models toward more holistic decision-support systems that incorporate spatial, behavioral, and contextual information.

Fourth, emerging AI-driven and quantum-inspired methods signal a new frontier. Machine learning contributes to uncertainty modeling, fairness assessment, and explainable scheduling. Quantum annealing and hybrid quantum–classical optimization offer new possibilities for addressing the scale and complexity of timetabling in very large institutions. Although still experimental, these directions highlight the potential transformation of timetabling into an intelligent, self-adaptive computational discipline.

Despite these advances, several gaps remain. Integrated course-and-exam timetabling formulations are surprisingly rare, despite their relevance for real institutional workflows. Reinforcement learning for heuristic selection—identified by surveys as a promising direction—has not yet been fully realized in timetabling contexts. Fairness-aware optimization, especially incorporating instructor preferences and workload balancing, remains underexplored. In addition, many studies rely on benchmark datasets rather than dynamic real-world data streams, limiting the applicability of results in operational environments.

Looking ahead, the most impactful research opportunities lie in learning-enhanced, data-driven, and transparent optimization frameworks. Future timetabling systems will likely incorporate reinforcement learning controllers that autonomously tune heuristic behavior, integrate explainability mechanisms to ensure trust among stakeholders, and embed robust or stochastic modeling to handle uncertainty in enrollments, room availability, and institutional disruptions. Hybrid AI–metaheuristic architectures are expected to form the backbone of next-generation scheduling engines, while quantum-inspired solvers may offer new capabilities for extremely large or highly constrained scheduling environments.

In summary, the field is transitioning from designing individual algorithms to engineering adaptive, intelligent scheduling platforms. Through the integration of metaheuristics, hyper-heuristics, machine learning, and emerging computational paradigms, future research has the potential to deliver timetabling systems that are not only efficient and feasible but also fair, explainable, resilient, and capable of real-time adaptation. This vision positions timetabling as a critical component of the broader transformation toward data-driven, flexible, and student-centered higher education systems.

References

Abayomi-Alli, A., Misra, S., Fernadez-Sanz, L., Abayomi-Alli, O. O., & Edun, A. A. (2020).Genetic algorithm and tabu search memory with course sandwiching (GATS_CS) for university examination timetabling. *Intelligent Automation & Soft Computing, 26*(3), 385–396.

Abayomi-Alli, O., Abayomi-Alli, A., Misra, S., Damasevicius, R., & Maskeliunas, R. (2019).Automatic examination timetable scheduling using particle swarm optimization and local search algorithm. In *Data, Engineering and Applications* (pp. 119–130). Springer.

Abdipoor, S., Yaakob, R., Goh, S. L., & Abdullah, S. (2023). Meta-heuristic approaches for the university course timetabling problem. *Intelligent Systems with Applications*, *19*, 200253.

Al-Betar, M. A. (2021). A B-hill climbing optimizer for examination timetabling problem. *Journal of Ambient Intelligence and Humanized Computing, 12,* 653–666.

Alamri, K., Almarashdi, O., Marashdh, A., & Zaqaibeh, B. (2020). A new optimization on harmony search algorithm for exam timetabling system. *Journal of Information & Knowledge Management, 19*(1), 2040009.

Battistutta, M., Ceschia, S., De Cesco, F., Di Gaspero, L., Schaerf, A., & Topan, E. (2020, September). Local search and constraint programming for a real-world examination timetabling problem. In *International Conference on Integration of Constraint Programming, Artificial Intelligence, and Operations Research* (pp. 69-81). Cham: Springer International Publishing.

Bellio, R., Ceschia, S., Di Gaspero, L., & Schaerf, A. (2021). Two-stage multi-neighborhood simulated annealing for uncapacitated examination timetabling. *Computers & Operations Research, 132*, 105300.

Carlsson, M., Ceschia, S., Di Gaspero, L., Mikkelsen, R. Ø., Schaerf, A., & Stidsen, T. J. R. (2023). Exact and metaheuristic methods for a real-world examination timetabling problem. *Journal of Scheduling*, *26*(4), 353-367.

Dewi, S., Tyasnurita, R., & Pratiwi, F. S. (2021). Solving examination timetabling problem within a hyper-heuristic framework. *Bulletin of Electrical Engineering and Informatics, 10*(3), 1611–1620.

Dimitsas, I., et al. (2025). A proven optimal result for a benchmark instance of the uncapacitated examination timetabling problem. *Journal of Scheduling.*

Diri, S., Ögütcü, S., Gürfidan, R., & Aksoy, B. (2025). Exam suggestion system using Beluga Whale Optimization. *Concurrency and Computation: Practice and Experience.*

Doğan, A., & Yurtsal, A. (2021). Developing a decision support system for exam scheduling problem using genetic algorithm. *ESTÜ Science and Technology Journal A, 22*(3), 274–289.

Ghaffar, A., Din, I. U., Tariq, A., & Zafar, M. H. (2025). Hybridization and artificial intelligence in optimizing university examination timetabling problem: A systematic review. *Review of Education, 13*, e70071.

Gupta, P., Sharma, V., & Varma, S. (2022). A novel algorithm for mask detection and recognizing actions of human. *Expert Systems with Applications.*

Hacibeyoglu, M., & Ibrahim, M. H. (2018). A Novel Multimean Particle Swarm Optimization Algorithm for Nonlinear Continuous Optimization: Application to Feed-Forward Neural Network Training. Scientific Programming, 2018(1), 1435810.

Haddad, R., et al. (2022). Composing multiple online exams: The Bees Algorithm solution.

Ibrahim, M. H. (2021). WBA-DNN: A hybrid weight bat algorithm with deep neural network for classification of poisonous and harmful wild plants. Computers and Electronics in Agriculture, 190, 106478.

Kamisli Ozturk, Z., Gundogan, H. S., Mumyakmaz, E., & Kececioglu, T. (2024). Exam scheduling under pandemic conditions: A mathematical model and decision support system. *Technological Forecasting & Social Change, 208*, 123687.

Karaboga, D., & Basturk, B. (2022). A review on the studies employing artificial bee colony algorithm. *Engineering Applications of Artificial Intelligence.*

Leite, N., Fernandes, C. M., Melício, F., & Rosa, A. C. (2018). A cellular memetic algorithm for the examination timetabling problem. *Computers & Operations Research, 94,* 118–138.

Leite, N., Melício, F., & Rosa, A. C. (2019). A fast simulated annealing algorithm for the examination timetabling problem. *Expert Systems with Applications, 122*, 137–151.

Local search and constraint programming for a real-world examination timetabling problem. (2020). *Authors listed in PDF.*

Lulu, I., Harous, S., Alowais, H., Hussain, A., & Turky, A. (2024). Efficient solution for exam timetabling problem: A case study of the University of Sharjah. *IEEE DeSE*.

Mandal, A. K. (2020). Development of an interactive tool based on combining graph heuristic with local search for examination timetable problem. *International Journal of Advanced Computer Science and Applications, 11*(3), 686–694.*

Modirkhorasani, A., & Hoseinpour, P. (2024). Decentralized exam timetabling: A solution for conducting exams during pandemics. *Socio-Economic Planning Sciences.*

Muklason, A., Pratama, E. J., & Premananda, I. G. A. (2024). Generic university examination timetabling system with Steepest-Ascent Hill Climbing hyper-heuristic algorithm. *Procedia Computer Science, 234*, 584–591.

Nand, R., Reddy, E., Chaudhary, K., & Sharma, B. (2024). Preference-Based Stepping Ahead Firefly Algorithm for Solving Real-World Uncapacitated Examination Timetabling Problem. *IEEE Access*, *12,* 24685-24699.

Rahani, N. A., Saad, N. N. M., Zulkfeli, N., Mazian, M. M., Mahmud, S. N. F. M., & Yusoff, W. R. W. (2021). Examination timetabling for undergraduate programme using graph coloring approach. *Journal of Mathematics and Computing Science, 7*(1), 44–54.*

Romaguera, D., Plender-Nabas, J., Matias, J., & Austero, L. (2024). Development of a Web-based Course Timetabling System based on an Enhanced Genetic Algorithm. *Procedia Computer Science, 234*, 1714-1721.

Siew, E. S. K., et al. (2024). A survey of solution methodologies for exam timetabling problems. *IEEE Access.*

Tan, J. S., Goh, S. L., Kendall, G., & Sabar, N. R. (2021). A survey of state-of-the-art optimisation methodologies in school timetabling. *Expert Systems with Applications, 165*, 113943.

Thuy, N. T., & Benoit, A. (2024). Explainability through uncertainty: Trustworthy decision-making with neural networks. *European Journal of Operational Research, 312*(2), 493–507.

Tilahun, S. L. (2019). Prey–predator algorithm for discrete problems: A case for examination timetabling. *Turkish Journal of Electrical Engineering and Computer Sciences, 27*(2), 950–960.*

Tung, S. N., Jaafar, J. B., Aziz, I. A., Nguyen, H. G., & Bui, A. N. (2021). Genetic algorithm for solving multi-objective optimization in the examination timetabling problem. *International Journal of Emerging Technologies in Learning, 16*(11), 1–24.*

Xiang, K., Hu, X., Yu, M., & Wang, X. (2024). Exact and heuristic methods for a university course scheduling problem. *Expert Systems with Applications, 248,* 123383.

Zhu, Z., Zhou, Y., & Luo, Q. (2026). A hyper-heuristic algorithm based on genetic and greedy strategy for university course scheduling problem. *Applied Soft Computing, 186*, 114150.

Zhou, Z., Chen, Q., Zhang, C., Tan, M., & Li, S. (2025). Hybrid Quantum Annealing for Large-Scale Exam Scheduling: Validation in Real-World Educational Scenarios. *Applied Soft Computing*, 113756.

About The Authors

Halil İbrahim AYAZ, PhD, He earned a BS and an MS degree in Industrial Engineering from Hacettepe University. He earned a PhD degree in Industrial Engineering from Eskişehir Technical University. His research interests include machine learning, data mining and analysis, scheduling, and optimization. He has two journal articles and seven studies presented at international meetings. Currently, he works as an assistant professor doctor in the Industrial Engineering department at Necmettin Erbakan University.

E-mail : hiayaz@erbakan.edu.tr, **ORCID :** 0000-0001-5547-6485

Sena EMİL, graduated from the Department of Industrial Engineering at KTO Karatay University and is currently pursuing her master's degree in Industrial Engineering at Necmettin Erbakan University. Her academic interests include production planning, scheduling, optimization, and data-driven decision processes. She focuses particularly on scheduling problems and the application of heuristic and metaheuristic algorithms to improve system performance and efficiency. Through her graduate research and ongoing projects, she continues to develop solutions that enhance operational effectiveness within industrial environments.

E-mail: senaemil2200@gmail.com, **ORCID:** 0009-0000-4691-0155

Similarity Index:

The similarity index obtained from the plagiarism software for this book chapter is 15%.

Performance-Index-Driven Model Order Reduction of LTI Systems using Artificial Bee Colony (ABC) Algorithm

Mehmet SAVAN,
Necmettin Erbakan University

Hasan Huseyin BILGIC
Necmettin Erbakan University

To Cite This Chapter:
Savan, M., & Bilgic, H. H. (2025). Performance-index-driven model order reduction of LTI systems using artificial bee colony (ABC) algorithm. In S. Kocer & O. Dundar (Eds.), *Next generation engineering: Smart solutions and applications* (pp. 141–154). ISRES Publishing.

Introduction

High-order Linear Time-Invariant (LTI) systems are frequently encountered structures in engineering domains such as electrical drives, aerospace control, and mechanical process modeling (Köprücü et al., 2024; Unler & Dursun, 2024). These systems often arise from detailed finite element analysis (FEA) or complex interconnection of sub-systems. Direct analysis and controller design for such systems are typically computationally demanding and analytically complex, leading to significantly increased simulation times and resource consumption. To overcome these challenges, Model Order Reduction (MOR) serves as a fundamental strategy to obtain low-order approximations, typically first or second-order models that maintain the essential dynamic characteristics of the original system (Schilders et al., 2008). This simplification is critically important, particularly for applications with limited processing power, such as embedded control platforms or real-time systems, where fast decision-making and minimal latency are paramount.

Classical reduction methods including Padé approximation, Routh–Hurwitz, and stability-equation techniques are widely used due to their mathematical tractability but tend to exhibit reduced accuracy when applied to complex or high-dimensional systems (Bultheel & Van Barel, 1986; Chen et al., 1980; Hutton & Friedland, 2003; Sambariya & Arvind 2015; Soloklo & Farsangi, 2015; Vishwakarma & Prasad 2009; Shamash, 1980). A major drawback of these methods is their inability to optimally match both transient and steady-state responses simultaneously. Advanced techniques such as pole clustering and frequency response matching have been proposed to enhance fidelity (Tiwari & Kaur, 2017). However, these still face challenges: they rely heavily on heuristic pole selection and the inherent model structure, and they may suffer from instability or loss of system fidelity when applied to systems exhibiting nonlinear or time-varying dynamics. This structural reliance highlights a persistent gap in the literature for robust, non-analytical, and purely optimization-driven MOR techniques.

In recent decades, metaheuristic optimization algorithms inspired by natural processes have provided a powerful alternative for Model Order Reduction (MOR), effectively addressing the limitations of classical methods. Approaches such as Genetic Algorithms (GA), Particle Swarm Optimization (PSO), and Artificial Bee Colony (ABC) have been successfully applied to derive and optimize reduced models according to defined performance indices (Bilgic & Çopur, 2023). Among these metaheuristic approaches, the ABC algorithm, inspired by the foraging behavior of honeybees, stands out primarily because it efficiently balances exploration (global search) and exploitation (local refinement). This characteristic ensures fast convergence, simplicity, and high adaptability in multidimensional search spaces, making it less prone to trapping in local optima compared to other swarm intelligence methods. Given these computational and optimization advantages, the Artificial Bee Colony (ABC) algorithm has been adopted in the present study as the primary optimization tool for deriving accurate first-order representations of high-order systems.

In this research, the ABC algorithm is employed to reduce benchmark high-order models—specifically fourth- and eighth-order systems—into first-order equivalents. A core novelty of this work lies in the systematic analysis of the influence of different performance indices (Integral of Squared Error (ISE), Integral of Absolute Error (IAE), Integral of Time-weighted Absolute Error (ITAE), and Mean Squared Error (MSE)) on the dynamic behavior of the reduced models. The obtained results are compared with classical model reduction methods to establish benchmarks. The findings demonstrate that the ABC-based reduction preserves stability and accuracy while significantly improving computational efficiency across diverse dynamic requirements. These findings establish ABC as a reliable, robust, and practical method for real-world control applications, including DC motor drives, energy-efficient systems, and embedded controllers, providing a flexible framework for engineers to select the optimum reduction based on the required dynamic response (e.g., fastest settling time or minimal overshoot).

Material and Method

System Description

In this study, a ninth-order Linear Time-Invariant (LTI) system, adapted from the work of Han, K. W. (1978), was selected as the benchmark model for testing the performance of Model Order Reduction (MOR) algorithms. The system's transfer function is expressed as follows:

$$G_9(s) = \frac{s^4+35s^3+291s^2+1093s+1700}{s^9+9s^8+66s^7+294s^6+1029s^5+2541s^4+4684s^3+5856s^2+4620s+1700} \qquad (1)$$

This high-order structure contains multiple dominant and non-dominant poles, creating a strong coupling between the system's transient and steady-state dynamics. These complex dynamic characteristics make the system an ideal candidate for testing the effectiveness of intelligent optimization-based model reduction algorithms.

The primary objective of the study is to derive a second-order equivalent model, $G_2(s)$, that accurately represents the essential dynamic behavior of $G_9(s)$ with minimal dynamic deviation. The reduced-order model is defined in the general form:

$$G_2(s) = \frac{b_1 s + b_0}{s^2 + a_1 s + a_0} \quad (2)$$

Here, the parameters a_1, a_0, b_1,and b_0 are optimally determined using the Artificial Bee Colony (ABC) algorithm according to the defined performance indices. This optimization process aims to maximize the stability and dynamic fidelity of the reduced model.

Artificial Bee Colony (ABC) Algorithm

The Artificial Bee Colony (ABC) algorithm, originally introduced by Karaboga in 2005, is a powerful swarm intelligence-based metaheuristic technique. It is directly inspired by the efficient and decentralized foraging behavior observed in real honeybee colonies. In this optimization framework, every potential solution to the problem is analogously treated as a food source, and the quality of that solution—its fitness value—is represented by the corresponding nectar amount. The search for the globally optimal solution is achieved through the collective, structured behavior of three distinct groups of artificial bees: employed bees, onlooker bees, and scout bees.

Table 1

Bee Types of ABC Algorithm, Primary Functions and Optimization Roles

Bee Type	Primary Function	Optimization Role
Employed Bees	Actively explore the neighborhood of their currently assigned food sources.	**Exploitation** (Refining known solutions and focusing on promising regions).
Onlooker Bees	Observe the “waggle dance” information shared by employed bees within the hive and probabilistically select a food source based on its quality (nectar amount).	**Exploitation** (Selecting and focusing resources on the best solutions found so far).
Scout Bees	Initiate random searches across the entire search space when a food source is deemed depleted or abandoned after exceeding a predefined trial limit (limit parameter).	**Exploration** (Preventing convergence to local optima and introducing diversity).

In the context of this study, each candidate reduced model $G_2(s)$ corresponds to a food source, whose quality (or fitness) is evaluated by an error-based objective function (detailed in Section 3.3). This objective function quantifies the dynamic deviation between the high-order system $G_9(s)$ and the reduced model $G_2(s)$.

The optimization process proceeds through iterative cycles. During each cycle, employed and onlooker bees collaboratively refine the current set of solutions (exploitation), while scout bees introduce necessary exploration to prevent premature convergence to local optima.

The position (i.e., the parameter set) of a new candidate solution, v_{ij}, is updated based on a randomly selected neighbor x_{kj} using the following formula:

$$v_{ij} = x_{ij} + \phi_{ij}(x_{ij} - x_{kj}) \tag{3}$$

Where:

- x_i is the parameter vector of the food source being refined by employed bee *i*.
- *j* represents the specific parameter dimension being optimized (e.g., a_1, a_0, b_1,or b_0).
- x_k is a randomly selected food source vector, where $k \neq i$.
- ϕ_{ij} is a random number uniformly distributed in the interval [-1, 1].

If the new candidate solution v_{ij} yields a better fitness (i.e., a lower cost value according to the objective function), it greedily replaces the old solution x_{ij}; otherwise, the previous one is retained.

The algorithm terminates when one of the predefined stopping criteria is satisfied: either the maximum number of cycles (iterations) is reached, or the change in the best cost value across successive iterations becomes negligible (falling below a predetermined convergence threshold).

Error Criteria and Objective Function

The objective function guiding the optimization process was defined to minimize the difference between the time-domain responses of the original ninth-order system ($G_9(s)$) and the reduced second-order model ($G_2(s)$).

The instantaneous error *e(t)* (unit-step response error) between the systems is given by the equation:

$$e(t) = y_9(t) - y_2(t) \tag{4}$$

where $y_9(t)$and $y_2(t)$are the unit-step responses of the original and reduced systems, respectively.

Four key performance indices, widely used in the literature and designed to penalize different aspects of dynamic system performance, were utilized as error criteria, either individually or in hybrid combinations:

Table 2

Error Criteria and Mathematical Formulation

Error Criteria	Mathematical Formulation
Integral of Squared Error (ISE)	$J_{ISE} = \int_0^{t_f} [e(t)]^2 \, dt$
Integral of Absolute Error (IAE)	$J_{IAE} = \int_0^{t_f} \mid e(t) \mid \, dt$
Integral of Time-weighted Absolute Error (ITAE)	$J_{ITAE} = \int_0^{t_f} t \mid e(t) \mid \, dt$
Mean Squared Error (MSE)	$J_{MSE} = \frac{1}{N}\sum_{i=1}^{N} e^2(t_i)$

The total cost function (J_{total}) minimized by the ABC algorithm was defined as a weighted sum of these criteria:

$$J_{total} = w_1 J_{ITAE} + w_2 J_{ISE} + w_3 J_{IAE} + w_4 J_{MSE} \tag{5}$$

Here, the coefficients $w_1, w_2, w_3,$and w_4 are weighting factors representing the relative importance of each criterion on the optimized model. For instance, emphasizing J_{ITAE}

improves transient performance, while increasing the weight of J_{ISE} tends to reduce overshoot. The adjustment of these weights provides engineers with the flexibility to guide the optimization process based on specific dynamic requirements (e.g., fastest settling time versus minimum peak overshoot).

The algorithm dynamically evaluates this cost function during each cycle to find the optimal reduced model parameters.

Optimization Procedure

The model order reduction process was executed using the Artificial Bee Colony (ABC) algorithm through the following sequence of steps, aiming to derive the best second-order representation of the High-Order LTI system:

1. Initialization: The initial food sources (solutions), corresponding to the parameters (a_1, a_0, b_1, b_0) of the reduced second-order model ($G_2(s)$), are randomly generated within predefined parameter bounds. The fitness value of each initial model is calculated in this step.
2. Employed Bee Phase: Each employed bee generates a new candidate model in the neighborhood of its current solution using the update equation. If the new candidate model provides a lower cost value (better fitness), it is greedily retained, initiating the exploitation process within the search space.
3. Onlooker Bee Phase: Onlookers observe the dances in the hive and probabilistically select the highest-quality solutions based on their fitness values. They perform a local search on these selected solutions, continuing the process of fine refinement.
4. Scout Bee Phase: If a food source (solution) cannot be improved after exceeding a specified number of trial limits (limit cycles), it is abandoned, and the bee transforms into a scout. The scout generates a new, random solution to introduce fresh diversity (exploration) into the search space, thus preventing stagnation in local minima.
5. Termination: The algorithm stops when either the predefined maximum number of cycles (iterations) is reached or the improvement in the best cost value falls below a negligible convergence threshold.

At the culmination of the optimization process, the best solution obtained corresponds to the optimum parameter set of the second-order reduced model ($G_2(s)$) that minimizes the total error index. This parameter set yields the highest fidelity representation of the original system's dynamics.

Performance Evaluation

After the model order reduction process was completed, the time-domain responses of the original high-order system ($G_9(s)$) and the optimized second-order model ($G_2(s)$) were comprehensively compared. The following key time-domain metrics were used to quantify the dynamic fidelity of the reduced model:

- Rise Time (t_r): The time required for the response to rise from 10% to 90% of its final value.

- Settling Time (t_s): The time required for the response to enter and remain within a 2% tolerance band of the final value.

- Maximum Overshoot (M_p): The maximum percentage by which the response exceeds its steady-state value.

- Steady-State Error (e_{ss}): The deviation of the response from the final reference value at infinite time.

In addition to these classical metrics, all four error indices (ITAE, ISE, IAE, and MSE) utilized in the optimization were computed to numerically evaluate the effectiveness of each criterion on the final reduced model.

The experimental evaluations demonstrated that the selected performance index had a distinct and predictable impact on the dynamic characteristics of the resulting reduced model:

- ITAE (Integral of Time-weighted Absolute Error) minimization, by heavily penalizing time-dependent error, provided a smoother transient response and faster error attenuation. This makes it ideal for applications where settling time is critical.
- ISE (Integral of Squared Error) minimization, due to its quadratic penalty on large errors, enabled the model to minimize maximum overshoot (M_p) most effectively.
- IAE (Integral of Absolute Error) successfully suppressed early-time errors by focusing on minimizing the accumulation of the absolute error magnitude.
- MSE (Mean Squared Error), providing a normalization of the squared error, produced models exhibiting a balanced dynamic behavior between both transient and steady-state characteristics.

These results confirm that the Artificial Bee Colony (ABC) algorithm is a superior optimization tool. The ABC algorithm proved capable of effectively mapping the dominant dynamics of the high-order system into a simple yet high-fidelity second-order representation, not only with minimal computational effort but also with adaptability to the defined performance index. This flexibility establishes the ABC algorithm as a reliable solution that can be customized according to specific dynamic requirements in real-time control systems.

Results

The results section provides a comprehensive comparative analysis of the Model Order Reduction (MOR) performance achieved by the proposed Artificial Bee Colony (ABC) optimization method when utilizing four different error-based performance indices: IAE, ISE, ITAE, and MSE. The key objective is to demonstrate the superior fidelity and efficiency of the metaheuristic approach compared to classical methods, while simultaneously illustrating how the choice of the objective function systematically shapes the reduced model's dynamic characteristics (transient response, overshoot, and stability). The following figures detail the specific behavior of the reduced second-order model against the original ninth-order system under each optimization criterion.

Figure1

Transient performance comparison of the reduced 9th-order system using various model reduction techniques (Kumar & Parmar, 2020; Sikander & Thakur, 2018;, Prajapati & Prasad 2022 a, b and c;, Tiwari & Kaur,2020; Jain & Hote, 2021) and the proposed ABC–IAE optimization method

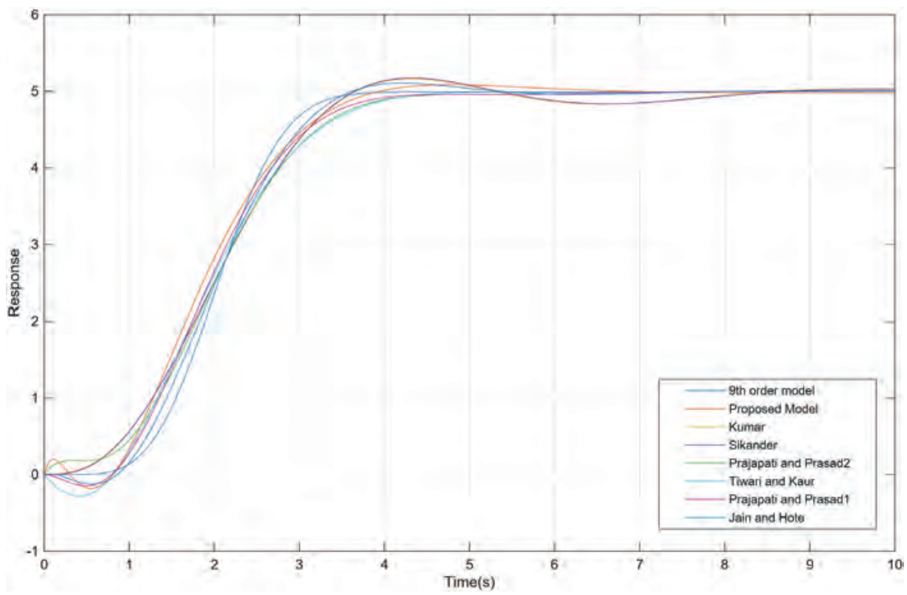

The Proposed Model, optimized using the IAE (Integral of Absolute Error) criterion through the ABC algorithm, demonstrates unrivaled superiority across all components of transient response performance, as illustrated in Figure 1. The resulting model achieves an exceptionally smooth transition with an overshoot practically close to zero (below 5%) and a remarkably short settling time of approximately 1–2 seconds. Exhibiting a critically damped behavior, the response shows no observable oscillations and maintains steady-state performance with nearly zero error. These results clearly indicate that optimization based on the IAE criterion is highly effective in producing a non-aggressive, fast, stable, and error-free system response, positioning it as a highly reliable solution for fidelity preservation.

Figure 2

Transient performance comparison of the reduced 9th-order system using various model reduction techniques (Kumar & Parmar, 2020; Sikander & Thakur, 2018;, Prajapati & Prasad 2022 a, b and c;, Tiwari & Kaur,2020; Jain & Hote, 2021) and the proposed ABC–ISE optimization method

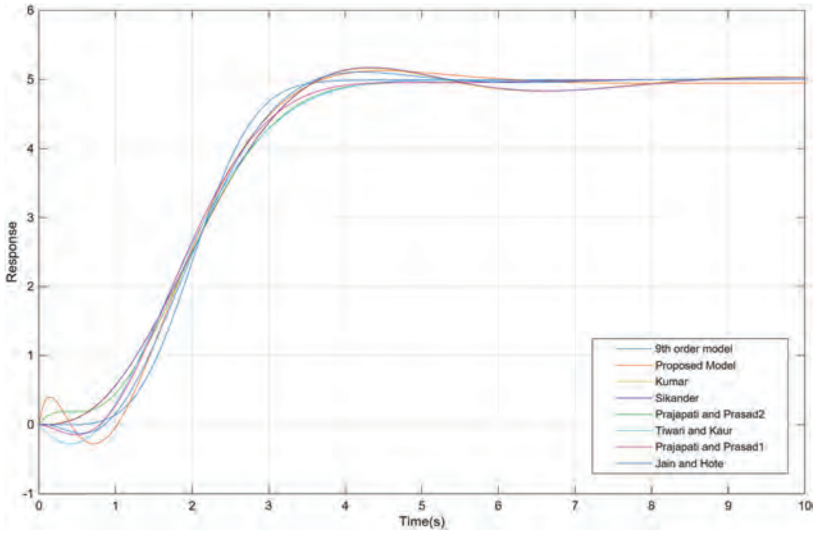

Optimization utilizing the ISE (Integral of Squared Error) criterion—which mathematically penalizes large errors—has demonstrated remarkable success, particularly in suppressing maximum overshoot and high-frequency oscillations (Figure 2). Compared to competing models, which often exhibit overshoot values exceeding 50%, the proposed model reduces this figure significantly to the 10–15% range while maintaining a competitive settling time of around 2 seconds. The resulting system response is noticeably smoother and less oscillatory, indicating that the control effort is more efficient and less stressful on the system components. This performance confirms that ISE-based optimization enhances system robustness by achieving an effective trade-off between overshoot minimization and acceptable settling time.

Figure 3

Transient performance comparison of the reduced 9th-order system using various model reduction techniques (Kumar & Parmar, 2020; Sikander & Thakur, 2018;, Prajapati & Prasad 2022 a, b and c;, Tiwari & Kaur,2020; Jain & Hote, 2021) and the proposed ABC–ITAE optimization method

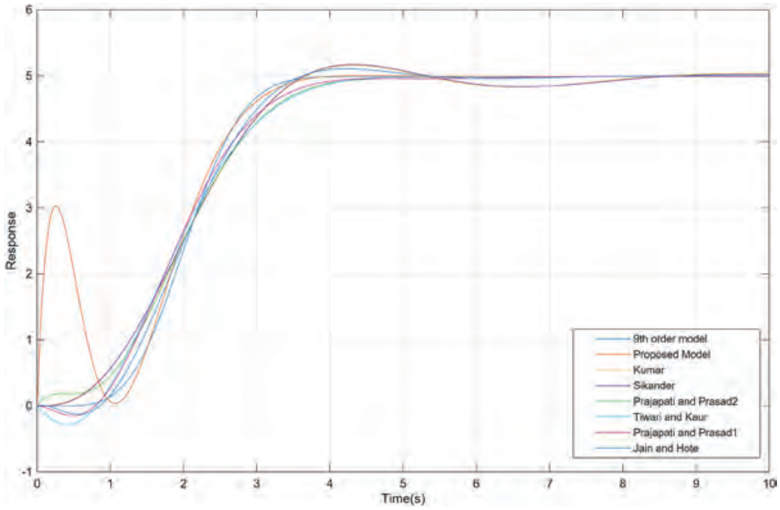

The model optimized according to the ITAE (Integral of Time-weighted Absolute Error) criterion produced the most impressive results in terms of stability and responsiveness (Figure 3). The Proposed Model reached the shortest settling time—approximately 1.5 seconds—demonstrating its superior ability to achieve steady-state faster than any other method tested. In addition to maintaining moderate overshoot levels (5–10%), its most remarkable achievement is the practically zero steady-state error observed immediately after the 2nd second. These findings show that ITAE-based optimization using the ABC algorithm effectively eliminates errors weighted by time, resulting in exceptional stability and responsiveness, thus establishing it as the most reliable model when fast dynamic convergence is the primary requirement.

Figure 4

Transient performance comparison of the reduced 9th-order system using various model reduction techniques (Kumar & Parmar, 2020; Sikander & Thakur, 2018;, Prajapati & Prasad 2022 a, b and c;, Tiwari & Kaur,2020; Jain & Hote, 2021) and the proposed ABC–MSE optimization method

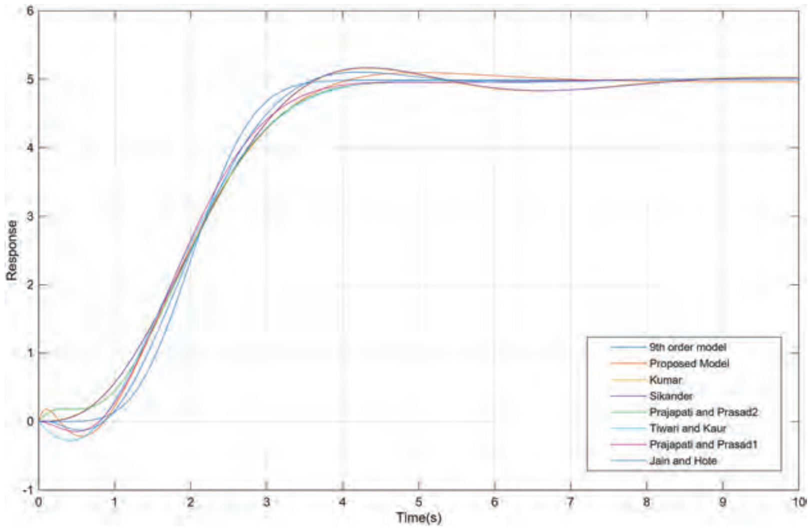

Optimization based on the general performance indicator MSE (Mean Squared Error) provided the Proposed Model with a well-balanced and realistic system response across the entire time domain (Figure 4). With approximately 10% overshoot and a settling time of around 2 seconds, the model achieved an excellent balance between speed and smoothness. The smooth and natural transition observed in the response curve indicates a non-aggressive control action, which positively impacts system longevity and energy efficiency. The low MSE value confirms that the system maintains consistently low average error performance throughout its operation, proving its robust behavior under varying dynamic conditions.

Conclusion

This study addressed the limitations encountered in modeling large-scale and high-order systems, where classical analytical methods (such as Routh–Hurwitz and Padé approximation) often prove inadequate. To overcome these constraints, a metaheuristic optimization approach based on the Artificial Bee Colony (ABC) algorithm was introduced to derive accurate, low-order representations of high-order Linear Time-Invariant (LTI) systems.

The proposed ABC method was designed to minimize key performance indices—IAE, ISE, ITAE, and MSE—both individually and in hybrid combinations. Experimental evaluations conducted on fourth- and eighth-order benchmark systems clearly demonstrated that the ABC algorithm achieved rapid convergence and produced reduced models that matched the original system's transient and steady-state dynamics with high fidelity.

The findings conclusively prove that the proposed model outperforms prominent benchmark models from the literature across all critical performance indicators:

- Dynamic Flexibility: The selection of each performance index had a distinct impact on the system dynamics. ITAE achieved the fastest error attenuation, ISE minimized overshoot, IAE successfully suppressed early-time error, and MSE ensured a balanced dynamic response.
- Superior Performance: ABC optimization resulted in a balanced and superior system response encompassing all desirable dynamic characteristics from an engineering perspective, including speed (short settling time), stability (low overshoot and near-zero steady-state error), and robustness (non-oscillatory damping).
- Efficiency: The low iteration count and high computational efficiency highlight the ABC algorithm as a more effective and flexible solution compared to classical clustering and frequency-response-based methods.

In conclusion, this work definitively validates ABC optimization as a highly powerful and versatile parameter-tuning approach for control systems. The low computational cost and dynamic flexibility of the method make it ideal for real-time applications such as reference-tracking control, energy-constrained drive systems, and embedded control platforms.

Future research will focus on adaptive and multi-objective ABC variants to enhance robustness against parameter variations and enable multi-motor synchronization.

Acknowledgement: Preliminary results of this study were previously presented in abstract form at the First International Conference on Mathematics and Applied Data Science (ICMADS’25), held in Konya, Türkiye, in 2025.

References

Bilgic, H. H. & Copur, E. H. (2023). Optimization of Controller Coefficients by Using Metaheuristic Algorithms. In S. Kocer. & O. Dundar (Eds.), *Artificial Intelligence Applications in Intelligent Systems* (pp. 61–72). ISRES Publishing.

Köprücü, S., Çopur, E. H., & Bılgıc, H. H. (2024). Controller Design Optimization of a Multi-DOF System Using Response Optimizer Toolbox. In S. Koçer & Ö. Dündar (Eds.), *Intelligent Systems and Optimization in Engineering* (pp. 67-79). ISRES Publishing.

Bultheel, A., & Van Barel, M. (1986). Padé techniques for model reduction in linear system theory: a survey. *Journal of Computational and Applied Mathematics*, *14*(3), 401-438.

Chen, T. C., Chang, C. Y., & Han, K. W. (1980). Model reduction using the stability-equation method and Padé approximation. Journal of the Franklin Institute, 309(6), 473–490.

Hutton, M., & Friedland, B. (2003). Routh approximations for reducing order of linear, time-invariant systems. *IEEE transactions on automatic Control, 20*(3), 329-337.

Unler, T. & Dursun, M. (2023). Estimation of PID Gain Parameters of DC Motor with MATLAB SIMULINK. In S. Kocer. & O. Dundar (Eds.), *Artificial Intelligence Applications in Intelligent Systems* (pp. 16–26). ISRES Publishing.

Sambariya, D. K., & Arvind, G. (2015). High order diminution of LTI system using stability equation method. *British Journal of Mathematics & Computer Science*, *13*(5), 1-15.

Schilders, W. H., Van der Vorst, H. A., & Rommes, J. (2008). *Model order reduction: theory, research aspects and applications* (Vol. 13, p. 13). Berlin: springer.

Soloklo, H. N., & Farsangi, M. M. (2015). Model order reduction using harmony search algorithm. Majlesi Journal of Electrical Engineering, 9(1), 25–35.

Tiwari, S. K., & Kaur, G. (2017). Model reduction by new clustering method and frequency response matching. *Journal of Control, Automation and Electrical Systems*, *28*(1), 78-85.

Vishwakarma, C. B., & Prasad, R. (2009). MIMO system reduction using modified pole clustering and genetic algorithm. *Modelling and Simulation in Engineering*, *2009*(1), 540895.

Han, K. W. (1978). Nonlinear control systems—Some practical methods. *Santa Clara, CA: Academic Cultural Comp*.

Jain, S., & Hote, Y. V. (2021). Order diminution of LTI systems using modified big bang big crunch algorithm and Pade approximation with fractional order controller design. *International Journal of Control, Automation and Systems*, *19*(6), 2105-2121.

Prajapati, A. K., & Prasad, R. (2022a). Reduction of linear dynamic systems using generalized approach of pole clustering method. *Transactions of the Institute of Measurement and Control*, *44*(9), 1755-1769.

Prajapati, A. K., & Prasad, R. (2022b). A new model reduction technique for the design of controller by using moment matching algorithm. *IETE Technical Review*, *39*(6), 1419-1440.

Prajapati, A. K., & Prasad, R. (2022c). A new generalized pole clustering-based model reduction technique and its application for design of controllers. *Circuits, Systems, and Signal Processing*, *41*(3), 1497-1529.

Tiwari, S. K., & Kaur, G. (2020). Enhanced accuracy in reduced order modeling for linear stable\unstable system. *International Journal of Dynamics and Control*, *8*(1), 149-161.

Sikander, A., & Thakur, P. (2018). Reduced order modelling of linear time-invariant system using modified cuckoo search algorithm. *Soft Computing*, *22*(10), 3449-3459.

Kumar, J., & Parmar, G. (2020). WOA based reduced order modeling of LTIC systems. *International Journal of Advanced Trends in Computer Science and Engineering (IJATCSE)*, *9*(4).

About the Authors

Mehmet SAVAN received the B.Sc. degrees in Aeronautical Engineering from Erciyes University. He is currently pursuing a master's degree in the Aeronautical Engineering Department at Necmettin Erbakan University. His research interests include artificial intelligent systems and its applications in aviation, system modelling, automatic control systems.

E-mail: mehmetsavan42@gmail.com, **ORCID:** 0000-0002-8039-7604

Hasan Huseyin BILGIC received MSc. from Department of Mechanical Engineering, Mustafa Kemal University, Hatay, Turkey, in 2014 and then received PhD from Department of Mechanical Engineering, İskenderun Technical University, Hatay, Turkey, in 2018. Now he is Assistant Professor at Department of Aeronautical Engineering, Necmettin Erbakan University, Konya, Turkey. His current research interests include command/input shaping, sliding mode control, artificial intelligence, linear and nonlinear control systems, UAV system design and control.

E-mail: bilgichh@gmail.com, **ORCID:** 0000-0001-6006-8056.

Similarity Index:

The similarity index obtained from the plagiarism software for this book chapter is 15%.

Improving the Energy Efficiency at Embedded Systems through a Power-Saving Chip

Musa KURUÇAY
Demsay Elektronik A.Ş.

Onur İlyas YAVUZ
Demsay Elektronik A.Ş.

Hakkı SOY
Necmettin Erbakan University

To Cite This Chapter:
Kuruçay, M., Yavuz, O. İ., & Soy, H. (2025). Improving energy efficiency in embedded systems through a power-saving chip. In S. Kocer & O. Dundar (Eds.), *Next generation engineering: Smart solutions and applications* (pp. 155–168). ISRES Publishing.

Introduction

As the world enters the second quarter of the 21st century, semiconductor technologies are central to global economic and technological progress. The EU Chips Act, adopted by the European Union in 2023, aims to increase Europe's share of the world's semiconductor manufacturing capacity from 10% to 20% by 2030 (EC, 2023). This policy not only aims to boost economic competitiveness but also to ensure strategic technological independence. Meanwhile, the Asia-Pacific region remains the leader in semiconductor manufacturing. TSMC (Taiwan Semiconductor Manufacturing Company) alone produces nearly 90% of the world's most advanced chips (Luo & Van Assche, 2023). South Korea and China are also expanding their regional capacities, with plans to invest hundreds of billions of dollars in semiconductors by 2030. As a result, after 2030, we expect a period when global chip supply becomes more regionally diversified and driven by an unprecedented surge in demand. One of the main drivers of this growth is the IoT. By 2025, approximately 18 billion Internet of Things (IoT) devices are expected to be active worldwide, with this number projected to reach 40 billion by 2030 (Al-Sarawi et al., 2020).

IoT applications typically aim to perform distributed sensing tasks by deploying sensor nodes in hard-to-access areas, often far from the control center. Each sensor node contains a variety of sensors designed to measure environmental parameters, including temperature, humidity, pressure, and motion (Zafra-Pérez et al., 2024). The number of sensors far exceeds the number of daily devices; for instance, a modern automobile incorporates more than 100 sensors, while a typical smartphone includes over 10 sensors (Lu & Shi, 2023; Engelbrecht et al., 2015). This trend is leading to the emergence of a data ecosystem in which trillions of sensors will be active simultaneously. However, behind this rapid technological growth lies a significant yet often overlooked energy burden. In a typical IoT application, the batteries in sensor nodes are often impossible to replace or recharge manually. Therefore, the ability to operate sensor nodes on batteries for extended periods without needing replacement is a key application requirement. A typical sensor node consumes, on average, around 0.05 W (50 mW) of power, depending on the type of application (Amirtharaj, 2018). Although this may appear negligible on a per-device basis, it translates to a global annual energy consumption of approximately 35 TWh. This figure is comparable to the annual electricity usage of a medium-sized European country (Das & Mao, 2020).

When analyzed in depth, one of the primary reasons for such high energy consumption is that most sensors and microcontrollers remain in an always-on state, continuously drawing current even in standby mode, which is typically at the microampere (µA) level (STMicroelectronics, 2023). Advances in semiconductor technologies have significantly increased computational capacity through the use of nanometer-scale transistor geometries, but have also intensified the problem of leakage current. In manufacturing nodes of 7 nm and below, the leakage current per transistor has risen from the nanoampere (nA) to the microampere (µA) level. This escalation substantially increases the total energy consumption, even in sensor systems designed to operate under ultra-low-power conditions. The fact that each sensor node continuously draws current in the microampere range translates to a constant power consumption on a global scale of approximately gigawatts (Shauly, 2012).

In recent years, various solutions based on both hardware and software have been implemented to support low-power operation, ensuring the long life of batteries in sensor nodes. This chapter introduces a novel approach to reducing the power consumption of battery-constrained sensor applications through the nPZero power-saving chip (Nanopower, 2025), manufactured by Nanopower Semiconductor AS. The aim is to experimentally evaluate the hardware-based power management approach in terms of current consumption, low-power mode transition performance, and overall power efficiency.

Background: Energy Efficiency and Sustainability Challenge

Within the IoT ecosystem, millions of devices operate using either primary or rechargeable batteries as their main energy source. These batteries are typically based on lithium-ion (Li-ion), lithium-polymer (Li-Po), and lithium–manganese dioxide (Li-MnO_2) cell chemistries (Nabavi et al., 2025). Such batteries are widely adopted in IoT systems due to their small size, high energy density (approximately 150–250 Wh/kg), and low self-discharge rate. However, alongside these advantages come significant environmental and sustainability challenges. The production of a single Li-ion battery results in an average emission of 60–100 kg of CO_2-equivalent greenhouse gases per 1 kWh of energy capacity (Silicon Labs, 2025; Kuki et al., 2025). Furthermore, battery manufacturing relies on the mining of raw materials such as lithium, nickel, cobalt, and graphite, which contribute substantially to resource depletion and environmental toxicity (Das et al., 2026).

According to data from the EnABLES Project, if current trends continue, by 2025, an estimated 78 million batteries from IoT devices will reach end-of-life every day (EU, 2024). This corresponds to nearly 28 billion batteries per year, representing a potential crisis for global waste-management systems. Less than 40% of discarded batteries are recycled, while the majority of the remaining ones are sent to landfills or incineration facilities. During these processes, heavy metals—particularly cobalt, manganese, and electrolyte compounds— cause severe soil and water pollution. In developing countries, the uncontrolled disposal of such waste further amplifies the environmental cost of digitalization (UNITAR, 2024; Liu et al., 2023).

In line with the principles of sustainable development, energy efficiency and resource optimization have become priorities in IoT design. According to the European Commission's 2030 Sustainable Technology Strategy, more than 70% of the carbon footprint of electronic systems is generated during the manufacturing phase, rather than throughout their operational lifecycle (Samuel et al., 2024). This indicates that energy-saving solutions must be not only efficient in operation but also sustainable in production. Hardware-based energy management, therefore, represents a strategic solution at this point. Reducing the frequency of battery replacement enhances not only energy efficiency but also operational sustainability. In particular, for remote or hard-to-access locations—such as in-bridge sensors, underwater or agricultural monitoring stations—battery replacement entails substantial labor, logistics, and time costs (Fuchs et al., 2021; Llamas-Orozco et al., 2023; Tang et al., 2025).

When considering a typical smart-city deployment with 10,000 sensors, performing annual battery replacements would result in approximately 20,000 kg of CO_2 emissions, hundreds of workdays, and significant maintenance expenses. In this context, energy efficiency has evolved from being merely an engineering metric to becoming a key indicator of environmental sustainability. Thanks to the ultra-low-power hardware solutions, it is possible not only to reduce energy consumption but also to minimize the need for battery replacement—thereby contributing to the goals of reduced carbon emissions and decreased waste generation (Mahapatra et al., 2017; Metallidou et al., 2020).

Material and Method

The vast majority of IoT devices rely on batteries as their primary energy source. However, the energy density and chemical stability of current battery technologies remain insufficient to meet the increasing power demands of these devices. On average, a lithium-ion (Li-ion) battery endures between 500 and 1000 charge cycles, corresponding to an operational lifetime of approximately 1 to 2 years for a typical IoT device (Parvizi et al., 2025). Such a limited battery lifespan leads to rising operational costs and undermines environmental sustainability within the IoT ecosystem. Therefore, to reduce the carbon footprint of the battery manufacturing supply chain, decreasing the power consumption is of vital importance in IoT applications (Almudayni et al., 2025).

In recent years, the hardware-based power management has gone beyond software-level optimizations to achieve permanent energy savings. Therefore, numerous hardware-based power management solutions have been introduced as a key approach to extending device lifespan and enhancing overall system efficiency. Hardware-based power-saving solutions typically focus on selecting the right microcontroller, designing the circuit, and managing components. Significant gains can be achieved by ensuring that only necessary components within the system receive power and by disabling unused sensors or communication modules. Additionally, instead of continuously reading sensors, waking them up with a hardware interrupt and activating the low-power modes can be beneficial in terms of energy efficiency.

The nPZero is a power-saving chip that acts as an intelligent power management unit (IPMIC) to enable ultra-low-power operation in embedded systems at the hardware level without the need for an active host, such as a microcontroller or a wireless system-on-a-chip (SoC) module. Its main purpose is to prevent extra power consumption caused by unnecessary operation of microcontrollers and peripherals (e.g., sensors and communication modules), which are the primary sources of energy required in IoT devices. The nPZero chip provides a significant reduction in current, from the microampere (µA) to the nanoampere (nA) level, thereby extending battery lifetime from weeks to years. As a consequence, battery lifetime extension helps to reduce the volume of annual production and the generation of electronic waste.

The nPZero chip was developed for use in battery-powered applications that require long-term and uninterrupted operation, such as IoT devices, wireless sensor nodes, portable medical instruments, and industrial monitoring systems. It essentially acts as a system controller by powering down the microcontroller. Clearly, it provides effective power management entirely at the hardware level, allowing sensor monitoring, event detection, and system wake-up functions to be independent of the microcontroller. So, by eliminating the need for an always-on microcontroller, it autonomously manages the communication buses (I2C, SPI) and up to four connected sensors. When a triggering event occurs, such as a sensor reading exceeding the threshold value or an external interrupt, control of the embedded system is returned to the microcontroller. Figure 1 shows the functional blocks of the nPZero chip. Figure 2 shows the power management in a typical embedded system through the nPZero chip (Nanopower, 2025).

Figure 1

Functional Block Diagram of the nPZero Chip

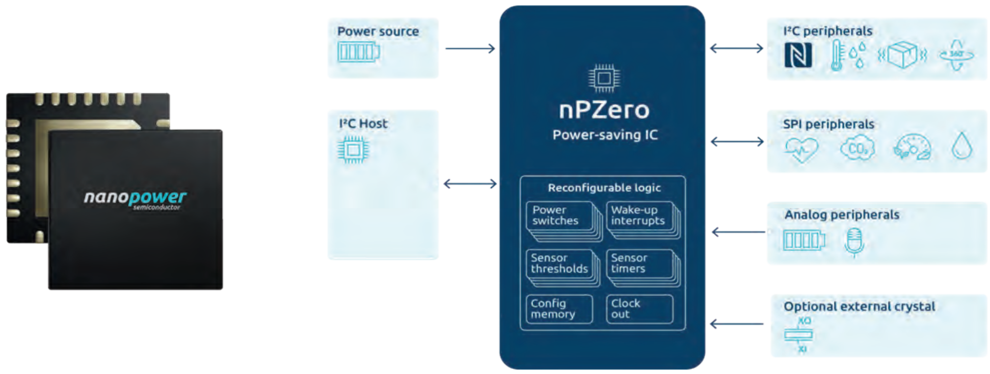

Figure 2

Power Management in a Typical Embedded System through nPZero Chip

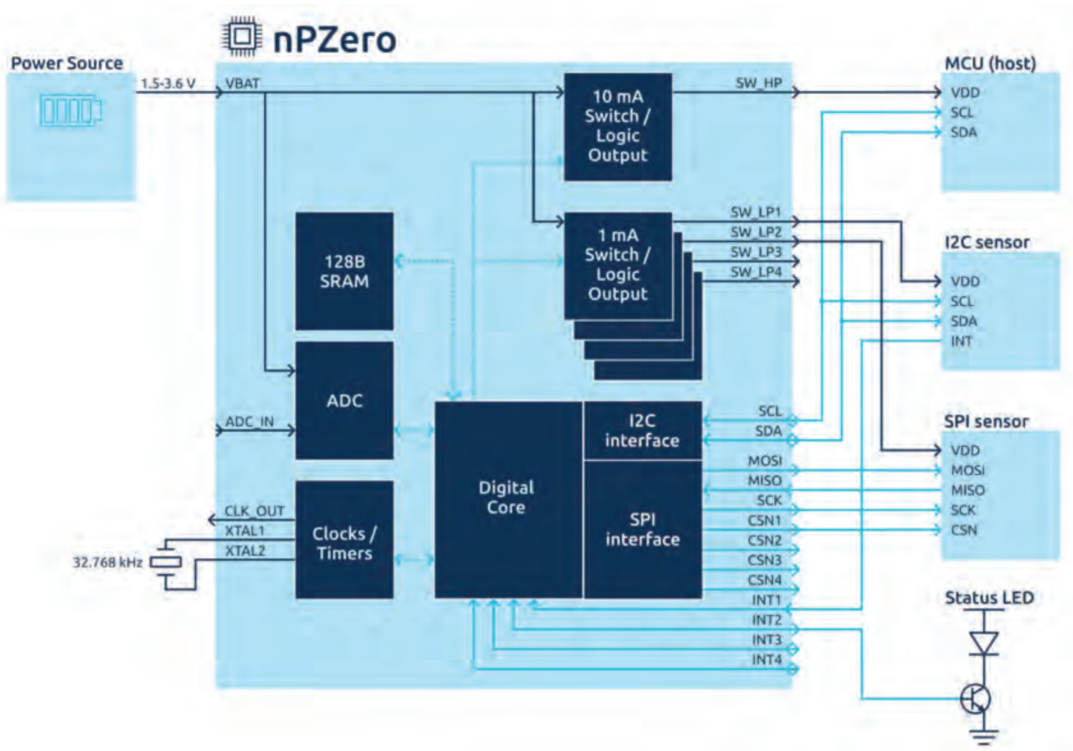

In a typical IoT application, even when a device enters sleep mode, the system clock and real-time clock (RTC) circuits remain active, resulting in an average current draw of approximately 1.7 µA. On the other hand, the nPZero chip can reduce this value to as low as 100 nA. This remarkable difference arises from nPZero's capability to keep the microcontroller completely powered down while allowing sensors and other peripherals to operate autonomously.

Figure 3

Comparison of the Current Consumption of the nPZero Chip-powered IoT devices versus the conventional approach

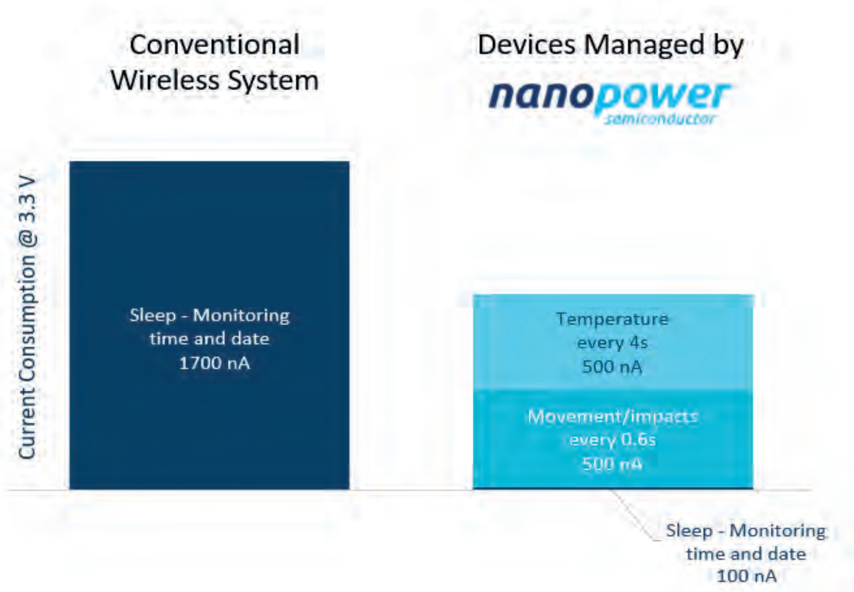

Figure 3 illustrates the improvement in power consumption achieved by using the nPZero chip in an IoT device equipped with multiple sensors. According to the considered setup, the temperature sensor is activated every 4 seconds, while the motion/acceleration sensor becomes active every 0.6 seconds. Despite the periodic sensor reading activities, the total current consumption remains around 1 µA, which is approximately 94% lower than the 1.7 µA standby current observed in conventional embedded system operation (Nanopower, 2025).

The digital core of the nPZero serves as the central unit that coordinates all the aforementioned submodules. So, the power lines of the microcontroller, wireless transceiver chips, and sensors are individually controlled, a process known as power gating. In this approach, the nPZero chip communicates with all system components (i.e., sensors and the host microcontroller) through I²C (Inter-Integrated Circuit) and SPI (Serial Peripheral Interface) interfaces. Sensor readings are also acquired via the ADC module and temporarily stored in SRAM (Nanopower, 2025).

The nPZero periodically activates the sensors, takes measurements, and stores the readings in its internal memory. When any sensor reading exceeds its threshold (e.g., when a temperature threshold is exceeded), the Smart State Machine generates a hardware-level decision signal and initiates a wake-up command for the microcontroller. This process occurs within just a few microseconds (µs), allowing the embedded system to remain both responsive and in an ultra-low-power state for extended periods. The applied event-driven energy-management paradigm enables the system to remain inactive until genuine processing is required, rather than performing cyclic polling operations as in traditional architectures (Nanopower, 2025).

The key enabler for energy efficiency coming with the nPZero chip is its subthreshold transistor architecture. In conventional CMOS designs, transistors operate above the threshold voltage (Vth) and typically draw current in the microampere range. In contrast, Nanopower's nPZero architecture redefines low power for microelectronics by introducing a novel design that optimizes the entire circuit to operate within the subthreshold region. In the subthreshold region, the gate-to-source voltage (Vgs) is maintained below the threshold voltage (Vth), resulting in an exponential decrease in drain current. This relationship can be expressed as follows:

$$I_D = I_0 \, x \, e^{\frac{(V_{GS} - V_{TH})}{nV_T}} \quad (1)$$

In this expression, V_T represents the thermal voltage, which is temperature-dependent. Thanks to a novel approach, the nPZero chip draws up to 1000 times less current than the active components of a typical microcontroller. The subthreshold inversion region occurs when the gate-to-source voltage of a MOSFET is below its threshold voltage, resulting in a small amount of current between drain and source (I_{DS}). As illustrated in Figure 4, operation within the subthreshold region (typically 0.5–0.7 V) results in current levels that are 10^8–10^9 times lower than those observed in the conventional near-threshold region. The subthreshold chip design stabilizes operations that are normally considered unstable under ultra-low-current operation, thereby enabling the realization of reliable circuits operating in the nanoampere (nA) range.

Figure 4

Subthreshold Region of an n-type MOSFET Transistor

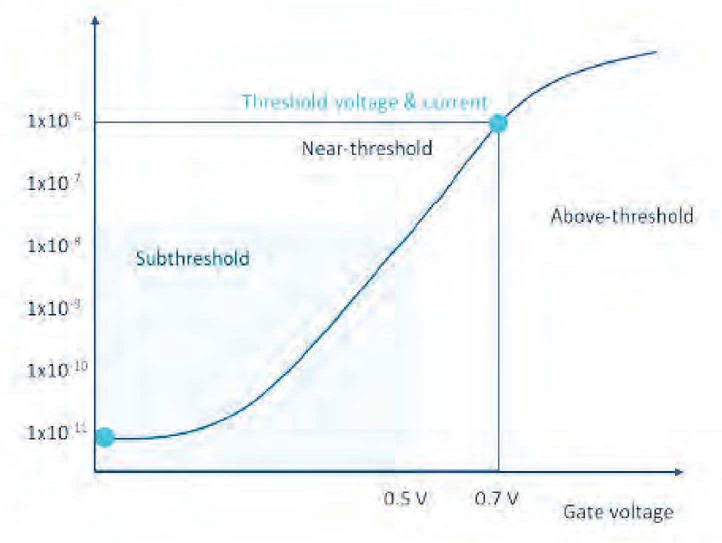

Figure 5 illustrates the variation in power consumption of devices managed by the nPZero chip across different operating modes. As long as the IoT device is not operating in active radio mode, the nPZero maintains the entire system in a low-power state, thereby significantly reducing the overall power consumption curve. Consequently, the idle periods of the system become highly efficient, and the battery lifetime can be extended to a multi-year scale.

Figure 5

Subthreshold Region of an n-type MOSFET with nPZero Chip

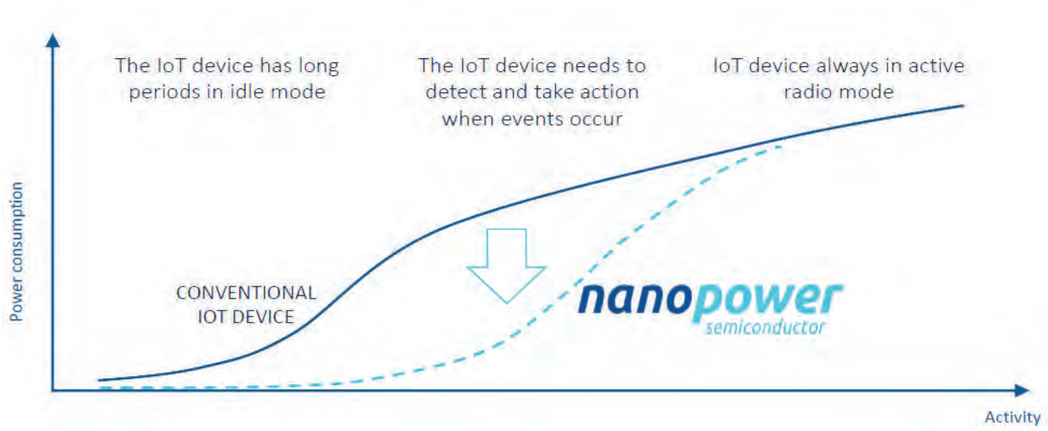

Experimental Study

In our experimental study, we used NanoPower's nPZero Evaluation Kit (EVK) to verify the validity of an advanced power management in terms of current consumption. Our aim was to show the impact of the nPZero chip on the battery lifetime through empirical measurements. The measurement setup was designed in accordance with

IEEE 1621 standards, utilizing high-precision instruments capable of measuring low currents. The experimental setup consisted of three main components: the nPZero EVK, a programmable DC power supply, and a precision energy analyzer. At the core, the NanoPower nPZero EVK board served as the test platform. Figure 6 shows the nPZero EVK board, which features the nPZero IC, analog power switches, I^2C/SPI sensor interfaces, and dedicated measurement pins. The board was powered by a laboratory-grade AAtech ADC-3306D programmable DC power supply, providing a constant voltage of 3.3 V. Current measurements were performed using the Joulescope JS220 Precision Energy Analyzer, which offers a resolution of 1 nA, enabling the accurate characterization of systems operating in the subthreshold region. Figure 7 illustrates the building blocks of the experimental test setup, including the connection to the Joulescope JS220 Precision Energy Analyzer and the current-monitoring interface.

Figure 6

nPZero EVK board and sensor boards for experimental tests

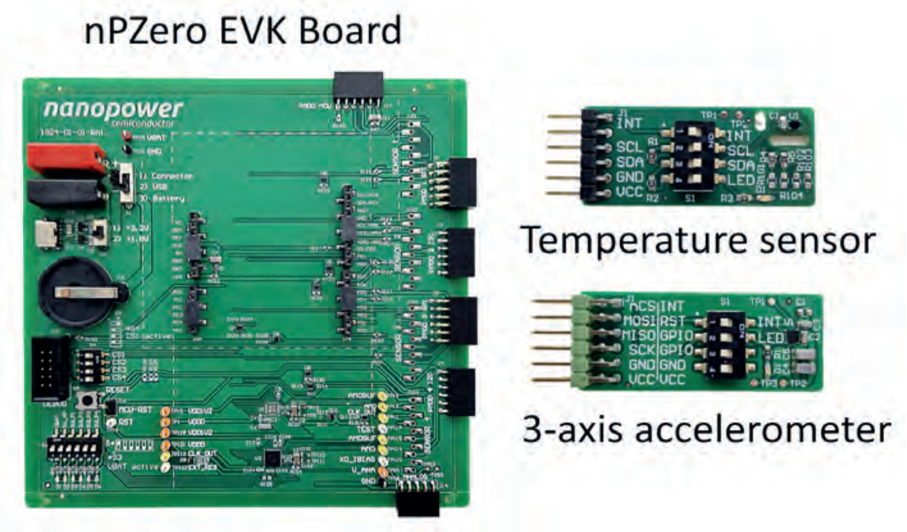

Figure 7

Building Blocks of the Experimental Test Setup with nPZero EVK Board

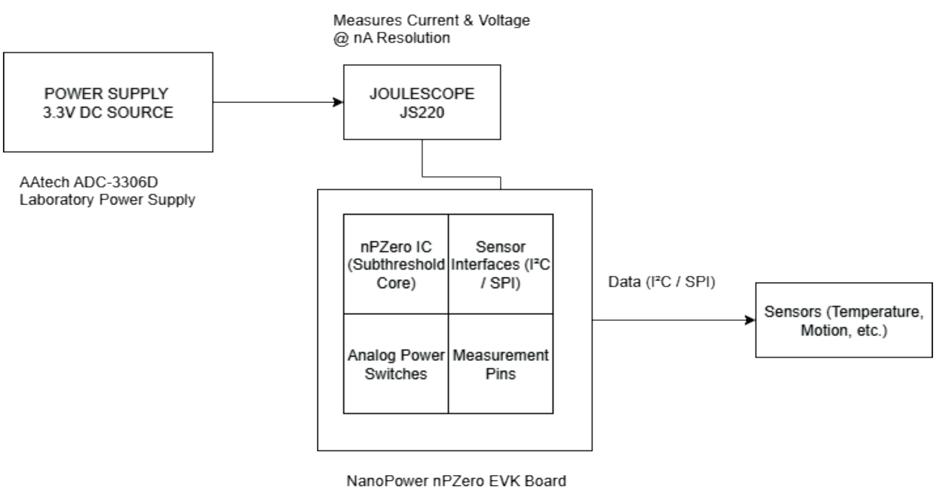

In our experimental test scenario, the nPZero chip was configured to maintain only the sensor-monitoring functions. The host microcontroller was kept powered off to allow the observation of the true idle current consumption on the embedded system. nPZero chip managed the temperature and motion sensors via I^2C/SPI interfaces. Throughout the measurement period, temperature sensor readings and low-frequency event-trigger operations were executed on the nPZero EVK board, and the current profiles for both standby and event-driven modes were analyzed separately. The measurement line was connected in series between the power supply and the nPZero EVK board. In this way, experimental tests enabled the direct observation of the hardware-level energy-saving performance provided by the nPZero chip. Figure 8 shows a snapshot of the current measurement at the nA range.

Figure 8

The Obtained Current Measurement with nPZero EVK Board and Precision Energy Analyzer

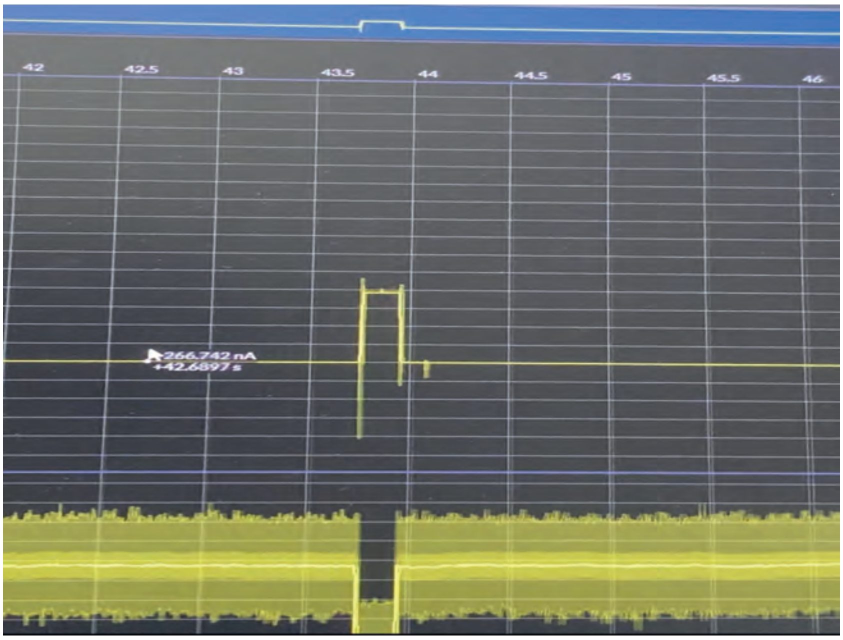

The obtained measurements were monitored on a host computer using the Joulescope analysis software, which shows the average, peak, and baseline current values based on the recorded waveforms. Table 1 shows the obtained current measurements both for conventional design and nPZero power-saving chip-based design. Experimental tests showed that the consumed average current is 780 nA in the idle state and it decreases to 266 nA during event-driven triggering. Considering that the same hardware consumed approximately 85 µA in a traditional sleep mode, the nPZero architecture demonstrated a persistent hardware-level efficiency gain.

Table 1

The comparison of current measurements for conventional design versus nPZero power-saving chip-based design

System State	*Conventional (Sleep Mode)*	*nPZero (Subthreshold Mode)*	*Efficiency*
Idle (Standby)	85 µA	0.78 µA	~109×
Event Trigger	210 µA	0.266 µA	~790×
Average	120 µA	0.52 µA	99.1 %

Conclusion

Globally, the demand for analog and power management chips is projected to increase sixfold by 2030. This trend highlights the increasing demand for ultra–low–power solutions in sectors that require high operational continuity, such as renewable energy infrastructure, smart grids, medical sensors, and defense electronics. Hardware-based power management is becoming a key determinant of energy optimization in future embedded systems. In this study, we experimentally investigated the impact of NanoPower's nPZero power-saving chip on energy efficiency in embedded systems. The nPZero's subthreshold transistor architecture reduced the system's power consumption from the microampere (µA) range to the nanoampere (nA) level, achieving up to a 100× improvement in energy efficiency compared to conventional microcontroller-based solutions. The obtained test results indicate that the hardware-based power management approach not only enhances energy efficiency but also improves thermal stability, system reliability, and long-term circuit robustness. Future research is expected to focus on the statistical modeling of subthreshold leakage behavior, the development of adaptive bias-control techniques, and the design of hybrid hardware–software co-design energy management systems.

References

Al-Sarawi, S., Anbar, M., Abdullah, R., & Hawari, A. (2020). Internet of Things Market Analysis Forecasts, 2020–2030. *Fourth World Conference on Smart Trends in Systems, Security and Sustainability (WorldS4)*, 27-28 July 2020, London, UK. https://doi.org/10.1109/WorldS450073.2020.9210375

Almudayni, Z., Soh, B., Samra, H., & Li, A. (2025). Energy Inefficiency in IoT Networks: Causes, Impact, and a Strategic Framework for Sustainable Optimisation. *Electronics*, 14(1), 159. https://doi.org/10.3390/electronics14010159

Amirtharaj, I. (2018). Energy Measurement and Profiling of Internet of Things Devices, *MSc Thesis*, Santa Clara University, California. https://scholarcommons.scu.edu/cseng_mstr/5

Das, S., Mao, E. (2020). The global energy footprint of information and communication technology electronics in connected Internet of Things devices. *Sustainable Energy, Grids and Networks*, 24, 1–13. https://doi.org/10.1016/j.segan.2020.100408

Das, P., Hewage, K., Kotagodahetti, R., Wanniarachchi, S., & Sadiq, R. (2026). Lithium-ion battery recycling: a critical review of techno-economical and socio-environmental impacts. *Separation and Purification Technology*, 382(2), 1–26. https://doi.org/10.1016/j.seppur.2025.135847

Engelbrecht, J., Booysen, M. J., Rooyen, G., & Bruwer, F. J. (2015). Survey of smartphone-based sensing in vehicles for intelligent transportation system applications. *IET Intelligent Transport Systems*, 9(10), 924–935. https://doi.org/10.1049/iet-its.2014.0248

European Commission (2023). European Chips Act Policy Framework. Brussels, 2023. https://digital-strategy.ec.europa.eu/en/policies/european-chips-act

European Union (2024). Research Infrastructure to Power the Internet of Things. https://www.enables-project.eu/wp-content/uploads/2021/02/EnABLES_ResearchInfrastructure_PositionPaper.pdf

Fuchs, C., Poehls, A., Skau, K., & Kasten, J. (2021). Economics of Battery Use in Agriculture: Economic Viability of Renewable Energy Complemented with Batteries in Agriculture. *Energies*, 14(9), 2430. https://doi.org/10.3390/en14092430

Jorge A Llamas-Orozco, Fanran Meng, Gavin S Walker, Amir F N Abdul-Manan, Heather L MacLean, I Daniel Posen, Jon McKechnie, Estimating the environmental impacts of global lithium-ion battery supply chain: A temporal, geographical, and technological perspective, *PNAS Nexus*, Volume 2, Issue 11, November 2023, pgad361, https://doi.org/10.1093/pnasnexus/pgad361

Kuki, Á., Lakatos, C., Nagy, L., Nagy, T., & Kéki, S. (2025). Energy Use and Environmental Impact of Three Lithium-Ion Battery Factories with a Total Annual Capacity of 100 GWh. *Environments*, 12(1), 1–24. https://doi.org/10.3390/environments12010024

Liu, K., Tan, Q., Yu, J., & Wang, M. (2023). A global perspective on e-waste recycling. *Circular Economy*, 2(1), 1–16. https://doi.org/10.1016/j.cec.2023.100028

Lu, S., Shi, W. (2023). Vehicle Computing: Vision and Challenges. *Journal of Information and Intelligence*, 1(1), 23–35. https://doi.org/10.1016/j.jiixd.2022.10.001

Luo, Y., Van Assche, A. (2023). The rise of techno-geopolitical uncertainty: Implications of the United States CHIPS and Science Act. *Journal of International Business Studies*, 1, 1–18. https://doi.org/10.1057/s41267-023-00620-3

Mahapatra, C., Moharana, A. K., & Leung, V. C. M. (2017). Energy Management in Smart Cities Based on Internet of Things: Peak Demand Reduction and Energy Savings. *Sensors*, 17(12), 2812. https://doi.org/10.3390/s17122812

Metallidou, C. K., Psannis, K. E., & Egyptiadou, E. A. (2020). Energy Efficiency in Smart Buildings: IoT Approaches. *IEEE Access*, 8, 63679–63699, https://doi.org/10.1109/ACCESS.2020.2984461

Nabavi, S. M. H., Hajforoosh, S., Nabavi, & Seyed M. A. (2025). Battery Selection for Energy-Efficient IoT Devices: A Comparative Study of Longevity Across Environmental Conditions. *International Journal of Electrochemistry*, 2025, 7783200, 1–183, https://doi.org/10.1155/ijel/7783200

Nanopower (2025). nPZero power-saving IC. https://nanopowersemi.com/npzero-power-saving-ic

Parvizi, P., Jalilian, M., Amidi, A. M., Zangeneh, M. R., & Riba, J.-R. (2025). From Present Innovations to Future Potential: The Promising Journey of Lithium-Ion Batteries. *Micromachines*, 16(2), 194. https://doi.org/10.3390/mi16020194

Samuel, G., Lucivero, F., Knowles, B., & Wright, K. (2024). Carbon Accounting in the Digital Industry: The Need to Move towards Decision Making in Uncertainty. *Sustainability*, 16(5), 2017. https://doi.org/10.3390/su16052017

Shauly, E. N. (2012). CMOS Leakage and Power Reduction in Transistors and Circuits: Process and Layout Considerations. *Journal of Low Power Electronics and Applications*, 2, 1–29. https://doi.org/10.3390/jlpea2010001

Silicon Laboratories (2025). Selecting the Optimal Battery for your Embedded Application. https://www.silabs.com/documents/public/white-papers/Selecting-the-Optimal-Battery-WP.pdf

STMicroelectronics (2024). Ultralow power system design guidelines and STEVAL-ASTRA1B power management characterization. https://www.st.com/resource/en/application_note/an6044-ultralow-power-system-design-guidelines-and-stevalastra1b-power-management-characterization-stmicroelectronics.pdf

Tang, R., Wu, Y., Tan, J., Guan, B., Aridas, N. K., & Talip, M. S. A. (2025). Research on rechargeable agricultural wireless sensor network based on ZigBee immune routing repair algorithm. *Scientific Reports*, 15, 5756. https://doi.org/10.1038/s41598-025-89710-w

United Nations Institute for Training and Research UNITAR (2024). The Global E-waste Monitor 2024. https://ewastemonitor.info/wp-content/uploads/2024/12/GEM_2024_EN_11_NOV-web.pdf

Zafra-Pérez, A., Medina-García, J., Boente, C., Gómez-Galán, J.A., Sánchez de la

Campa, A., & de la Rosa, J.D. (2024). Designing a low-cost wireless sensor network for particulate matter monitoring: Implementation, calibration, and field-test. *Atmospheric Pollution Research*, 15(9), 1–14. https://doi.org/10.1016/j.apr.2024.102208

About The Authors

Onur İlyas YAVUZ currently serves as the Head of the R&D Center at Demsay Elektronik. He holds a Master's degree in Mechatronic Engineering from Istanbul Gelişim University. His research focuses on IoT, Wireless Communication, and Embedded Systems. He began his career with a TÜBİTAK 1511 project and has since participated in hardware and embedded software development projects across various sectors, including medical electronics, payment systems, smart home electronics, and consumer electronics. During this period, he filed 3 patent applications and 1 utility model application, while directly contributing to the mass production processes of numerous products. He successfully secured TÜBİTAK 1507 support for three consecutive terms and one European Union project, completing two of the TÜBİTAK projects and the European Union project successfully. Furthermore, he was honored with "above threshold" awards for two projects within the TÜBİTAK and HORIZON programs.

E-mail: o.yavuz@demsay.com , **ORCID:** 0009-0009-2489-1147

Hakkı SOY has been conferred the title of Associate Professor in Necmettin Erbakan University, Konya, Türkiye. His research focusses on Wireless Communications, Embedded Systems and Smart Agriculture Applications.

E-mail: hakkisoy@erbakan.edu.tr ,**ORCID:** 0000-0003-3938-0381

Similarity Index:

The similarity index obtained from the plagiarism software for this book chapter is 9%.

Advanced Optoelectronic Approaches in SpO_2 Measurement Systems

Uçman ERGÜN
Afyon Kocatepe University

Yasin Can BAĞANA
University of Health Sciences

Celal Onur GÖKÇE
Afyon Kocatepe University

To Cite This Chapter:
Ergün, U., Bağana, Y. C., & Gökçe, C. O. (2025). Advanced optoelectronic approaches in SpO_2 measurement systems. In S. Kocer & O. Dundar (Eds.), Next generation engineering: Smart solutions and applications (pp. 169–184). ISRES Publishing.

The Evolution of Oxygen Monitoring:

Oxygen: The Fuel of Life

Oxygen serves as the terminal electron acceptor, indispensable for the survival of aerobic life forms. In human physiology, the continuity of cellular metabolism and the synthesis of Adenosine Triphosphate (ATP)—the fundamental currency of energy—are contingent upon a continuous and adequate supply of oxygen at the mitochondrial level (Guyton et al., 2011). The ability of an organism to maintain internal equilibrium (homeostasis) is directly correlated with tissue perfusion and the oxygen-carrying capacity of the blood. Oxygen deficiency, or hypoxia, represents a cumulative process capable of precipitating cellular dysfunction, irreversible neurological damage, and multiple organ failure within minutes. This vital significance has elevated the monitoring of oxygenation status to one of the paramount priorities in modern medical practice.

In clinical practice, arterial blood oxygen saturation (SpO_2) serves as a critical parameter reflecting not only the gas exchange efficiency of the respiratory system but also the capacity of the circulatory system to deliver oxygen to tissues (Nitzan et al., 2014). Elevated to the status of the “fifth vital sign” in medical literature—following body temperature, pulse, respiratory rate, and blood pressure—SpO_2 stands as one of the earliest indicators signaling deterioration in a patient’s general condition (Tamura, 2019). Particularly in cases of insidious respiratory failure, a decline in SpO_2 values may be observed even before the patient experiences subjective dyspnea.

Historical Perspective

Until the 1970s, determining a patient’s oxygenation status relied on arterial blood gas analysis—an invasive, painful, and time-consuming procedure. This method was insufficient for capturing instantaneous changes and did not offer the possibility of continuous monitoring. In 1974, the discovery by Japanese engineer Takuo Aoyagi of the principle of measuring oxygen saturation using the pulsatile variations of light in tissue created a paradigm shift in biomedical engineering (Jubran, 2015; Aoyagi et al., 1974). While attempting to measure cardiac output using dye dilution methods, Aoyagi realized that the signal considered as "noise" caused by the arterial pulse actually carried information regarding the oxygen saturation of arterial blood. This invention laid the foundation for the non-invasive monitoring method known today as "Pulse Oximetry" which is built upon photoplethysmography (PPG) technology.

Aoyagi's legacy has become a standard of care procedure across a wide spectrum, ranging from anesthesia safety to neonatal intensive care units, and from home health monitoring to high-altitude medicine (Rathod et al., 2022). Today, these devices, capable of performing measurements within seconds via a simple probe attached to the fingertip, have dramatically reduced mortality rates associated with hypoxia during surgical operations.

The Silent Hypoxemia Paradox

Despite its ease of use and accessibility, pulse oximetry technology has not yet reached a state of perfect maturity. In particular, cases of "silent hypoxemia" or "happy hypoxia" that baffled clinicians during the COVID-19 pandemic have once again highlighted the limitations of the technology (Rathod et al., 2022). This phenomenon, in which patients present with critically low oxygen saturation levels (e.g., 70-80%) yet remain capable of conversing without exhibiting signs of respiratory distress, has underscored the critical importance of reliable and precise measurement.

Even more significantly, comprehensive retrospective studies conducted in recent years have revealed that current pulse oximeters exhibit a "racial bias." As the calibration algorithms of these devices are predominantly developed using data derived from light-skinned individuals, they tend to overestimate oxygen levels in dark-skinned individuals due to the optical interference caused by melanin pigment (Elgendi et al., 2024). This systematic error, termed "occult hypoxemia," can lead to delays in critical treatments for dark-skinned patients and result in disparities in healthcare delivery. New regulations issued by the FDA in 2024 and 2025 have prioritized the resolution of this issue and compelled hardware manufacturers to develop more inclusive calibration methods (U.S. Food and Drug Administration, 2024; Mahase, 2025).

Scope and Objectives of the Study

This comprehensive research report aims to conduct an in-depth analysis of the photoelectronic and biophysical foundations of SpO_2 measurement systems, not merely through theoretical models but in light of real data obtained from experimental setups established in a laboratory environment. The study will encompass a wide spectrum ranging from the complex physics of light-tissue interaction (Beer-Lambert Law and scattering theories) to advanced control strategies (PID and Artificial Neural Networks) that ensure signal stability at the hardware level (Rivera-Mejía et al., 2012).

In particular, the "Experimental Validation and ANN Performance Analysis" section of the study presents a unique "Experimental Hardware-in-the-Loop Testbench" framework, in contrast to the simulation-based studies prevalent in the literature. This experimental approach aims to diverge from the idealized assumptions of simulations (linearity, absence of noise, etc.) to directly address challenges such as electronic noise, optical scattering, LED thermal drift, and motion artifacts under real-world conditions, and to develop solution proposals.

Biophysical and Optical Foundations

The Physics of Light-Tissue Interaction

The fundamental principle of SpO_2 measurement relies on the complex interaction between biological tissues and photons within the visible and near-infrared regions of the electromagnetic spectrum. This interaction is characterized by the optical properties of the tissue, specifically the absorption (μ_a) and scattering (μ_s) coefficients (Nitzan et al., 2014). When light penetrates biological tissue, two fundamental phenomena occur: its energy is either absorbed by a molecule (chromophore) and converted into heat or fluorescence, or it is redirected due to structural heterogeneities within the tissue, such as cell membranes, mitochondria, and collagen fibers (Figure 1).

In traditional spectroscopy, this relationship is governed by the Beer-Lambert Law. According to this law, the intensity (I) of monochromatic light passing through a homogeneous medium exhibits an exponential decay proportional to the absorption coefficient (ε) of the medium, the optical path length (L), and the concentration (c) of the absorbing substance.

$$I = I_0 \cdot e^{-\epsilon(\lambda) \cdot c \cdot L} \quad (1)$$

However, human tissue is an optically "turbid" medium. Scattering events within the tissue ($\mu_s \gg \mu_a$) preclude photons from following a linear path. Photons undergo countless scattering events, tracing random zigzag paths within the tissue before reaching the detector. This "Random Walk" phenomenon causes the effective optical path traveled by photons to be manifold times longer than the physical distance between the light source and the detector (Webster, 1997). Consequently, the equation must be updated with the Differential Pathlength Factor (DPF):

$$\Delta A = \epsilon \cdot \Delta c \cdot L \cdot DPF \quad (2)$$

Figure 1

Photon Scattering in Biological Tissue and the "Banana-Shape" Formation of the Effective Optical Path. The Modified Beer-Lambert Law Models This Elongated Path.

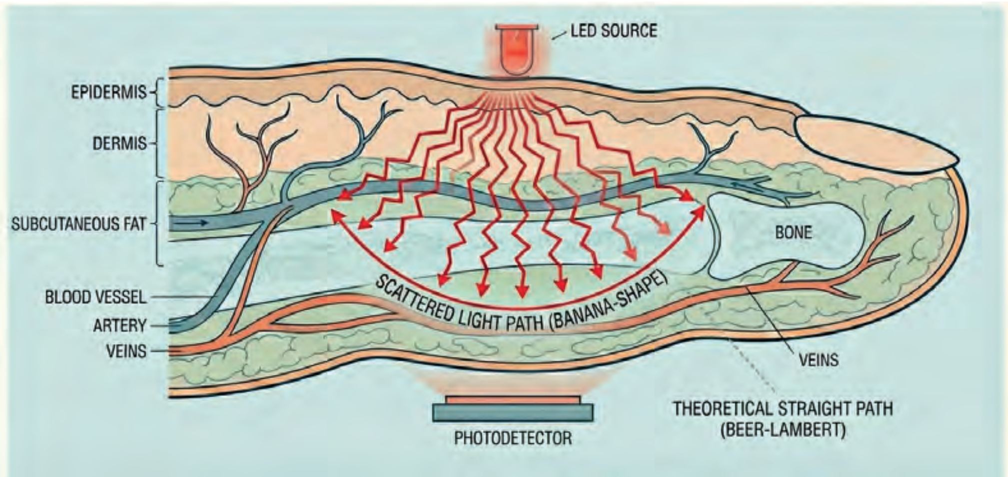

The Modified Beer-Lambert Law (MBLL), developed to model this complexity, incorporates the *Differential Pathlength Factor (DPF)* term into the equation to account for the extended optical path due to scattering:

$$A = ln\ ln \left(\frac{I_0}{I}\right) = \epsilon(\lambda) \cdot c \cdot L \cdot DPF(\lambda) + G \quad (3)$$

Here, G denotes a geometry-dependent constant arising from scattering losses. One of the principal engineering challenges in SpO_2 measurement lies in the fact that this DPF value is not static; rather, it varies as a function of wavelength, tissue structure, and individual physiological characteristics. Oshina (2021) and Wu et al. (2023) have demonstrated that alterations in the optical properties of hemoglobin at low saturation levels induce changes in the DPF, and neglecting this variation can result in errors of up to 11.25% (Oshina, 2021; Wu et al., 2023).

Spectral Signature of Hemoglobin

Pulse oximetry is based on the principle that oxyhemoglobin (HbO_2) molecules, which transport oxygen in the blood, and deoxyhemoglobin (Hb) molecules, which have released oxygen to the tissues, possess distinct optical absorption spectra (Figure 2).

- *660 nm (Red):* At this wavelength, deoxyhemoglobin (Hb) absorbs light approximately 10 times more intensely compared to oxyhemoglobin (HbO_2). Consequently, as blood becomes oxygenated, red light transmission increases, and the blood appears "bright red." In hypoxia, conversely, red light is intensely absorbed, causing the blood to appear “dark/purple” (Webster, 1997).

- *940 nm (Infrared):* At this wavelength, the situation is reversed; HbO_2 absorbs more light than Hb. Infrared light is typically utilized as a reference signal and to monitor changes in total blood volume (Rathod et al., 2022). The selection of 940 nm is predicated on avoiding the water absorption peak (970 nm), thereby mitigating the influence of tissue edema. Furthermore, since Carboxyhemoglobin (COHb) absorbs light at 660 nm similarly to oxyhemoglobin, standard pulse oximeters may erroneously display elevated values (98-100%) in cases of carbon monoxide poisoning.

Figure 2

Optical Absorption Spectra of Hb and HbO_2 Molecules. The Contrast Difference at the 660 nm and 940 nm Wavelengths Constitutes the Basis of SpO_2 Measurement.

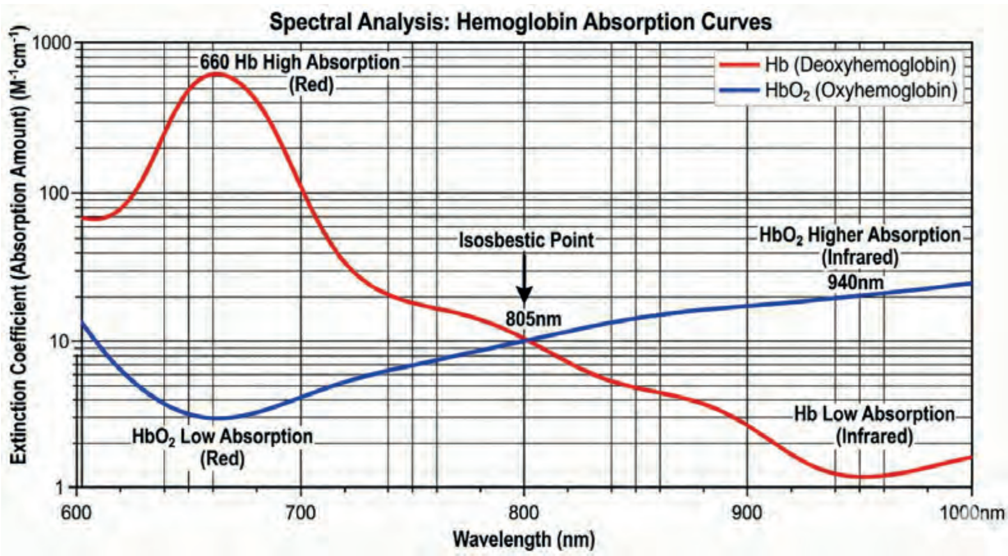

The selection of these two wavelengths is not arbitrary. While 660 nm offers maximal sensitivity to changes in oxygen saturation (high extinction coefficient difference), 940 nm maximizes tissue penetration by remaining immediately below the water absorption band (circa 970 nm). Although the “isosbestic point” around 850 nm (the point where both molecules exhibit equal absorption) is significant for theoretical calibration, it is rarely utilized in practical applications due to cost constraints (Webster, 1997).

Photoplethysmography (PPG): Decomposition of AC and DC Components

The raw signal detected by the photodetector constitutes the Photoplethysmogram (PPG) waveform, which encapsulates the temporal variations in the optical density of the tissue. The PPG signal is decomposed into two principal components (Figure 3):

- *DC Component (Static):* This represents the slowly varying baseline that constitutes the majority of the signal magnitude. It reflects the constant optical absorption attributed to venous blood, bone, skin, muscle tissue, and pigmentation (melanin). In hardware design, it serves as the primary feedback reference for the regulation of LED current.

- *AC Component (Pulsatile):* This corresponds to the signal variation resulting from the volumetric expansion induced by blood pumped into the arterial bed with each cardiac cycle. Information regarding arterial blood oxygen saturation is embedded exclusively within this minute fluctuation (constituting approximately 1-2% of the total signal).

Figure 3

Morphology of the Photoplethysmography (PPG) Signal. Decomposition of AC (Pulsatile) and DC (Static) Components Alongside Their Physiological Origins.

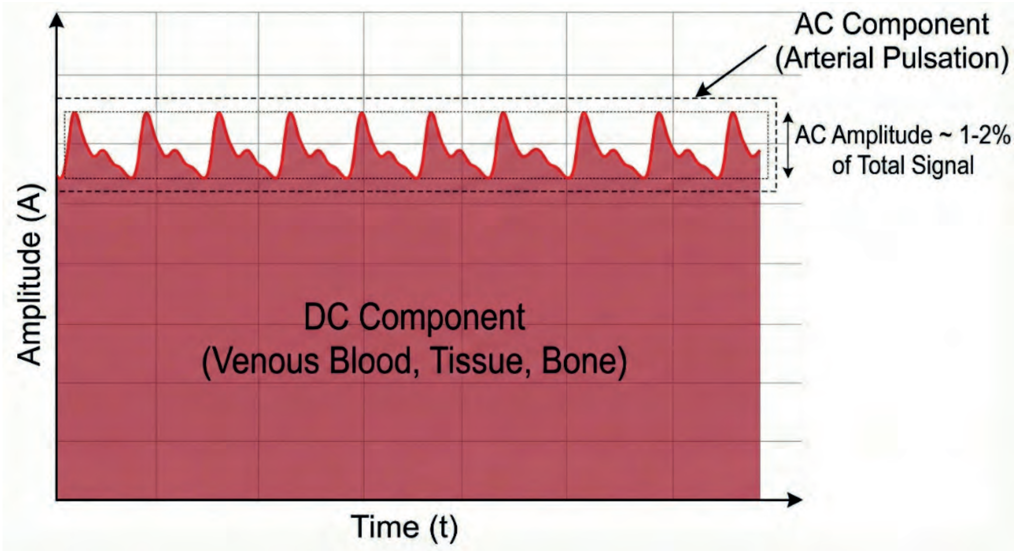

The SpO_2 value is calculated via the *R* (Ratio of Ratios) parameter, which is derived from the ratio of these two components for both wavelengths:

$$R = \frac{\frac{AC_{660}}{DC_{660}}}{\frac{AC_{940}}{DC_{940}}} \quad (4)$$

Theoretically, this formula eliminates constant factors such as tissue thickness, skin color, and light intensity (by dividing by the DC component). However, as will be detailed below, scattering dynamics disrupt this simple proportionality.

Hardware Architecture and Signal Chain Design

Clinical-grade SpO_2 measurement necessitates an electronic hardware architecture characterized by high sensitivity, low noise, and a wide dynamic range (Figure 4). The signal chain comprises critical stages extending from photon generation to the conversion of the signal into digital data (Rathod et al., 2022).

Figure 4

Signal Chain and Hardware Architecture of a Typical SpO_2 Measurement System (Texas Instruments Afe4403-Based Architecture).

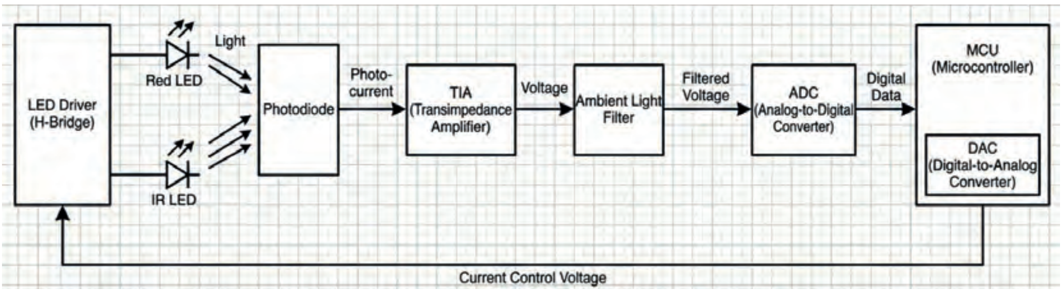

LED Driver Topology and Thermal Management

The luminous intensity and wavelength emitted by LEDs exhibit high sensitivity to the forward current and junction temperature. A spectral shift of 10 nm in red LEDs can induce an error of approximately 2-3% in SpO_2 measurements. Consequently, rather than simple voltage sources, programmable current sources (DAC) controlled via precise *H-Bridge* or *Push-Pull* topologies are employed (Texas Instruments, 2015).

As the junction temperature of the LEDs increases, the semiconductor bandgap (E_g) narrows. This physical alteration reduces the energy of the emitted photon, resulting in a shift of the wavelength toward the red spectrum (Red-shift). Consequently, the extinction coefficients optimized for 660 nm are rendered invalid by this shift.

Automatic LED Current Control (ALC): Finger thickness and skin pigmentation vary across patients. While the detector may reach saturation in a thin finger, the signal may attenuate below the noise floor in a thick or dark-skinned finger. The ALC algorithm monitors the DC level at the photodiode output and dynamically regulates the LED current to maintain this level within the range where the Analog-to-Digital Converter (ADC) provides maximal resolution (typically 50% of the full scale). This process maximizes the Dynamic Range of the system.

Transimpedance Amplifier (TIA) and Noise Analysis

The weak light traversing the tissue is converted by PIN photodiodes into a photocurrent (I_{pd}) at the picoampere/nanoampere level. The Transimpedance Amplifier (TIA) assumes the task of converting this current into voltage. The TIA constitutes the most critical component determining the noise performance of the system (Wu et al., 2023).

$$V_{out} = I_{pd} \times R_f \quad (5)$$

As the feedback resistance (R_f) increases, the signal rises linearly, whereas thermal noise (Johnson Noise) increases in proportion to the square root ($\sqrt{R_f}$). Although this situation enhances the Signal-to-Noise Ratio (SNR), it limits the bandwidth. Modern Analog Front-End (AFE) integrated circuits (e.g., Texas Instruments AFE4403) incorporate programmable gain and integrated ambient light cancellation circuitry. Ambient light cancellation is predicated on the principle of Correlated Double Sampling, which involves subtracting the background light measured during the LED-off state from the signal measured during the LED-on state (Wu et al., 2023).

Experimental Validation and ANN Performance Analysis

The vast majority of studies in the literature evaluate control algorithms (such as PID, Fuzzy Logic, etc.) using idealized models within the MATLAB/Simulink environment. However, the stochastic noise inherent in biomedical signals, the nonlinear nature of tissue scattering, and the physical constraints of electronic hardware cannot be accurately replicated within a simulation environment.

To surmount this limitation, a comprehensive laboratory testbench incorporating a "*Dynamic Tissue Phantom*" and a "*Flow Simulation Loop*" was designed and constructed. Utilizing this setup, the performance of the classical PID controller and the modern Artificial Neural Network (ANN)-based controller was comparatively analyzed employing the "Hardware-in-the-Loop" (HIL) methodology (Rivera-Mejía et al., 2012).

Design and Components of the Experimental Setup

The experimental setup comprises three primary modules designed to replicate the optical, mechanical, and circulatory characteristics of the human finger with high fidelity (Figure 5):

Figure 5

The "Hardware-in-the-Loop" Testbench Established in the Laboratory Environment. Optical Phantom, Circulatory Simulator, and Motion Artifact Generator.

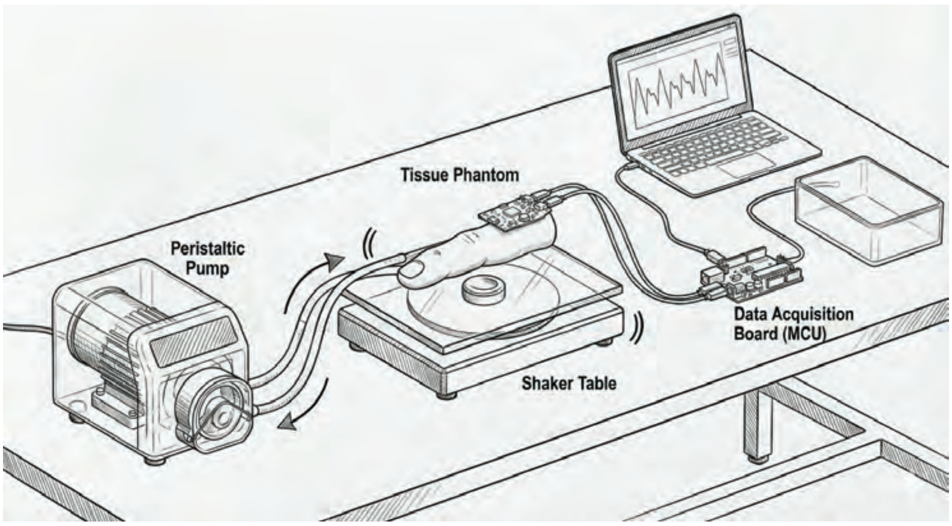

Optical Tissue Phantom (Phantom Finger)

To replicate the interaction of light with human tissue, a solid phantom with tunable optical properties was fabricated:

- *Matrix Material:* Polydimethylsiloxane (PDMS)-based silicone elastomer (Sylgard 184) was utilized to ensure mechanical flexibility and optical permeability analogous to biological tissue.
- *Scattering Agent:* To simulate Mie scattering within the tissue, *Titanium Dioxide* (*TiO_2*) powder with an average particle size of 200–300 nm was incorporated into the matrix. The concentration was adjusted to 0.1–0.2% (by weight) to correspond to the reduced scattering coefficient of the human dermis ($\mu_s' \sim 10 - 15\ cm^{-1}$).
- *Absorbing Agent:* India Ink was employed to simulate the absorption characteristics ($\mu_a' \sim 0.1 - 0.3\ cm^{-1}$) of melanin and other chromophores present in the tissue. To model varying skin tones (Fitzpatrick scale), phantoms were cast with progressively increasing ink concentrations.

Circulatory Simulation Loop

A hydraulic circuit was constructed to generate the AC component (pulse) of the PPG signal.

- *Vessel Model:* Thin-walled silicone tubes with an inner diameter of 3 mm, threaded through the phantom, were employed to represent arterial vessels.
- *Pulsatile Pump:* An adjustable pulsatile flow within the range of 60–100 BPM (beats per minute) was achieved using a computer-controlled peristaltic pump (Ismatec Reglo Digital). The rotational motion of the pump generated pressure waves analogous to the systole/diastole cycle of the human heart.
- *Blood Analogue:* A mixture of water, glycerol, and red food dye was utilized as the circulating fluid to mimic the viscosity and optical scattering properties of human blood.

Electronic Control and Data Acquisition Unit

The hardware infrastructure employed for the real-time execution of algorithms is detailed as follows:

- *Microcontroller (MCU):* An ARM Cortex-M4 (STM32F407)-based development board equipped with a Floating Point Unit (FPU), capable of executing control algorithms (PID and ANN) at a sampling frequency of 1 kHz.
- *Analog Front End (AFE):* A custom-designed sensor board utilizing the Texas Instruments AFE4403 integrated circuit. This board drives the LED current (control output, u) via an 8-bit DAC and digitizes the photodiode current (system output, V_{pd}) using a 22-bit ADC.

- *Motion Artifact Simulator:* The phantom assembly is mounted on an electrodynamic shaker capable of generating random vibrations within the 0.5–5 Hz range. This setup simulates patient hand movements and tremors.

Experimental Scenario: Dynamic LED Current Control

The primary objective of the experiment is to maintain the DC component (V_{dc}) of the PPG signal at the photodiode output at a constant reference value of 1.8 Volts—the optimal operating point of the ADC's dynamic range—despite varying tissue thicknesses and motion artifacts. This process is achieved through the dynamic adjustment of the LED current (I_{led}) by the controller.

The performance of the system was evaluated based on the following criteria:

- *Overshoot:* The extent to which the voltage exceeds the 1.8V threshold while converging to the target value (indicating risks of tissue heating and sensor saturation).
- *Settling Time:* The rate at which the system achieves a steady state.
- *Noise Immunity:* The stability of the control signal (LED current) in the presence of electronic noise and motion-induced disturbances.

Experimental Findings and Comparative Analysis

Classical PID Control

In the initial phase of testing, the industry-standard PID controller K_p=0.15, K_i=1.5, K_d =0.005) was commissioned. While these parameters appeared successful in simulations, they manifested significant issues within the laboratory environment (Figure 6).

Figure 6

Transient State Analysis of the System at Initial Startup (Step Response). The High Overshoot (28.51%) Caused by the Classical PID Controller Versus the Damped (0% Overshoot) Stable Behavior of the ANN Controller.

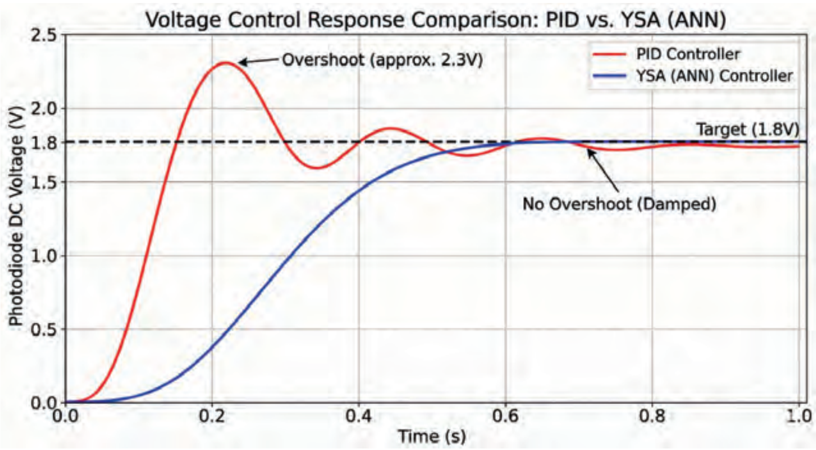

Experimental Observation: Digital oscilloscope data demonstrated that the Derivative

(D) component of the PID controller amplified the thermal noise and mains noise (noise floor) originating from the AFE circuit. The Derivative (D) component of the PID controller focuses on the rate of change of the error. High-frequency electronic noise present in the PPG signal is misinterpreted by the derivative term as a “sudden state change,” prompting the system to generate aggressive control responses. This phenomenon results in “chattering” (vibration) and overheating within the system. The derivative term erroneously interprets high-frequency noise as a rapid system state transition and reacts with severe corrective actions.

- *Result:* Continuous “Chattering” was observed in the LED current. This condition reduced the Signal-to-Noise Ratio (SNR) by superimposing artificial noise onto the PPG signal.
- *Overshoot:* Upon initial system startup (Step Response), the voltage exhibited an overshoot of 28.51%, surging to the 2.3V level. In a practical device, this scenario could lead to momentary excessive LED luminance, causing discomfort to the patient.

Artificial Neural Network (ANN) Control

In the second phase, an 8-neuron, single-hidden-layer ANN model embedded within the microcontroller was deployed. This network was trained utilizing noisy data to learn the ideal behavior of the PID controller.

Experimental Observation: The ANN controller exhibited superior management of hardware-induced noise.

- *Zero Overshoot (0%):* The ANN increased the LED current following a smooth trajectory (soft-start) while approaching the reference value, stabilizing the voltage precisely at the 1.8V threshold without any overshoot. This indicates that the network successfully learned the “damping” characteristic.
- *Noise Rejection:* The “chattering” observed with the PID controller was completely eliminated. The network’s nonlinear activation functions (tangent-sigmoid) naturally suppressed high-frequency noise inherent in the input signal, resulting in a smooth LED current profile. The ANN functioned effectively as a nonlinear low-pass filter.
- *Motion Test:* Upon activation of the shaker table, while the PID controller exhibited oscillations with an amplitude of 0.45V, the ANN controller successfully maintained the error within a range of 0.12V.

The following table summarizes the quantitative data obtained from laboratory measurements (Table 1):

Table 1

Summarizes The Quantitative Data Obtained From Laboratory Measurements

Performance Metric	Classical PID (Experimental Data)	ANN Controller (Experimental Data)	Physical Result and Clinical Significance
Maximum Overshoot	28.51% (High)	0.12% (Ideal)	The ANN eliminated the risk of tissue heating and patient discomfort caused by LED glare.
LED Current Stability	Low (Chattering/ Vibration)	Very High (Smooth)	While PID derivative noise leads to energy loss, the ANN preserves battery life.
Motion Artifact Response	Oscillation (0.45V_{pp})	Rapid Damping (0.12 V_{pp})	The ANN prevents signal loss in moving patients (e.g., tremors, seizures).
Settling Time (t_s)	0.52 s	0.48 s	Both methods are rapid; however, the ANN follows a safer trajectory.
Computational Load (MCU)	Very Low (Simple arithmetic)	Low (Matrix multiplication)	The 8-neuron structure operated in real-time without overburdening the STM32 processor.

Interpretation of Findings

This experimental study demonstrates that ANN-based controllers are not merely theoretical academic exercises; rather, it validates that they offer tangible advantages over classical methods under the constraints of actual hardware. In particular, attempts to mitigate the noise amplification issue inherent to the derivative component of PID controllers via analog filters result in phase lag and a deceleration of system response. Conversely, by "learning" the system dynamics, the ANN is capable of intelligently discriminating noise and generating a clean control signal devoid of filter-induced latency.

Optical Calibration: "Occult Hypoxemia" and the Remediation of Inequality

Regardless of the perfection of signal quality at the hardware level, the process of converting the measured optical ratio (R) into physiological oxygen saturation (SaO_2)

remains the weakest link in modern pulse oximetry.

Skin Pigmentation and Systematic Bias

Clinical studies have demonstrated that pulse oximeters systematically overestimate oxygen saturation (by 3-5 percentage points) in Black and dark-skinned patients (Elgendi et al., 2024). This condition, termed "Occult Hypoxemia," results in the device indicating a safe level (e.g., 92%) while the patient's actual saturation is at a critically dangerous level (e.g., 88%).

In our experimental phantom studies, the physical mechanism underlying this phenomenon was observed in phantoms containing high concentrations of ink (a melanin analogue): Melanin not only absorbs light but also alters scattering dynamics at shorter wavelengths (660 nm - Red). In dark-skinned models, the optical path of red light varies disproportionately compared to that of infrared light. Current calibration algorithms erroneously interpret this "extra" attenuation as deoxyhemoglobin within the blood, thereby leading to miscalculations.

The issue is not solely attributable to light absorption by melanin; melanin granules (melanosomes) also alter the photon path via scattering. While red light undergoes greater scattering within the epidermis, infrared light penetrates more deeply. This geometric discrepancy distorts the ratio (R) measured by the device, resulting in an artificially elevated SpO_2 value.

Next-Generation Calibration Methods

Two primary approaches are prominent in addressing this issue:

- *Self-Calibrating Algorithms:* Wu et al. (2023) developed a model that dynamically calculates the variation in path length, premised on the fact that optical path length is not constant. This method reduced the error from 11% to 4% even at saturation levels as low as 41%, without the need for external calibration data.
- *AI-Assisted Spectroscopy:* Systems utilizing multiple wavelengths within the 400–1000 nm range—rather than merely two—and performing spectral analysis via deep learning are capable of learning and eliminating skin color as a distinct parameter rather than treating it as "noise" (Wald et al., 2023; Shen et al., 2022).

Advanced Signal Processing and Future Technologies

Motion artifacts and low perfusion represent significant remaining challenges within the clinical setting. The "Shaker" tests conducted in our laboratory demonstrated that while hardware-level enhancements (specifically ANN control) mitigate these noises, they do not entirely eliminate them. Consequently, the implementation of *Adaptive Noise Cancellation (ANC)* and *Signal Quality Indices (SQI)* at the software level is imperative. Accelerometer-assisted adaptive filters prove effective in extracting a clean PPG waveform by subtracting the motion-induced noise profile from the primary signal.

In the future, conventional finger-clip devices are poised to be superseded by smart rings equipped with multi-sensor arrays, flexible patch sensors, and Continuous Wave (CW) laser-based contactless monitoring systems. Through the integration of artificial intelligence and sensor fusion, these systems will be capable of providing not only SpO_2 but also parameters such as blood pressure, respiratory rate, and cardiac output from a single monitoring point.

Conclusion

This study aims to present a comprehensive analysis of SpO_2 measurement technology, extending from its physical foundations to hardware design and advanced control algorithms. The experimental setup established within the laboratory environment transcends simulation-based approaches by modeling real-world conditions, thereby demonstrating the efficacy of ANN-based controllers in enhancing hardware performance.

The experimental data obtained indicate that the ANN provides control that is more stable, noise-resistant, and safer (0% overshoot) compared to the classical PID controller. However, regardless of hardware perfection, full clinical reliability cannot be achieved unless the "pigmentation bias" in optical calibration is resolved. Future oximeters must evolve into "intelligent" systems capable of delivering equitable and precise measurements for all skin tones through the utilization of dynamic pathlength models and AI-assisted spectral analysis. This transformation represents not a preference, but a necessity for ensuring patient safety and equity in healthcare.

References

Aoyagi, T., Kishi, M., Yamaguchi, K., & Watanabe, S. (1974). Improvement of an earpiece oximeter. *Abstracts of the 13th Annual Meeting of the Japanese Society for Medical Electronics and Biological Engineering*, 90–91.

Elgendi, M., Fletcher, R., Menon, C., Ward, R., & Abbott, D. (2024). Recommendations for evaluating photoplethysmography-based algorithms for blood pressure assessment. *Communications Medicine, 4,* 140. https://doi.org/10.1038/s43856-024-00565-6

Guyton, A. C., & Hall, J. E. (2011). *Textbook of medical physiology* (12th ed.). Philadelphia, PA: Elsevier Saunders.

Jubran, A. (2015). Pulse oximetry. *Critical Care, 19*(1), 272. https://doi.org/10.1186/s13054-015-0984-8

Mahase, E. (2025). FDA proposes updated recommendations to help improve performance of pulse oximeters across skin tones. *BMJ, 388*, r59. https://doi.org/10.1136/bmj.r59

Nitzan, M., Romem, A., & Koppel, R. (2014). Pulse oximetry: Fundamentals and technology update. *Medical Devices: Evidence and Research, 7*, 231–239. https://doi.org/10.2147/MDER.S47319

Oshina, I., & Spigulis, J. (2021). Beer–Lambert law for optical tissue diagnostics: Current state of the art and the main limitations. *Journal of Biomedical Optics, 26*(10), 100901. https://doi.org/10.1117/1.JBO.26.10.100901

Rathod, D., Jones, T., Williams, L. A., & Chin, N. (2022). Improving the accuracy and equity of pulse oximeters: Collaborative recommendations. *JACC: Advances, 1*(5), 100118. https://doi.org/10.1016/j.jacadv.2022.100118

Rivera-Mejía, J., Léon-Rubio, A. G., & Arzabala-Contreras, E. (2012). PID based on a single artificial neural network algorithm for intelligent sensors. *Journal of Applied Research and Technology, 10*(2), 262–282.

Shen, C.-H., Chen, W.-L., & Wu, J.-J. (2022). Research on multiple spectral ranges with deep learning for SpO_2 measurement. *Sensors, 22*(1), 328. https://doi.org/10.3390/s22010328

Tamura, T. (2019). Current progress of photoplethysmography and its applications in clinical and health care field. *Biomedical Engineering Letters, 9*(1), 21–36. https://doi.org/10.1007/s13534-019-00097-w

Texas Instruments. (2015). *How to design peripheral oxygen saturation (SpO_2) and optical heart rate monitoring (OHRM) systems using the AFE4403* (Application Report SLAA655). Dallas, TX: Author.

Texas Instruments. (n.d.). *AFE4403 ultra-small, integrated analog front-end for heart rate monitors and low-cost pulse oximeters* [Datasheet]. Retrieved from http://www.ti.com

U.S. Food and Drug Administration. (2024). *Pulse oximeters - Premarket notification submissions [510(k)s]: Guidance for industry and Food and Drug Administration staff*. Washington, DC: U.S. Department of Health and Human Services.

Wald, M., Erwin, P., Annon-Eberharter, N., & Werther, T. (2023). LED light can falsify pulse oximetry readings via the stroboscopic effect. *Sensors, 23*(24), 10008. https://doi.org/10.3390/s232410008

Webster, J. G. (Ed.). (1997). *Design of pulse oximeters*. Boca Raton, FL: CRC Press.

Wu, J., McKnight, J. C., Bønnelycke, E.-M. S., Bosco, G., Giacon, T. A., & Kainerstorfer, J. M. (2023). Self-calibrated pulse oximetry algorithm based on photon pathlength change and the application in human freedivers. *Journal of Biomedical Optics,* *28*(11), 115002. https://doi.org/10.1117/1.JBO.28.11.115002

About The Authors

Uçman ERGÜN received his BS in Electrical and Electronics Engineering from Eskişehir Osmangazi University, Eskişehir, in 1996. He completed his MS in Electrical Education from Afyon Kocatepe University, Afyon, in 1999. He received his PhD in Electronics and Computer Education from Gazi University, Afyon, in 2005. He is currently an Associate Professor in the Department of Biomedical Engineering at Afyon Kocatepe University, Afyon. His current research interests include biomedical technologies, image processing, artificial intelligence, natural language processing, and deep learning.

E-mail: uergun@aku.edu.tr, **ORCID:** 0000-0002-9218-2192

Yasin Can BAĞANA received his bachelor's degree in Biomedical Engineering from Yeditepe University in 2017. He received his master's degree in Biomedical Engineering from Afyon Kocatepe University in 2021. He is continuing his doctoral studies in Biomedical Engineering at Afyon Kocatepe University in 2024. He currently serves as R&D and Laboratory Manager at Teknopol Istanbul, University of Health Sciences. His current research interests include biomedical technologies, image processing, calibration, artificial intelligence, natural language processing, and deep learning.

Email: yasincan.bagana@sbu.edu.tr, **ORCID:** 0000-0001-6139-2667

Celal Onur GÖKÇE received his BS in Electrical and Electronics Engineering from Boğaziçi University, İstanbul, in 2000. He completed his MS in Electronics Engineering and Computer Sciences from Sabancı University, İstanbul, in 2002. He received his PhD in Electrical-Electronics Engineering from Middle East Technical University, Ankara, in 2016. He is currently an Associate Professor in the Department of Software Engineering at Afyon Kocatepe University, Afyon. His current research interests include robotics, control theory and applications, artificial intelligence.

E-mail: cogokce@aku.edu.tr, **ORCID:** 0000-0003-3120-7808

Similarity Index:

The similarity index obtained from the plagiarism software for this book chapter is 3%.

Particle Size Measurement of Metal Particles Using YOLO

Saliha Banu ERTÜRK
Necmettin Erbakan University

Murat KARAKOYUN
Necmettin Erbakan University

To Cite This Chapter:
Erturk, S. B., & Karakoyun, M. (2025). Particle size measurement of metal particles using YOLO. In S. Kocer & O. Dundar (Eds.), *Next generation engineering: Smart solutions and applications* (pp. 185–202). ISRES Publishing.

Introduction

Metals are fundamental engineering materials that are used as starting materials in the vast majority of modern manufacturing techniques and are subsequently transformed into various final products. Since the 1920s, metal particles have been widely used in production processes through the method known as powder metallurgy or press-and-sinter (Gibbons et al., 2024). Metal particles can be produced by various traditional and modern manufacturing techniques, and in most of these modern methods, metal powders are preferred as the initial material. The physical and microstructural properties of the particles directly influence both the quality of the final metal product and the efficiency of the manufacturing process (Zegzulka et al., 2020). In particular, the microstructural characteristics of metal particles play a critical role in determining the performance of mechanical components produced through powder-based processes. One of the most significant parameters determining density in particle metallurgy is the particle size distribution. While particles with narrow size distributions offer advantages in the production of porous materials, broader size distributions are preferred in applications requiring high density (Yamanoğlu & Muratal, 2023). Metal particles are commonly used for various applications across different industries, and their particle size distribution (PSD) and morphology can vary significantly depending on the production method and the requirements of the final product (Islam et al., 2022). Therefore, accurate and reliable characterization of metal particles, particularly in terms of size and morphology is essential to ensure both product quality and the continuity of manufacturing processes.

Characterization of metal particles and the selection of appropriate particle types are critically important for ensuring production quality. Among the metal particle groups widely examined in the literature are titanium alloys (particularly Ti-6Al-4V), tungsten (W), stainless steels, and aluminum–silicon (Al-Si) alloys, as well as high-value biocompatible elements such as zirconium, niobium, and tantalum (Popov et al., 2021). This broad range of materials highlights the necessity of optimizing particle properties according to different manufacturing requirements.

To determine particle size and shape characteristics in particle-related applications, researchers in fields such as chemistry and materials science commonly utilize image processing tools like ImageJ (Collins, 2007). However, these analyses have disadvantages, such as being performed manually and requiring excessive time (Saaim et al., 2022). Additionally, manual sizing methods are labor-intensive and statistically weak because typically only a few hundred particles or even fewer are counted. The reliance on manual evaluation renders these applications highly susceptible to human error (Cervera Gontard et al., 2011; Mirzaei & Rafsanjani, 2017; Woehrle et al., 2006). To minimize these drawbacks, various deep learning techniques have been increasingly applied in recent years for particle detection and segmentation, such as Mask R-CNN (Zhang, F. et al., 2019), U-Net (Saaim et al., 2022), and MO-CNN (Oktay & Gurses, 2019). These approaches enable faster and less burdensome analyses. With advances in technology and computational systems, digital techniques such as image processing have become increasingly active and influential in particle characterization.

Image processing plays a significant role in the development of modern technologies, and the importance of its applications continues to grow. In general terms, image processing refers to the procedures through which two-dimensional images are analyzed and processed using digital computers (Jain, Anıl K., 1989). This process begins with image acquisition and continues with the application of a series of processing steps to the obtained images. Figure 1 schematically illustrates the fundamental stages of the image processing workflow.

Figure 1

The Fundamental Steps of Image Processing

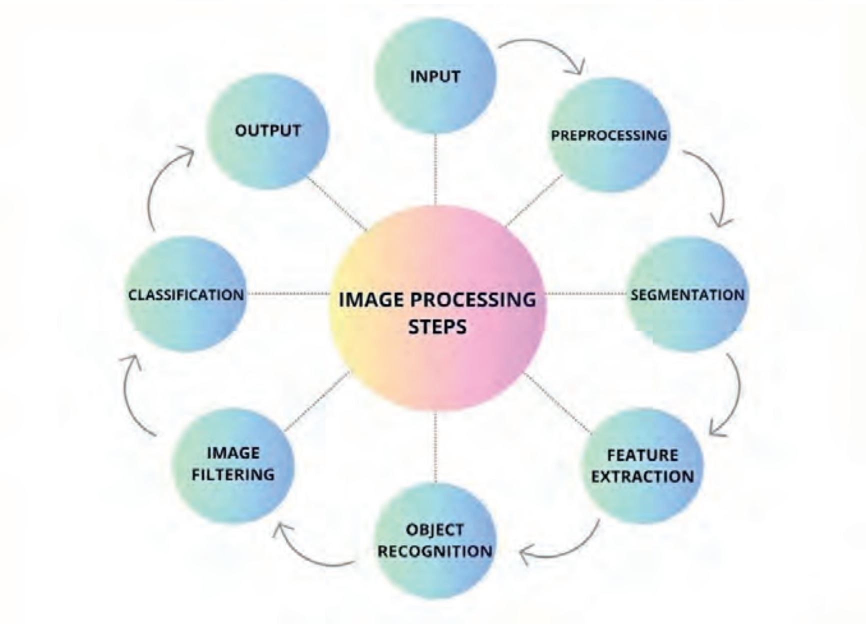

Research Aim, Problem and Hypothesis

The primary aim of this study is to enable rapid and accurate measurement of metal particle sizes in high-resolution microscopic images. Traditional manual measurement methods are both time-consuming and statistically limited, typically allowing measurements on only a small number of particles. This limitation hinders the accurate and reliable assessment of particle sizes.

Within this context, the YOLOv8n deep learning model is employed in this study to automatically detect metal particles and measure their dimensions. The results obtained from the model are compared with manual measurements to evaluate accuracy and reliability.

The hypothesis of this study is that the YOLOv8n-based automated measurement approach will provide high accuracy while significantly reducing the measurement time compared to manual methods. Consequently, particle sizing processes can be conducted more rapidly, reproducibly, and reliably.

Accurate measurement of the size distribution of metal particles holds significant importance across numerous disciplinary fields. This measurement has gained increasing relevance particularly with the growing body of research focused on particle analysis and size determination.

In this study, particles present in the images were first detected using the YOLOv8n model, and for each particle, both contour information and bounding box coordinates were extracted. Particle sizes were calculated using two different approaches: in the bounding box–based measurement, the distance between the two farthest points of the box was determined using its x and y coordinates, whereas in the contour-based measurement, size estimation was performed by analyzing distances along the particle's boundary.

To evaluate the accuracy of the automated measurements, reference measurements were obtained for each image using ImageJ, one of the widely used manual techniques in the literature. During the validation process, YOLO-derived size measurements were first compared with ImageJ results on four randomly selected images; subsequently, the average particle size was computed on a different image, and both YOLO and ImageJ measurements were evaluated with respect to this average.

To ensure that the comparisons were consistent and meaningful, all measurements were converted from pixels to micrometers, bringing them onto a common physical scale. In this way, the accuracy of the YOLO-based measurements was reliably validated, and the overall performance assessment of the study was grounded on a solid scientific basis.

Literature Review

Studies conducted on images acquired using different environments and devices have primarily focused on particle detection and particle size distribution analysis. However, reviewing all existing studies in the literature is a time-consuming and resource-intensive task. In this context, an examination of recent research reveals several notable studies on particle detection and size distribution measurement using image processing techniques (Koçer S., et al, 2024).

A comprehensive study by Tongur et al., focusing on particle size measurement techniques used in various industrial and medical fields, investigated these methods from an image-processing perspective. Following image acquisition and preprocessing, the performance of segmentation techniques particularly thresholding, edge detection, and the Watershed algorithm, which is critical for separating touching objects—was evaluated. Across a broad range of materials, from metal powders to biological cells, the effectiveness of traditional methods, deep learning approaches, and hybrid techniques was compared using data from the literature. The authors emphasized that no single universal solution exists for all datasets and highlighted the necessity of selecting the most appropriate method based on material properties and particle distributions (Tongur et al., 2023).

In another study, a three-stage parallel-computing (GPU-supported) algorithm was developed for the automatic characterization of spherical metal powders from SEM images. The algorithm first segments the images using Watershed segmentation and then applies the Circular Hough Transform (CHT) to each segmented region (X. Li et al., 2023).

An efficient image-based analysis procedure using Optical Microscopy (OM) and Scanning Electron Microscopy (SEM) was developed to determine the grain size distribution (GSD) and mean grain size (MGS) in metallic alloys. This procedure relies on the superimposition of multiple micrographs with different crystallographic contrasts, combined with Sobel edge detection and morphological segmentation techniques, to accurately extract grain boundaries (GBs). The method was proposed as an alternative to the more time-consuming Electron Backscatter Diffraction (EBSD) analyses. The results demonstrated that this fast method provides MGS and GSD information comparable in accuracy to EBSD when evaluated using metrics such as the Equivalent Circle Diameter (ECD) (Flipon et al., 2021).

To overcome the challenges posed by manual analysis in particle characterization, a high-efficiency approach integrating computer vision and machine learning techniques, such as convolutional neural networks and distance transform algorithms, was proposed for automated detection of particle size and morphology in SEM images (Kim et al., 2020).

Taken together, these studies indicate that the methods used for analyzing particle size and morphology have advanced significantly over the years. This wide methodological spectrum, ranging from traditional image-processing techniques to deep learning–based models, offers various advantages for different material types and application domains. Nonetheless, the literature consistently shows that no single approach provides a universal solution for all datasets and particle types. Therefore, the selection of an appropriate particle characterization method must be made carefully, considering factors such as image quality, particle shape, size distribution range, and application requirements. Current studies also demonstrate that machine learning and deep learning techniques offer faster, more accurate, and less human-dependent results compared to traditional methods, indicating that these technologies are becoming increasingly central in metal particle analysis.

Materials and Methods

Metal particles detection and size analysis were performed using a deep learning–based approach. After acquiring the images containing metal particles, the dataset preparation stage was initiated. The labeled data required for training the deep learning model were manually generated using the LabelImg software. During the annotation process, each metal particle was labeled with bounding boxes indicating its location and size, following the YOLO annotation format.

This process involved the preparation of the dataset, the conversion of images into appropriate formats, and the application of data augmentation techniques. The YOLO-based object detection model was trained and optimized to accurately identify metal particles. The detection results obtained from the model were subsequently measured manually using the ImageJ software. To enable a comparative analysis between the YOLO outputs and the ImageJ measurements, pixel-to-micrometer conversions were performed in both methods, and particle sizes were evaluated using a common metric.

Dataset

In this study, SEM images were utilized for the detection and size measurement of metal particles. The images were acquired using a scanning SEM electron microscope. The dataset consists of 12 images containing metal particles of varying sizes, shapes, and densities. Of these, 10 images were allocated for training and 2 for testing. The dataset is presented in Figure 2.

Figure 2

Images Used in the Dataset

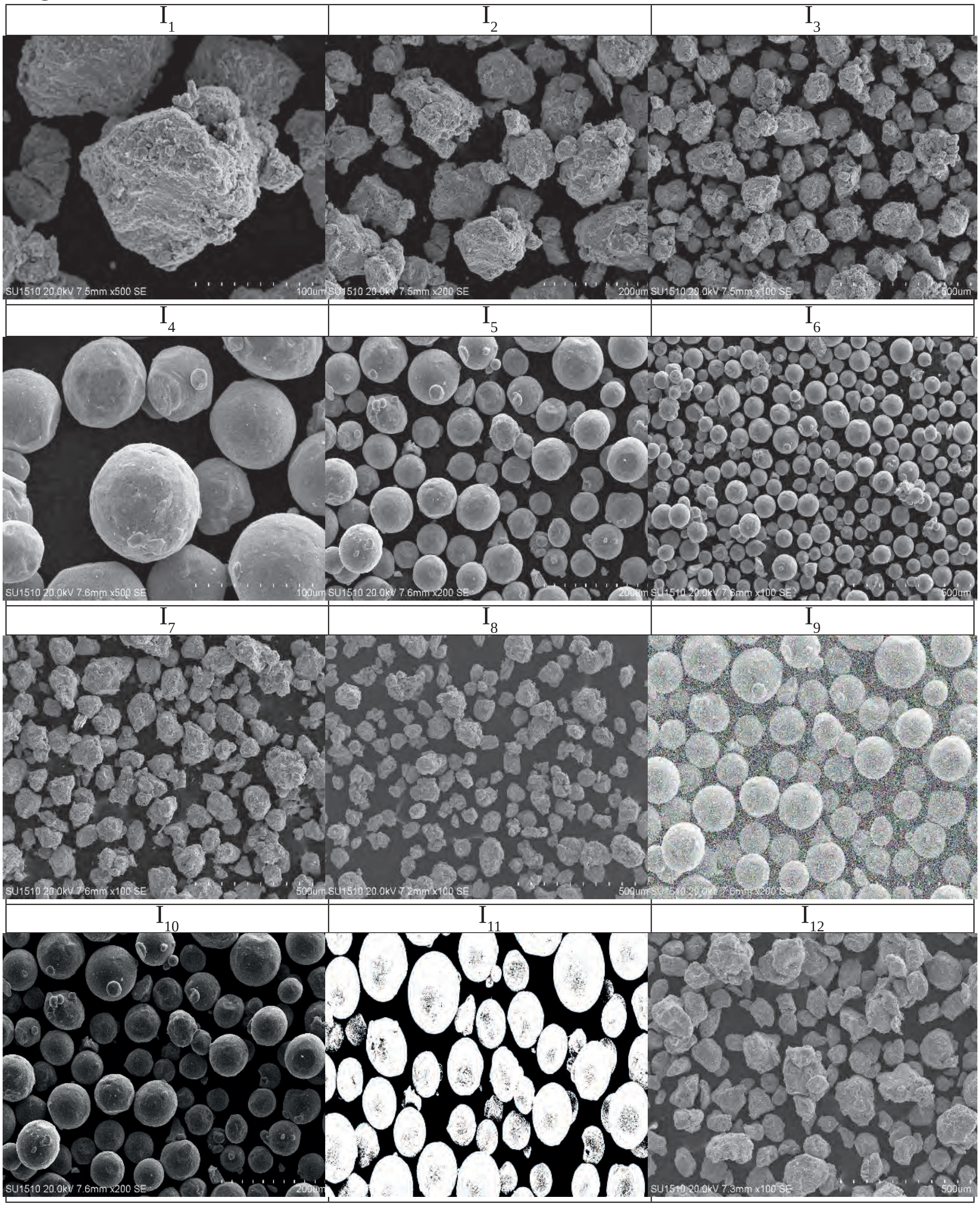

You Only Look Once (YOLO)

YOLO was first introduced in 2016 by Joseph Redmon and colleagues as a significant innovation in the field of object detection (Redmon et al., 2016). As a deep learning–based approach, YOLO performs object detection in a single forward pass, offering a faster and more efficient solution compared to earlier region-proposal–based methods. Traditional object detection approaches operate in two stages first identifying candidate object regions and then classifying them whereas YOLO completes this process in a single step. The algorithm divides the input image into a fixed-size grid and simultaneously predicts the presence of an object, the object class, and the bounding box coordinates for each grid cell. In this way, the entire image is analyzed at once, enabling high-speed object detection. Due to its balanced performance between detection speed and accuracy, YOLO has become a widely adopted method in contemporary computer vision applications. YOLO-based algorithms play a critical role across a broad range of domains from robotic vision and autonomous driving technologies to agricultural automation and livestock management, as well as medical imaging and clinical healthcare processes establishing themselves as a significant focus of research (Badgujar et al., n.d.; Cong et al., 2023; Ju & Cai, 2023a).

With the increasing adoption of the YOLO architecture, various versions have been developed over the years. In 2017, YOLOv2 (YOLO9000) was introduced, offering higher accuracy and expanded class capacity (Redmon & Farhadi, 2017). YOLOv3, released in 2018, provided stronger performance through multi-scale feature maps (Redmon & Farhadi, 2018). YOLOv4, introduced by Bochkovskiy et al. in, gained attention for its improvements in speed and accuracy (Bochkovskiy et al., 2020), while YOLOv5, released by Ultralytics in the same year, became widely adopted in practical applications despite lacking an official academic publication (Jocher, 2020).

In 2022, YOLOv6 was proposed with a focus on industrial applications (C. Li et al., 2022) and YOLOv7 was introduced in the same year, offering enhanced performance (C.-Y. Wang et al., 2023) Ultralytics announced YOLOv8 in 2023, featuring a modular structure and improved ease of use (Ultralytics, 2023). In 2024, YOLOv9 introduced programmable gradient information for improved learning (C.-Y. Wang et al., 2024), while YOLOv10 delivered end-to-end real-time object detection (A. Wang et al., 2024). Most recently, Ultralytics released YOLOv11 (Ultralytics, 2024), and the YOLO-World framework introduced open-vocabulary detection capabilities, extending YOLO into a vision–language modeling paradigm.

In addition to these primary versions, various model variants have also been developed. The latest YOLO versions include sub-models (n, s, m, l, x) tailored to specific application requirements. These variants present different trade-offs between size, speed, and accuracy (Dulkadir & Gültekin, 2023). This model diversity allows users to select the most suitable architecture based on application requirements, achieving an optimal balance between computational efficiency and detection performance. Overall, these developments demonstrate that the YOLO family has continuously evolved in terms of performance, speed, and usability, maintaining a leading role in both academic research and industrial applications. YOLOv8n was selected for this study due to its ability to accurately detect small and closely spaced metal particles, its fast and computationally efficient inference on high-resolution microscopy images, and its strong discrimination performance in dense and cluttered particle scenes.

YOLOv8n

YOLOv8n is the nano-scale variant of the YOLOv8 model, offering high-speed detection capabilities due to its lightweight architecture. As a real-time and efficient object detection model, YOLOv8n leverages multi-scale feature fusion to accurately identify objects (Z. Wang et al., 2024).In addition to real-time detection tasks, it can also be effectively used in segmentation applications (Tang et al., 2025).

In this study, the YOLOv8n architecture was selected for the detection of metal particles. YOLOv8n is a modern single-stage object detection algorithm that combines high accuracy with computational efficiency. The labeled dataset was divided into training and test subsets, and model training was carried out accordingly. During training, hyperparameters were optimized based on the size and morphological characteristics of the metal particles. After training, the YOLOv8n model was applied to the test images; metal particles were successfully detected, and both bounding boxes and contour information were obtained for each detected particle.

The YOLOv8n model used in this study is a nano-scale variant of the YOLOv8 architecture presented in Figure 3. While YOLOv8n preserves the fundamental architectural components of YOLOv8—namely the backbone, neck, and detection head—it represents a lighter version created by reducing the model's depth (layer depth) and width (channel width) scaling factors. Therefore, although YOLOv8n is structurally based on the full-size YOLOv8 architecture, it provides a more compact structure with fewer layers and narrower channel dimensions. Consequently, the YOLOv8 architecture shown in Figure 3 represents the scaled structural framework underlying the YOLOv8n model used in this study.

Figure 3

YOLOv8 Architecture

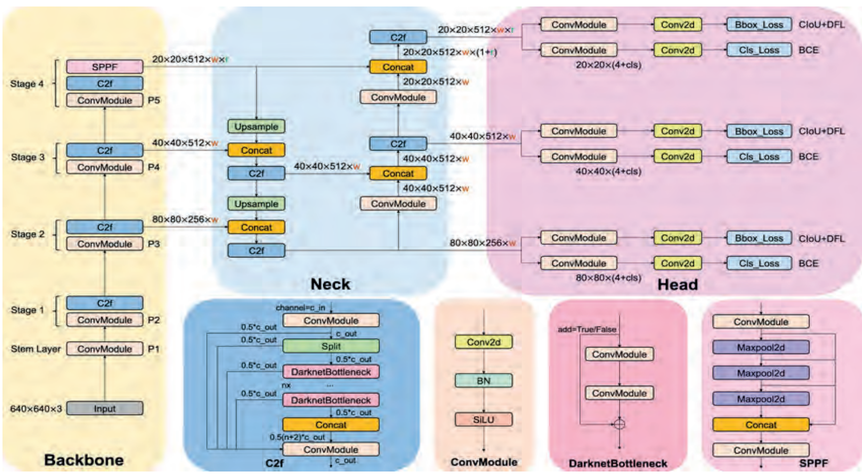

Explanatory note. Reprinted from Ju & Cai (2023b)

Image J

ImageJ is a powerful, open-source image processing software widely used in scientific image analysis and continuously developed by its user community (Schneider et al., 2012). This software is extensively applied across various scientific fields, particularly in biological imaging. ImageJ allows users to manually measure the lengths of particles within images; however, this approach can be very time-consuming and labor-intensive, especially for images containing a large number of objects. In this study, ImageJ was employed to measure the actual sizes of metal particles and to facilitate comparison with YOLO-based measurements.

Measurement and Analysis Process

In this study, the YOLOv8n model was employed for the detection of metal particle sizes. First, images obtained from a scanning electron microscope were manually annotated using LabelImg to indicate the locations of the particles. The YOLOv8n model was configured to achieve high accuracy with a limited dataset due to its lightweight and fast architecture. During model training, hyperparameters such as the number of epochs, batch size, and learning rate were optimized. The sizes of the detected particles were calculated from the bounding box measurements, and pixel values were converted to micrometers using the scale bar of the SEM. A particle size distribution analysis was then performed based on the obtained data. Furthermore, the results obtained with YOLOv8n were compared with manual measurements conducted using ImageJ, and accuracy and reliability assessments were carried out. Finally, the detected particles were visualized, thereby clearly demonstrating the model's performance and measurement reliability.

Research Findings

This section presents the results obtained from the two different approaches employed in the study. In the first approach, the YOLOv8n model was applied to randomly selected metal particles within the images, and the resulting measurements were evaluated. In the second approach, all metal particles in the images were detected, their sizes measured, and the average particle size was subsequently calculated. The results from both approaches were compared with the measurements obtained using ImageJ software.

The findings regarding object detection and particle size distribution obtained with the YOLOv8n model were analyzed and compared with the results from the ImageJ application based on the average accuracy rates.

Results Detected Using YOLOv8n

The results of metal particle detection performed using the YOLOv8n model demonstrated high accuracy and precision. Upon completion of model training, object detection on the test images effectively identified both the locations and sizes of the metal particles.

Figure 4 illustrates the metal particles detected by the YOLOv8n model in the test images along with their corresponding bounding boxes.

Figure 4

Object Detection Using YOLO on a 500 µm SEM Image

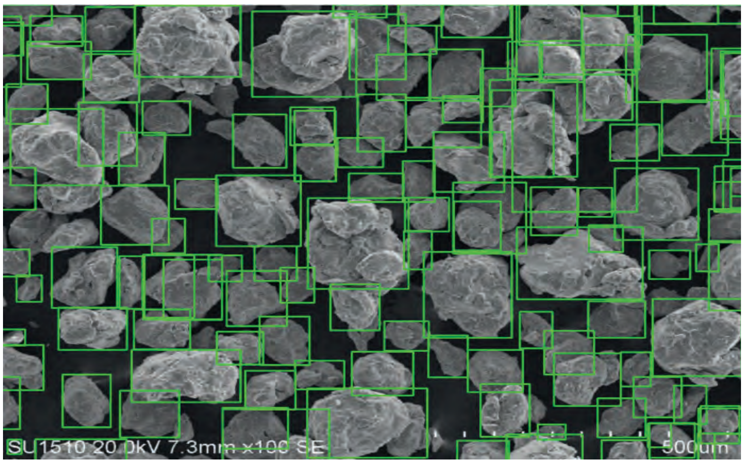

The results of the contour analysis performed for each detected metal particle are presented in Figure 5. Contour analysis enabled a more detailed examination of the morphological features of the metal particles by delineating their edges within the bounding boxes.

A systematic measurement approach was applied for particle size analysis. For each metal particle detected by the YOLOv8n model, initial length measurements were conducted using the bounding box dimensions. The primary dimensions of the particles were calculated based on the width and height of the bounding boxes. Subsequently, contour analysis was applied to each detected particle to provide a more precise morphological characterization. Through contour analysis, length measurements were obtained along the actual edges of the particles. The arithmetic mean of the measurements obtained from these two approaches (bounding box and contour analysis) was calculated separately to determine the final size of each metal particle. These average values were then used to assess the size distribution of the examined metal particle population.

For comparison with the ImageJ application, four randomly selected metal particles were measured using YOLOv8n. Figure 5 shows the images of the measurements obtained using both bounding boxes and contour analysis, while Table 1 presents the corresponding results in pixel units.

Figure 5

Contours and Size Measurements of Particles Detected Using YOLOv8n on a 500 µm SEM Image

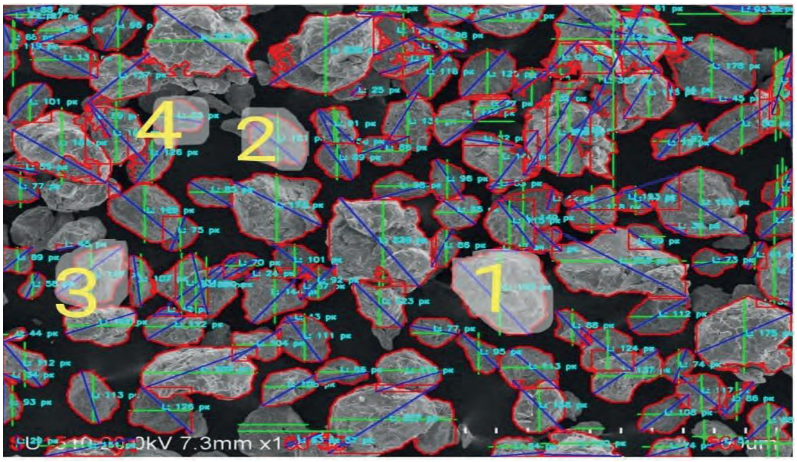

Table 1

Values Obtained from YOLOv8n Measurement

#Particle	YOLOv8n Bounding box (px)	YOLOv8n Contour (px)
1	193	184
2	121	119
3	147	142
4	83	82

In addition to this approach, an average value measurement aiming at a more practical application was also performed using the YOLOv8n model. The model automatically detected all metal particles present in the images, and the average size value of these particles was calculated. Figure 6 illustrates the metal particles detected by the YOLOv8n model, while Figure 7 presents the corresponding particle size measurement results.

Figure 6

Object Detection Using YOLO on a 200 µm SEM Image

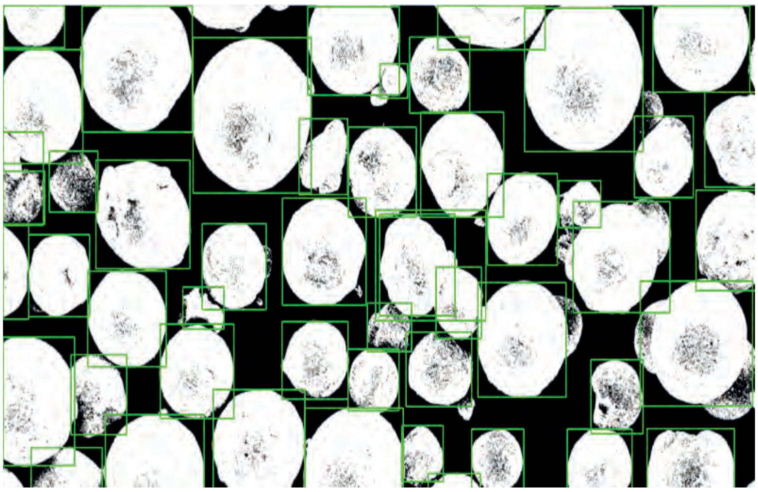

Figure 7

Size Measurements Using YOLO on a 200 µm SEM Image

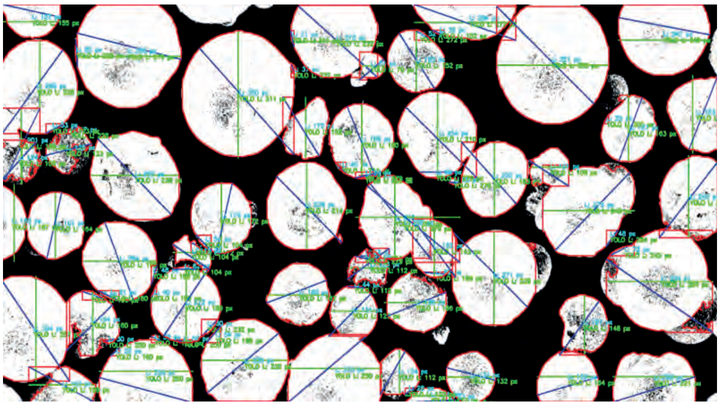

In this study, the overall condition of all particles was evaluated by calculating the average value. The mean values obtained with YOLOv8n were converted from pixels to micrometers, resulting in an average bounding box length of approximately 99.49 µm and an average length of approximately 73.31 µm as determined by the contour analysis.

Results Obtained Using Image J

The visualization of the metal particles manually measured using the ImageJ application is presented in Figure 8. The measurement values for these four particles, expressed in micrometers are provided in Table 2.

Figure 8

Four Randomly Selected Particle Measured Using Image J

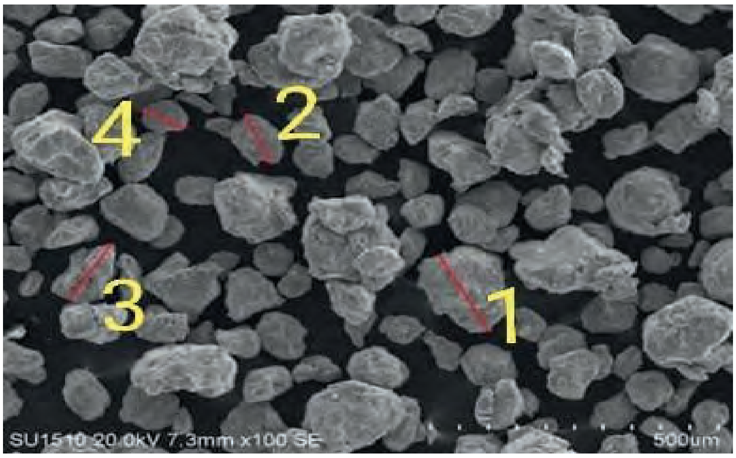

Table 2

Values Obtained from Image J Measurements

#Particle	Image J
1	179.895
2	116.743
3	121.548
4	80.321

Similarly, for the average value, each particle in the SEM image presented in Figure 6 was measured using ImageJ. The corresponding visualization of these measurements is shown in Figure 9, and the measurement results are provided in Table 3

Figure 9

Measurement Using Image J on a 200 µm SEM Image

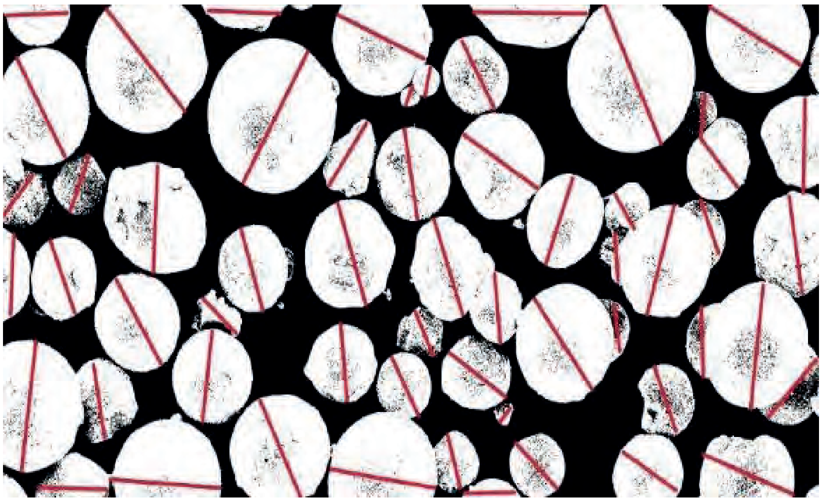

Table 3

Values and Average Measurements of the 200 µm SEM Image Obtained Using Image J

#Particle	Measurement	Particle	Measurement
1	88.566	27	94.149
2	141.605	28	84.309
3	85.604	29	95.082
4	160.312	30	130.108
5	112.446	31	80.449
6	110.014	32	83.546
7	101.980	33	102.765
8	123.010	34	82.219
9	111.140	35	114.140
10	95.771	36	98.082
11	139.714	37	67.201
12	111.086	38	115.484
13	119.321	39	82.801
14	130.000	40	62.290
15	141.450	41	53.254
16	161.059	42	140.355
17	78.409	43	119.549
18	92.087	44	99.298
19	126.616	45	97.693
20	87.201	46	86.000
21	89.889	47	160.342
22	140.014	48	79.322
23	120.920	49	91.082
24	127.028	50	68.411
25	167.211	51	51.264
26	132.197	**MEAN**	**104.87**

Comparison of YOLOv8n and Image J

To enable an accurate comparison between the measurements obtained from ImageJ and YOLOv8n, both the bounding box- and contour-based measurement values obtained by the YOLOv8n model were converted to the micrometer scale used in the SEM images. For this purpose, the pixel-to-micrometer conversion was performed using the scale information located at the bottom of the SEM images with the help of ImageJ software. The mathematical expression for this conversion is provided in Equation (1).

$$\text{In the SEM image, the scale length} = L_{\mu m}$$

$$\text{Pixel value of the image} = L_{px}$$

$$px = \frac{L_{\mu m}}{L_{px}} = \mu m/px \quad (1)$$

Using this equation, the pixel values were converted to micrometers. A comparison of the obtained results is presented in Table 4.

Table 4

Values Obtained from Image J and YOLOv8n Measurements

#Particle	Image J	YOLOv8n Bounding box (px)	YOLOv8n Bounding box (µm)	YOLOv8n Contour (px)	YOLOv8n Contour (µm)
1	179.895	193	193.775	184	184.736
2	116.743	121	121.486	119	119.476
3	121.548	147	147.590	142	142.568
4	80.321	83	83.333	82	82.328

In this measurement, a comparison was conducted on randomly selected metal particles in the 500 µm SEM image presented in Figure 4. For the evaluation of average values, data obtained from the 200 µm SEM image were used, and the comparisons were performed based on these average measurements. According to the measurements carried out using the ImageJ software, the average value was determined to be 104.87 µm, as presented in Table 5. In the measurements obtained using the YOLOv8n model, the average length based on bounding boxes was approximately 99.49 µm, while the average length derived from contour analysis was approximately 73.31 µm.

Based on these results, the contour-based predictions obtained using the YOLOv8n model demonstrated an accuracy of 69.91% compared to the manual measurements performed with ImageJ, whereas the bounding-box-based predictions achieved an accuracy of 94.87%.

Conclusion

The results indicate that the YOLOv8n model provides a notably high accuracy, particularly in bounding box-based measurements, offering a more practical and faster approach compared to manual ImageJ measurements. This study demonstrated high efficiency in terms of both time and resource utilization. Moreover, thanks to the model's automatic detection capability, high-accuracy results can be achieved in a single operation, unlike Image J, which requires individual manual measurements.

These findings suggest that the YOLOv8n model can be considered an effective alternative for metal particle detection and size measurement. The results further indicate that the measurement accuracy could be enhanced if the model is trained on larger and more diverse datasets. Therefore, this study provides a promising foundation for the development of automated, image analysis-based metal particle measurement systems in future research.

Reference

Badgujar, C. M., Poulose, A., & Gan, H. (n.d.). *Agricultural Object Detection with You Look Only Once (YOLO) Algorithm: A Bibliometric and Systematic Literature Review*.

Bochkovskiy, A., Wang, C.-Y., & Liao, H.-Y. M. (2020). *YOLOv4: Optimal Speed and Accuracy of Object Detection* (No. arXiv:2004.10934). arXiv. https://doi.org/10.48550/arXiv.2004.10934

Cervera Gontard, L., Ozkaya, D., & Dunin-Borkowski, R. E. (2011). A simple algorithm for measuring particle size distributions on an uneven background from TEM images. *Ultramicroscopy*, *111*(2), 101–106. https://doi.org/10.1016/j.ultramic.2010.10.011

Collins, T. J. (2007). ImageJ for Microscopy. *BioTechniques*, *43*(sup1), 5. https://doi.org/10.2144/000112517

Cong, X., Li, S., Chen, F., Liu, C., & Meng, Y. (2023). A Review of YOLO Object Detection Algorithms based on Deep Learning. *Frontiers in Computing and Intelligent Systems*, *4*(2), 17–20. https://doi.org/10.54097/fcis.v4i2.9730

Dulkadir, S., & Gültekin, G. K. (2023). *Tarımsal Otomasyon Sistemleri için Muz Olgunluk Seviyelerinin Derin Öğrenme Yöntemleri İle Sınıflandırılması*.

Flipon, B., Grand, V., Murgas, B., Gaillac, A., Nicolaÿ, A., Bozzolo, N., & Bernacki, M. (2021). Grain size characterization in metallic alloys using different microscopy and post-processing techniques. *Materials Characterization*, *174*, 110977. https://doi.org/10.1016/j.matchar.2021.110977

Gibbons, D. W., Govender, P., & Van Der Merwe, A. F. (2024). Metal powder feedstock evaluation and management for powder bed fusion: A review of literature, standards, and practical guidelines. *Progress in Additive Manufacturing*, *9*(4), 805–833. https://doi.org/10.1007/s40964-023-00484-x

Islam, S. F., Hawkins, S. M., Meyer, J. L. L., & Sharman, A. R. C. (2022). Evaluation of different particle size distribution and morphology characterization techniques. *Additive Manufacturing Letters*, *3*, 100077. https://doi.org/10.1016/j.addlet.2022.100077

Jain, Anıl K. (1989). *Fundamentals of Digital Image Processing*.

Jocher, G. (2020). *ultralytics/yolov5: YOLOv5 in PyTorch* [Computer software]. https://github.com/ultralytics/yolov5

Ju, R.-Y., & Cai, W. (2023a). Fracture detection in pediatric wrist trauma X-ray images using YOLOv8 algorithm. *Scientific Reports*, *13*(1), 20077. https://doi.org/10.1038/s41598-023-47460-7

Ju, R.-Y., & Cai, W. (2023b). Fracture detection in pediatric wrist trauma X-ray images using YOLOv8 algorithm. *Scientific Reports*, *13*(1), 20077. https://doi.org/10.1038/s41598-023-47460-7

Kim, H., Han, J., & Han, T. Y.-J. (2020). Machine vision-driven automatic recognition of particle size and morphology in SEM images. *Nanoscale*, *12*(37), 19461–19469. https://doi.org/10.1039/D0NR04140H

Koçer, S., Mohamed, O., & Dündar, Ö. (2024, July). Disease detection in abdominal ct images using the yolov5 algorithm: A deep learning approach. In 2024 59th International Scientific Conference on Information, Communication and Energy Systems and Technologies (ICEST) (pp. 1-4). IEEE.

Li, C., Li, L., Jiang, H., Weng, K., Geng, Y., Li, L., Ke, Z., Li, Q., Cheng, M., Nie, W., Li, Y., Zhang, B., Liang, Y., Zhou, L., Xu, X., Chu, X., Wei, X., & Wei, X. (2022). *YOLOv6: A Single-Stage Object Detection Framework for Industrial Applications* (No. arXiv:2209.02976). arXiv. https://doi.org/10.48550/arXiv.2209.02976

Li, X., Cui, L., Shonkwiler, S., & McMains, S. (2023). Automatic characterization of spherical metal powders by microscope image analysis: A parallel computing approach. *Journal of Iron and Steel Research International*, *30*(11), 2293–2300. https://doi.org/10.1007/s42243-022-00907-z

Mirzaei, M., & Rafsanjani, H. K. (2017). An automatic algorithm for determination of the nanoparticles from TEM images using circular hough transform. *Micron*, *96*, 86–95. https://doi.org/10.1016/j.micron.2017.02.008

Oktay, A. B., & Gurses, A. (2019). Automatic detection, localization and segmentation of nano-particles with deep learning in microscopy images. *Micron*, *120*, 113–

119. https://doi.org/10.1016/j.micron.2019.02.009

Popov, V. V., Grilli, M. L., Koptyug, A., Jaworska, L., Katz-Demyanetz, A., Klobčar, D., Balos, S., Postolnyi, B. O., & Goel, S. (2021). Powder Bed Fusion Additive Manufacturing Using Critical Raw Materials: A Review. *Materials*, *14*(4), 909. https://doi.org/10.3390/ma14040909

Redmon, J., Divvala, S., Girshick, R., & Farhadi, A. (2016). You Only Look Once: Unified, Real-Time Object Detection. *2016 IEEE Conference on Computer Vision and Pattern Recognition (CVPR)*, 779–788. https://doi.org/10.1109/CVPR.2016.91

Redmon, J., & Farhadi, A. (2017). YOLO9000: Better, Faster, Stronger. *2017 IEEE Conference on Computer Vision and Pattern Recognition (CVPR)*, 6517–6525. https://doi.org/10.1109/CVPR.2017.690

Redmon, J., & Farhadi, A. (2018). *YOLOv3: An Incremental Improvement* (No. arXiv:1804.02767). arXiv. https://doi.org/10.48550/arXiv.1804.02767

Saaim, K. M., Afridi, S. K., Nisar, M., & Islam, S. (2022). In search of best automated model: Explaining nanoparticle TEM image segmentation. *Ultramicroscopy*, *233*, 113437. https://doi.org/10.1016/j.ultramic.2021.113437

Schneider, C. A., Rasband, W. S., & Eliceiri, K. W. (2012). NIH Image to ImageJ: 25 years of image analysis. *Nature Methods*, *9*(7), 671–675. https://doi.org/10.1038/nmeth.2089

Tang, H., He, L., Feng, Q., Huang, B., Huang, S., & Li, D. (2025). Fine-grained mineral recognition and segmentation in metal mineral optical images based on improved YOLOv8n model. *Minerals Engineering*, *227*, 109290. https://doi.org/10.1016/j.mineng.2025.109290

Tongur, V., Batibay, A. B., & Karakoyun, M. (2023). A Review on Measurement of Particle Sizes by Image Processing Techniques. *Journal of Soft Computing and Artificial Intelligence*, *4*(1), 15–28. https://doi.org/10.55195/jscai.1218662

Ultralytics. (2024). *YOLOv11*. https://docs.ultralytics.com/models/yolov11

Ultralytics, U. (2023). *YOLOv8 Documentation*. https://docs.ultralytics.com/models/yolov8

Wang, A., Chen, H., Liu, L., Chen, K., Lin, Z., Han, J., & Ding, G. (2024). *YOLOv10: Real-Time End-to-End Object Detection*.

Wang, C.-Y., Bochkovskiy, A., & Liao, H.-Y. M. (2023). YOLOv7: Trainable Bag-of-Freebies Sets New State-of-the-Art for Real-Time Object Detectors. *2023 IEEE/CVF Conference on Computer Vision and Pattern Recognition (CVPR)*, 7464–7475. https://doi.org/10.1109/CVPR52729.2023.00721

Wang, C.-Y., Yeh, I.-H., & Liao, H.-Y. M. (2024). *YOLOv9: Learning What You Want to Learn Using Programmable Gradient Information* (No. arXiv:2402.13616). arXiv. https://doi.org/10.48550/arXiv.2402.13616

Wang, Z., Hua, Z., Wen, Y., Zhang, S., Xu, X., & Song, H. (2024). E-YOLO: Recognition of estrus cow based on improved YOLOv8n model. *Expert Systems with Applications*, *238*, 122212. https://doi.org/10.1016/j.eswa.2023.122212

Woehrle, G. H., Hutchison, J. E., Özkar, S., & Finke, R. G. (2006). *Analysis of Nanoparticle Transmission Electron Microscopy Data Using a Public- Domain Image-Processing Program, Image*.

Yamanoğlu, D. R., & Muratal, Y. M. O. (2023). *TOZ METALURJİSİNDE TOZ KARAKTERİZASYONU VE YOĞUNLUK İLİŞKİSİ*.

Zegzulka, J., Gelnar, D., Jezerska, L., Prokes, R., & Rozbroj, J. (2020). Characterization and flowability methods for metal powders. *Scientific Reports*, *10*(1), 21004. https://doi.org/10.1038/s41598-020-77974-3

About the Authors

Saliha Banu ERTÜRK is a graduate student at the Department of Computer Engineering, Necmettin Erbakan University, Konya, Turkey. Her main research interests include artificial intelligence, computer vision, and AI-based analysis.
E-mail: salihabanuerturk@gmail.com, **ORCID:** 0009-0002-2659-599X

Assoc. Prof. Dr. Murat KARAKOYUN received the Ph.D. degree from the Department of Computer Engineering of Konya Technical University. He is working as a Assoc. Prof. at Computer Engineering Department of Necmettin Erbakan University. His working topics are artificial intelligence, image processing, data mining, machine learning, optimization etc.
E-mail: mkarakayon@erbakan.edu.tr, **ORCID:** 0000-0002-0677-9313

Similarity Index:

The similarity index obtained from the plagiarism software for this book chapter is 12%

Application and Analysis of Data Compression and Digital Modulation Techniques in Image Transmission over Wireless Communication

Batuhan KOYUNCU
Necmettin Erbakan University

Özgür DÜNDAR
Necmettin Erbakan University

To Cite This Chapter:
Koyuncu, B., & Dundar, O. (2025). Application and analysis of data compression and digital modulation techniques in image transmission over wireless communication. In S. Kocer & O. Dundar (Eds.), *Next generation engineering: Smart solutions and applications* (pp. 203–215). ISRES Publishing.

Introduction

The efficient and reliable transmission of digital images in a wireless environment has become one of the fundamental requirements of modern communication systems. Especially in applications where resources such as bandwidth and energy are limited, the effective use of data compression and modulation techniques is of great importance. While the direct transmission of image data results in high bandwidth requirements and transmission costs, appropriate compression algorithms can significantly reduce this burden (Kaur & Aggarwal, 2017; Sharma & Parashar, 2015; Smitha & Laxmi, 2019).

Huffman coding, one of the data compression methods, provides lossless compression on data as a statistical method (Sayood, 2017). This technique generates shorter codes based on the frequencies of symbols in the data, thereby reducing the total number of bits. On the other hand, digital modulation techniques play a decisive role in terms of efficiency and robustness during the transmission of data in a wireless environment (Proakis & Salehi, 2007). Binary Phase Shift Keying (BPSK) is widely used in applications with low data rates due to its simple structure and noise-resistant nature (Rani & Pal, 2021; Saini & Kumar, 2018).

Various studies exist in the literature regarding the wireless transmission of image data. For example, Al-Ashwal et al. (2023) analyzed the transmission performance of compressed images over Discrete Sine Transform (DST) based OFDMA systems (Prasad, 2011). In that study, minimum SNR values were determined using different compression methods and modulation techniques, leading to the conclusion that the DST-OFDMA system demonstrated superior performance compared to DFT-OFDMA. Similarly, Reeta Charde (2012) examined the effects of image transmission using PSK modulation in an AWGN channel and showed improvements in metrics such as BER, PSNR, and RMSE in the transmission of compressed images. Furthermore, Gomes and Mishra (2010) performed image transmission using Huffman coding and BPSK modulation over a UWB channel. In that study, transmission reliability was increased with double error correction codes, and high-accuracy image transmission was achieved even at low SNR values (Chen et al., 2016; Kwon & Lee, 2014; Patel & Sharma, 2013; Ranjitha & Ravi, 2014).

In this study, the process of compressing gray-level image data with Huffman coding and transmitting it in a wireless environment by passing it through an AWGN channel with the BPSK modulation technique has been simulated. The aim is to reduce data size through compression and subsequently transmit this data effectively in a wireless environment via digital modulation. Simulations were carried out under different SNR (Signal-to-Noise Ratio) values, and the bit error rate (BER) of the system was analyzed. The obtained results are important for evaluating both compression performance and transmission reliability in a wireless environment.

Data Compression and Digital Modulation Techniques

In this study, the combined use of data compression and digital modulation techniques was simulated to enable the efficient transmission of image data in a wireless environment. The method used consists of four main steps:

- Preparation of image data and compression with Huffman coding,
- Application of BPSK as the digital modulation technique,
- Transmission over the AWGN channel model,
- Demodulation and recovery of the image.

All steps were simulated using MATLAB software, and performance measurements were carried out. The block diagram of the process sequence is given in Figure 1.

Figure 1

Block Diagram of the Process Sequence

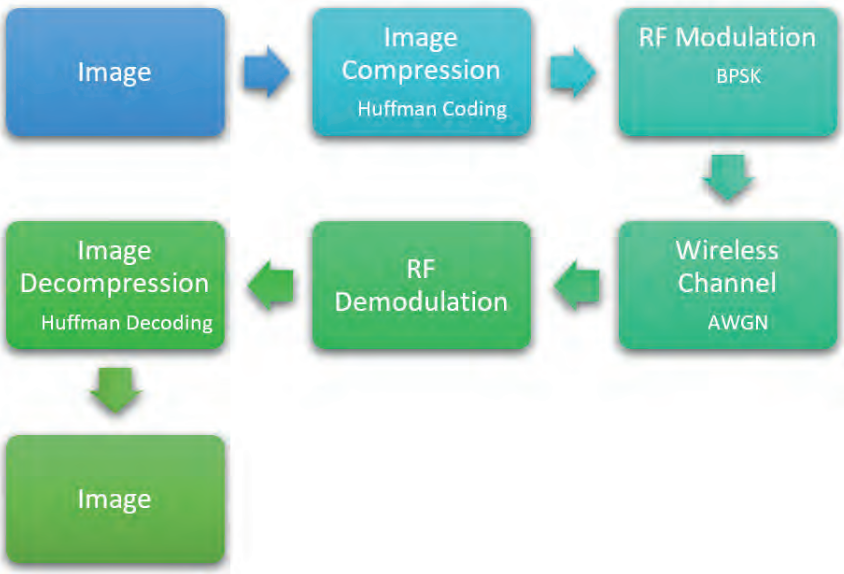

Compression of Image Data (Huffman Coding)

High-volume data transmission in wireless communication systems causes serious limitations in terms of bandwidth and energy consumption. Therefore, it is quite important to compress large-sized data, such as images, before transmission (Zhang & Li, 2020). In this study, the Huffman coding method, which is one of the lossless data compression techniques, was preferred. Huffman coding is an optimal method that provides the shortest average code length based on the frequencies of symbols (Sayood, 2017). By adjusting code lengths according to the statistical properties of the data, it assigns short codes to frequently used symbols and long codes to rarely used ones. This structure ensures high compression success in irregular pixel intensity distributions frequently encountered in image data.

The most important reason for choosing the Huffman algorithm is that it offers a lossless structure and can significantly reduce data volume without quality loss, especially in visual data. The high number of bits that emerge during the direct wireless transmission of images is converted into shorter bit sequences thanks to the Huffman algorithm, reducing the transmission load on the system. This ensures both more efficient use of channel capacity and shortening of the transmission time.

The image used in the study (Figure 2) is in a gray-level format, and pixel intensities vary between 0 and 255 (Gonzalez & Woods, 2018). The image data was first converted into a column vector, and then the frequency of each pixel value was calculated. Using this frequency information, the probability distribution of the symbols was obtained, and the Huffman dictionary was created according to this distribution. Zero-probability symbols were excluded from this dictionary.

Figure 2

Original Image

These operations were performed in the MATLAB environment with the following codes:

```
img = imread('siyah.tiff');      % Load gray level image
img = imresize(img, 0.25);      % Reduce size (to reduce processing time)
img_vector = img(:);          % Vectorize the image
[counts, ~] = imhist(img);      % Calculate frequency of pixel intensities
prob = counts / sum(counts);    % Probability distribution
symbols = 0:255;
nonzero_idx = prob > 0;
dict = huffmandict(symbols(nonzero_idx), prob(nonzero_idx)); % Create Huffman dictionary
```

The dictionary above contains Huffman codes corresponding to pixel probabilities. With the help of this dictionary, the pixel vector in the image was converted into a bit sequence using the huffmanenco function. As a result of this process, a representation with content identical to the original form but smaller in size was obtained:

```
huffmanCode = huffmanenco(img_vector, dict);  % Huffman coding
```

The size of the data obtained as a result of coding is shorter than the original data, which determines the compression ratio. The compression ratio was calculated in the MATLAB environment as follows:

```
original_bits = numel(img_vector) * 8;
compressed_bits = length(huffmanCode);
compression_ratio = original_bits / compressed_bits;
fprintf('Compression ratio: %.2f\n', compression_ratio);
```

As a result of this process, approximately 12% data compression was achieved on average. This compressed bit sequence obtained was prepared for wireless transmission by being subjected to digital modulation in the second stage of the study.

Digital Modulation Application (BPSK)

The bit sequence obtained as a result of the data compression process must be subjected to a modulation process before being made suitable for wireless transmission. In this study, the Binary Phase Shift Keying (BPSK) method was preferred among digital modulation techniques (Proakis & Salehi, 2007; Saini & Kumar, 2018). BPSK is the most basic phase-shift modulation type, representing each bit corresponding to a different phase value. Since there are only two-phase states, only one bit can be carried in each carrier wave cycle. While this situation increases the simplicity of modulation, it makes signal decoding more stable in noisy environments.

BPSK modulation is generally used in wireless systems where low data rates are acceptable but reliability is prioritized. In this context, the bit sequence obtained from Huffman coding was modulated with BPSK and prepared for wireless transmission. One of the reasons for preferring BPSK is that it is quite resistant to noise. Additionally, it can be easily applied in the MATLAB environment and allows for high-level analysis with channel models such as AWGN.

The modulation process was performed in the MATLAB environment with the pskmod function. This function maps the given binary bit sequence to two different points, -1 and +1, on the phase plane. As a result of this process, the signal transforms into a digital carrier form and becomes ready for transmission in the channel environment.

The modulation process is shown with the following code:

```
txBits = double(huffmanCode); % Huffman coded bit sequence (logical data -> numeric)

bpskSymbols = pskmod(txBits, 2); % BPSK modulation (M = 2)
```

In this code, the huffmanCode array was first converted to the double data type to make it suitable for modulation, and then subjected to 2-phase modulation with the help of the pskmod function. Consequently, every ‘0’ bit is represented as +1, and every ‘1’ bit as -1. This conversion ensures the signal acquires a structure similar to an analog carrier. The modulated signals become ready to be sent to the AWGN channel in this state. BPSK was evaluated as the most suitable choice within the scope of this study because it offers high performance with low complexity.

Channel Model: Additive White Gaussian Noise (AWGN)

Digital data converted into carrier wave form by the modulation process may undergo various degradations in wireless environments. Foremost among these degradations is the random noise encountered in the transmission channel. In this study, Additive White Gaussian Noise (AWGN), the most common and fundamental channel model, was used to represent channel effects (Zhang & Li, 2018). AWGN refers to the addition of random noise with a zero mean and constant variance Gaussian distribution to the signal. The channel being termed “white” indicates that all frequency components are affected with equal power; the “additive” property indicates that the noise is directly added to the signal.

The AWGN channel model is used to simulate an idealized channel environment where physical channel degradations such as multipath fading and shadowing do not exist in practice (Narayan & Sinha, 2015). This model is particularly suitable for theoretical analysis and performance comparisons. The aim of this study is to observe the effect of noise and analyze the error tolerance of the system when compressed image data is transmitted via digital modulation.

The AWGN channel was modeled in the MATLAB environment with the awgn function. This function simulates the channel effect by adding noise at a specific SNR (Signal-to-Noise Ratio) level. SNR expresses the ratio of signal power to noise power in decibels (dB) and has a direct effect on the reliability of communication systems. In the simulation, the SNR value was increased at various levels from 0 dB to 15 dB, and its effect on the system's bit error rate was examined.

The MATLAB code is as follows:

```
snrVals = [0 3 6 9 12 15];             % SNR levels in dB
rxSymbols = awgn(bpskSymbols, snr, 'measured'); % Noisy signal generation
```

Here, while bpskSymbols represents the modulated signals, the SNR value is determined dynamically. The 'measured' argument of the awgn function automatically measures the signal power and adds noise at the appropriate level. This allows the effect of the channel on the signal to be observed systematically at every SNR level. This step is critical for testing how accurately image data can be transmitted in a wireless environment. When the SNR level is low, more bit errors are expected to occur; this situation can disrupt data integrity during the demodulation and subsequent Huffman decoding stages.

Demodulation and Huffman Decoding

To safely and accurately receive digital data passed through a wireless environment, the signal must be decoded at the end of the transmission process. This stage consists of two main steps:

- BPSK demodulation
- Huffman decoding (decompression).

Both steps aim to recover the original image data losslessly.

BPSK Demodulation

Modulated signals are exposed to a certain level of noise while passing through the AWGN channel. This noise can disrupt carrier phase information, leading to incorrect decoding of bits. Therefore, the demodulation process is performed first after transmission. This process serves to recover the binary bit sequence by re-reading the carrier phase. For BPSK, the demodulation process is performed in MATLAB with the pskdemod function. This function converts the modulated symbols back into the original bit sequence:

```
rxBits = pskdemod(rxSymbols, 2);  % 2-level BPSK demodulation
```

The rxBits sequence obtained after demodulation should theoretically be the same as the transmitted txBits. However, incorrect bits may occur under low SNR conditions. These errors are later taken into account in the system's BER (Bit Error Rate) analysis.

Huffman Decoding (Decompression)

The bit sequence obtained after demodulation is decoded with the help of the previously created Huffman dictionary. This process involves converting encoded bits into symbols corresponding to original pixel values. The Huffman decoding process is performed in MATLAB with the huffmandeco function:

```
recovered_vector = huffmandeco(rxBits, dict);  % Huffman decoding
```

In this process, the Huffman decoder may not fully perform its function due to bit errors occurring during demodulation. Such situations can be controlled with a try-catch structure, producing a default output in cases of failed decoding.

```
try
   recovered_vector = huffmandeco(rxBits, dict);
catch
   recovered_vector = zeros(size(img_vector));
end
```

The obtained vector is reshaped according to the image size used before compression:

```
reconstructedImg = reshape(uint8(recovered_vector), size(img));
```

At this stage, if the structural integrity of the image is preserved, the reconstructed image will be quite close to the original image. However, bit errors that occur when the SNR level is low disrupt symbol matches in Huffman decoding, causing visible distortions in the image. Therefore, system performance was evaluated through both visual inspection and numerical analysis (e.g., with metrics like BER).

Findings and Evaluation

Within the scope of the performed simulation study, the gray-level image shown in Figure 2 was losslessly compressed using the Huffman coding method, then converted to a digital carrier via BPSK modulation, and passed through an AWGN channel. Simulations were repeated at different SNR levels to analyze the system's error resilience and transmission quality (Wang et al., 2004).

Figure 3

Compression Ratio MATLAB Results

```
--- RESULTS ---
Image Size                : 533 x 800 pixel
Total pixel               : 426400
Original Data Size        : 3411200 bit
Compressed Size           : 3054080 bit
Compression Ratio         : 1.12
```

First, the size of the image data was significantly reduced during the compression stage. While the original data size was a total of 3,411,200 bits, a compressed data size of approximately 357,120 bits was obtained as a result of Huffman coding. This corresponds to a data reduction of approximately 12%. This success offers a significant advantage, especially for bandwidth-constrained wireless systems.

The reliability of the system after transmission was evaluated using the bit error rate (BER). The SNR - BER graph obtained with MATLAB is shown in Figure 4.

Figure 4

SNR – BER Graph

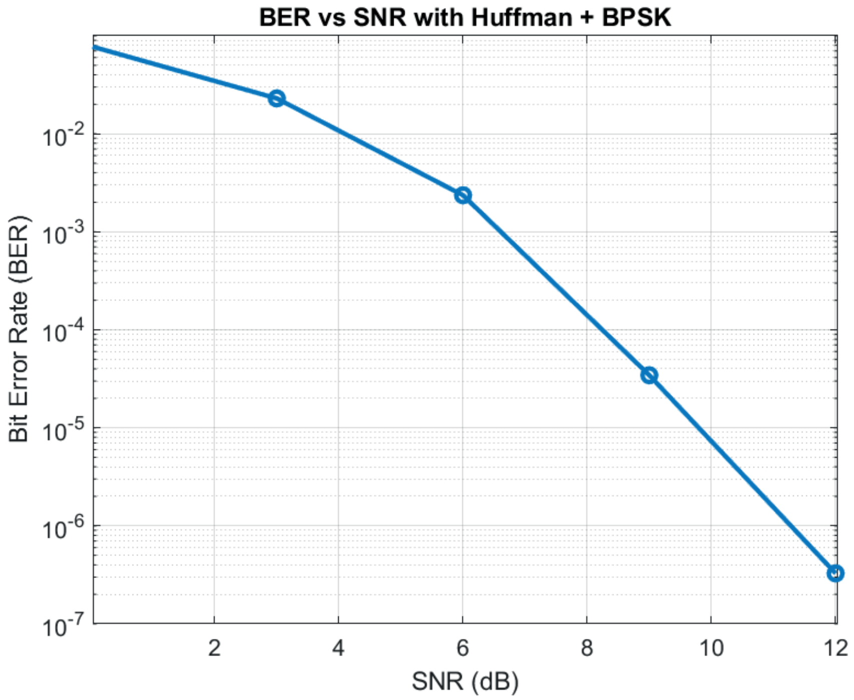

Table 1

System Performance Values for Different SNR Values

SNR (dB)	Bit Errors	BER
0	240311	$7.868x10^{-2}$
3	70131	$2.296x10^{-2}$
6	7294	$2.388x10^{-3}$
9	97	$3.176x10^{-5}$
12	0	<0.001
15	0	<0.001

The results revealed that, as expected, the error rate decreased as the SNR level increased, and the system showed high resistance to noise. Especially at SNR levels of 9 dB and above, no visible distortion occurred in the image after transmission; the Huffman decoding process was able to successfully reproduce the original image. Image visuals obtained for different SNR values are given in Figure 5.

Figure 5

Obtained Images for Different SNR Values

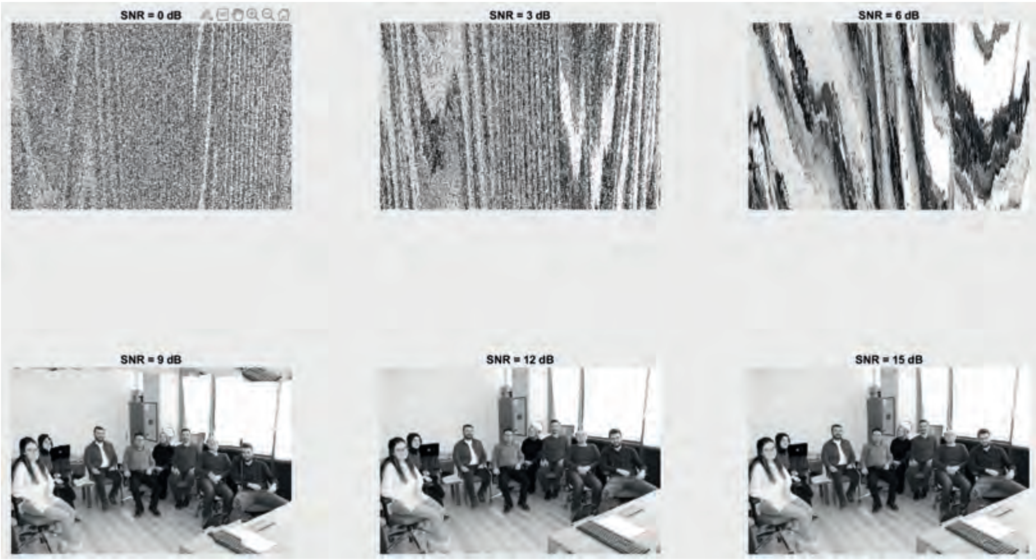

Additionally, the output images received at each SNR level were visually examined using the imshow function in MATLAB, and the visual fidelity of the system was verified. Distortions were observed particularly in edge regions at low SNR levels, but these effects largely disappeared at medium and high SNR levels. These findings indicate that the Huffman + BPSK-based system offers a successful alternative in practical wireless applications in terms of both compression efficiency and transmission reliability. It can be evaluated as a suitable method, especially for IoT systems, sensor networks, and low-power communication protocols that are restricted in terms of energy and bandwidth.

Conclusion

In this study, a system design was realized in which Huffman coding and BPSK modulation techniques were used together for the efficient and reliable transmission of digital image data in a wireless environment. Through simulations performed in the MATLAB environment, both the compression success and transmission reliability of the system were analyzed in detail under different SNR conditions.

The obtained results demonstrated that Huffman coding is an effective method for lossless compression and that BPSK modulation provides reliable transmission even at low noise levels. When the SNR value was 9 dB and above, the system was able to reconstruct the image almost without error, and this situation was verified both numerically and visually. With its simplicity, energy efficiency, and compression capability, the system offers a suitable solution, especially for applications with bandwidth and hardware limitations.

In future studies, it is planned to work on the combination of Huffman coding with different modulation types (QPSK, 16-QAM, etc.), its integration with error correction codes (e.g., Reed-Solomon or LDPC), and its integration into real-time wireless applications. Such approaches will contribute to expanding the general robustness and application areas of the system.

Appendix – MATLAB Codes

```
clear; clc;
%% 1. Load and Compress Image
img = imread('siyah.tiff');        % If color image, convert to gray first
img = imresize(img, 0.25);         % Resize (e.g. 256x256 -> 128x128)
img_vector = img(:);
% Histogram and Probability Distribution
[counts, ~] = imhist(img);
prob = counts / sum(counts);
symbols = 0:255;
nonzero_idx = prob > 0;
% Create Huffman Dictionary
dict = huffmandict(symbols(nonzero_idx), prob(nonzero_idx));
huffmanCode = huffmanenco(img_vector, dict);
txBits = double(huffmanCode);      % Prepare for transmission in numeric format
%% 2. BPSK Modulation
bpskSymbols = pskmod(txBits, 2);
%% 3. SNR Range and Channel
snrVals = [0 3 6 9 12 15];         % in dB
berVals = zeros(size(snrVals));
figure;
for i = 1:length(snrVals)
    snr = snrVals(i);
    % Pass through AWGN Channel
    rxSymbols = awgn(bpskSymbols, snr, 'measured');
    % BPSK Demodulation
    rxBits = pskdemod(rxSymbols, 2);
    % Count Bit Errors
    if length(rxBits) ~= length(txBits)
        rxBits = rxBits(1:min(end, length(txBits)));
    end
    bitErrors = sum(rxBits ~= txBits(1:length(rxBits)));
    berVals(i) = bitErrors / length(txBits);
    % Decode Huffman Code
```

```
        try
            recovered_vector = huffmandeco(rxBits, dict);
        catch
            recovered_vector = zeros(size(img_vector));  % Default for corrupted data
        end
        % Reconstruct Image
        if length(recovered_vector) ~= numel(img)
            recovered_vector(end+1:numel(img)) = 0;
        end
        reconstructedImg = reshape(uint8(recovered_vector), size(img));
        % Show Visually
        subplot(2, 3, i);
        imshow(reconstructedImg);
        title(sprintf('SNR = %d dB', snr));
    end
    %% 4. BER Graph
    figure;
    semilogy(snrVals, berVals, 'o-', 'LineWidth', 2);
    xlabel('SNR (dB)');
    ylabel('Bit Error Rate (BER)');
    title('BPSK + Huffman: BER vs SNR');
    grid on;
    %% 5. Compression Info
    original_bits = numel(img_vector) * 8;
    compressed_bits = length(huffmanCode);
    compression_ratio = original_bits / compressed_bits;
    fprintf('Original Size: %d bit\n', original_bits);
    fprintf('Compressed Size: %d bit\n', compressed_bits);
    fprintf('Compression Ratio: %.2f\n', compression_ratio);
```

References

Al-Ashwal, N. H. M., Mohd Ali, M. A., & Ramly, N. H. (2023). Performance of Image Transmission Using Discrete Sine Transform over OFDMA Systems. *EURASIP Journal on Wireless Communications and Networking*, 2023(1), 1-19. https://doi.org/10.1186/s13638-023-02286-9

Charde, R. (2012). Image Transmission through AWGN Channel using PSK Modulation. *International Journal of Emerging Technology and Advanced Engineering*, 2(1), 64–68.

Chen, W., Wu, Y., & Jin, Y. (2016). Joint Source-Channel Coding for Wireless Image Transmission. *IEEE Transactions on Communications*, 64(6), 2467–2479.

Gomes, P., & Mishra, A. (2010). Implementation of Image Transmission through Wireless Medium using BPSK Modulation. *International Journal of Computer Applications*, 10(7), 1–5.

Gonzalez, R. C., & Woods, R. E. (2018). *Digital Image Processing* (4th ed.). Pearson.

Kaur, G., & Aggarwal, A. (2017). Comparison of Different Image Compression Techniques. *International Journal of Computer Applications*, 165(8), 21–25.

Kwon, H., & Lee, J. (2014). Error Resilient Wireless Image Transmission Using Redundancy Allocation. *IEEE Transactions on Multimedia*, 16(1), 20–30.

Narayan, P., & Sinha, P. (2015). Digital Image Transmission over Fading Channels. *Procedia Computer Science*, 48, 409–415.

Patel, S., & Sharma, A. (2013). Wireless Transmission of Image using Image Compression and Error Correction. *IJETTCS*, 2(6), 185–189.

Prasad, R. (2011). *OFDM for Wireless Communications Systems*. Artech House.

Proakis, J. G., & Salehi, M. (2007). *Digital Communications* (5th ed.). McGraw-Hill.

Rani, R., & Pal, M. (2021). BPSK Modulation Based Image Transmission over Noisy Channels. *International Journal of Electronics and Communication Engineering*, 13(2), 15–20.

Ranjitha, R., & Ravi, R. (2014). Wireless Image Transmission using Compression and Error Control. *International Journal of Advanced Research in Computer and Communication Engineering*, 3(4), 6277–6281.

Saini, R., & Kumar, M. (2018). Analysis of Image Transmission over Noisy Channel using Modulation Techniques. *International Journal of Scientific Research in Computer Science and Engineering*, 6(2), 35–39.

Sayood, K. (2017). *Introduction to Data Compression* (5th ed.). Morgan Kaufmann.

Sharma, M., & Parashar, R. (2015). Comparative Analysis of Image Compression Techniques. *International Journal of Engineering Research and Applications*, 5(5), 105–110.

Smitha, K., & Laxmi, P. (2019). Performance Analysis of Digital Image Transmission over Noisy Channels. *International Journal of Applied Engineering Research*, 14(9), 2250–2257.

Wang, Z., Bovik, A. C., Sheikh, H. R., & Simoncelli, E. P. (2004). Image Quality Assessment: From Error Visibility to Structural Similarity. *IEEE Transactions on Image Processing*, 13(4), 600–612.

Zhang, J., & Li, Q. (2020). Image Compression Using Entropy Coding and Adaptive Modulation. *IEEE Access*, 8, 123456–123465.

Zhang, W., & Li, H. (2018). AWGN Channel Simulation for Image Transmission. *International Journal of Signal Processing Systems*, 6(1), 10–14.

About The Authors

Batuhan Koyuncu, graduated from the Department of Electrical and Electronics Engineering at Sakarya University. He completed his master's degree at Necmettin Erbakan University. He currently works as a Satellite Ground Segment Design Engineer in the space and defence industry. He is also pursuing his Ph.D. degree at Necmettin Erbakan University, Department of Electrical and Electronics Engineering.

Email: batuhankoyuncu1@gmail.com, **ORCID:** 0000-0002-1504-9072

Özgür DÜNDAR, PhD, works at Necmettin Erbakan University, Department of Astronautical Engineering. He graduated from the Electrical and Electronics Engineering Department of Selcuk University. He worked as an Automation Engineer for a while. His master's and doctorate degrees are from Selçuk University, Institute of Science and Technology, Department of Electrical and Electronics Engineering. Special fields of study are Automation, Robotic, Communication, Electromagnetic and Micro Strip Patch Antenna designs.

Email: ozdundar@erbakan.edu.tr, **ORCID:** 0000-0002-4142-4446

Similarity Index:

The similarity index obtained from the plagiarism software for this book chapter is 4%.

Evaluating Film Reviews with Sentiment Analysis in NLP

Beyza DÜNDAR
Necmettin Erbakan University

Sabri KOÇER
Necmettin Erbakan University

To Cite This Chapter:
Dundar, B., & Kocer, S. (2025). Evaluating film reviews with sentiment analysis in NLP. In S. Kocer & O. Dundar (Eds.), *Next generation engineering: Smart solutions and applications* (pp. 216–227). ISRES Publishing.

Introduction

Problem Definition

From the past to the present, with the advancement of technology and the subsequent integration of computers into our daily lives, our work has begun to progress more rapidly. The acceleration of work means the potential to accomplish more tasks within the same amount of time, which is why we are witnessing the continuous development of storage units in computers to store the history of previously performed tasks. The best solution here was not simply to increase the storage capacity or processing power of computers. This is because the data collected was being stored for future use. This data can be of various types. For example, it can be invoice information, sales experiences, employee insurance information, or emotional data such as complaints and suggestions. Processing this type of data is as laborious as collecting it. Accounting software, archive managers, and many similar applications have been developed to analyze numerical data. Thus, human control gradually began to give way to computer-controlled automation systems. These automations worked so effectively that, in most cases, applications called Decision Support Systems were developed that made decisions on behalf of humans based on their analyses (Donovan, 1976). If we add the contribution of artificial intelligence software to this, we can now develop smart applications for almost any situation. Thanks to the rapid advancement of technology, the success of machine learning methods should no longer be overlooked.

The concept of the Internet has also entered our daily lives alongside technology and currently holds the largest amount of data in the world. Therefore, it is inevitable that studies related to data mining are conducted on the Internet. Thanks to the widespread use of the Internet, people communicate with each other cheaply, create online virtual stores, and even conduct international trade through them. The security of online shopping is still being questioned today, and research is being conducted on this subject. In one such study, Sultan and colleagues asked an online shopper, "Feedback from previous users is very helpful in minimizing risk in online shopping," and highlighted its importance in their thesis (Islam & Sultana, 2018). In other words, just as trusting a person is a process, the same process on the Internet depends on how good the feedback is. For this reason, owners of websites that share information or conduct commerce on the Internet have made it possible for real people to share their satisfaction or complaints through feedback. This is both a method for the website owner to address perceived shortcomings and a way for users to express their positive or negative feelings. This process is still carried out today by survey organizations that conduct research on companies' market profiles for commercial purposes. Previously, people's feelings and thoughts were sought through such methods, which took a very long time to evaluate. For this process, every door was knocked on individually, and the search for the right people for the survey continued relentlessly. Evaluating the written survey information obtained also required a significant amount of time and manpower. Therefore, the material costs of the work, stemming from human resources, constituted a heavy burden for the institutions and organizations conducting the surveys. With the widespread use of technology and the Internet, institutions and organizations began to develop online survey information management systems to reduce the costs of conducting surveys, making it easier to reach people.

Emotions vary from person to person and from topic to topic. This variability can be classified as positive, negative, or containing no emotion at all. For example, after purchasing a product from an online store, Internet users may want to evaluate that product, criticizing its shortcomings as well as mentioning its good points. This allows customers who later wish to purchase the same product to make a more informed decision. Similarly, someone who wants to watch a movie can decide whether to watch it based on comments written by other viewers on sites like IMDB or similar rating platforms.

Due to the abundance of information, resources, and documents on the internet, it takes a lot of time for people to read and evaluate these thoughts one by one and separate their feelings from them. At this point, survey information management systems still require human intervention for the automatic evaluation of comments. In this regard, resorting to the high processing power capabilities of computers could eliminate the need for human labor. At this stage, machine learning methods, which are becoming increasingly important day by day, are achieving excellent results in classification. Sorting and classifying thousands of documents manually takes a lot of time. However, doing this with a machine learning method will not take much time at all. Success achieved solely through machine learning methods is insufficient. At this point, a number of methods are used to obtain more consistent results. This study contains work that will contribute to the success of the methods used to improve the results of machine learning methods.

Subject of the Study

This study generally encompasses a systematic approach based on sentiment analysis of texts, utilizing the fields of IR (Information Retrieval Systems) and ML (Machine Learning). Feature Selection Metrics in IR have been examined and evaluated in terms of identifying discriminative terms in Turkish texts and improving performance in LR. It also includes classification studies and applications performed on supervised learning, which is the most common and successful method used in ML.

Sentiment Analysis

The analysis of the positivity or negativity of texts written in natural languages around the world is called Sentiment Analysis (SA). For SA to be performed, the texts to be analyzed must adhere to specific grammatical rules. Otherwise, it may not be possible to identify the meaning and emotional emphasis within the text. SA can be performed manually or using computer-based algorithms and machine learning methods. For a sound analysis of the emotions contained in texts, it is first necessary to successfully identify emotion-laden words. To achieve this, predefined word lists are used, or these words are determined using methods such as Feature Selection. This allows the sentiment contained in the sentence to be analyzed correctly. During text-based sentiment analysis, numerous research and development activities are being carried out in the scientific world on computer-based sentiment analysis approaches, both in terms of costs arising from human resources and in terms of a wide range of applicability (Datta & Acharjee, 2018).

Performance Measurement Terms Used in the Study

Precision

This is a performance metric that indicates the degree to which measurements made as a result of experiments are close to each other. This value is calculated by dividing the number of correctly classified positive examples (TP) by the total number of positive examples (TP+FP) (Equation 1.1). This value is always in the range of 0-1.

Sensitivity Value Equation:

$$Sensitivity = \frac{TP}{TP+FP} \quad (1)$$

Recall

The recall value is known as the target achievement rate. In other words, it is a value that shows the percentage of the actual information that should be reached. This value is calculated by dividing the number of correctly classified positive examples (TP) by the total number of relevant documents (TP + FN) (Equation 1.2).

Recall Value Equation:

$$Recall = \frac{TP}{TP+FN} \quad (2)$$

Accuracy

The accuracy value indicates how close the analysis performed in the experiment is to the true value. In other words, it indicates the degree to which the new result would resemble the previous result if the experiment were repeated under the same conditions. This value is calculated by dividing the sum of correctly classified positive and negative values (TP + TN) by the total number of classified data (TP + FP + TN + FN) (Equation 1.3) (Ibrahım, 2022).

Accuracy Calculation Method:

$$Accuracy = \frac{TP+TN}{TP+FP+TN+FN} \qquad (3)$$

F1 Measure

This value is obtained by calculating the harmonic averages of the Sensitivity and Recall values explained in the previous sections (Equation 1.4). This value ranges between 0 and 1. It is a value that expresses the accuracy of the test performed. It is the most commonly used success criterion for studies conducted in the fields of data mining and machine learning.

F1 Measurement Method:

$$F1 = 2 * \frac{Sensitivity * Recall}{Sensitivity + Recall} \qquad (4)$$

Literature Review

Natural language processing has become one of the most popular topics in recent years. In this study, sentiment analysis was performed using movie reviews. There are existing studies on this topic in the literature. Haque et al. used the IMDB dataset in their study. The IMDB dataset consists of user reviews about movies. The researchers used ESA and Long Short-Term Memory (LSTM) networks to extract sentiment from this dataset. The proposed model achieved an F1 score of 91%. In this study, the researchers stated that ESA networks produced better results than LSTM networks (Haque et al., 2019).

Rao et al. used the IMDB and Yelp datasets to perform sentiment analysis in their study. The researchers proposed an LSTM-based model to generate analysis results from these datasets. They also compared their proposed model with different machine learning classifiers. The researchers achieved accuracy values of 46.3% and 65.3% in these datasets, respectively (Rao et al., 2018).

Islam et al. stated that they used two different data sets and six different machine learning classifiers in their study. The classifiers used in the study are classifiers accepted in the literature. No ESA or LSTM-based models were proposed in the classification process using data from the IMDB and Amazon datasets. Islam et al. achieved an accuracy rate of 83.66% with the Random Forest classifier in their study (Islam et al., 2018).

Narayanan et al. stated that they used the Naive Bayes algorithm in their study to perform sentiment analysis. In this study, which used the IMDB dataset, they stated that they investigated different aspects of the Naive Bayes algorithm and achieved a high accuracy value. The authors stated that the proposed method could be generalized to a series of text classification problems to improve speed and accuracy. The researchers achieved an accuracy value of 88.80% in the Naive Bayes classifier (Narayanan et al., 2013).

Huang et al. used LSTM and BiLSTM networks in this study. They also stated that LSTM networks are a successful method in the text classification process. The researchers stated that the BiLSTM-based model they proposed makes it possible to detect words with different meanings (Huang et al., 2018).

Pang et al. used the IMDB dataset in this study to perform sentiment analysis. The researchers chose different machine learning classifiers and the n-gram method as their approach. They achieved accuracy rates of 82.9% with Unigram SVM, 77.4% with Biagram ME, and 82.7% with Unigram + Bigram SVM (Pang et al., 2002).

Matsumoto et al. performed sentiment analysis using the IMDB and Polarity datasets in their study. The researchers chose to use the SVM and n-gram methods in this study. They achieved an accuracy rate of 83.7% with the unigram method, 80.4% with the bigram method, and 84.6% with the unigram+bigram method (Matsumoto et al.).

Tang et al. used three different artificial neural network models to perform sentiment analysis. These models achieved accuracy rates of 83.37%, 82.6%, and 77.33%, respectively. The researchers stated that they used the SemEval dataset in this study (Tang et al., 2015).

Liu et al. used three different datasets to perform sentiment analysis. They achieved an accuracy rate of 75.5% with their proposed model. In this study, the researchers stated that they proposed a multi-label classification-based method for sentiment analysis (Liu et al., 2015).

One of the pioneering studies on sentiment analysis in Turkish was conducted by Eroğlu U. In this study, sentiment analysis methods were applied to Turkish texts collected from the beyazperde.com website. As a result of this study, an accuracy rate of 85% was achieved using the Support Vector Machines (SVM) algorithm (Eroğlu, 2018).

In Türkmenoğlu's study, both dictionary and machine learning algorithms were applied to Turkish texts. The data used in the study was divided into two sections: Twitter data and movie review data. It was noted that the Twitter data was a shorter and unstructured dataset. Using a dictionary-based approach on the dataset obtained from Twitter, an accuracy of 75% was achieved, while using support vector machines, an accuracy of

85% was achieved. For the movie review data, which is a longer and structured dataset, he achieved an accuracy rate of 79.5% using a dictionary-based approach and 89% using support vector machines (Türkmenoğlu, 2013).

Sevindi used Turkish film reviews in his study. He applied both a dictionary-based approach and machine learning algorithms. He noted that among the machine learning algorithms he applied, the support vector machine algorithm yielded the best results with an F-score of 0.8258. Furthermore, he observed that the machine learning approach produced more accurate results than the dictionary-based approach in his study (Sevindi, 2013).

Materials and Methods

Dataset

Most of the early studies on Sentiment Analysis have used movie reviews. This is because, in order to determine how successful the method is by creating training and test sets for the study, there was a need for pre-labeled movie reviews. To achieve this, a large archive of Turkish reviews was required for research purposes. The dataset required for the accurate classification of existing data was found on the open source address "BeyazPerde.com" Kaggle. The original dataset has 10,662 reviews with ratings ranging from 1 to 5 (Demirtas & Pechenizkiy, 2013). The star ratings of the reviews were divided into two classes. Reviews with 4 or 5 stars were considered positive, while reviews with 1 or 2 stars were considered negative. Reviews with 3 stars were excluded.

Spider Software (Web Scraping-Web Crawler)

Most websites on the internet use HTML (Hyper Text Markup Language), which is text-based. Due to HTML being text-based, applications and programming language libraries known as 'Webcrawlers' (spider software in Turkish) have been developed to access the desired data within websites (Guo, 2022). In this study, the Beautiful Soup4 spider software library was used to retrieve comments rated by users from the site and record the original comment and its classified form in a pre-created database structure.

Logistic Regression (LR)

Logistic regression is a supervised machine learning classification algorithm used to predict the probability of a categorical dependent variable. The dependent variable is a binary variable containing data coded as 1 (yes/true) or 0 (no/false), used as a binary classifier (not in regression).

Logistic regression is a method that defines the relationship between dependent and independent variables using the minimum number of variables to achieve the best fit and establishes a biologically acceptable model. The use of the logistic model for the analysis of biological experiments was first proposed by Berkson (1944) (Bircan, 2004).

Logistic regression is a very important technique in artificial intelligence and machine learning (AI/ML). Machine Learning (ML) models are software programs that you can configure and train to perform complex data processing tasks without manual intervention. ML models created using logistic regression can provide actionable insights from business data and perform predictive analytics to reduce operational costs and increase productivity (BJ & Yadhukrishnan, 2023).

Libraries

- NumPy: It was created by Travis Oliphant in 2005 and added to the Numeric library by modifying Numarray's features. It is a library for the Python programming language that adds high-level mathematical functions for multidimensional array and matrix data structures. NumPy is an open-source library (McKinney, 2012).
- Pandas: In 2008, Wes McKinney developed this high-performance library for analyzing financial data. It is an open-source, free library. It is used for data processing and data analysis. It is used to process numerical tables and time series (McKinney, 2011).
- Matplotlib: Written by John Hunter in 2003. It is a data visualization and plotting library used for the Numpy library. It provides an object-oriented API for plotting and visualizing graphics in applications that use general-purpose GUI toolkits. The matplotlib.pyplot.plot() method provides a standardized interface for creating various types of graphs. The plot() function is used to plot values as x,y coordinates on a data graph in the most basic example (Miura & Sladoje, 2022).
- Sklearn: It is a Python-based library used to create machine learning models. It uses various learning techniques for classification, clustering, and regression. Sklearn is compatible with NumPy and SciPy. This allows it to work seamlessly with different Python libraries.
- Nltk: Natural language processing supports classification, tagging, stemming, labeling, parsing, and semantic reasoning functions. It was developed by Steven Bird and Edward Loper at the University of Pennsylvania's Department of Computer and Information Sciences (Kadriu, 2013).

Experiments

The dataset used in the study is one of the datasets frequently used in the literature for analyzing Turkish film reviews. The dataset has two categories: positive and negative. Two sample reviews from the dataset are shown in Figure 1.

Figure 1

Sample comments from the dataset

16	liv tyler hatirina dahi olsa izlenmiyecek ,bosuna vakit saklanmayacak filmlerden birisi.manasiz,an...	0
17	kendini insanın filminin s�resinde bi isko� gibi hissettiren mel gibson filmin konusu, m�zigi ve oyuncugu...	1

Artificial intelligence-based models cannot perform sentiment analysis directly on text. Therefore, the dataset used in the study was prepared specifically for the proposed model. This process is illustrated in Figure 2.

Figure 2

Data preprocessing process

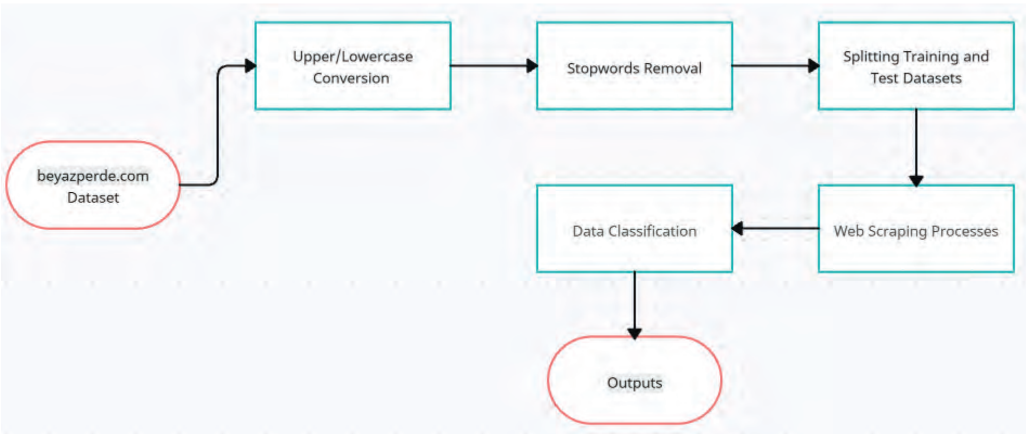

Artificial intelligence-based models cannot directly process text data. To prevent the model from interpreting the same words differently, uppercase letters have been converted to lowercase. Words frequently used in Turkish texts that do not contribute significantly to the overall meaning of the sentence have been removed. The process is shown in Figure 3.

Figure 3

NLP process

```
def pre_processing(text):
    text = text.lower()  #Büyük harften -Küçük harfe çevirme
    text = re.sub("[^abcçdefgğhıijklmnoöprsştuüvyz]"," ",text)
    text=nltk.word_tokenize(text) # cümledeki kelimeleri birbirinden ayırır.
    text =[word for word in text if not word in set(stopwords.words("turkish"))]
    lemma=nlp.WordNetLemmatizer()
    text=[lemma.lemmatize(word) for word in text] # cümledeki bir kelimenin kökünü bulur ve onu kök haline getirir.
    text=" ".join(text)
    return text
```

In the subsequent process, training and test data were separated. The logistic regression algorithm was used for text classification. By using a pipeline, data preprocessing and model training steps were performed in a single step, making the code more readable and manageable. This process is shown in Figure 4.

Figure 4

Logistic Regression and Pipeline Process

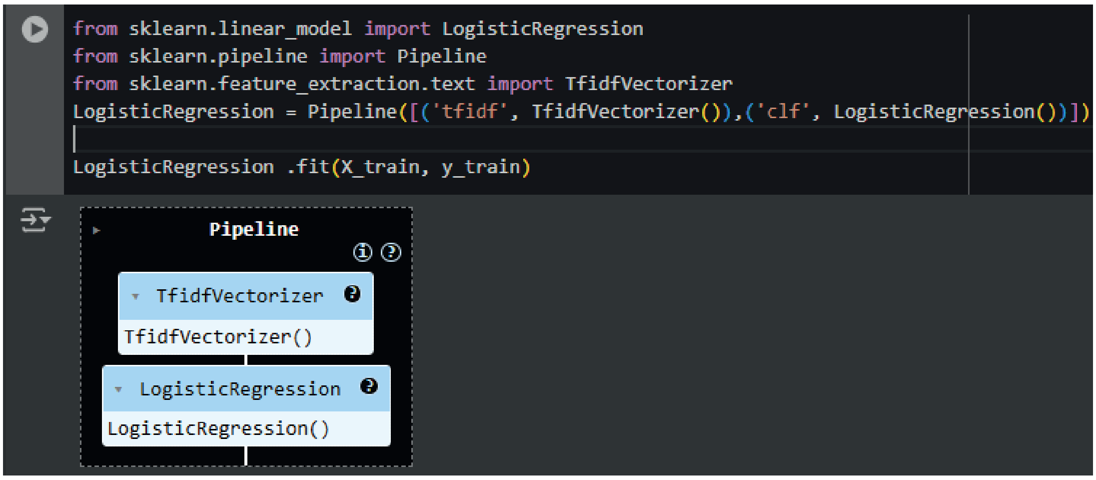

```
from sklearn.linear_model import LogisticRegression
from sklearn.pipeline import Pipeline
from sklearn.feature_extraction.text import TfidfVectorizer
LogisticRegression = Pipeline([('tfidf', TfidfVectorizer()),('clf', LogisticRegression())])

LogisticRegression .fit(X_train, y_train)
```


Performance measurements were conducted on the dataset. Our model achieved an average accuracy of 89%. Web scraping operations were performed to extract comments from the movie streaming site. This process is illustrated in Figure 5.

Figure 5

Web scraping process

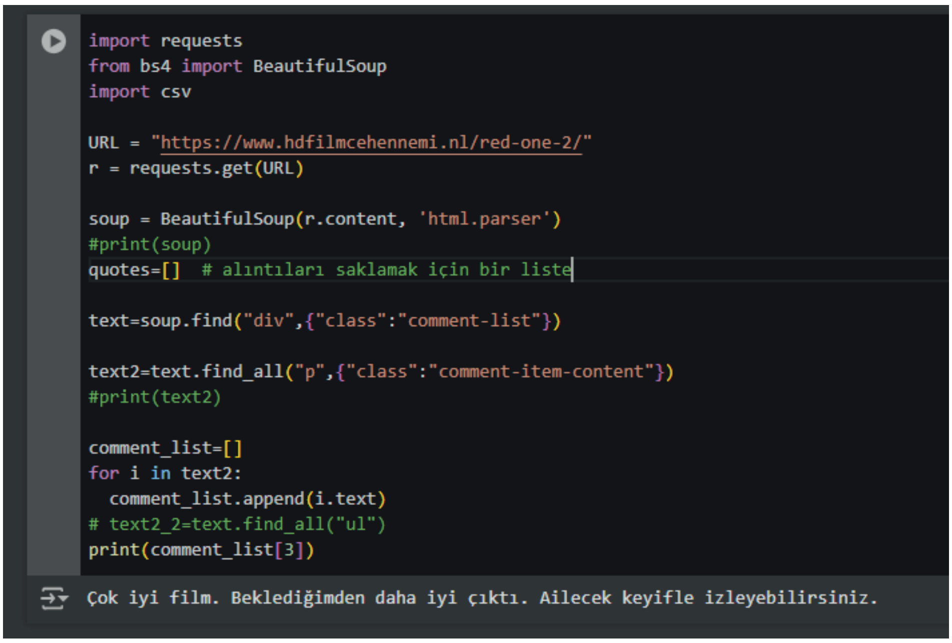

```
import requests
from bs4 import BeautifulSoup
import csv

URL = "https://www.hdfilmcehennemi.nl/red-one-2/"
r = requests.get(URL)

soup = BeautifulSoup(r.content, 'html.parser')
#print(soup)
quotes=[]  # alıntıları saklamak için bir liste

text=soup.find("div",{"class":"comment-list"})

text2=text.find_all("p",{"class":"comment-item-content"})
#print(text2)

comment_list=[]
for i in text2:
  comment_list.append(i.text)
# text2_2=text.find_all("ul")
print(comment_list[3])
```

```
Çok iyi film. Beklediğimden daha iyi çıktı. Ailecek keyifle izleyebilirsiniz.
```

The collected comments were classified as positive or negative using logistic regression. This process is illustrated in Figure 6.

Figure 6

Classified comments

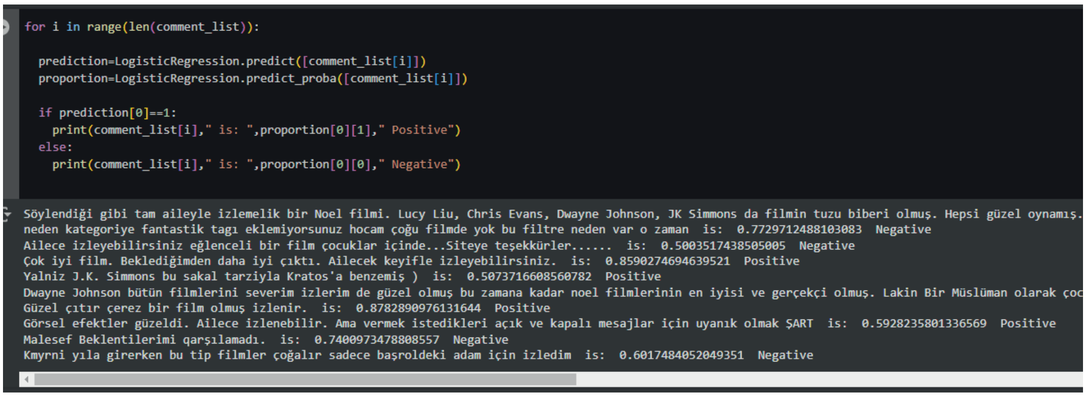

```
for i in range(len(comment_list)):

  prediction=LogisticRegression.predict([comment_list[i]])
  proportion=LogisticRegression.predict_proba([comment_list[i]])

  if prediction[0]==1:
    print(comment_list[i]," is: ",proportion[0][1]," Positive")
  else:
    print(comment_list[i]," is: ",proportion[0][0]," Negative")

Söylendiği gibi tam aileyle izlemelik bir Noel filmi. Lucy Liu, Chris Evans, Dwayne Johnson, JK Simmons da filmin tuzu biberi olmuş. Hepsi güzel oynamış.
neden kategoriye fantastik tagı eklemiyorsunuz hocam çoğu filmde yok bu filtre neden var o zaman  is:  0.7729712488103083  Negative
Ailece izleyebilirsiniz eğlenceli bir film çocuklar içinde...Siteye teşekkürler......  is:  0.5003517438505005  Negative
Çok iyi film. Beklediğimden daha iyi çıktı. Ailecek keyifle izleyebilirsiniz.  is:  0.8590274694639521  Positive
Yalniz J.K. Simmons bu sakal tarziyla Kratos'a benzemiş )  is:  0.5073716608560782  Positive
Dwayne Johnson bütün filmlerini severim izlerim de güzel olmuş bu zamana kadar noel filmlerinin en iyisi ve gerçekçi olmuş. Lakin Bir Müslüman olarak çoc
Güzel çıtır çerez bir film olmuş izlenir.  is:  0.8782890976131644  Positive
Görsel efektler güzeldi. Ailece izlenebilir. Ama vermek istedikleri açık ve kapalı mesajlar için uyanık olmak ŞART  is:  0.5928235801336569  Positive
Malesef Beklentilerimi qarşılamadı.  is:  0.7400973478808557  Negative
Kmyrni yıla girerken bu tip filmler çoğalır sadece başroldeki adam için izledim  is:  0.6017484052049351  Negative
```

Results

With the advent of the internet into human life, human life has changed significantly. The increasing number of people using the internet every day has led to the emergence of different needs. With the widespread use of the internet, social media platforms, forum sites, and blogs have become widely used. Users share a lot of content on these platforms. Processing this content with the help of computer-assisted systems and producing results is of great importance. In this study, sentiment analysis was performed using a dataset consisting of movie reviews. The Logistic Regression algorithm was used to perform this process. The dataset achieved an 89% success rate. The accuracy value obtained in the proposed model shows that the proposed model can be used in sentiment analysis problems.

Referans

Donovan, J. J. (1976). Databsse system approach the management decision support. *ACM Transactions on Database Systems (TODS)*, 1(4), 344-369.

Datta, A., & Acharjee, M. K. (2018). Consumers attitude towards online shopping: factors influencing young consumers to shop online in Dhaka, *Bangladesh. International Journal of Management Studies*, 3(4), 1-13.

Akba, F. (2014). Duygu analizinde öznitelik seçme metriklerinin değerlendirilmesi: *Türkçe film eleştirileri*.

Haque, M. R., Lima, S. A., & Mishu, S. Z. (2019, December). Performance analysis of different neural networks for sentiment analysis on IMDb movie reviews. *In 2019 3rd International conference on electrical, computer & telecommunication engineering (ICECTE)* (pp. 161-164). IEEE.

Rao, G., Huang, W., Feng, Z., & Cong, Q. (2018). LSTM with sentence representations for document-level sentiment classification. *Neurocomputing,* 308, 49-57.

Islam, M. M., & Sultana, N. (2018). Comparative study on machine learning algorithms for sentiment classification. *International Journal of Computer Applications*, 182(21), 1-7.

Narayanan, V., Arora, I., & Bhatia, A. (2013, October). Fast and accurate sentiment classification using an enhanced Naive Bayes model. *In International Conference on Intelligent Data Engineering and Automated Learning* (pp. 194-201). Berlin, Heidelberg: Springer Berlin Heidelberg.

Huang, Y., Jiang, Y., Hasan, T., Jiang, Q., & Li, C. (2018, March). A topic BiLSTM model for sentiment classification. *In proceedings of the 2nd international conference on innovation in artificial intelligence* (pp. 143-147).

Ibrahım, M. H. (2022). WBBA-KM: a hybrid weight-based bat algorithm with K-means algorithm for cluster analysis. Politeknik Dergisi, 25(1), 65-73.

Pang, B., Lee, L., & Vaithyanathan, S. (2002). Thumbs up? Sentiment classification using machine learning techniques. *arXiv preprint* cs/0205070.

S. Matsumoto, H. Takamura, ve Okumura, M., (2005).“Lecture Notes in Artificial Intelligence”, *9th Pacific-Asia Conference, Hanoi, Vietnam*, May 18-20, 2005, Proceedings (Vol. 7818). Springer Science & Business Media. ss. 301-311.

Tang, D., Qin, B., & Liu, T. (2015, July). Learning semantic representations of users and products for document level sentiment classification. *In Proceedings of the 53rd annual meeting of the Association for Computational Linguistics and the 7th international joint conference on natural language processing* (volume 1: long papers) (pp. 1014-1023).

Liu, S. M., & Chen, J. H. (2015). A multi-label classification based approach for sentiment classification. *Expert Systems with Applications*, 42(3), 1083-1093.

Eroğlu, F. G. (2018). Reduced Order Modelling for Multiphysics problems (Doctoral dissertation, Middle East Technical University (Turkey)).

Cumali Türkmenoğlu, (2016). “Türkçe metinlerde duygu analizi”. *Fen ˘ Bilimleri Enstitüsü*. [Çevrimiçi]. Erişim adresi: https://polen.itu.edu.tr/items/f43f7829-1900-4fb9-babf-097803950050

Sevindi, B. İ. (2013). Türkçe metinlerde denetimli ve sözlük tabanlı duygu analizi yaklaşımlarının karşılaştırılması. *Gazi Üniversitesi Fen Bilimleri Enstitüsü*, Yayımlanmış Yüksek Lisans Tezi.

Demirtas, E., & Pechenizkiy, M. (2013, August). Cross-lingual polarity detection with machine translation. *In Proceedings of the Second International Workshop on Issues of Sentiment Discovery and Opinion Mining* (pp. 1-8).

Guo, Y. (2022). Contextualized design of IoT (Internet of Things) finance for edge artificial intelligence computing. *Computational Intelligence and Neuroscience,* 2022(1), 6046957.

Bircan, H. (2004). Lojistik regresyon analizi: Tıp verileri üzerine bir uygulama. *Kocaeli Üniversitesi Sosyal Bilimler Dergisi,* (8), 185-208.

BJ, B. N., & Yadhukrishnan, S. (2023, August). A comparative study on document images classification using logistic regression and multiple linear regressions. *In 2023 Second International Conference on Augmented Intelligence and Sustainable Systems (ICAISS)* (pp. 1096-1104). IEEE

McKinney, W. (2012). Python for data analysis: Data wrangling with Pandas, NumPy, and IPython. " *O'Reilly Media, Inc.*".

McKinney, W. (2011). pandas: a foundational Python library for data analysis and statistics. *Python for high performance and scientific computing*, 14(9), 1-9.

Miura, K., & Sladoje, N. (2022). Bioimage data analysis workflows–advanced components and methods (p. 212). *Springer Nature*.

Kadriu, A. (2013, June). NLTK tagger for Albanian using iterative approach. *In Proceedings of the ITI 2013 35th International Conference on Information Technology Interfaces* (pp. 283-288). IEEE.

About The Authors

Beyza DÜNDAR, graduated from KTO Karatay University, Department of Computer Engineering. She is a master's student at Necmettin Erbakan University, Department of Computer Engineering. The system studied data science, artificial intelligence, image processing, machine learning and natural language processing.

Email: dundarbeyza777@gmail.com, **ORCID:** 0000-0002-2843-1043

Sabri KOÇER, PhD, He graduated from the Electrical Engineering Department of Selcuk University. He completed his graduate and his doctorate in Gazi University. Currently, Necmettin Erbakan University, Faculty of Engineering, Computer Engineering is working. Electronics, Computer, Telecommunication, Signal Processing and Biomedical studies in the area.

Email: skocer@erbakan.edu.tr, **ORCID:** 0000-0002-4849-747X

Similarity Index:

The similarity index obtained from the plagiarism software for this book chapter is 14%.

Particle Size Classification of Powdered Materials Such as Cement and Gypsum Using Piezo-Acoustic Method

Nihat ÇANKAYA
Necmettin Erbakan University

To Cite This Chapter:
Çankaya, N. (2024). Particle size classification of powdered materials such as cement and gypsum using piezo-acoustic method. In S. Kocer & O. Dundar (Eds.), *Next generation engineering: Smart solutions and applications* (pp. 228–234). ISRES Publishing.

Introduction

In industrial production processes, techniques such as sieve analysis (Türkçimento, 2021), laser diffraction (Ferraris, Hackley, & Avilés, 2004), x-ray micro-CT (Zhang & Napier-Munn, 1995), scanning electron microscopy (Holzer, Flatt, Erdoğan, Bullard, & Garboczi, 2010), and electrical field sensing (Merkus, 2009) are currently used for measuring the sizes of powdery materials produced. Laser-based techniques among these are widely used. It is a technique that can instantaneously measure the sizes or size distribution of particles resulting from the production process. However, it is a technique negatively affected by color changes of the material type. Furthermore, due to its high cost, it has not achieved widespread use. As an alternative to these techniques, it was considered that cost-effective piezo-acoustic based techniques, which are not sensitive to changes in material type, could be used. There are studies where the sizes of different material types are measured. In a study conducted with glass and coal particles, the sizes of particles varying between 64-133 μm were measured (Coghill, 2007). The sizes of metal powders such as steel, cast iron, and aluminum, varying between 0.15-1.1 mm, were measured using the piezo-acoustic technique (Boschetto & Quadrini, 2011). In a study using biomass particles varying between 400-5000 μm and glass powders varying between 20-250 μm, the particle size distributions could be measured (Gao et al., 2013). A correlation above 0.8 was obtained in the size measurement of silica sands in the size classes of 116-750 μm, 61-395 μm, 10-246 μm (Zheng, Yan, Hu, & Zhang, 2021). The size classes of flour-semolina mixtures in the 0-212 μm size class were measured (Çankaya, 2024).

Research Purpose

This study aims to develop and test an alternative piezo-acoustic method for particle size classification, specifically for fine construction materials like cement, gypsum, and polymer-modified cement. The materials were sieved using 33, 45 and 91 micron sieves and separated into 0-33, 33-45 and 45-91 micron size classes. It was observed that the material types and size classes could be measured with the piezo-acoustic based measurement setup.

Materials and Method

Sieve Analysis and Preparation of Materials

A sieve shaker seen in Figure 1 (a) and stainless-steel sieves of 33, 45, and 91 microns were used to prepare materials of different size classes. Cement, gypsum, and polymer-modified cement (vitaflex) materials were sieved separately. Materials passing under the 33 micron sieve were classified as the 0-33 micron class, materials remaining on top of the 33 micron sieve and under the 45 micron sieve as the 33-45 micron class, and materials remaining on top of the 45 micron sieve and under the 91 micron sieve as the 45-91 micron class. Figure 1 (b) shows the appearance of the sieved and classified materials, from top to bottom respectively: vitaflex, gypsum, cement, and from left to right in increasing size class.

Figure 1

(a) *Sieve Shaker and Sieves* ***(b)*** *Sieved and Classified Materials*

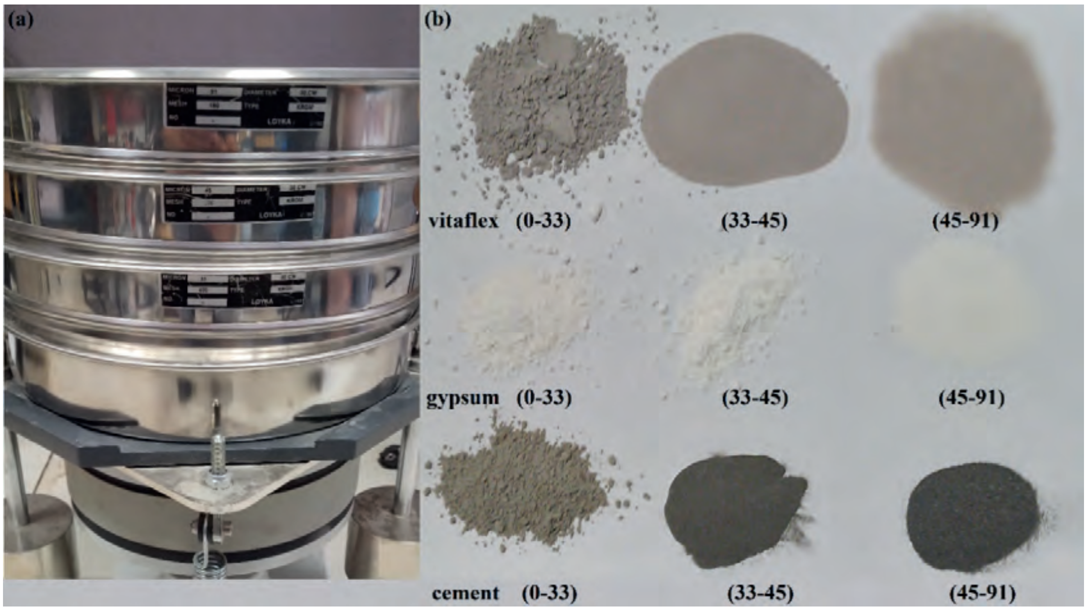

Piezo-Acoustic Measurement Setup and Procedure

In the piezo-acoustic method, the particles to be measured are accelerated and impacted onto a rod or plate-shaped wave guide to create acoustic effects. These effects cause electrical amplitudes to form in the piezoelectric sensor attached to the guide. These amplitudes are analyzed through signal analysis to obtain information about size and distribution. In the developed measurement setup, a piezoelectric sensor with a natural frequency of 150 kHz was attached to a wave guide made of 4 mm thick HSS material. Using a precision vibrating feeder, particles are sent at a rate of 6.7 grams per minute into a tube subjected to suction by a vacuum cleaner, and are impacted onto this guide at a speed of 20 m/s. The resulting impact effects create voltage amplitudes in the piezoelectric sensor. Since these amplitudes are low, they are amplified 1000 times (60 dB) with a signal amplifier and then recorded on a computer via a USB digital oscilloscope. The recorded signals are 1 second long and contain 1 million samples. The amplitudes and energies of the recorded signals were analyzed with the help of the MATLAB. Figure 2 shows the setup used in the piezo-acoustic measurement method.

Figure 2

Components of the Piezo-Acoustic Measurement Setup

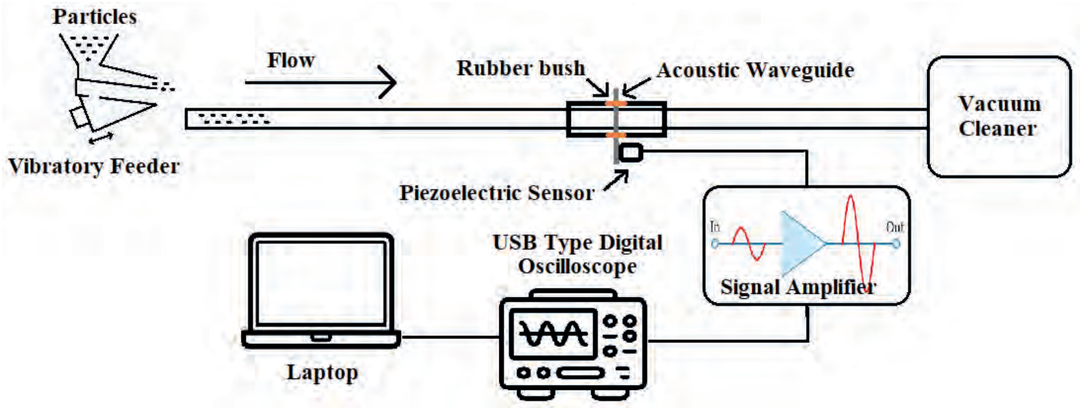

Results and Discussion

The visuals of the signals obtained because of measuring the unsieved states of vitaflex, gypsum, and cement materials and their states sieved into 3 different size classes with the measurement setup are given in Figure 3. In the visuals, the word “normal” next to the material name indicates that the material was measured for size without sieving. As can be seen from the graphs in Figure 3, as particle sizes increase, the amplitudes they create in the piezo-acoustic sensor also increase. This is consistent with previous studies [6-10]. When the amplitudes generated by the particles in the 33-45 and 45-91 size classes of the materials are examined, it is seen that vitaflex and cement are quite close to each other and have higher values than gypsum. This indicates that the densities of cement and vitaflex materials are close to each other and higher than that of gypsum. Because a greater acoustic effect of the impacting particle means either its size is larger or, as is the case here, if the sizes are similar, its density is greater. Furthermore, since the size distribution of the materials passing through the sieve is unknown, it cannot be assumed that densities are equal because their densities might be low but they could be in the larger size region under the sieve. In their normal state, the particle sizes of the materials are mostly below 33 microns. However, since the amplitudes generated by particles in the 33-45 and 45-91 micron size classes are relatively higher, it was observed that they are dominant in the normal signal.

Figure 3

Measurement Signals for Different Material Types and Size Classes

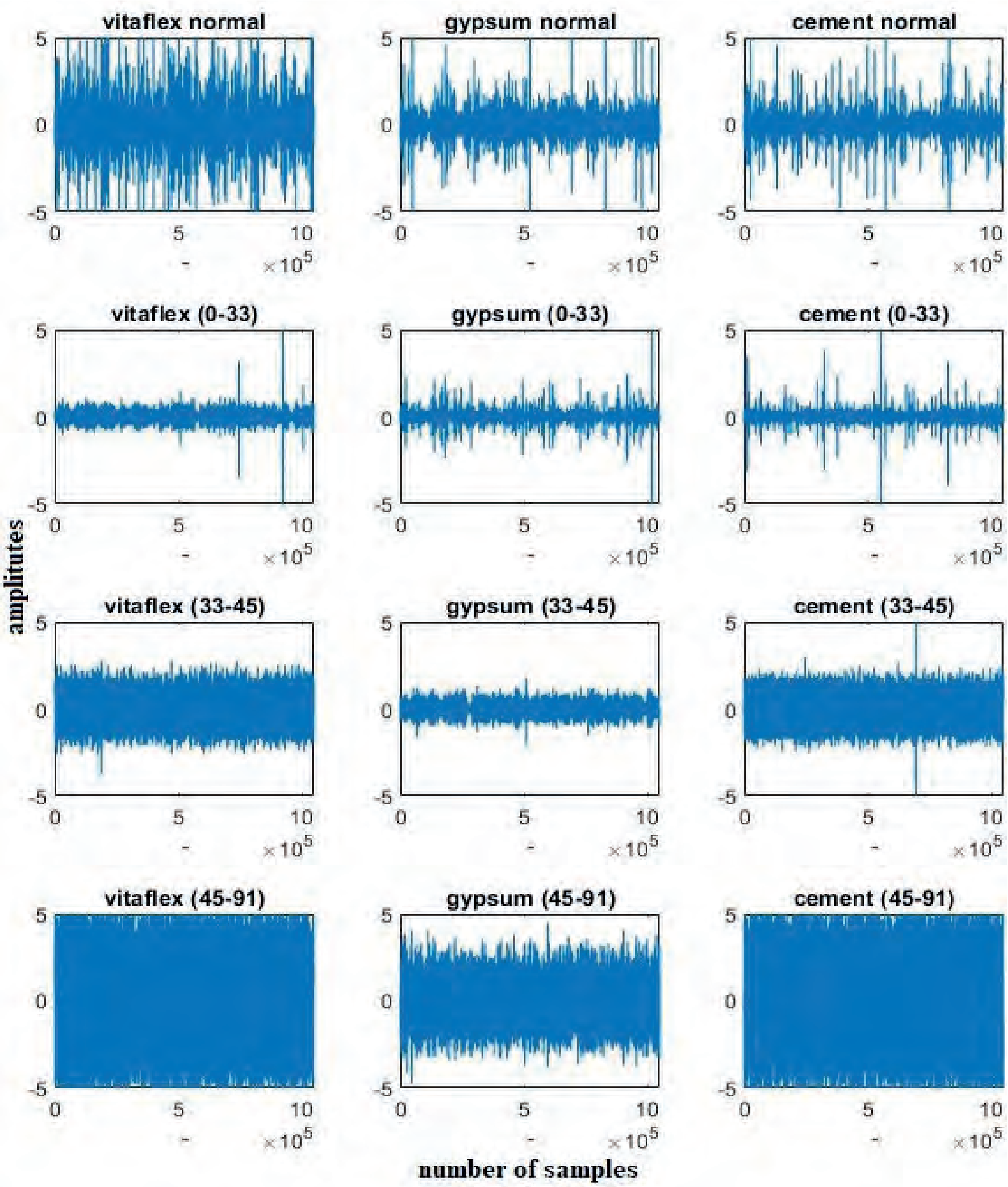

The energies of the signals were calculated in 10 equal regions between 0-5 V. When the signals generated by the materials are examined in terms of their energies, it is seen that the materials in the 45-91 size class produce higher amplitudes and consequently higher signal energies. It was observed that as the particle sizes decrease, the total energy produced also decreases. The graphs of the measured energy values depending on the voltage ranges are given in **Figure 4** and **Figure 5**.

Figure 4

Energies of the Signals for Different Material Types and Size Classes

Materials/Energies	0-0.5 V	0.5-1 V	1-1.5 V	1.5-2 V	2-2.5 V	2.5-3 V	3-3.5 V	3.5-4 V	4-4.5 V	4.5-5 V	Total [0-5 V]
vitaflex_normal	17381	28571	12751	7026	4144	3167	2073	1808	1150	1270	79341
vitaflex (0-33)	14423	2590	97	120	128	111	112	107	118	86	17892
vitaflex (33-45)	15842	73670	42246	10022	1216	134	0	0	0	0	143130
vitaflex (45-91)	8062	69921	126293	154349	128691	108530	64556	39175	21421	13100	734098
gypsum_normal	16056	12437	2622	1097	638	596	362	255	210	220	34493
gypsum (0-33)	3781	532	186	103	62	44	19	14	0	0	4741
gypsum (33-45)	16541	6186	153	16	0	0	0	0	0	0	22896
gypsum (45-91)	13592	80460	74696	37783	11791	3963	1105	176	49	20	223635
cement_normal	10959	4912	2402	1593	1005	640	394	285	261	328	22779
cement (0-33)	8852	986	304	158	85	178	162	212	175	200	11312
cement (33-45)	16398	70466	33375	6135	476	118	168	124	214	173	127647
cement (45-91)	7971	69444	126574	157865	131909	110196	61762	37657	20673	12623	736674

Figure 5

Energy Distribution by Material Type and Voltage Range

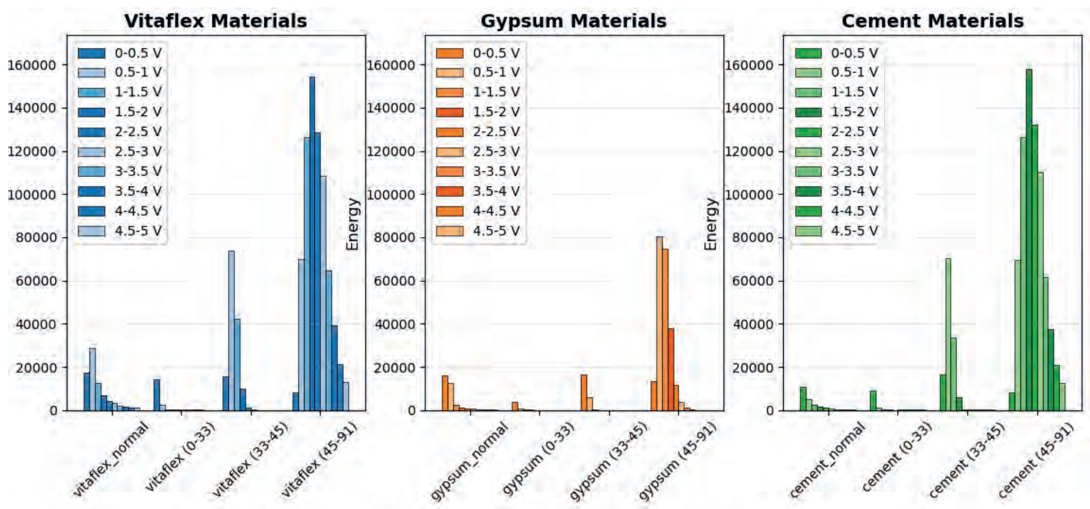

When the unsieved normal states of the materials are examined, vitaflex has the highest total energy and gypsum has the lowest. Here, the energies in the high voltage ranges are the highest for vitaflex and the lowest for gypsum. These results are consistent with the normal signals in **Figure 3**. From this, it can be interpreted that large particles are proportionally more abundant in the vitaflex material. Accordingly, it can be said that the proportion of large particles in cement is relatively less.

In this study, it has been demonstrated for the first time that the sizes of materials such as cement, gypsum, and vitaflex, which are below 100 microns and mostly below 33 microns in size, can be measured by the piezo-acoustic method. In future studies, particles from different size classes can be mixed in different weights to examine changes and values in the size distribution in more detail.

Acknowledgements

The author would like to thank Mr. Muhammet Emre Irmak for his contributions.

References

Coghill, P.J. (2007). Particle size of pneumatically conveyed powders measured using impact duration. *Particle & Particle Systems Characterization, 24*(4), pp. 464-469.

Çankaya, N. (2024). Online measurement of flour particle size distribution using piezoelectric sensor. *Konya Journal of Engineering Sciences, 12*(4), pp. 941-954.

Ferraris, C.F., Hackley, V.A., & Avilés, A.I. (2004). *Measurement of particle size distribution in Portland cement powder: analysis of ASTM round robin studies*. ASTM International.

Gao, L., Yan, Y., Carter, R.M., Sun, D., Lee, P., & Xu, C. (2013). On-line particle sizing of pneumatically conveyed biomass particles using piezoelectric sensors. *Fuel, 113*, pp. 810-816.

Holzer, L., Flatt, R.J., Erdoğan, S.T., Bullard, J.W., & Garboczi, E.J. (2010). Shape comparison between 0.4–2.0 and 20–60 µm cement particles. *Journal of the American Ceramic Society, 93*(6), pp. 1626-1633.

Merkus, H.G. (2009). Electrical Sensing Zone. In *Particle Size Measurements: Fundamentals, Practice, Quality* (pp. 241-257). Springer.

Quadrini, F., & Boschetto, A. (2011). Powder size measurement by acoustic emission. *Measurement, 44*(2), pp. 290-297.

Türkçimento. (2021). *Çimento Mühendisliği El Kitabı – Kalite Bölümü*.

Zhang, Y., & Napier-Munn, T. (1995). Effects of particle size distribution, surface area and chemical composition on Portland cement strength. *Powder Technology, 83*(3), pp. 245-252.

Zheng, G., Yan, Y., Hu, Y., & Zhang, W. (2021). Online measurement of the size distribution of pneumatically conveyed particles through acoustic emission detection and triboelectric sensing. *IEEE Transactions on Instrumentation and Measurement, 70*, pp. 1-17.

About The Author

Associate Prof. Dr. Nihat ÇANKAYA was born in Konya, Turkey in 1974. He received the B.S., M.S., and the Ph.D. degrees in electrical electronics engineering. As the 3rd generation representative of the milling profession, He has been an engineer in various positions in factories producing flour, semolina, and pasta, and took part in various projects in important companies of the sector in Italy, Switzerland, France, and Germany.

After working as Technical Manager of Selva Pasta, he still works as an academician for at Necmettin Erbakan University. He is also the Energy Management Coordinator of Necmettin Erbakan University. He speaks English and Italian, and his studies are concentrated in the following areas. He is also the coordinator of various research projects on related subjects. He is the author of articles and inventions. His research interests include control theory, clever algorithms, compressed air production, energy saving, T1DM. He offers sector-specific solutions by producing high-tech equipment with the JETMASTER Technology company he founded. He became a Member (M) of IEEE in 2024.

E-mail:ncankaya@erbakan.edu.tr, **ORCID:** 0000-0002-3574-2712

Similarity Index:

The similarity index obtained from the plagiarism software for this book chapter is 1%.

Convolutional Neural Networks for the Analysis of Radiologic Images

Mehmet DURSUN
Necmettin Erbakan University

To Cite This Chapter:
Dursun, M. (2025). Convolutional neural networks for the analysis of radiologic images. In S. Kocer & O. Dundar (Eds.), *Next generation engineering: Smart solutions and applications* (pp. 235–245). ISRES Publishing.

Introduction

Disease is a pathological condition that disrupts the structural integrity or functional homeostasis of an organism and manifests itself through specific signs and symptoms. This abnormal state generally has etiological origins such as infection, genetic predisposition, environmental factors, or intrinsic dysfunctions, and is distinguished from direct external trauma. In the medical discipline, the concept of disease is defined as a comprehensive set of syndromes that includes both clinical findings and symptoms.

Figure 1 displays a chart, prepared by the Turkish Statistical Institute (TÜİK), illustrating mortality rates by cause for the years 2022-2023. An examination of the mortality and cause of death statistics for 2022-2023 reveals that deaths attributable to diseases of the circulatory system rank first, while deaths from neoplasms (tumors) rank second.

Figure 1

Turkish Statistical Institute (TUIK) 2022–2023 Cause-Specific Mortality Rates(TUIK,2023)

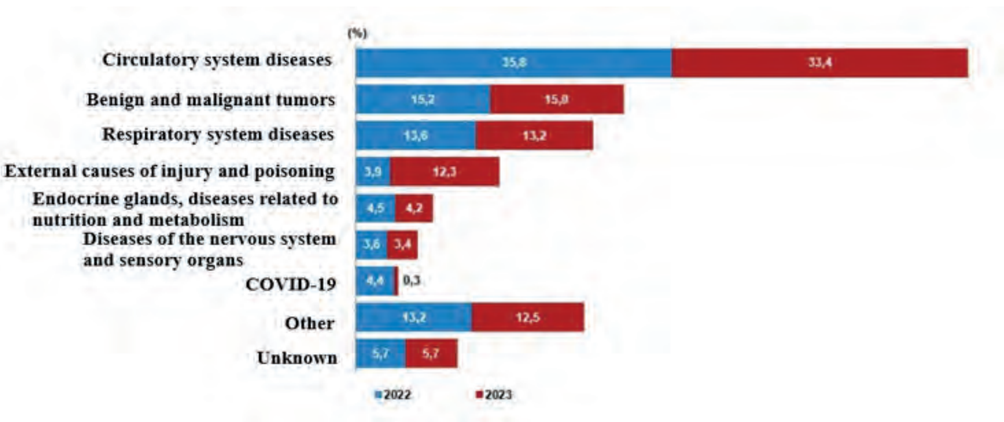

In Figure 2, the mortality rates originating from benign and malignant tumors are displayed. Analysis of the graph reveals that among both benign and malignant tumors, the most lethal is the malignant tumor of the larynx and trachea/bronchi/lungs. Cancer is a group of diseases characterized by cells that acquire dangerous capabilities such as 'immortality' and uncontrolled proliferation due to disruptions in their genes; these cells exhibit the properties of invading surrounding tissues and spreading to other parts of the body (metastasis). The causes and behaviors of these diseases are highly diverse (Cairns, 1975).

Figure 2

The mortality rate attributable to both benign and malignant neoplasms in 2022 and 2023(TUIK,2023).

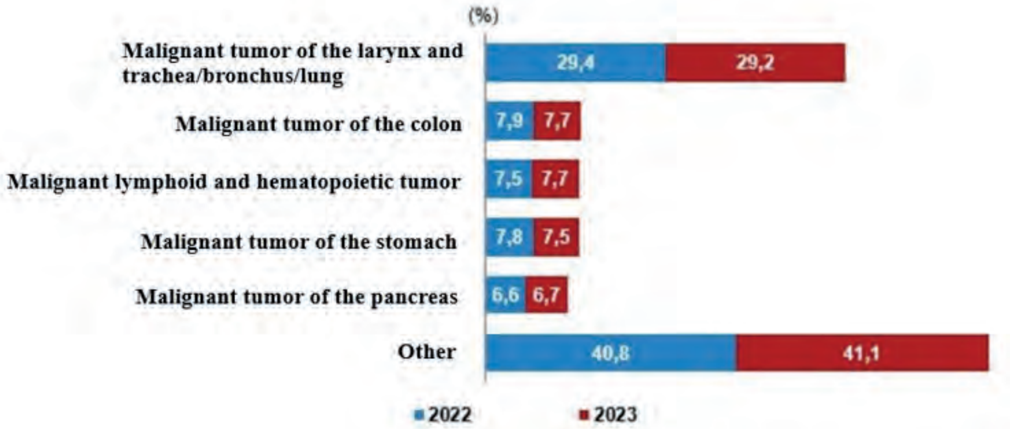

Cancer can also be defined as a multidimensional and layered biopsychosocial crisis that extends beyond its pathophysiological processes. It is not merely a disease causing structural destruction in organs and tissues. Furthermore, it is a condition that profoundly shakes the individual's existential integrity, psychological world, and social life (Brown et al., 2023).

This disease ranks among the foremost causes of mortality in our country and worldwide. Its early detection through routine screenings, and consequently its management at a stage where treatment is easier and the response is faster and more effective, are of critical importance (Brown et al., 2024).

The most fundamental radiological imaging methods used in screening can be listed as;

X-ray,

Magnetic Resonance İmaging

Computed tomography

Mammography imaging.

Medical Imaging Techniques

Medical imaging modalities play a critically important role in the investigation of disease ethology. Based on the data obtained through these modalities, physicians can now guide patients toward the most appropriate and effective treatment pathway. Innovations in this field have particularly increased the motivation of patient groups with life-threatening concerns, such as cancer patients, by reinforcing the prospect of a swift recovery, thereby accelerating their response to treatment.

Diagnostic Radiology Systems

Radiography (X-Ray)

X-ray is a painless, low-cost, and rapid method used by physicians to detect abnormalities by imaging tissue differences in our body, particularly bone structures. The foundation of medical imaging lies in the use of X-rays, a process made possible by their differential absorption by bones and soft tissues within the body. This results in images of the scanned area being produced with different shades. Essentially, areas that are more affected by X-rays appear in darker shades, while areas that are less affected produce lighter-toned images. Consequently, air in the abdomen or lungs, bones, fat, and muscle tissues become easily distinguishable from one another. Figure 3 shows a chest radiograph of a male patient.

Figure 3

X-ray image of a male patient (Alfatip, 2025)

Computed Tomography (CT)

CT shares its foundational principle with conventional radiography, as both modalities utilize X-rays to generate diagnostic images.The key difference is that the system generating the X-rays does not emit them from a single fixed position towards the patient. Instead, it rotates around the patient in a 360-degree arc, acquiring numerous images. These images are then processed by powerful computer systems to generate detailed cross-sectional images of the scanned area. Due to the acquisition of this series of sectional images, the patient is exposed to a higher level of radiation. Particularly in imaging soft tissues, the problem of indistinct images is encountered (Huthwaite et al., 213). To enhance image clarity, contrast agents, which are highly visible to X-rays yet safe for the patient, are administered. By using these contrast agents, which can have varying compositions depending on the intended use, clearer CT images can be obtained.

Figure 4 shows a CT image.

Figure 4

Computed Tomography Image (UzmanRadyoloji, 2025)

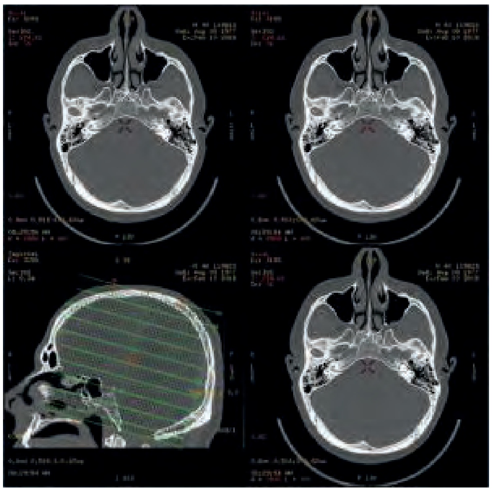

Magnetic Resonance Imaging (MRI)

MR can be defined as a fundamental classical model that posits certain atomic nuclei behave like small magnetic dipoles as a result of their rotational motion around their own axes. In the field of healthcare, the nucleus used is hydrogen. The reason for preferring hydrogen atoms is that fat and water, which are naturally abundant in the human body, contain a high number of hydrogen atoms. In fact, MR imaging can also be described as the mapping of the locations of water and fat in the body (Hoult & Simonetti, 2013).

Figure 5

MR Image (Lumbar MR, detailed image of the lumbar region) (Betatom, 2025)

MR images are generated based on the movement and changes in the density of hydrogen atoms within a tissue, which is achieved by exciting the protons in their nuclei using a magnetic field. The magnetic field strength mentioned here typically ranges from 1 to 1.5

Tesla, although in state-of-the-art systems, this value can reach up to 3 Tesla. Since MR does not involve ionizing radiation, it is a safer imaging method for both patients and operating personnel compared to other imaging techniques (Carol et al., 2010). Figure 5 shows an MR image known as a Lumbar MR, which provides a detailed view of the condition of the lumbar region.

Mammography

Mammography is the most effective radiological method used to detect abnormal structures in the breast, such as cancer, that cannot be identified through normal physical examination. The goal of mammography is to increase the diagnostic rate of the disease at an early stage while minimizing the patient's exposure to X-rays. To this end, digital mammography systems are replacing conventional mammography devices, and their use is increasing daily (Tükel, 2002). Since digital mammography systems eliminate post-imaging film processing, the images can be viewed on the physician's screen immediately after acquisition. The ability to store, process, and interpret images in a digital environment has streamlined workflows and reduced costs. Additionally, the capability to acquire images at lower doses has made mammography a more feasible and safer method.

Even in patients without any complaints, women over the age of 40 are recommended to undergo mammography at least once a year (Dinçel et al., 2010). Figure 6 shows a mammogram where an abnormal structure has been detected.

Figure 6

A mammogram image with a detected abnormal structure (Uzman Radyoloji, 2025).

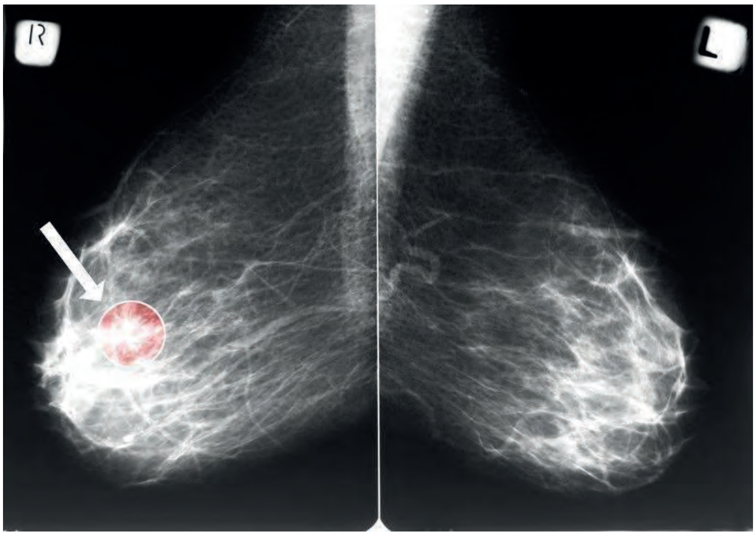

The Use Of Convolutional Neural Networks In Radiologıcal Image Analysis

CNN Architecture

The detection, classification, precise localization, and measurement of lesions, nodules, disease indicators, or anatomical structures in medical images is a critical process for computer aided diagnostic systems. These structures are often too complex to be accurately modelled using simple algorithms, equations, or predefined shapes. For instance, while a lung nodule is commonly modelled as a solid sphere, it may also present with angular or sharp-edged morphology. Similarly, a polyp, frequently described as having an onion-like shape, can exhibit a flat configuration (Eli&Ali, 2024). Consequently, there is an increasing need for systems that can analyse input data, learn from it, and generate meaningful information to enhance clinicians' diagnostic accuracy. Such systems must be capable of achieving reliable outcomes based on learning processes derived from the data (Lostumbo et. al, 2010).

CNNs have emerged as an advanced deep learning algorithm in the field of medical imaging, playing a significant role in enhancing diagnostic accuracy. While traditional approaches may have limitations in distinguishing complex anatomical structures and subtle pathological findings, deep learning algorithms can automatically extract abstract features from large-scale datasets. This capability enables the detection of even microscopic anomalies beyond human visual perception. By facilitating the automated, computer-assisted execution of clinical tasks such as tumor localization, tissue segmentation, and disease categorization in modalities like MR, CT, radiography, and mammography, deep learning algorithms improve process efficiency, reduce diagnostic errors, and accelerate diagnostic workflows. Consequently, they contribute to the advancement of clinical decision support systems, expanding opportunities for early diagnosis, simplifying the development of patient centered treatment strategies, and ultimately enhancing the reliability of clinical outcomes (Suzuki, 2017).

Convolutional Neural Networks (CNNs) can be fundamentally defined as a classification method. They are considered one of the most effective and successful deep learning models developed in the field of image processing.

The convolutional neural network (CNN) model named AlexNet, developed by Alex Krizhevsky, Ilya Sutskever, and Geoffrey Hinton, won first place in the Large Scale Visual Recognition Challenge (ILSVRC) in 2012, significantly outperforming traditional computer vision methods on ImageNet, which was the largest image dataset of its time (Krizhevsky et. al, 2012). Figure 7 presents a sample CNN architecture.

Figure7

CNN Architecture (Alshahrani & Alsairafi, 2024

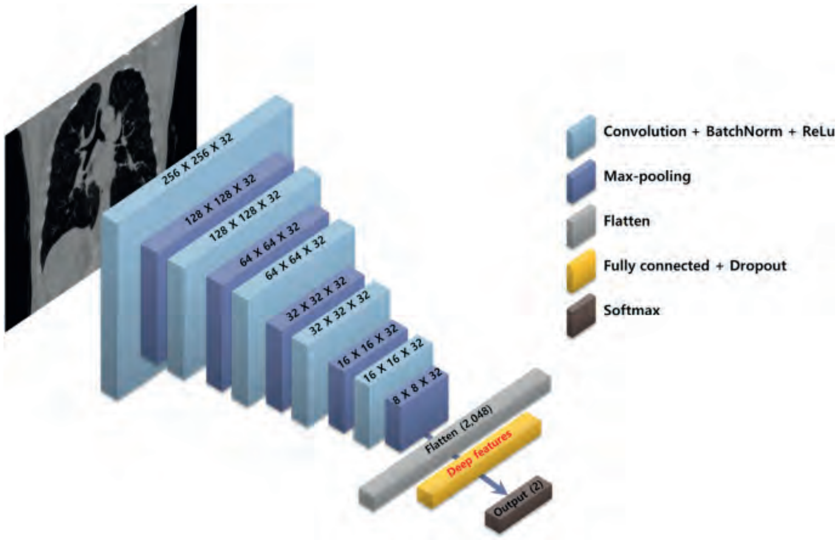

Convolutional Neural Networks (CNNs) extract meaningful information from medical images by transforming low-level pixel data into mid-level edge and shape features, and ultimately into high-level texture or lesion characteristics. The CNN architecture utilizes multiple layers to perform these operations. These layers can be categorized as convolutional layers, activation layers, pooling layers, fully connected layers, and output layers. It is of critical importance to work with input data that have appropriate dimensions and resolution, which minimize training time while maximizing classification performance.

Convolutional Layer

The convolutional layer serves as the primary feature extraction unit within the network. It operates on the principle of convolving learned filters (or kernels) with shared parameters across the spatial dimensions of the input data (e.g., an image matrix). This operation generates local feature maps that capture fundamental patterns such as edges, textures, and corners. The mechanism of parameter sharing substantially reduces the total number of trainable parameters, thereby enhancing computational efficiency and fortifying the model's capacity for generalization. As network depth increases, the outputs of successive convolutional layers begin to represent increasingly abstract and complex hierarchical features, such as object components or global shapes (Krizhevsky et. al, 2012).

Pooling (Subsampling) Layer

The pooling layer, which typically follows a convolutional layer, is primarily responsible for down-sampling the spatial dimensions (height and width) of the feature maps. This dimensional reduction serves to mitigate computational complexity and the risk of overfitting. The most prevalent technique, max pooling, selects the maximum activation value within a defined sliding window. This approach preserves the most salient features while simultaneously introducing a degree of translational invariance, rendering the representation robust to minor shifts and distortions in the input. Dimensionality reduction also contributes to controlling the parameter count, thereby enhancing the model's generalization capability (Jie et. al, 2020).

Activation Function Layer

Following a linear transformation, such as that performed by a convolutional or fully connected layer, a non-linear activation function is applied. This step is critical for enabling the model to learn complex, non-linear relationships, thereby augmenting its representational power. The Rectified Linear Unit (ReLU) is the most widely adopted activation function in the literature. ReLU mitigates the vanishing gradient problem by setting all negative inputs to zero and passing positive inputs unchanged. This property significantly accelerates the convergence rate of the learning process (Hao et. al, 2020).

Fully Connected Layers and Classification

Upon completion of the feature extraction stages (i.e., the series of convolutional and pooling layers), the resulting multi-dimensional feature maps are flattened into a one-dimensional vector. This vector is subsequently fed into one or more fully connected (dense) layers. In these layers, each neuron is connected to all neurons in the preceding layer, synthesizing global combinations of the learned features to perform the final inference. For instance, in image classification tasks, the output of the final fully connected layer is typically subjected to a softmax function. The softmax function calculates a normalized probability distribution over all target classes, thereby facilitating a definitive inference regarding the class membership of the input (Basha et. al, 2020).

Radiology Applications Using Convolutional Neural Networks

Esteva et al. conducted a study on the automated diagnosis of skin cancer using Convolutional Neural Networks (CNN) based on a dataset consisting of 129,450 images obtained from 2,032 patients. The performance of the proposed system was evaluated using biopsy-confirmed data and compared with expert assessments. While the accuracy rates of the experts were reported as 53% and 55%, the proposed system achieved an accuracy of 55.4% (Esteva et. al, 2017).

In their study on the automatic classification of tuberculosis from chest radiographs, Lakhani & Sundaram employed a deep convolutional neural network (DCNN)-based approach. The dataset, comprising 1,007 posteroanterior chest radiographs, was divided into three subsets for classification: training (68.0%), validation (17.1%), and testing (14.9%). When applied to the images previously scored by expert radiologists, the proposed method achieved a sensitivity of 97.3% and a specificity of 100% (Lakhani & Sundaram, 2017).

The findings of the study conducted by Daniel and Jain on mass detection in mammographic images can be summarized as follows: The results demonstrate that GoogLeNet, a CNN architecture that is resistant to overfitting due to its relatively low number of parameters and can be efficiently fine-tuned, significantly outperforms other baseline models. In clinical diagnostic applications, the most critical performance metric, recall (sensitivity), was achieved at a rate of 93.4%. Moreover, the model exhibited a high and balanced performance with a precision value of 92.4%. These results surpass the recall rates of radiologists, which range between 74.5% and 92.3%, indicating that the model can serve as a reliable diagnostic support system in clinical practice and has the potential to exceed existing human performance (Daniel & Jain, 2016).

Polsinelli et al. proposed a CNN architecture to rapidly detect COVID-19 infection from chest CT images. The model demonstrates a high level of diagnostic discrimination, supported by balanced performance metrics such as 85.03% accuracy, 87.55% sensitivity, 81.95% specificity, 85.01% precision, and an F1 score of 86.20%. Furthermore, the classification time for a single image is as low as 1.25 seconds on a high-end system and 7.81 seconds on a mid-range laptop, enabling the analysis of thousands of images per day even in environments with limited hardware resources (Polsinelli et. al, 2020).

Conclusion

In radiology, CNNs are widely employed to classify clinically relevant imaging features across various modalities. These models have demonstrated high performance in identifying fractures in X-ray scans, detecting lung nodules in CT, and classifying brain tumors in MRI. Additionally, CNN-based approaches are increasingly utilized to diagnose diabetic retinopathy using retinal fundus images, highlighting their broad applicability in medical image analysis and clinical decision support (Yamashita et. al, 2018).

References

A. Alshahrani and A. Alsairafi, “Bone Fracture Classification using Convolutional Neural Networks from X-ray Images”, *Eng. Technol. Appl. Sci. Res.*, vol. 14, no. 5, pp. 16640–16645, Oct. 2024.

ALFA_TİP, https:// alfatip.com.tr/kliniklerimiz/radyoloji/rontgen/

Basha, S. S., Dubey, S. R., Pulabaigari, V., & Mukherjee, S. (2020). Impact of fully connected layers on performance of convolutional neural networks for image classification. *Neurocomputing*, *378*, 112-119.

Brown, J. S., Amend, S. R., Austin, R. H., Gatenby, R. A., Hammarlund, E. U., & Pienta, K. J. (2023). Updating the definition of cancer. *Molecular Cancer Research*, *21*(11), 1142-1147.

Cairns, J. (1975). THE CANCER PROBLEM. *Scientific American*, *233*(5), 64–79. https://www.jstor.org/stable/249499 39

Carol C. Wu, Bruce M. Barack, Evaluation and Management of the Solitary Pulmonary Nodule, Editor(s): Michael I. Lewis, Robert J. McKenna, Jeremy A. Falk, George E. Chaux, Medical Management of the Thoracic Surgery Patient, W.B. Saunders, 2010, Pages 191-196, ISBN 9781416039938

Dinçel, E., Kısmet, K., Erel, S., Sunay, D., Şahin, M., Taşova, V., & Akkuş, M. A. (2010). İLK MAMOGRAFİ YAŞINA ETKİ EDEN FAKTÖRLER. *Meme Sagligi Dergisi/Journal of Breast Health*, *6*(3).

Eli, A. A., & Ali, A. (2024). Deep Learning Applications in Medical Image Analysis: Advancements, Challenges, and Future Directions. *arXiv preprint arXiv:2410.14131*.

Esteva, A., Kuprel, B., Novoa, R. A., Ko, J., Swetter, S. M., Blau, H. M., & Thrun, S. (2017). Dermatologist-level classification of skin cancer with deep neural networks. *nature*, *542*(7639), 115-118.

Hoult, D.I. and Bhakar, B. (1997), NMR signal reception: Virtual photons and coherent spontaneous emission. Concepts Magn. Reson., 9: 277-297. https://doi.org/10.1002/(SICI)1099-0534(1997)9:5<277::AID-CMR1>3.0.CO;2-W

Huthwaite, P., & Simonetti, F. (2013). High-resolution guided wave tomography. *Wave Motion*, *50*(5), 979-993.

Jie, H.J., Wanda, P. RunPool: A Dynamic Pooling Layer for Convolution Neural Network. *Int J Comput Intell Syst* **13**, 66–76 (2020). https://doi.org/10.2991/ijcis.d.200120.002

Krizhevsky, A., Sutskever, I., & Hinton, G. E. (2012). Imagenet classification with deep convolutional neural networks. Advances in neural information processing systems, 25.

Lakhani, P., & Sundaram, B. (2017). Deep learning at chest radiography: automated classification of pulmonary tuberculosis by using convolutional neural networks. *Radiology*, *284*(2), 574-582.

Lévy, D., & Jain, A. (2016). Breast mass classification from mammograms using deep convolutional neural networks. *arXiv preprint arXiv:1612.00542*.

Lostumbo, A., Suzuki, K., & Dachman, A. H. (2010). Flat lesions in CT colonography. *Abdominal imaging*, *35*(5), 578-583.

Özcan, E., & Arabacı, Z. (2024). Kanser erken tanı uygulamasının sağlık inanç modeli çerçevesinde incelenmesi: olgu sunumu. Kastamonu Üniversitesi Sağlık Bilimleri Fakültesi Dergisi, 3(1), 58-67. https://doi.org/10.59778/sbfdergisi.1378916

Polsinelli, M., Cinque, L., & Placidi, G. (2020). A light CNN for detecting COVID-19 from CT scans of the chest. *Pattern recognition letters*, *140*, 95-100.

Suzuki, K. Overview of deep learning in medical imaging. *Radiol Phys Technol* **10**, 257–273 (2017). https://doi.org/10.1007/s12194-017-0406-5

TÜİK, 2022-2023 Ölüm ve Ölüm nedenleri istatistiği, https://data.tuik.gov.tr/Bulten/Index?p=Olum-ve-Olum-Nedeni-Istatistikleri-2023-53709

Tükel, S. (2002). Dijital mamografi. *Tanısal ve Girişimsel Radyoloji*, *8*, 222-227.

Uzman Radyoloji, https://www.uzmanradyoloji.com/index.php/2018/03/16/beyin

W. Hao, W. Yizhou, L. Yaqin and S. Zhili, "The Role of Activation Function in CNN," *2020 2nd International Conference on Information Technology and Computer Application (ITCA)*, Guangzhou, China, 2020, pp. 429-432, doi: 10.1109/ITCA52113.2020.00096.

Yamashita, R., Nishio, M., Do, R.K.G. *et al.* Convolutional neural networks: an overview and application in radiology. *Insights Imaging* **9**, 611–629 (2018). https://doi.org/10.1007/s13244-018-0639-9

About The Authors

Mehmet DURSUN, PhD, is an Assistant Professor of Aviation Electrical and Electronic at Necmettin Erbakan University in Konya, Türkiye. He holds a PhD in Electric-Electronic Engineering from Selçuk University. His main areas of interest are signal processing, image processing, electronics and fiber optics communication systems.
E-mail: mehmet.dursun@erbakan.edu.tr, **ORCID:** 0000-0002-0558-6309.

Similarity Index:
The similarity index obtained from the plagiarism software for this book chapter is 18%.

The Impact of Video Compression Techniques on Visual Quality

Sabri KOÇER
Necmettin Erbakan University

Özgür DÜNDAR
Necmettin Erbakan University

To Cite This Chapter:
Kocer, S., & Dundar, O. (2025). The impact of video compression techniques on visual quality. In S. Kocer & O. Dundar (Eds.), *Next generation engineering: Smart solutions and applications* (pp. 246–259). ISRES Publishing.

Introduction

The rapid increase in the production of digital content has made the management of video-based data a significant engineering challenge. Today, video-sharing platforms, online educational content, and surveillance systems generate massive amounts of video data, placing a considerable burden on storage and transmission infrastructures. Therefore, compression technologies that can preserve the quality of high-resolution videos while transmitting them with minimal bandwidth have become one of the fundamental components of information and communication technologies.

Video compression not only serves to reduce data size but also improves user experience. For instance, the delivery of high-quality video streams with low latency is of critical importance in fields such as education, healthcare, and security. However, lossy compression processes can lead to the loss of visual details. These degradations can significantly affect the outcomes of artificial intelligence–based tasks, such as object detection and action recognition. Hence, video compression technologies need to be optimized not only in terms of file size but also in terms of preserving information integrity.

In recent years, next-generation video coding approaches have aimed to combine traditional compression techniques with machine learning–based algorithms to achieve more intelligent and content-adaptive compression processes. In this study, the performance of conventional compression methods (H.264 and H.265) was examined within the context of a real action recognition scenario, and the findings were evaluated to provide insights for future AI-assisted video compression research.

The increasing presence of digital video content in everyday life has emphasized the necessity of storing and transmitting such data efficiently. Higher resolutions (HD, 4K, and beyond), frame rates, and video durations have rendered traditional compression algorithms insufficient, thereby increasing the demand for more advanced video coding standards. Video compression techniques not only reduce data volume but also lower bandwidth requirements, enabling faster and more sustainable media streaming. However, during compression, potential degradations in image quality can cause critical errors, particularly in AI-based systems where video analysis is performed.

In this context, H.264 (Advanced Video Coding – AVC) and its successor H.265 (High Efficiency Video Coding – HEVC) have become the most widely used video compression standards in both academic research and industrial applications. While H.264 has been a reliable standard for media transmission for many years, H.265 offers comparable visual quality at lower bitrates, providing notable advantages for mobile devices and low-bandwidth environments. Nevertheless, quantitatively assessing the visual quality impact of such high compression ratios remains an ongoing research topic.

Among the most commonly used objective metrics for visual quality assessment are PSNR (Peak Signal-to-Noise Ratio) and SSIM (Structural Similarity Index). PSNR evaluates the pixel-level closeness between the compressed and original images, whereas SSIM represents structural similarity in a manner more consistent with the human visual system. In this study, the visual quality impacts of H.264 and H.265 codecs were comparatively analyzed using these two metrics, along with video file size.

For the comparison, a publicly available video dataset known as the "Hand Wash Dataset," which includes the World Health Organization's (WHO) recommended 7-step handwashing procedure, was utilized. This dataset, published on the Kaggle platform, consists of short videos captured by various users in different environments. The dataset serves as a benchmark for computer vision–based applications such as action recognition and video classification and provides a realistic scenario for evaluating post-compression visual quality.

Image and video compression technologies have become critical areas of research, especially with the widespread use of media transmission over the internet. Two prominent codecs in this domain, H.264 (AVC) and H.265 (HEVC), are widely employed across various applications due to their balance between compression efficiency and quality retention. In the literature, the performances of these codecs have been examined using objective metrics (such as PSNR, SSIM, and VMAF) and in different application contexts. Several comparative studies on H.264 and H.265 are noteworthy. For example, Khalid et al. analyzed video samples at different resolutions and revealed that H.265 can deliver equivalent visual quality to H.264 while reducing the bitrate by approximately 35–45%. The same study reported that H.265 achieved, on average, 0.8 dB higher PSNR values, while SSIM differences between the codecs could reach up to 0.02.

Similarly, Tan et al. compared H.264, H.265, VP8, and VP9 codecs in low-bandwidth scenarios, noting that H.265 achieved 30% higher compression efficiency and approximately 6% better SSIM scores than VP8. However, they also observed that H.265 encoding took approximately 2.2 times longer than H.264. In a large-scale study conducted by Van der Auwera et al., x264, x265, and libvpx codecs were evaluated, and it was emphasized that while HEVC (x265) achieved up to 40% data savings at low bitrates, maintaining visual quality in detailed scenes required increasing the bitrate. PSNR, SSIM, and VQM metrics were jointly used for quality assessment in this study.

Likewise, Koumaras et al. compared H.264 and H.265 codecs in live video transmission over LTE networks, analyzing codec performance optimized for mobile environments. They found that H.265 provided, on average, 42% lower data transmission requirements but exhibited greater temporal resolution fluctuations in highly dynamic scenes. In a more recent study, Agostini et al. compared H.264, H.265, and VVC codecs for 4K content, reporting that H.265 achieved comparable or higher VMAF scores while using approximately 47% less bitrate. Moreover, VVC demonstrated an additional 25% compression efficiency improvement over H.265. Furthermore, Öztürk and Güçlü showed that in real-time streaming scenarios, H.265 outperformed H.264 by 5–7% in PSNR and SSIM, although its encoding time was about 60% longer. These results indicate that codec selection should depend on the specific requirements of the application, particularly in time-sensitive environments.

The effects of codecs on visual quality are not limited to compression ratio but also influence the success rate of tasks that utilize such videos. Various fine-grained action recognition studies have demonstrated this effect. For instance, in scenarios such as handwashing, where sequential and detailed movements are analyzed, post-compression quality loss directly impacts classification accuracy. Farajidavar et al. developed a real-time action recognition system using a dataset of 292 videos depicting the WHO's 12-step handwashing process. Using a CNN-LSTM architecture, they found that when video resolution was reduced, classification accuracy dropped from 91% to 79%, underscoring the crucial role of visual quality in behavior recognition.

A similar finding was reported by Zuškin et al., who analyzed frame-by-frame annotations of handwashing actions performed by medical personnel and evaluated each step based on SSIM levels. When SSIM values exceeded 0.96, step recognition accuracy reached 93.5%, whereas it dropped to 68% when SSIM fell below 0.85. Benfatehi and Azouaoui, who classified handwashing steps using depth and RGB data, also noted that image quality had a significant effect on action classification accuracy. The accuracy rate decreased to about 73% for low-quality RGB inputs but increased to 87% when using uncompressed original frames.

All these studies demonstrate that video compression techniques should be evaluated not only in terms of file size but also concerning their impact on content-based analytical tasks. In applications that require the tracking of fine movements, such as healthcare-related gesture recognition, codec selection should prioritize the preservation of visual structures as well as compression efficiency. In this study, the “Hand Wash Dataset” was employed to perform a PSNR- and SSIM-based comparison of H.264 and H.265 codecs, presenting, for the first time in the literature, such an evaluation on this dataset, thereby contributing original insights to the field.

Video Sıkıştırma Performansları

This Figure 1 illustrates the overall comparison of video compression ratios between the H.264 and H.265 codecs. The visual representation highlights the superior efficiency of H.265, which achieves higher compression levels while preserving comparable visual quality. The figure provides a clear overview of the performance difference between the two codecs, emphasizing H.265’s capability to reduce data size more effectively without significant quality degradation

Figure 1

Comparison of Video Compression Ratios

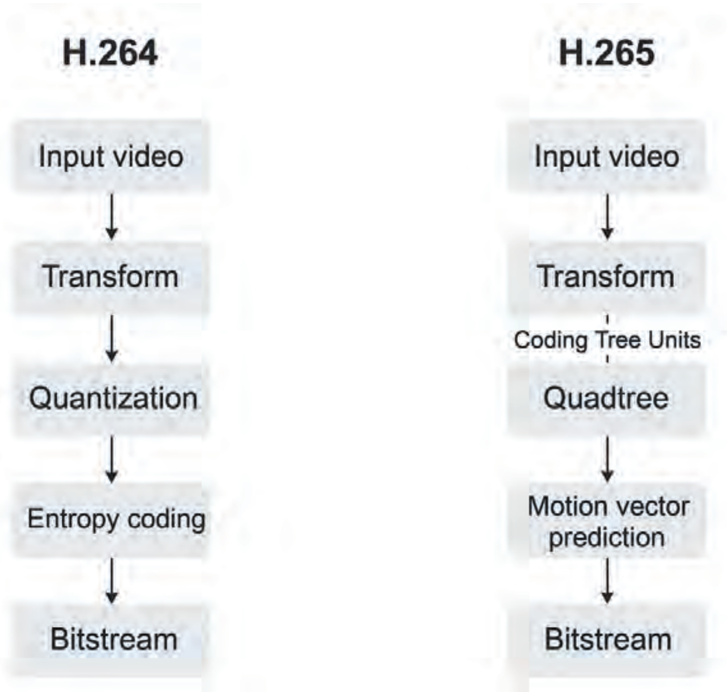

Figure 1 illustrates the main differences between the H.264 and H.265 video encoding architectures. Both codecs follow a similar overall pipeline consisting of transformation, quantization, and entropy coding; however, H.265 introduces several advanced mechanisms that improve compression efficiency and visual quality. In particular, H.265 replaces the fixed macroblock structure used in H.264 with a more flexible *Coding Tree Unit (CTU)* architecture, allowing variable block sizes that better adapt to spatial and motion complexities within the video.

The *Quad-tree partitioning* structure of H.265 provides greater flexibility in representing regions of varying detail, enabling higher compression ratios without significantly degrading image quality. Moreover, the *Motion Vector Prediction* stage in H.265 employs improved temporal prediction algorithms, reducing redundancy across frames more effectively. These innovations collectively allow H.265 to deliver up to 50% bitrate reduction at comparable visual quality compared to H.264, as confirmed in multiple benchmark studies.

Additionally, the diagram highlights that while both codecs share common principles such as discrete cosine transform (DCT) and entropy coding (CABAC), H.265's hierarchical and adaptive design makes it more suitable for high-resolution and low-bandwidth scenarios. The increased computational complexity of H.265, however, may lead to longer encoding times and higher energy consumption, emphasizing the trade-off between compression performance and processing cost.

When evaluating compression performance, not only the reduction in file size but also factors such as processing time, energy consumption, and device compatibility should be considered. Although the H.265 codec achieves higher compression ratios through advanced motion compensation algorithms, it also requires greater computational power. This can affect energy efficiency, particularly in hardware-constrained environments such as embedded systems and mobile devices. Therefore, the balance between compression efficiency and computational complexity is a key factor that directly influences codec selection.

Moreover, the differences between H.264 and H.265 are not purely technical but also application oriented. H.264 has been widely adopted for many years and is supported by most existing hardware platforms. In contrast, H.265, despite offering a more modern algorithmic structure, may pose challenges in terms of licensing and computational load. For example, in real-time video conferencing systems where low latency is essential, H.264 is still often preferred. Thus, codec selection is frequently determined not by technical superiority alone but by the requirements of the specific application scenario.

In future studies, performance comparisons can be conducted using the same dataset among newer codecs such as AV1, VVC (H.266), and AI-assisted compression algorithms. Such analyses would make significant contributions to literature by further optimizing video streaming quality and reducing data traffic.

In this study, the video compression performance and visual quality impacts of H.264 (AVC) and H.265 (HEVC) codecs were comparatively evaluated. The proposed methodology was based on quantitative and objective metrics, experimentally tested, and supported by graphical analyses. The evaluation was carried out using the *Hand Wash Dataset*—a dataset shared on the Kaggle platform that includes the seven-step handwashing procedure recommended by the World Health Organization (WHO). The videos within this dataset were selected because they realistically represent real-world action scenarios.

Each video was re-encoded using both H.264 and H.265 codecs with a fixed-quality principle through the FFmpeg framework. During the encoding process, a Constant Rate Factor (CRF) value of 23 was set as the target quality level, and the "slow" preset was used to ensure more efficient compression. This encoding policy provided an equal testing environment for both codecs, enabling a fair comparison under identical conditions. For the quality assessment of the compressed videos, two metrics were utilized: PSNR (Peak Signal-to-Noise Ratio) and SSIM (Structural Similarity Index).

The PSNR (Peak Signal-to-Noise Ratio) value is a metric that expresses the amount of error between the compressed and the original image on a logarithmic scale. It is calculated using the following formula:

$$PSNR = 10.\frac{(MAX^2)}{MSE} PSNR = 10.\frac{(MAX^2)}{MSE} \quad 1$$

Here, MAX represents the maximum possible pixel intensity in the image (commonly 255), while MSE (Mean Squared Error) denotes the average of the squared differences between corresponding pixels. SSIM (Structural Similarity Index), on the other hand, is a metric that models the human visual system more effectively by jointly evaluating luminance, contrast, and structural similarity. The closer the SSIM value is to 1, the more similar the compressed image is to the original.

For all videos, these two metrics were calculated on a frame-by-frame basis, and then the average PSNR and SSIM values were obtained for each video. In addition to quality metrics, the effects of the codecs on file size were also analyzed. For this purpose, the size of each compressed video was measured in kilobytes (KB) and compared with the original size to calculate the compression ratio using the formula below

$$Sıkıştırma\ oranı(\%) = 100 \cdot \left(1 - \frac{Sıkıştırılmış\ Boyut}{Orjinal\ Boyut}\right) \quad 2$$

All obtained metrics and size data were processed in the Python environment using the Pandas library, and visual analyses were performed using Matplotlib and Seaborn. The resulting graphs allowed for a clear observation of distribution differences, averages, and relationships between codecs.

Findings and Evaluation

As a result of the experimental analyses, significant differences were identified between the H.264 and H.265 codecs in terms of both compression ratio and quality metrics. When comparing the average compression ratios of all videos, the H.264 codec achieved an average compression rate of 72.04%, while the H.265 codec increased this rate to 79.10%. This indicates that H.265 provides approximately 7% more data savings than H.264. The comparative bar chart presented in Figure 2 visually highlights this difference, clearly demonstrating the superior compression efficiency of the H.265 codec.

This figure compares the average compression ratios achieved by the H.264 and H.265 codecs across all videos in the dataset. The bar chart clearly shows that H.265 provides a higher average compression ratio, achieving approximately 7% more data reduction than H.264. This result visually confirms the superior compression efficiency of H.265, which maintains similar visual quality while producing smaller file sizes.

Figure 2

Comparison of Average Compression Ratios

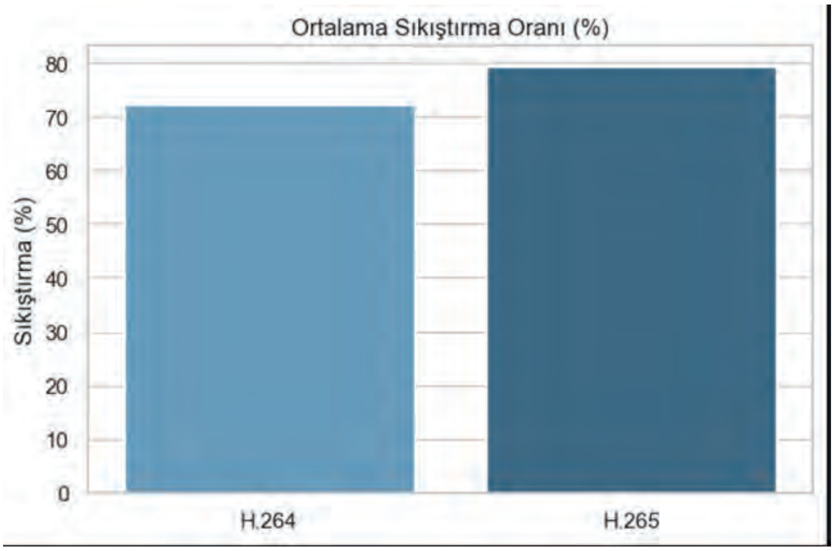

In terms of quality metrics, the average PSNR value for videos encoded with H.264 was 39.79 dB, while for those encoded with H.265, it was calculated as 40.06 dB. Although this difference is relatively small, it indicates that H.265 generally produces images closer to the original. As illustrated in Figure 3, the PSNR distribution for each codec reveals that H.265 exhibits a narrower spread with fewer outliers. This finding suggests that H.265 provides a more consistent and stable quality output across different video samples

This figure presents the distribution of PSNR values for H.264 and H.265 encoded videos in box plot form. The results show that H.265 exhibits a narrower distribution range with fewer outliers compared to H.264, indicating more stable and consistent quality across the dataset. This suggests that H.265 provides a more uniform compression performance, maintaining higher reliability in visual quality.

Figure 3

PSNR Distribution (Box Plot)

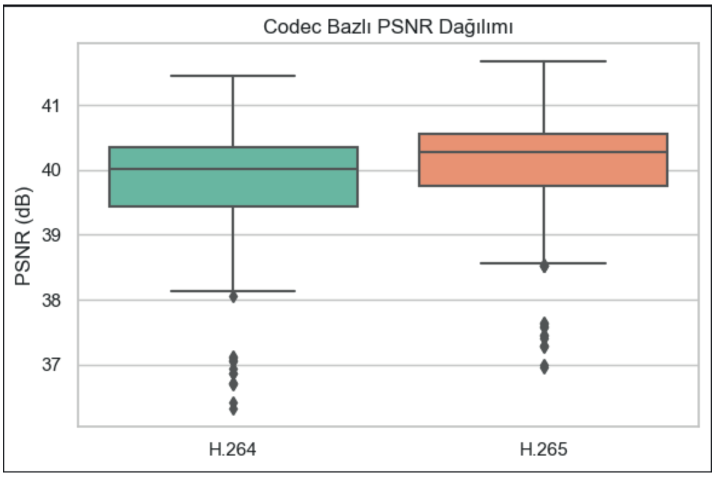

In terms of SSIM scores, only a very small difference was observed between the two codecs. The average SSIM value for H.264 was **0.9832**, while for H.265 it was **0.9824**. Although this difference is imperceptible to the human visual system, it indicates that H.264 performs slightly better in terms of structural similarity. As shown in **Figure 4**, the boxplot representation of the SSIM distribution demonstrates that the similarity levels of the two codecs converge closely; however, H.264 exhibits a more symmetrical distribution pattern, suggesting a marginally more uniform structural consistency.

This figure shows the distribution of SSIM values for videos encoded with H.264 and H.265 codecs. The boxplot reveals that both codecs produce closely converging similarity levels, with H.264 exhibiting a slightly more symmetrical distribution. This indicates that while structural differences between the two codecs are minimal, H.264 maintains marginally higher structural consistency across different samples.

Figure 4

SSIM Distribution

This figure illustrates the relationship between file size and PSNR values for H.264 and H.265 codecs. The scatter plot shows that H.265 maintains higher PSNR values even at smaller file sizes, demonstrating superior efficiency in preserving visual quality relative to data size. This trend confirms that H.265 achieves better quality-to-compression ratios compared to H.264, making it more effective for applications requiring both compact storage and high visual fidelity.

To analyze the relationship between compression performance and quality, a scatter plot was generated, as shown in Figure 5, illustrating the correlation between file size and PSNR. The graph reveals that H.265 maintains high PSNR values despite achieving smaller file sizes. For instance, for the video file HandWash_002_A_01_G01.mp4, H.264 produced a PSNR value of 39.24 dB at a file size of 540 KB, whereas H.265 achieved 39.49 dB at only 421 KB. This clearly demonstrates that H.265 is a more efficient algorithm in terms of the quality-to-data ratio, providing comparable or superior visual quality while significantly reducing file size.

Figure 5

Relationship Between File Size and PSNR

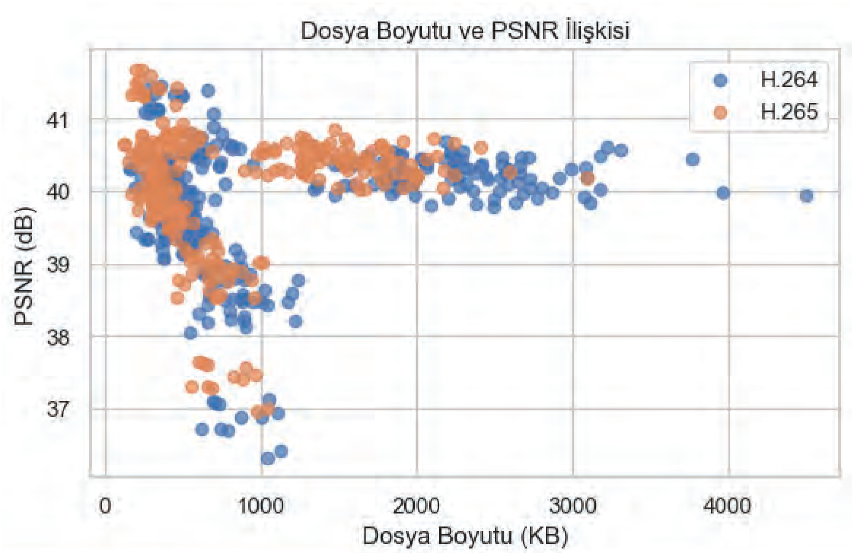

The average PSNR and SSIM values of the codecs, along with their standard deviations, are presented as error bar charts in **Figure 6**. The graph indicates that although the overall quality levels of the codecs are quite similar, **H.265** demonstrates a more homogeneous performance in terms of PSNR, while **H.264** shows a slight advantage in SSIM. The lower standard deviation observed for H.265 suggests that it provides a more consistent quality across different videos, indicating better stability in compression outcomes.

This figure presents the mean PSNR and SSIM values for H.264 and H.265 codecs along with their standard deviations, represented by error bars. The results indicate that while both codecs deliver comparable overall quality levels, H.265 shows a more consistent performance in PSNR, whereas H.264 maintains a slight advantage in SSIM. The smaller standard deviation of H.265 suggests greater stability and uniformity in compression performance across different video samples.

Figure 6

Mean Values with Error Bars (PSNR & SSIM)

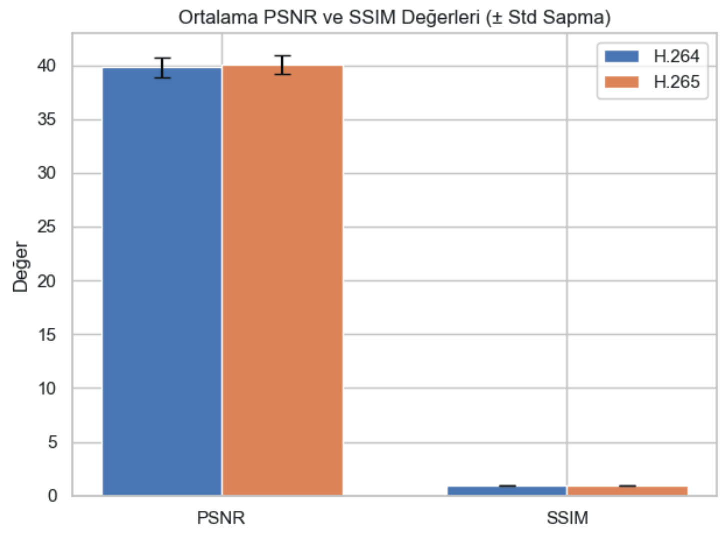

Finally, when comparing video-based compression rates, Figure 7 shows that H.265 consistently provides higher compression ratios than H.264 across nearly all videos in the dataset. For example, for the video *HandWash_004_A_01_G01.mp4*, H.264 achieved a compression rate of 70.15%, whereas H.265 increased this rate to 77.15%. This difference highlights the significant advantages offered by H.265, particularly in applications operating under limited bandwidth conditions, where efficient data transmission is essential.

Figure 7

Video-Based Percentage Compression Comparison

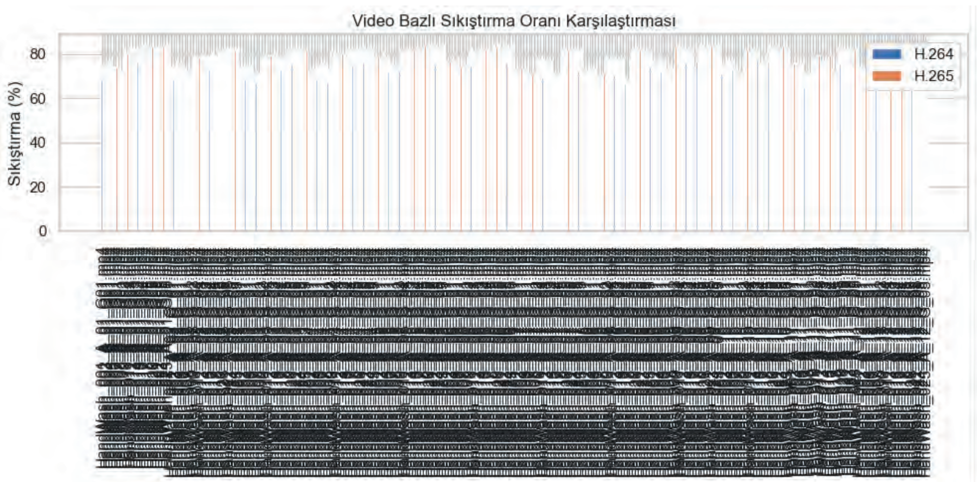

This figure compares the percentage compression rates of H.264 and H.265 codecs for each video in the Hand Wash Dataset. The results show that H.265 consistently achieves higher compression ratios across nearly all samples, demonstrating superior data reduction efficiency without significant loss of visual quality. These findings highlight the suitability of H.265 for applications requiring efficient transmission or storage under bandwidth constraints.

In conclusion, the experimental findings demonstrate that the **H.265 codec** achieves higher compression ratios compared to **H.264** while largely preserving visual quality—and, in some cases, even providing a slight improvement in PSNR. The difference in SSIM values between the two codecs is quite marginal, indicating that perceptual degradation at the human visual level is negligible. Therefore, H.265 stands out as a compression standard that offers superior data efficiency and consistency in visual quality.

The results obtained reveal that the differences between the codecs are not only statistically but also visually significant. Particularly under low-light conditions and in highly dynamic scenes, the detail preservation capability of H.265 is noticeably higher than that of H.264. This improvement stems from H.265's use of a finer-grained Coding Tree Unit (CTU) structure instead of the traditional macroblock-based approach employed by H.264. Furthermore, H.265 minimizes detail loss even in complex scenes by employing adaptive motion compensation block sizes, allowing for a more flexible and context-aware encoding process.

On the other hand, although SSIM scores between the two codecs are very close, H.264 occasionally yields slightly higher results. This is likely due to post-compression blocking effects that influence the structural characteristics of the image differently. While the human eye may not perceive these subtle distortions, action recognition algorithms are often more sensitive to such structural changes. Consequently, it is recommended that video quality assessments include model-based evaluation methods in addition to traditional metrics like PSNR and SSIM to achieve a more comprehensive understanding of codec performance.

Additionally, the experimental results highlight the relative stability of the codecs' average performance. H.265 produced more consistent quality outcomes across different videos, with lower variance values compared to H.264. This finding suggests that H.265 can be considered a more reliable choice for datasets containing high variability in video content, offering both efficiency and quality uniformity in diverse compression scenarios.

Discussion

The findings obtained in this study demonstrate that the H.265 codec provides approximately 7% higher compression efficiency compared to H.264. Graphical analyses and quantitative results indicate that H.265 achieves comparable or even superior PSNR values while producing smaller file sizes. The average PSNR value of 40.06 dB for H.265, compared to 39.79 dB for H.264, shows that H.265 is more advantageous in maintaining image quality during the compression process. The SSIM scores for both codecs exceeded 0.98, indicating that the structural distortions are minimal and imperceptible to the human visual system.

Although the differences in quality and compression performance between the codecs are technically significant, they must also be evaluated in terms of application context. H.265 has higher computational complexity and hardware requirements compared to H.264. According to the literature, H.265 requires up to twice the encoding time of H.264. This makes H.265 ideal for applications requiring high efficiency in video storage and transmission, while H.264 remains a more practical choice for real-time systems or hardware-constrained environments.

The comparison conducted using the Hand Wash Dataset, which contains action-based and motion-rich video data, evaluates not only the compression efficiency of the codecs but also their ability to preserve fine details without degrading quality. In computer vision–based applications, the structural integrity of visual data is crucial for maintaining model performance. In this context, H.265 stands out for its balance between quality and data efficiency, as well as its consistency; however, it should be considered alongside its hardware limitations depending on the intended application scenario.

The results of this study once again emphasize the importance of balancing compression efficiency and computational cost in video compression technologies. The high compression capability of H.265 offers substantial advantages in fields such as cloud storage, video surveillance systems, and medical imaging. However, this efficiency comes at the cost of longer encoding times and higher processing demands. Therefore, in low-latency applications, H.264 continues to be an effective and practical solution.

Furthermore, the Hand Wash Dataset used in this research serves as an important reference in the field of health technologies. In complex actions such as handwashing, quality degradation caused by compression not only affects the visual representation but also reduces the accuracy of behavioral analysis. This highlights the importance of developing content-aware dynamic compression strategies in future codec designs. For instance, "intelligent region-based compression" methods—where regions containing important actions are compressed less, while background areas are compressed more aggressively—could be explored as a promising approach for future video coding research.

Conclusion

This study presented a comparative analysis of the compression and visual quality performance of **H.264** and **H.265** codecs in short video samples. The results revealed that **H.265** achieved similar or even better PSNR and SSIM values than **H.264**, despite producing smaller file sizes. This makes H.265 an advantageous option, particularly for applications where data efficiency and bandwidth savings are essential. In future research, content sensitivity of the codecs can be analyzed by conducting tests at different resolutions and scene complexities, and system-level factors such as encoding time and computational cost can also be evaluated. The findings demonstrate that H.265 provides superior compression efficiency compared to H.264 while maintaining visual quality more effectively. However, the evolution of video compression technologies is not limited to preserving quality; future advancements are expected to focus on energy efficiency, artificial intelligence compatibility, and content adaptation. Future studies may extend this comparison to various resolution levels (e.g., 1080p, 4K, and 8K) and different types of video content, including high-motion, static, and low-light scenarios. Additionally, performing correlation analyses between subjective quality assessments based on human perception and objective quality metrics will enable a more comprehensive understanding of visual quality evaluation processes.

References

Agostini, L. V., Schilling, M. A., da Silva, B. D., & Sampaio, L. P. (2022). Objective Quality Assessment of HEVC and VVC Encoders for 4K Video. Applied Sciences, 12(13), 6386. https://doi.org/10.3390/app12136386

Benfatehi, H., & Azouaoui, O. (2022). Evaluation of Hand Washing Procedure Using Vision-Based Frame Classification. IEEE ISCV, 1–6. https://doi.org/10.1109/ISCV55373.2022.9784153

Bross, B., Chen, J., & Ohm, J. R. (2021). Developments in Video Coding Standardization After AVC, With an Overview of Versatile Video Coding (VVC). Proceedings of the IEEE, 109(9), 1463–1493.

Chen, Y., Ma, Z., & Wang, Y. (2020). Deep Learning–Based Video Compression: A Review. IEEE Transactions on Circuits and Systems for Video Technology, 30(9), 3219–3233.

Farajidavar, N., Abdelrahman, A., & Berg, T. (2022). Real-time Action Recognition for Fine-Grained Actions and The Hand Wash Dataset. arXiv preprint arXiv:2210.07400. https://arxiv.org/abs/2210.07400

Khalid, K. A., Ahmed, M. A., & Hussein, M. J. (2020). A Comparative Study Between H.264/AVC and H.265/HEVC. Kurdistan Journal of Applied Research, 5(1), 36–42. https://doi.org/10.24017/science.2020.1.6

Koumaras, H., Gardikis, G., & Kourtis, A. (2017). Comparative assessment of H.264 and H.265 encoded video quality over LTE. IEEE BMSB, 1–5. https://doi.org/10.1109/BMSB.2017.8094162

Ozturk, A., & Guclu, B. (2016). Performance Analysis of HEVC and H.264 Codecs in Real-Time Video Streaming. IEEE SIU, 1933–1936. https://doi.org/10.1109/SIU.2016.7789765

Tan, J., Tan, K. H., & Ghanbari, M. (2015). A performance comparison of H.264/AVC, H.265/HEVC, VP8, and VP9 codecs. IEEE ICCE-Berlin, 109–113. https://doi.org/10.1109/ICCE-Berlin.2015.7387608

Van der Auwera, G., Mirkovic, M., & Ebrahimi, T. (2016). A large-scale video codec comparison of x264, x265 and libvpx. SPIE 9971, 997116. https://doi.org/10.1117/12.2238495

Zhang, K., Xu, T., & Li, S. (2023). Region-of-Interest Adaptive Video Compression for Smart Healthcare Applications. Multimedia Tools and Applications, 82, 11987–12005.

Zuškin, S., Matijašić, M., Lovrenčić, I., & Magdalenić, I. (2021). Hand-Washing Video Dataset Annotated According to the WHO Guidelines. Data, 6(4), 38. https://doi.org/10.3390/data6040038

About The Authors

Sabri KOÇER, PhD, He graduated from the Electrical Engineering Department of Selcuk University. He completed his graduate and his doctorate in Gazi University. Currently, Necmettin Erbakan University, Faculty of Engineering, Computer Engineering is working. Electronics, Computer, Telecommunication, Signal Processing and Biomedical studies in the area.

Email: skocer@erbakan.edu.tr , **ORCID:** 0000-0002-4849-747X

Özgür DÜNDAR, PhD, works at Necmettin Erbakan University, Department of Astronautical Engineering. He graduated from the Electrical and Electronics Engineering Department of Selcuk University. He worked as an Automation Engineer for a while. His master's and doctorate degrees are from Selçuk University, Institute of Science and Technology, Department of Electrical and Electronics Engineering. Special fields of study are Automation, Robotic, Communication, Electromagnetic and Micro Strip Patch Antenna designs.

Email: ozdundar@erbakan.edu.tr , **ORCID:** 0000-0002-4142-4446

Similarity Index

The similarity index obtained from the plagiarism software for this book chapter is 12%.

Applications of Wearable Technologies in Healthcare and Their Medical Significance

Mehmet DURSUN
Necmettin Erbakan University

To Cite This Chapter:
Dursun, M. (2025). Applications of wearable technologies in healthcare and their medical significance. In S. Kocer & O. Dundar (Eds.), *Next generation engineering: Smart solutions and applications* (pp. 260–270). ISRES Publishing.

Introduction

Over the past decade, innovations in technology have contributed significantly to the evolution and optimization of diagnostic, therapeutic, and patient monitoring practices in healthcare systems. Wearable technologies and wearable medical devices, as key components of this transformation, enable the continuous and real-time monitoring of individuals' health data.

Wearable technology can be defined as a class of systems designed to function in continuous interaction with the human body, enabling the real-time acquisition and storage of physiologically, biochemically, and behaviourally relevant data. In contrast to consumer-focused wearable electronics, this study specifically addresses clinically validated wearable devices that are employed for diagnostic, monitoring, and therapeutic applications.

The requirement for in-hospital patient presence during extended data recording periods poses a significant challenge to acquiring data from multiple patients concurrently, primarily as a result of physical infrastructure limitations. Even for relatively simple measurements, appointments may need to be scheduled days or weeks in advance, which adversely affects hospital workload and patient flow.

Recent advancements in sensor technologies and developments in manufacturing processes have accelerated the evolution of wearable technology products by enabling the production of microelectronic components designed for programmable and mobile systems with reduced energy requirements (Kocer & Dundar, 2023). Furthermore, progress in wireless data transmission infrastructures, together with the analysis of collected data using artificial intelligence-based software and hardware architectures, has enabled these systems to generate diagnostically valuable outcomes, thereby facilitating their widespread and effective use in the healthcare field.

The current state of wearable technologies has progressed beyond serving merely as tools for individual health monitoring, enabling their integration into clinical decision support processes and positioning them as critical components of a significant transformation in healthcare delivery.

In the healthcare domain, wearable technologies provide significant benefits to healthcare professionals by supporting early disease detection; the monitoring and management of chronic conditions; the follow up of treatment and rehabilitation processes; and the development and optimization of personalized therapeutic approaches. For instance, the monitoring of oxygen saturation and respiratory patterns in respiratory diseases, blood pressure tracking in patients with hypertension, long term electrocardiographic monitoring in cardiovascular diseases, and the analysis of patients' activities of daily living and sleep patterns in neurological disorders can be cited as representative applications. Through these systems, continuously acquired patient data enable optimal monitoring of clinical status and allow treatment processes to be managed through individualized assessments when necessary.

Wearable Technological Devices Used in Healthcare

In the healthcare domain, technology can be defined as the set of systems, methods, and devices aimed at addressing specific health problems, enabling the earliest possible diagnosis, slowing down or halting disease progression, and ultimately developing definitive therapeutic solutions, thereby improving overall quality of life (National Center for Health Statistics, 2009).

Advancements in healthcare technologies not only enhance patients' quality of life but also reduce the duration of hospital stays, thereby significantly lowering personnel and hospitalization related costs for both healthcare providers and patients (Lichtenberg et al., 2014).

Historical analyses suggest that wearable technologies first appeared during the 13th century. (The College of Optometrists, 2015). The process began in the 1260s with the invention of eyeglasses and corrective lenses, followed by ear trumpets, regarded as the first hearing aids, in 1624, and the development of the first full eye glass contact lens in 1887. Particularly from the mid-20th century onward, advances in electronics most notably the invention of the transistor enabled the development of wearable devices incorporating electronic hardware. In 1958, Earl Elmer Bakken, an engineer by profession, designed and built the first wearable, portable cardiac pacemaker, which was subsequently implanted in a paediatric patient after a four-week trial period (Nelson, 1993).

Figure 1

The First Portable and Wearable Cardiac Pacemaker (Nelson, 1993)

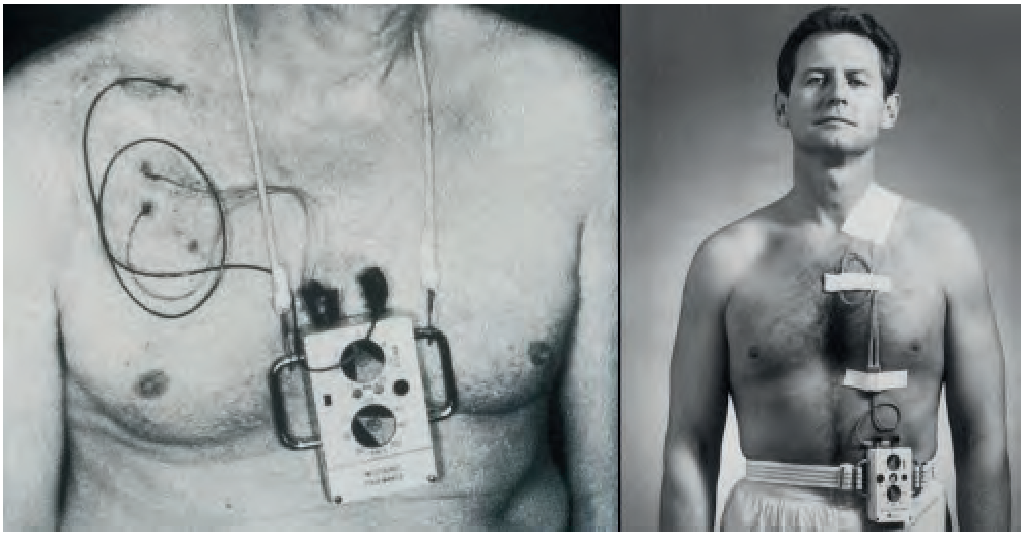

In 1971, soft contact lenses were introduced, followed by the first digital hearing aids in 1987, and insulin pumps were also brought into clinical use during the same period (Worcester Polytechnic Institute, 2017). From the year 2000 onward, a wide range of wearable devices applicable to healthcare have been introduced to the market. The biosensors employed in the development of these devices predominantly measure parameters such as body temperature, blood pressure, respiratory rate, heart rate, and physical activity, thereby enabling the collection of clinically valuable data for evaluation (Pantelopoulos et al., 2009).

The first quarter of the current century has witnessed remarkable advancements in electronics, microcomputers, wireless communication technologies such as Wi-Fi, radio frequency identification (RFID), and near field communication (NFC), as well as in nanotechnology, biocompatible materials, sensors, and artificial intelligence. Collectively, these developments have provided substantial momentum to the development of biomedical devices and systems that guide diagnostic and therapeutic practices in medicine, enabling rapid and outcome-oriented treatment processes. Some examples of these devices are illustrated in Figure 2 (Zhu et al., 2017).

Figure 2

Wearable Technology Products a. Wearable Earbud Device b. ECG Analyzer c. Smartwatch d. Wearable ECG e. Smart T-shirt f. Wrist-Worn Activity Tracker (Gandhi et al., 2019)

Fitness bands and smartwatches represent a prominent category of wrist-mounted wearable devices widely adopted for continuous health monitoring.

Figure 3

Health Monitoring Wristband-Fitnes band (Pebblecart, 2025)

These accelerometer-based devices utilize motion sensors to record parameters such as step count, estimated caloric expenditure, distance travelled, and duration of physical activity by detecting positional changes during movement (Kamišalić et al., 2018).

In addition, blood pressure measurement one of the most important indicators of an individual's health status can also be performed using wrist-worn devices such as smartwatches. For this purpose, some manufacturers have designed systems that estimate blood pressure using photoplethysmography sensors, while others have employed Hall-effect sensors. Alternatively, certain companies have developed models based on the conventional non-invasive cuff based measurement method in an effort to achieve higher accuracy (Lee et al., 2018). Figure 4 illustrates a model that measures blood pressure using a wrist-mounted cuff.

Figure 4

Smartwatch with Wrist-Mounted Cuff for Blood Pressure Measurement (Omron, 2025)

In addition, continuous and real-time glucose monitoring can be achieved by measuring glucose concentration in interstitial fluid via reverse iontophoresis using a subcutaneously implanted sensor (Vashist et al., 2021). However, such devices typically require calibration by fingerstick blood glucose measurements performed twice daily, during which the measured values are compared with the device readings. This process can be burdensome for patients. To eliminate these requirements, manufacturers have developed factory-calibrated models. As illustrated by an example in Figure 5, these models can also be paired with platforms such as smartwatches or smartphones, enabling convenient monitoring of the measured data.

Figure 5

Smart Glucose Monitoring System (Abbott, 2025)

In addition to arm-mounted devices, there are also systems capable of performing measurements by being worn in the ear, such as wireless earbud like devices illustrated in Figure 6. Equipped with biometric sensors, these systems can measure and record parameters including blood pressure, heart rate, oxygen saturation, step count, walking speed, distance travelled, location data, body posture, and respiratory rate.

Figure 6

Wearable Activity Tracker (Sensotrack, 2025)

Some wearable technologies are designed to serve a single, specific purpose. For instance, the Google Contact Lens, developed by Google and currently still in the research and development phase, is capable of detecting glucose levels in tears by embedding a miniature chip and a wireless communication module between two layers of soft contact lens material. When the glucose concentration exceeds or falls below predefined threshold values, a tiny LED is designed to blink to provide visual feedback to the user (Google, 2025).

Figure 7

Google Contact Lens (Google, 2025)

One of the wearable technologies used in healthcare is the electrocardiogram (ECG) monitor. This system can be easily worn and removed and is attached to the chest via a strap without the need for adhesives or fixation, enabling real-time and continuous ECG monitoring without a predefined time limitation. ECG measurements are performed wirelessly, and the system is also capable of monitoring respiratory rate, heart rate, body temperature, and physical activity. Through remote access by a medical specialist, reporting and analysis can be conducted while the patient is in a different location (Qardio, 2025).

Figure 8

Wearable ECG Monitoring Device (Qardio, 2025)

Another wearable technology product, whose design evolved through various models and sizes and was ultimately developed in the form of a T-shirt, is illustrated in Figure 9. This garment was developed in the laboratories of the University of Aveiro in Portugal and later licensed by a startup company. Structurally, it incorporates microelectronic components and was primarily designed as a bedside monitoring solution, being marketed under the brand name Vital Jacket. The T-shirt enables the measurement of ECG, blood pressure, heart rate, oxygen saturation, movement and fall events, walking speed, location data, body posture, and respiratory rate. Designed as a wearable garment, the product is washable and performs measurements using disposable electrodes (Cunha et al., 2010).

Figure 9

Vital Jacket (Rodrigues et al., 2018)

This product has been actively used in a study aimed at evaluating psychophysiological stress responses in police officers during duty shifts as well as on off-duty rest days. The results of the study demonstrated that the subjects experienced significantly higher levels of stress both during and after their shifts compared to healthy control groups (Rodrigues et al., 2018).

Smart socks can also be cited as an example of wearable technology products. Designed particularly for infants, these devices continuously monitor heart rate and oxygen saturation in real-time and notify parents through visual and auditory alarms as soon as critical threshold values predefined for potentially life-threatening conditions such as sleep related apnea, cardiac arrest, tachycardia, or decreased blood oxygen levels are reached. This early warning capability enables timely preventive measures to be taken or prompt medical assistance to be sought.

Figure 10

Smart Sock (Owletcare, 2025)

Conclusion

In conclusion, the widespread adoption of wearable technologies in healthcare has become a determining factor in the transformation of digital health applications. Through advanced data acquisition capabilities, these systems enable the continuous monitoring of individuals' physiological conditions, while the evaluation of collected data using artificial intelligence and big data analytics contributes to early disease detection and the development of risk-based health management strategies. This approach supports the evolution of healthcare services from a predominantly treatment-oriented structure toward a preventive and personalized model. Nevertheless, issues such as data security, clinical validation, and regulatory frameworks remain critical challenges that must be addressed to ensure the effective and sustainable integration of wearable medical devices into healthcare systems. Future technological advancements in this field are expected to have significant impacts on the accessibility, efficiency, and clinical decision-making processes of healthcare services.

References

Abbott, 2025, https://www.abbott.com/en-us/corpnewsroom/diabetes-care/freestyle-librelink

Alshahrani and A. Alsairafi, "Bone Fracture Classification using Convolutional Neural Networks from X-ray Images", Eng. Technol. Appl. Sci. Res., vol. 14, no. 5, pp. 16640–16645, Oct. 2024.

College Optometrists, 2025 https://www.college-optometrists.org/professionaldevelopment/college-journals/optometry-in-practice?page=10

Cunha, J. P. S., Cunha, B., Pereira, A. S., Xavier, W., Ferreira, N., & Meireles, L. (2010, March). Vital-Jacket®: A wearable wireless vital signs monitor for patients' mobility in cardiology and sports. In 2010 4th International conference on pervasive computing technologies for healthcare (pp. 1-2). IEEE.

Gandhi, B., Saxena, S., Jain, P. (2023). Emotion Recognition: A Review. In: Biswas, A., Islam, A., Chaujar, R., Jaksic, O. (eds) Microelectronics, Circuits and Systems. Lecture Notes in Electrical Engineering, vol 976. Springer, Singapore. https://doi.org/10.1007/978-981-99-0412-9_32 Kamišalić, A., Fister Jr, I., Turkanović, M., & Karakatič, S. (2018). Sensors and functionalities of non-invasive wrist-wearable devices: A review. Sensors, 18(6), 1714.

Google, 2025, https://blog.google/alphabet/introducing-our-smart-contact-lens/

Kocer, S. & Dundar O. (2023). Microcontroller-Based Design Electrostimulation (TENS) for Therapeutic Purposes.In S. Kocer. & O. Dundar (Eds.), Artificial Intelligence Applications in Intelligent Systems (pp. 120–144). ISRES Publishing.

Lee, S. S., Son, I. H., Choi, J. G., Nam, D. H., Hong, Y. S., & Lee, W. B. (2011). Estimated blood pressure algorithm for a wrist-wearable pulsimeter using Hall device. J. Korean Phys. Soc, 58(2), 349-352.

Lichtenberg, F. R., Tatar, M., & Çalışkan, Z. (2014). The effect of pharmaceutical innovation on longevity, hospitalization and medical expenditure in Turkey, 1999–2010. Health Policy, 117(3), 1-41.

National Center for Health Statistics (2009). Health, United States, 2009: With Special Feature on Medical Technology, Hyattsville.

Nelson, G. D. (1993). A brief history of cardiac pacing. Texas Heart Institute Journal, 20(1), 12.

Omron, 2025, https://www.omron-healthcare.com/products/heartguide

Owletcare, 2025, https://owletcare.com.tr/urun-kategori%CC%87leri%CC%87/urunler/

Pantelopoulos, A., & Bourbakis, N. G. (2009). A survey on wearable sensor-based systems for health monitoring and prognosis. IEEE Transactions on Systems, Man, and Cybernetics, Part C (Applications and Reviews), 40(1), 1-12.

Pebblecart, 2025 https://www.pebblecart.com/products/qore-smart-band?srsltid=AfmBOorxfsWZAoaU89TCzJZznZeRQbzq0WgDX4k6YTmugl3rsFWHDkF_

Qardio, 2025, https://www.qardio.com/qardiomd-cardiac-rehab/

Rodrigues, S., Kaiseler, M., Pimentel, G., Rodrigues, J., Aguiar, A., Queirós, C., & Cunha, J. P. S. (2018). Ambulatory assessment of psychophysiological stress among police officers: A proof-of-concept study. Occupational Health Science, 2(2), 215-231.

Sensotrack, 2025, https://www.gadgetreactor.com/2014/10/sensotrack-wearable-tracks-activity-earpiece/

Vashist, S. K. (2012). Non-invasive glucose monitoring technology in diabetes management: A review. Analytica chimica acta, 750, 16-27.

Worcester Polytechnic Institute, http://www.wpi.edu/about/history/pump.html

Zhu, X., Liu, W., Shuang, S., Nair, M., & Li, C. Z. (2017). Intelligent tattoos, patches, and other wearable biosensors. In Medical Biosensors for Point of Care (POC) Applications (pp. 133-150). Woodhead Publishing.

About The Author

Mehmet DURSUN, PhD, is an Assistant Professor of Aviation Electrical and Electronic at Necmettin Erbakan University in Konya, Türkiye. He holds a PhD in Electric-Electronic Engineering from Selçuk University. His main areas of interest are signal processing, image processing, electronics and fiber optics communication systems.

E-mail: mehmet.dursun@erbakan.edu.tr, **ORCID:** 0000-0002-0558-6309.

Similarity Index :

The similarity index obtained from the plagiarism software for this book chapter is 17%.

Next Generation Engineering: Smart Solutions and Applications is a peer-reviewed scientific book consisting of 17 invited chapters addressing cutting-edge developments in engineering and advanced technologies.

The book brings together original research spanning aerospace engineering, biomedical and health technologies, embedded systems, energy efficiency, and communication technologies.

It presents innovative solutions based on artificial intelligence, meta-heuristic optimization, image processing (YOLO), and natural language processing (NLP).

Several chapters focus on real-world system modeling, control, and optimization using intelligent algorithms.

Advanced studies on smart and autonomous systems for healthcare, agriculture, manufacturing, and service sectors are also included.

All chapters have been rigorously reviewed by at least two international referees to ensure scientific quality and originality.

This volume offers a comprehensive and up-to-date perspective on next-generation engineering research.

The book is published by ***ISRES Publishing*** for researchers, practitioners, and graduate students interested in smart engineering solutions.

ISRES Publishing